PNNL-25234

Pacific Northwest
NATIONAL LABORATORY

Proudly Operated by Battelle Since 1965

PNNL Development and Analysis of Material-Based Hydrogen Storage Systems for the Hydrogen Storage Engineering Center of Excellence

February 2016

K Brooks
K Alvine
K Johnson
K Klymyshyn
R Pires
E Rönnebro
K Simmons
M Weimar
M Westman

U.S. DEPARTMENT OF ENERGY

Prepared for the U.S. Department of Energy
under Contract DE-AC05-76RL01830

DISCLAIMER

PACIFIC NORTHWEST NATIONAL LABORATORY
operated by
BATTELLE
for the
UNITED STATES DEPARTMENT OF ENERGY
under Contract DE-AC05-76RL01830

Printed in the United States of America

Available to DOE and DOE contractors from the
Office of Scientific and Technical Information,
P.O. Box 62, Oak Ridge, TN 37831-0062;
ph: (865) 576-8401
fax: (865) 576-5728
email: reports@adonis.osti.gov

Available to the public from the National Technical Information Service,
U.S. Department of Commerce, 5285 Port Royal Rd., Springfield, VA 22161
ph: (800) 553-6847
fax: (703) 605-6900
email: orders@ntis.fedworld.gov
online ordering: http://www.ntis.gov/ordering.htm

This document was printed on recycled paper.
(9/2003)

PNNL-25234

PNNL Development and Analysis of Material-Based Hydrogen Storage Systems for the Hydrogen Storage Engineering Center of Excellence

K Brooks
K Alvine
K Johnson
K Klymyshyn
R Pires
E Rönnebro
K Simmons
M Weimar
M Westman

February 2016

Prepared for
U.S. Department of Energy
Energy Efficiency and Renewable Energy
Office of Fuel Cell Technology

Pacific Northwest National Laboratory
Richland, Washington 99352

Executive Summary

The Hydrogen Storage Engineering Center of Excellence is a team of universities, industrial corporations, and federal laboratories with the mandate to develop lower-pressure, materials-based, hydrogen storage systems for hydrogen fuel cell light-duty vehicles. Although not engaged in the development of new hydrogen storage materials themselves, it is an engineering center that addresses engineering challenges associated with the currently available hydrogen storage materials. Three material-based approaches to hydrogen storage are being researched: 1) chemical hydrogen storage materials 2) cryo-adsorbents, and 3) metal hydrides. The U.S. Department of Energy through its USDRIVE program has established storage system targets to ensure that light-duty vehicles using these technologies have driving ranges comparable to currently available vehicles while meeting commercial performance, cost, and reliability requirements. Specific target values are provided for specific years to help guide the system development. The targets include gravimetric and volumetric density, cost, operating temperatures and pressures, charging and discharging rates, transient behavior, and safety. As a member of this Center, Pacific Northwest National Laboratory (PNNL) has been involved in the design and evaluation of systems developed with each of these three hydrogen storage materials.

The scope of PNNL's efforts in the development of chemical hydrogen storage materials includes the following five major tasks as delineated below:

- Develop storage system designs that are amenable to vehicle applications. The goal of these storage systems is to meet the DOE Technical Targets for light-duty vehicles.
- Collect the key properties of the storage materials that are required to develop these system designs. Such things as thermodynamic characteristics, reaction kinetics, and transport properties were measured.
- Develop models that predict the system's performance in a vehicle and allow the storage system to be appropriately sized to meet a set of drive cycles.
- Perform experimental work to guide the system design of individual components and ultimately validate the storage system models.
- Develop system costs for production ranges between 10,000 and 500,000 units for the most viable systems developed. The cost estimates were developed using both top-down and a bottom-up approaches.

Work on chemical hydrogen storage materials was performed in both Phase I and Phase II. DOE determined not to continue work with chemical hydrogen storage materials in Phase III. The PNNL Phase-I work focused on the development of a storage system using solid ammonia borane as the storage material in the form of a powder or pellet. The PNNL Phase-II work focused on development of a chemical hydrogen storage material using slurry material. Rather than focusing only on slurry forms of ammonia borane, it included the evaluation of a slurry form of alane as well. Both phases included development of system designs, measurements of key properties, model development, validation testing, and cost modeling.

The scope of PNNL's efforts in the development of cryo-adsorbent materials includes the following five major tasks as delineated below:

- Design and assess the types of tanks that can be used for cryo-adsorbent materials. Assist in the down-selection of the tank type based on gravimetric and volumetric density, cost, and compatibility.
- Develop a method to cool the outer wall of the tank and reduce the refueling time and hydrogen required for refueling.

- Identify and consolidate, if possible, the balance of plant components for the target designs to meet performance targets, and reduce system mass, volume, and cost.
- Develop system costs for production ranges between 10,000 and 500,000 units for the most viable systems developed. The cost estimates were developed using both top-down and a bottom-up approaches.
- Identify system components that are chemically and physically compatible with the conditions of the cryo-adsorbent system.

In the case of cryo-adsorbents materials, the work performed in Phase I continued into Phase II and III with no significant change in scope. In Phase I, PNNL began the development of the *Tankinator* code that provides estimates of mass, volume, and material cost for Type I, III, and IV tanks. Further refinements were performed in Phase II. Modification of the balance of plant components and the cost estimates for the cryo-adsorbent systems were initiated in Phase I and completed in Phase III. Phase III included work in the development of the liquid nitrogen (LN2) cooled-wall tank concept accelerates the cooling process and minimizes the amount of cold hydrogen required during refueling. In Phase II, tensile and dynamic mechanical analysis tests performed on potential tank liner materials at cryogenic temperatures. This work was continued in Phase III with cryogenic compression tests being performed with polymers saturated with high-pressure (5000 psi) hydrogen.

The scope of PNNL's efforts in the development of metal hydrides was much smaller than the other two areas and included two tasks as delineated below:

- Identify and consolidate, if possible, the balance of plant components for the target designs to meet performance targets, and reduce system mass, volume, and cost.
- Develop system costs for production ranges between 10,000 and 500,000 units for one metal hydride-based system. As with the other materials, the cost estimates were developed using both top-down and a bottom-up approaches.

The metal hydride materials work did not continue beyond Phase I as a result of their low gravimetric density. As a result, the systems designs described here are not as well developed.

Acknowledgments

This material is based upon work supported by the U.S. Department of Energy, Office of Energy Efficiency and Renewable Energy, Fuel Cell Technologies. The authors would like to thank all members of the Hydrogen Storage Engineering Center of Excellence for stimulating discussions and Jesse Adams, Ned Stetson, and Bob Bowman for their outstanding support.

Acronyms and Abbreviations

AB	ammonia borane
AFA	anti-foaming agents
BOP	balance of plant
CAD	computer-aided design
CH	chemical hydride
CHS	chemical hydrogen storage
CHCoE	Chemical Hydride Center of Excellence
CNG	compressed natural gas
COMSOL®	interactive computer modeling program for solving coupled partial differential equations in one or more physical domains simultaneously
CRF	capital recovery factor
DMA	dynamic mechanical analysis
DOE	U.S. Department of Energy
EAB	elongation at break
ECTFE	ethylene chlorotrifluoroethylene
ENG	enhanced natural graphite
EPDM	ethylene propylene diene monomer
ETFE	ethylene tetrafluoroethylene
CSA	Canadian Standards Association
FCRF	fixed capital recovery factor
FEP	fluorinated ethylene propylene
GGE	gallons of gasoline equivalent
HDPE	high-density polyethylene
HSECoE	Hydrogen Storage Engineering Center of Excellence
HT	P-alkyl aromatics
HTR	synthetic hydrocarbons

KJMA	Kolmagorov-Johnson-Mehl-Avrami
LANL	Los Alamos National Laboratory
LDPE	low-density polyethylene
MATI	Modular Adsorbent Tank Insert
MC	methyl cellulose
MEPS	MEPS North American Steel
MLVSI	multilayer vacuum super insulation
MOF	metal organic frameworks
MOR	Materials Operating Requirement
MWAB	molecular weight AB (ammonia borane)
NETL	National Engineering Technology Laboratory
NPV	net present value
O&M	operations and maintenance
OD	outer diameter
OEM	original equipment manufacturer
OSU	Oregon State University
PCT	pressure-composition-temperature
PCTFE	polychlorotrifluoroethylene
PVDF	polyvinylidene fluoride
PEEK	polyaryletheretherketone
PFA	perfluoroalkoxy alkanes
PI	polyimide
PNNL	Pacific Northwest National Laboratory
PTFE	polytetrafluoroethylene
Simulink®	block diagram environment for multi-domain simulation and model-based design
SRNL	Savannah River National Laboratory
TC	thermocouple

TPD	temperature-programmed desorption
UHMWPE	ultra-high molecular weight polyethylene
UTRC	United Technologies Research Center

Units and Measurements

°C	degrees Celsius
A	area (m^2)
A’	Arrhenius factor (s^{-1})
C	concentration (ppm)
Cp	heat capacity (J/kg/K)
D	radiator diameter (m)
D	reactor diameter (m)
F	mass fraction
H	heat-transfer coefficient ($W/m^2/K$)
k	reaction rate (s^{-1})
k’	thermal conductivity (W/m/K)
k’’	constant for β calculation (1/°C)
L	length (m)
$\dot{m}$	mass flow rate (kg/s)
M	mass of CH (kg)
MW_{CH}	molecular weight of chemical hydride
$\dot{n}$	molar flow rate (mol/s)
n	exponent
$n_{H2total}$	total hydrogen in ballast tank
Nu	Nusselt Number
P	pressure (atm)
p_{fin}	fin pitch

Pr	Prandtl Number
Q	heat (kW/m)
Re	Reynolds Number
T	temperature (K)
t	time (s)
u	velocity (m/s)
V	volume (L)
x_{CH}	fraction chemical hydride
y	turbulator twist ratio
z	axial distance (m)
α	extent of reaction
β	stoichiometric ratio of hydrogen to CH
δ_{fin}	surface area ratio for the radiator fins
ΔH	reaction enthalpy (kJ/mol H_2)
P	density (kg/m^3)

Subscripts

air	relating to air
ambient	ambient
ballast	associated with the ballast tank
BT	ballast tank
bulk	bulk property of slurry
CH	chemical hydride
CHP	chemical hydride product
exterior	outer surface of the radiator tube
FC	fuel cell
feed	feed

fin	fin dimensions
heater	heater
HX	heat exchanger
i	reaction number (e.g., 1, 2)
in	inner diameter reactor
inert	inert material (slurrying agent)
innerwall	inner wall of the recuperator
interior	inner surface of the radiator tube
loss	heat loss
metal	metal for reactor or radiator
out	outer diameter of a reactor
outerwall	outer wall of the recuperator
PI	proportional-integral controller value
radiator	associated with the radiator
rxn	reaction property
setpoint	associated with a set point value
slurry	slurry
stir	reactor stirrer
target	associated with a target value

Contents

Figures

Tables

1.0 Introduction

Commercializing an integrated fuel cell power system for automotive applications is a topic that has received continued interest because of the potential political and environmental benefits. The political benefits of such a system include the need to remove or relax the nation's dependence on foreign oil. Hydrogen for a fuel cell can be generated using non-petroleum processes. The environmental benefits include reduction in vehicle emissions such as pollutants and greenhouse gases—the only byproduct being water. Hydrogen fuel cells also offer unprecedented vehicle efficiencies of up to 60% (DOE 2014a).

One of the shortcomings of fuel cells is the low gravimetric and volumetric densities of the hydrogen fuel. Gaseous hydrogen must be stored at low temperature (≈80 K) and/or high pressure (>350 bar) to provide acceptable driving ranges in automobiles. Liquid hydrogen offers increased volumetric capacities but requires storage temperatures around 20 K (DOE 2014b). In both cases, dormancy and safety issues are the critical challenges in storing neat hydrogen for automotive applications.

In an attempt to remove the limits imposed by the gravimetric and volumetric storage capacities of neat hydrogen, DOE's Fuel Cell Technologies Office has funded the HSECoE. The HSECoE is a team of universities, industrial corporations, and federal laboratories with the mandate to develop lower-pressure, materials-based, hydrogen storage systems for hydrogen fuel cell, light-duty vehicles (DOE 2014c).

The objective of HSECoE is to develop the necessary hardware to build material-based hydrogen storage systems for light-duty vehicle applications. The storage systems should provide similar performance, cost, and reliability as currently available vehicles. The material-based hydrogen storage systems have the advantage of operating at lower pressures and closer to ambient temperature as compared to gaseous hydrogen storage or cryogenic liquid hydrogen storage. Three materials are under consideration as part of this center: 1) chemical hydrogen storage materials (CHS), 2) cryo-adsorbent materials, and 3) metal hydrides. In each of these categories, materials were identified and storage systems designed around their properties.

Chemical hydrogen storage materials require breaking of chemical bonds to release their hydrogen. They are defined as materials requiring off-board processing to regenerate them before they can be reused. Although many chemical hydrogen storage materials have been investigated, the research reported here was based on ammonia borane (AB) and alane, two relatively high gravimetric capacity materials. These materials decompose to produce hydrogen at relatively moderate temperatures (~200°C). Transporting the material on and off the vehicle and through the reactor and performing separations to achieve high hydrogen purity are the challenges of this class of materials.

Cryo-adsorbent hydrogen storage materials rely on physical adsorption of hydrogen on high-surface-area materials at cryogenic temperatures to achieve high storage capacities. Although these materials require cooling similar to liquid hydrogen, liquefaction is not required and the temperature and pressure of these systems are less extreme. In this case a metal organic framework (MOF-5) was selected as the material upon which the system was designed. This material and other similar adsorbents operate over the range of 80 to180 K and at pressures near 100 bar. Meeting the volumetric density and addressing the cooling required during refueling and dormancy are the challenges with these materials.

Metal hydride storage materials undergo chemical reaction during the charging and discharging process similar to chemical hydrogen storage materials, however, the reaction is reversible and they can be refueled onboard the vehicle with the addition of high-pressure hydrogen. Although a suitable metal hydride was not identified, sodium alanate was used in the development of a metal hydride storage system. The challenge with these materials is identifying a material with a low gravimetric density and a high thermal conductivity. The large parasitic loss associated with hydrogen production is another challenge with this class of materials.

This report describes the work performed by Pacific Northwest National Laboratory (PNNL) on the development of these three systems for the HSECoE. Cost estimates for all three systems were developed as part of the PNNL scope and are included in Chapters 2, 3, and 4 of this report. In addition, Chapter 2 describes the system development and testing of chemical hydrogen storage materials. During Phase 1 of the project, work emphasized the development and testing of materials and components for a solid material system design. Phase 2 of the project changed the emphasis to use slurry material to suspend the chemical hydrogen storage materials for easier transport. Both these approaches are described. Chapter 3 describes the work performed on cryo-adsorbents. PNNL's work did not involve direct testing of the adsorbent materials, but rather focused on development of the key system components including the tank, the balance of plant (BOP), and an approach to cooling the walls. Chapter 4 describes the work PNNL performed on metal hydrides. Beyond the cost estimate performed at PNNL, only BOP components were identified for the metal hydride system.

2.0 Hydrogen Storage using Chemical Hydrogen Storage Materials

2.1 Introduction and Objective

Engineering of onboard hydrogen storage materials for fuel cell applications is one of the key objectives of HSECoE program. The goal is to develop, design, model, test, and optimize the necessary hardware required to build hydrogen storage systems for light-duty vehicle applications (DOE 2014a). This chapter contains the work that has been performed by the Pacific Northwest National Laboratory for the DOE's HSECoE in developing chemical hydrogen storage (CHS) materials.

Chemical hydrogen storage materials typically release large amounts of hydrogen at low temperatures (<200°C), but cannot easily be rehydrided like a metal hydride. Instead, regeneration schematics have been developed and some of the most promising materials are AB and alane, which were CHS candidates considered during this program.

These CHS materials are solids at room temperature. Initial work with these materials was performed using them in their solid form as pellets or powders. Work focused primarily on neat AB and mixtures of AB and other materials. Studies were performed to understand the properties of these materials as powder and processes were developed for transporting these materials on and off-board a vehicle, conveying them within the vehicle during reaction to produce hydrogen. Ammonia borane showed good reaction kinetics and adequate flowability as a powder or pellet. The primary challenges of using solid AB for hydrogen storage on a vehicle are provided in Table 2.1. The challenges of designing and validating the solid AB-based CHS system are primarily associated with material movement and the need to maintain a low-mass and low-cost system. In addition, there was the challenge of measuring material properties and demonstrating the key components with minimal available AB.

Table 2.1. Challenges Addressed with Solid AB

Challenge Topic	Challenge Description
Material Movement	Move powder/pellets of fresh CHS material onboard and spent CHS material off-board within the DOE required 4.2 minutes (2010 technical target for 5 kg hydrogen)
Material Movement	Prevent H_2 loss and maintain high-pressure storage within the CHS system while reacting a solid material and the required rate to meet DOE required 80-kWe system
System Mass/Cost	Minimize system mass and cost while maintaining its functionality
System Validation	Demonstrate operating of critical system components with minimal AB material

At the end of Phase I of this HSECoE project, a decision was made to remove solid CHS materials from consideration by the HSECoE. The challenge of moving solid pellets through a pressurized system while preventing loss of hydrogen to the environment was considered significant enough that the use of solids was rejected in the HSECoE. Alternatively, pure liquid systems would be ideal in terms of transport both within and outside of the vehicle. However, successfully developing a solvated fluid at high concentration that remains a liquid both pre- and post-reaction has been elusive. As a result, the focus of the research in Phase II was the development of CHS materials in a slurry form. Work was expanded beyond AB to alane during Phase II.

The primary challenges of using slurry AB and alane for hydrogen storage on a vehicle are provided in Table 2.2. Once again, material movement, minimizing system mass and cost, and successfully demonstrating the system components on a small scale were similar challenges to those addressed with solid AB.

Table 2.2. Challenges addressed with Slurry AB and Alane

Challenge Topic	Challenge Description
Material Movement	Challenges of pumping slurries and preventing settling and plugging in the lines and tanks
Material Movement	Challenges of reacting the materials and separating the H_2 from the slurryagent and any impurities
System Mass/Cost	Minimize system mass and cost while maintaining its functionality
System Validation	Demonstrate operating of critical system components with minimal AB material

This report summarizes of the work performed by PNNL with both solid and slurry CHS materials.

2.2 Phase I: Evaluation of Solid Ammonia Borane

Ammonia borane has one of the highest hydrogen storage capacities of any CHS material. Its use as a solid maintains that high gravimetric capacity. Solid powders and pellets have been moved and processed in a variety of industries, and as a result, technologies are available that can be readily applied to the vehicle application of CHS for hydrogen storage. The Chemical Hydride Center of Excellence (CHCoE), which preceded the HSECoE, developed conditions for the successful reaction of AB. By adding methyl cellulose (MC) to the AB, foaming that prevented good heat transfer and hydrogen recovery was reduced (Ott 2010). While the CHCoE had done significant work in understanding the thermodynamics and kinetics of AB, the properties associated with transport of a solid material had not been investigated. Work in the HSECoE has focused primarily on these material properties that specifically affect system design.

At the beginning of Phase I, no system design had been selected. As a result, wide-ranging innovative system-design concepts were evaluated, and transient models of these systems were developed. Significant effort was made to evaluate these concepts both on paper and experimentally to determine that approach that should be pursued. In the end, only a single system design could be evaluated completely relative to the DOE 2010 Technical Targets and system costs estimated for 10,000 and 500,000 units. The DOE, the HSECoE technology team, and all of the HSECoE partners provided input for the decision regarding the system design to focus on during Phase I.

2.2.1 Material Operating Requirements

As part of the HSECoE, the Materials Operating Requirement (MOR) Technical Area provided measured data of materials engineering properties to support the systems modeling effort and other engineering efforts within HSECoE. The materials engineering properties include hydrogen capacity, kinetics, thermodynamics, densities of reactants and products, form factor, and thermal conductivity. At PNNL, the MOR related to CHS materials was established. Key tasks were to select candidate materials for the materials groups and provide materials engineering properties to fill in gaps in the literature and to validate the systems modeling.

This work also targeted optimizing the performance characteristics of the hydrogen storage system as a whole by reducing its size, weight, and cost. This is accomplished in the MOR task by better understanding and tailoring of bulk storage media for improved performance within the storage system. Materials engineering properties were measured for experimental validation of the systems models when literature data are not available. Materials engineering properties to support the sensitivity analysis and transportability studies included thermal conductivity, kinetics, hydrogen capacity, heat of reaction, thermal stability, and form factor. Data from the literature and measured data were used in systems modeling in an iterative process between experiments and modeling to validate and refine the system models.

2.2.1.1 Down-Selection Criteria

For a material to be considered for application within the HSECoE, it must first pass minimum screening criteria that give the HSECoE a rough assessment of its capabilities. A material that passes the screening criteria is selected for further consideration within the HSECoE. Materials that do not improve system performance relative to selected materials and that cannot meet DOE technical targets are not considered for further evaluation.

The selected materials were grouped into selected (Tier 1 and 2) and rejected (down-selected) materials. For Tier 1 "Developed Materials," a database was assembled, and appropriate parametric models developed and verified where system data were available. Tier 2 "Developing Materials" were selected as promising candidate materials for system consideration.

- *Developed Materials, Tier 1*: System analysis is being performed on up-selected candidates and necessary engineering properties measured.
- *Developing Materials, Tier 2*: Up-selected materials undergoing performance evaluation. Material properties are determined and measured if necessary.
- *Down-Selected Materials*: Materials found to not improve system performance relative to up-selected materials, and thus not for further consideration.

The minimum screening criteria for CHS materials are as follows:

- Capacity: >9wt% materials capacity to meet the DOE 2015 system target
- Desorption: Room Temperature to 150°C rate >30g/s
- Enthalpy of reaction: <20kJ/mol
- Crystal density: >1g/cm^3
- Availability: (quantitative cost and time; that is, <$10,000/kg with delivery in 30 days).

The materials considered for CHS were AB, lithium alanate, and alane. Each of these materials was evaluated against the established MOR. Based on this evaluation, solid AB was selected as a baseline material for further development because it met the "minimum screening criteria" for chemical hydrogen storage and also showed promise for meeting DOE targets. It was up-selected to Tier 1, and system modeling was initiated. Although it meets most of the criteria within at least 40%, there were two hurdles that could not be resolved if solid AB were to be used "as is"—excessive foaming upon hydrogen release and generation of volatile impurities—both of which would be detrimental for the fuel cell. We therefore decided to down-select solid AB "as is," and move forward with composite materials, specifically solid AB, preferably mixed with MC, as a Tier 2 Developing Material.

2.2.1.2 Material Properties

Material properties of reaction kinetics, dynamic mechanical analysis (DMA), and angle of repose were measured for the AB:MC mixture to provide the needed information to design a storage system and develop comprehensive system models. The approach to measuring these properties as well as the results of these test are described in the subsequent sections.

Reaction Kinetics

A key input parameter for reactor modeling is kinetics. Studies on reaction kinetics are valuable when engineering the size of a device that might be used to release hydrogen from hydrogen carriers. The AB decomposition reaction is an irreversible chemical nucleation and growth reaction that occurs with hydrogen release. A major difference between reversible metal hydrides and exothermic CHS is that

Sievert's data of a reversible metal hydride can be performed under equilibrium conditions by dosing hydrogen in aliquots to collect isotherms at a set temperature. For a CHS material with an exothermic hydrogen release reaction, it is to some extent self-propagating; thus, temperature will not be fixed and equilibrium states are difficult to obtain, and to our knowledge, performing isotherms is not possible. In this section, we discuss our experimental kinetics study.

Studies of hydrogen capacity and bulk reaction kinetics of AB and AB/MC composites at various operating conditions were conducted to provide system modelers with information needed to update their kinetics models. These results are also documented in the literature (Choi et. al. 2014). To take measurements at higher temperatures, a Sievert's type pressure-composition-temperature (PCT) gas-solid reaction instrument (Setaram) was adopted to characterize the kinetics of hydrogen release reactions of AB and AB/MC composites at various target temperatures (160 to 300°C) under 1 bar of hydrogen backpressure. Temperature-programmed desorption (TPD), which is a common technique for surveying the overall hydrogen storage behavior of solid hydride materials, was applied in this study. During TPD, temperature is increased at a constant heating rate. The pressure change during the temperature ramp is measured in a calibrated volume and converted to corresponding percentages of hydrogen release. A cold trap filled with dry ice was placed between the pressure transducer and the sample holder to capture undesirable and condensable byproducts such as borazine ($N_3B_3H_6$) or diborane (B_2H_6) during the dehydrogenation process. Our preliminary results indicated that the amount condensable byproduct is temperature dependent. We assumed that the pressure change from the large amount of hydrogen gas would not be substantially impacted by gas cooling and the condensable byproducts removal. By removing the byproducts, we could study the kinetics of hydrogen release without impacts from other species.

Based on the maximum release rates of first equivalent, the value of hydrogen release rate at 300°C per gram AB increased almost twice compared with that of release rate at 160°C
. The hydrogen release rate was calculated from the experimental slope (shown in Figure 2.1) occurring during heating (after the induction period) by simply calculating the gram of release hydrogen per gram AB.

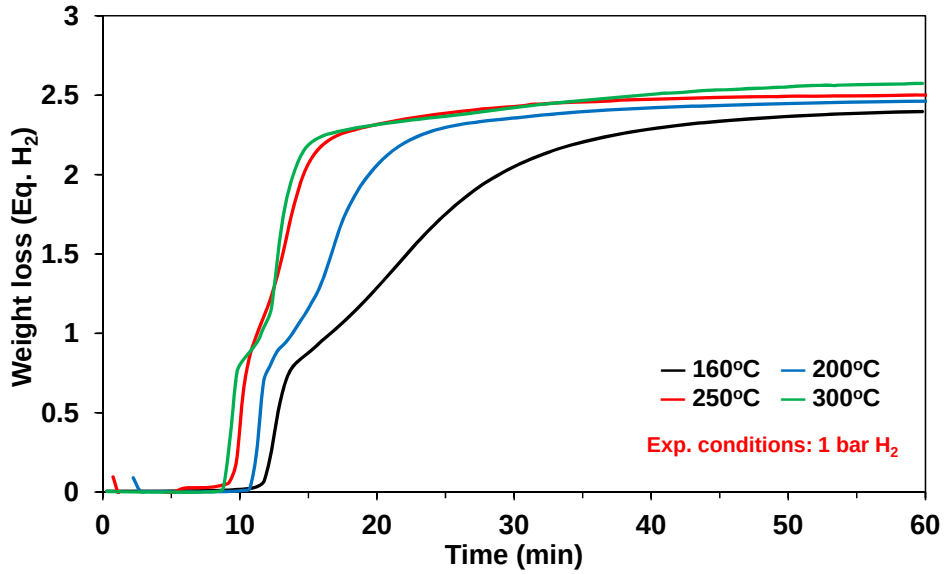

Figure 2.1. TPB Measurements of Hydrogen Capacity and Bulk Kinetics Comparisons of Solid AB at 160°C (black), 200°C (blue), 250°C (red), and 300°C (green)

Figure 2.2 presents a comparison of the hydrogen capacity and bulk kinetics of the AB/MC composite material from 160 to 300°C. The kinetic rates are rapid, and the sharp feature of the curve is most likely due to slow software response to data collection. The dehydrogenation experiments were carried out

under the same conditions as described above. We attribute the time lag observed in all the measurements to the non-isothermal heating process. First, the measured hydrogen capacities of AB/MC were comparable to the theoretical value (i.e., ~2.5 equivalents or ~16.2 wt% of hydrogen) between 160°C and 300°C under 1 bar hydrogen pressure. Note that the experimental weight loss from AB/MC composites is normalized. Second, the TPD profiles in Figure 2.2 indicate that there are substantial differences in the onset dehydrogenation temperature and time for complete hydrogen release between neat AB and AB/MC composites.

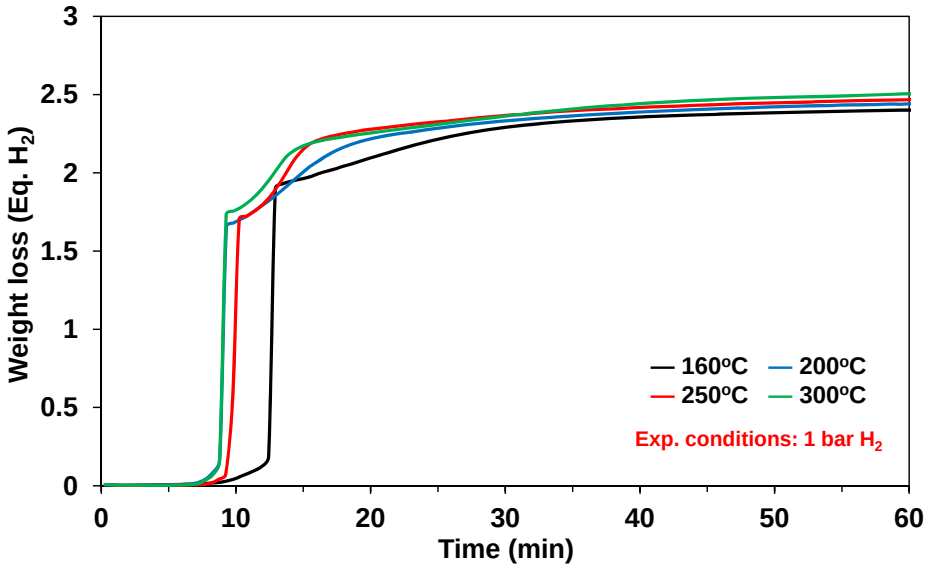

Figure 2.2. TPD Measurements of Hydrogen Capacity and Bulk Kinetics Comparisons of Solid AB/MC at 160°C (black), 200°C (blue), 250°C (red) and 300°C (green)

The result shows that the first equivalent hydrogen started to release at ~95°C from AB/MC composites, which is approximately 22°C lower than that of neat AB. In addition, more than 2.0 equivalents of hydrogen were released within 16 minutes from AB/MC composites, which is considerably faster than that from neat AB. When comparing desorption of AB and AB/MC in Figure 2.1 and Figure 2.2, it can be seen that the hydrogen release rate for AB/MC is significantly faster than for AB. The release rate of AB/MC is so fast that our instrument could not record it; hence, the curves initially have the features of straight-line features that eventually change to curve-like features. Because we were not able to record the release rate adequately, it is difficult to provide an estimate for how much faster the hydrogen release rate of AB/MC is compared to AB, but roughly, it is at least two times faster.

Overall, the measured hydrogen capacities of AB and AB/MC composites were comparable to the theoretical value. The hydrogen release rates of AB were, as expected, faster as the target temperatures increased from 160 to 300°C under 1 bar hydrogen pressure. Because of the excessive foaming that accompanied hydrogen release, spent AB is tough, sticky foam and, therefore, is difficult to remove from the sample holder, which indicates poor ability to physically move the material within a system. However, AB/MC composites maintained their form factor and reduced foaming (no foaming was observed under these conditions) when hydrogen was released under the experimental conditions. The powder could be removed easily from the sample, which indicates the material could move throughout a system. The desorption kinetics from the Sievert's apparatus compared to PNNL's Burette system are shown in Figure 2.3. Because the hydrogen release from AB was recorded as a function of time at isothermal reaction temperatures in the Burette system (Rassat et al. 2010), a time lag from AB and AB/MC composites in the PCT measurement was offset for the direct comparison. Maximum hydrogen capacity (i.e., ~2.5 equivalents or ~16.2 wt% of hydrogen for the Burette system and ~2.25 equivalents or 14.6

wt% for PCT system) was obtained after about 30 minutes in all cases at 160°C under atmospheric hydrogen pressure.

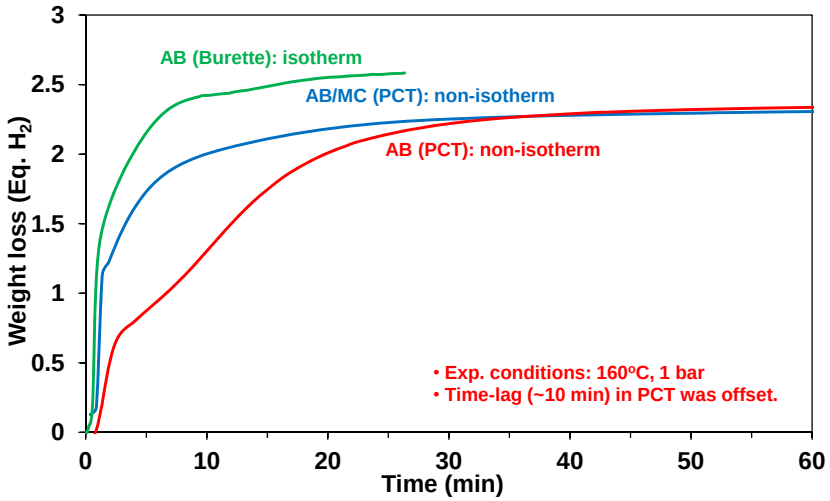

Figure 2.3. Hydrogen Capacity and Bulk Kinetics Comparisons of AB and AB/MC at 160°C using Different Experimental Techniques

To illustrate the need for operating AB at temperatures above 160°C, Figure 2.4 shows six hydrogen-release experiments carried out between 100°C and 350°C. As can be seen, at 100°C, hydrogen release is very slow, and only a fraction of maximum hydrogen capacity can be obtained within 6 hours. For practical applications, the temperature needs to be 160°C and above to obtain necessary hydrogen release rate and hydrogen capacity for practical applications.

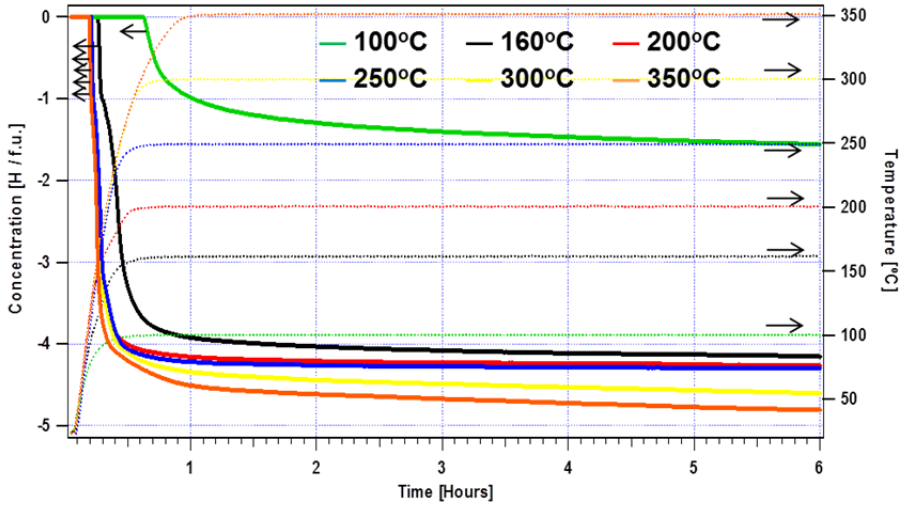

Figure 2.4. Reaction Rates of AB over the Temperature Range of 100°C to 350°C

When operating a fuel cell, a backpressure of hydrogen will exist. Therefore, although it is very common to measure release rates of hydrogen storage materials under vacuum, we also measured at 1 and 5 bar of hydrogen pressure at 160°C, and the results are plotted in Figure 2.5. Overall, kinetic rates are not affected significantly by pressure; however the hydrogen capacity did increase with pressure.

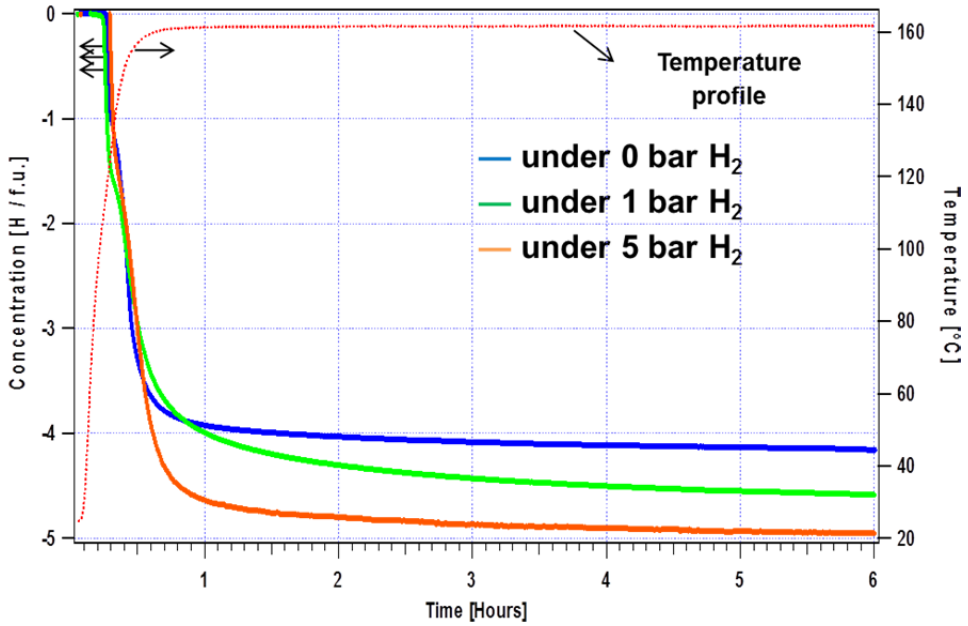

Figure 2.5. Reaction Rates of AB at Two Hydrogen Pressures (1 and 5 bar)

Summary of Kinetic Experiments

We measured kinetics of hydrogen release from AB and from AB/MC composites and found that it is necessary to operate at temperatures above 110ºC to obtain rapid kinetics for practical applications. The experimental data were used to validate kinetics models. We investigated the kinetics of hydrogen release from AB and from an AB-methyl cellulose (AB/MC) composite at temperatures of 160–300ºC using both experiments and modeling. The hydrogen release rate at 300ºC is twice as fast as at 160ºC. AB/MC released hydrogen at 20ºC lower than neat AB and at a faster release rate in that temperature range. Based on the experimental results, the kinetics equations were revised to better represent the growth and nucleation process during decomposition of AB.

Dynamic Mechanical Analysis

Dynamic mechanical analysis is a technique that has not been applied previously to investigate hydrogen storage materials. Dynamic mechanical methods enable accurate and rapid quantification of the viscoelastic properties of materials. Here, we focused on the dynamic mechanical properties of neat AB, spent AB, MC, and AB/MC compounded under different conditions. These results are also documented in the literature (Chen et. al. 2016).

Dynamic mechanical analyses were performed on a TA Instruments apparatus (TA Q800) to assess the mechanical and visco-elastic (rheological) properties of various AB-containing samples. In DMA, an oscillating force is applied to a solid sample (e.g., 6.35-mm diameter by 2-mm thick pellet) with a cylindrical probe, and the response of the material to that force is analyzed. In addition to investigating properties in the fuel end states, DMA is being used to assess properties at the various states of reaction to be expected in onboard vehicle transport systems. For the latter assessment, understanding the properties of the fuel as a function of temperature, as well as degree of AB reaction (e.g., polymerization), is important. The material characteristics near room temperature are of primary concern for refueling processes. Stress-strain curves were prepared by operating the DMA in controlled force mode at a rate of 1 N/min. Before testing, samples were heated in the DMA and held isothermally for 5 minutes. Elastic modulus was calculated as the initial slope. The viscoelastic properties of AB were investigated using the compression mode with a 31.6-mm diameter tip. Sample pellets were tested in multi-frequency stress

controlled mode with 1-μm amplitude and 1-Hz frequency of. A temperature ramp of 1 K/min with a range of 35°C to 210°C was implemented. Prior to testing, the linear viscoelastic region was determined by a series of strain sweeps.

The stress-strain curves for neat AB and AB compounds were obtained by applying a penetration force at a uniform rate to a compressed pellet at each single constant temperature. For polymer materials, the stress-strain curve profiles are strongly influenced by the polymer structure, degree of cross-linking, chain orientation, extent of crystallization, crystal structure, size and shape of crystal, ionic interaction (for ionomers), processing conditions, and temperature. The stress-strain curve gives information about the Young's modulus (slope at the origin), yield point, break point, elongation at break, and the recovery behavior of polymeric films (Freeman 1990, Eisenberg and Kim 1998, Hatakeyama and Quinn 1999). The initial points of the stress-strain curve are usually of primary interest from the standpoint of measuring dynamic mechanical (viscoelastic) properties of materials.

Figure 2.6a show that the elastic modulus E (initial slope of the curve) of neat AB depended on the testing temperature. The elastic modulus of neat AB decreased as temperature increased, suggesting that neat AB softened at elevated temperature. As seen in Figure 2.6a, the initial slope decreases with increasing temperature. In fact, the modulus becomes near zero at 110°C when AB begins to melt. This suggests that, as the AB nears it melting point, its resistance to deformation decreases and the material softens. We observed that the neat AB melted and turned into a foam-like material between clamps in the DMA furnace when the temperature reached 110°C (figure not shown). Accordingly, the yield stress of neat AB decreased as temperature increased (Figure 2.6b), also revealing that stiffness is reduced with increasing temperature.

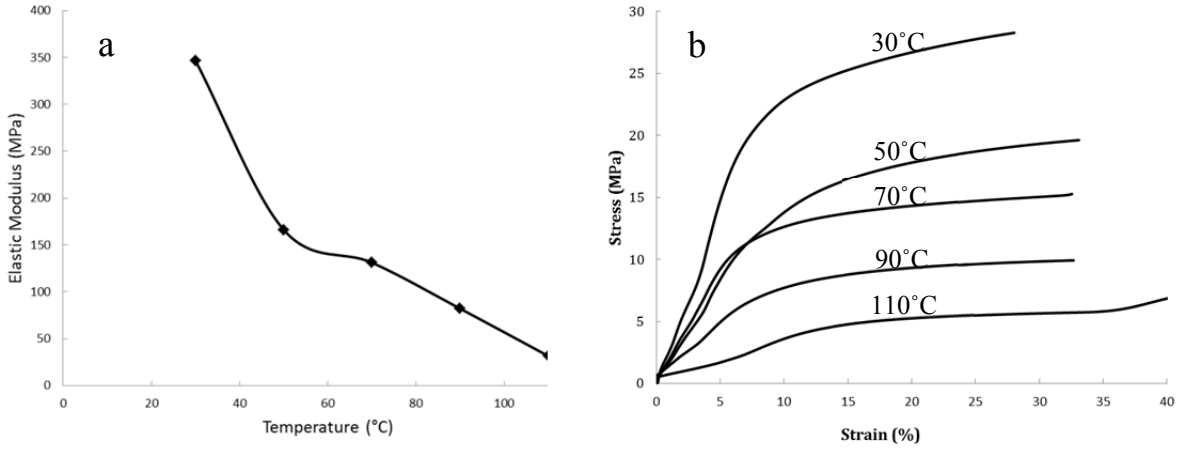

Figure 2.6. Neat AB Specimen Tested in Controlled Force Mode of DMA using Compression Clamp. Modulus of elasticity (E) vs. temperature (a), and stress-strain curve at each constant temperature (b). The tests were performed at 30°C, 50°C, 70°C, 90°C, and 110°C.

Spent AB displayed significantly different dynamic mechanical properties compared with neat AB. The initial slopes (elastic modulus) of the stress-strain curves for spent AB are much steeper than those of neat AB within the testing temperature range of 30 to 210°C (Figure 2.7a). Stress applied on the spent AB specimen hit the instrument limit within the initial strain range. It is not hard to tell that the specimen at 30°C and 150°C ended up with the lowest strain and the highest strain, respectively, under the stress limit of 28 MPa. From Figure 2.7a, it can be seen that spent AB is much stiffer than neat AB at the same temperature condition. We noticed that elastic modulus increased gradually in a very small amount until the temperature reached 150°C, at which point the value E increases dramatically, indicating pseudo-solid properties of the spent AB (Figure 2.7b). It is well known that the elastic modulus of composite materials is determined by many factors, such as chemical composition, phase structure, crystallinity, etc. The dramatic increase of elastic modulus at 150°C suggests that cross-linking may have occurred in the spent AB phase structure (Menard 1999). This interconnected network structure could greatly increase the modulus and stiffness as well as other mechanical and thermal properties of polymer materials.

To verify the formation of the cross-linking (or "gelated") structure, the same sample was tested again in the same procedure from 150 to 210°C (noted as the "second run"). The elastic modulus of the materials was revealed to be much higher than that tested during the first run at the same temperature (Figure 2.7b); the stress and stiffness in the second run also improved significantly (Figure 2.7c), These findings suggest the formation of interconnected structure during the first run. The significant decrease of the elastic modulus at 210°C may result from a collapse of the spent AB structure or depolymerization of the structure resulting from degradation.

Figure 2.8a shows that the elastic modulus of AB/20%MC compounds decrease with increasing temperature (similar to that of neat AB). The decreased stress and stiffness with temperature suggested a softening effect of the compound. We observed that the elastic modulus remained at 1724 MPa for the AB/MC compound at 30˚C as compared to an elastic modulus of 346.5MPa at 30˚C for the neat AB. The AB/MC compound exhibits solid-like behavior at temperatures below 110˚C while neat AB does not, suggesting that the dynamic mechanical properties of the AB/MC compound are superior to those of neat AB.

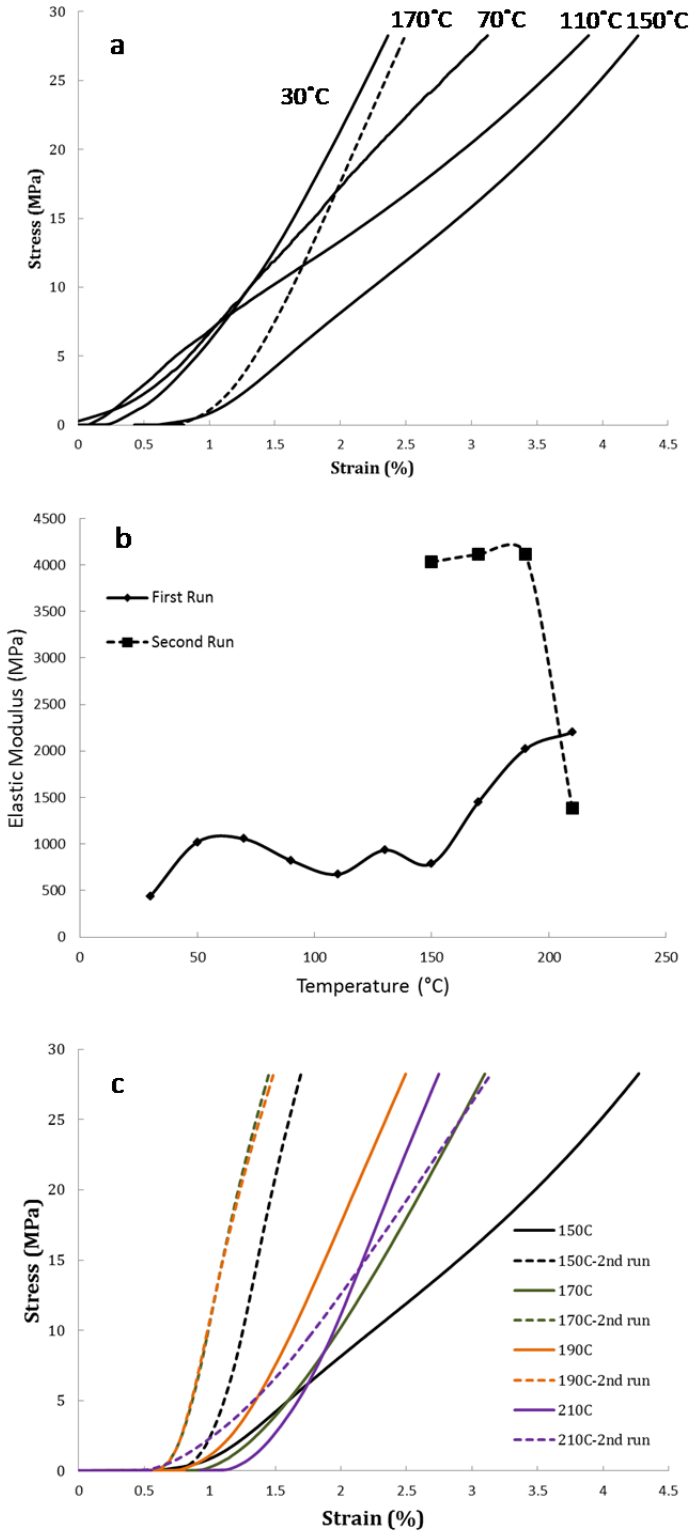

Figure 2.7. Stress-Strain Curve of Spent AB at Temperatures Ranging from 30°C to 210°C (a); Comparison of Stress-Strain Curve of Spent AB at High Temperature Ranging from 150°C to 210°C in the First and Second Runs (b); Effect of Temperature on the Elastic Modulus of Spent AB (c) Stress-Strain Curve Comparison of Spent AB between first and second run between 150 and 210°C

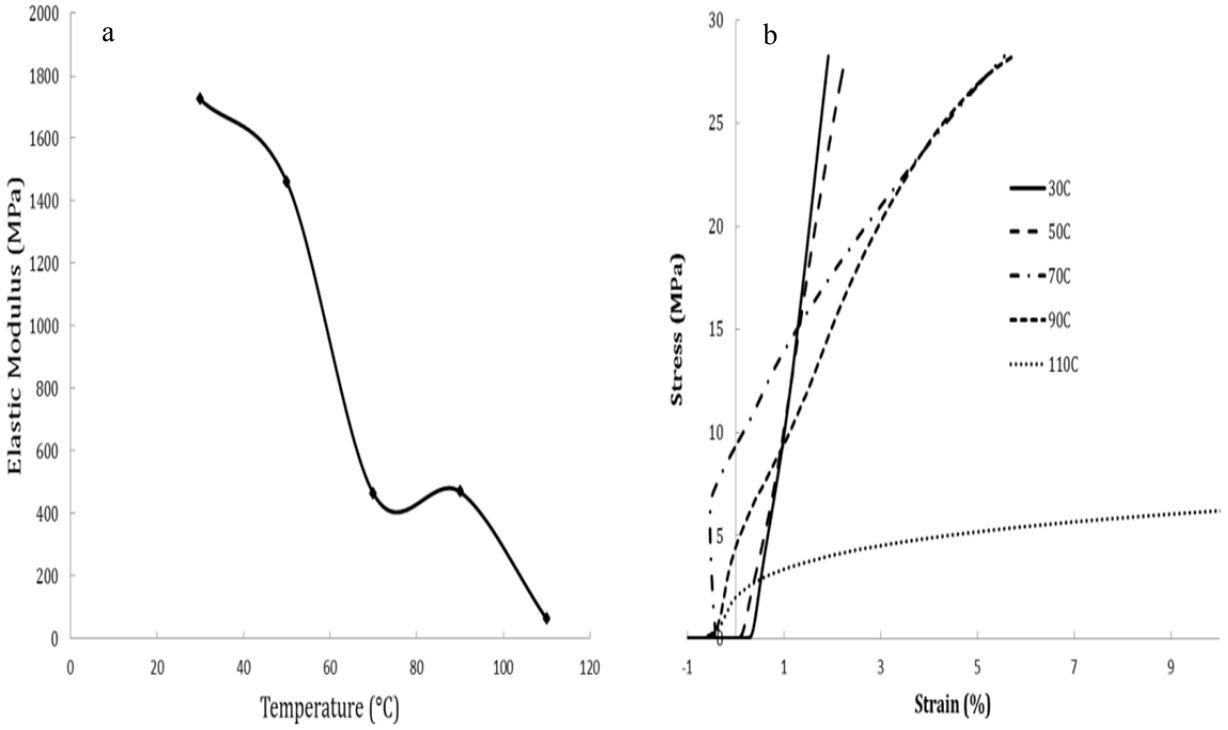

Figure 2.8. (a) Elastic Modulus and (b) Stress-Strain Curve of AB/MC under Controlled Force in Compression Mode. Tests were performed at 30°C, 50°C, 70°C, 90°C, and 110°C.

Summary of Dynamic Mechanical Properties Testing

This study focused on the dynamic mechanical properties of four types of materials related to AB - neat AB, spent AB, neat methyl cellulose (MC), and AB/MC compound. Dynamic mechanical analysis (DMA) constitutes a sensitive tool for the detection of the molecular relaxations of polymers and could effectively reveal their viscoelastic properties. The change of stiffness, modulus of elasticity, storage modulus, and loss modulus with temperature were investigated in depth for the four types of AB-related compounds. Phase structure transformation was studied by the elastic and viscous response, as well as damping property of the compounds. Predicted elastic modulus of AB/MC compound from rule of mixture was compared with the experimental results of neat AB, neat MC, and AB/MC. The different trends at different temperatures suggested that the interfacial bonding between components AB and MC is very temperature sensitive. Significantly improved dynamic mechanical properties of AB/MC compound over neat AB were demonstrated.

Except spent AB, all the other three materials, neat AB, methyl cellulose, and the AB/MC compound showed reduced elastic modulus with elevated temperature. The elastic modulus of spent AB has a sudden jump at 150˚C, suggesting the formation of crosslinking structure, which could also be revealed from the crossover of storage modulus and loss modulus. Spent AB, neat MC and AB/MC compound showed much higher elastic modulus than neat AB. The compound AB/MC showed complex dynamic mechanical properties of neat AB and neat MC. The deviation of experimental elastic modulus from the value predicted by rule of mixture for the two phase AB/MC compound suggesting weak interfacial bonding at temperatures above 50˚C. However, at low temperature, the MC component demonstrated the dominating role on the dynamic mechanical properties of AB/MC compounds. AB/MC compound exhibited solid-like behavior at temperature below 110˚C, indicating superior dynamic mechanic properties than neat AB. Neat AB was observed to melt into foam around 110˚C.

Angle of Repose

In addition to DMA, a number of relatively simple tests were setup and run to help assess the physical properties and flow characteristics of the various AB-containing materials and potential surrogate materials (for use in bulk refueling transport tests). Experiments included optical microscopy to determine particle size and shape, measurements of loose and tapped bulk densities, and measurement of poured angle of repose. Similar to instruments described in an ASTM method and other literature, a laboratory-built apparatus was assembled to determine the angle of repose. Figure 2.9 shows a representative conical pile of AB (Aviabor, as-received) poured onto a ~43-mm diameter circular base. The average angle of repose of this material was ~42 degrees from horizontal for a number of repeat experiments with circular bases of 43- and 50-mm diameter. This is in the middle of the "fair flowing" range, which is 38 to 45 degrees. Comparable experiments with AB synthesized by PNNL and a sample acquired from Sigma-Aldrich gave a higher angle of repose, ≥49 degrees ("cohesive" range, 45 to 55 degrees). The differences in flowability of these neat AB samples are thought to be correlated to particle shape and size; for example, the PNNL AB was fibrous and needle-like (1- to 5-mm long), whereas the Aviabor tended to be more rounded (0.1 to 1.5-mm diameter). Like the neat Aviabor AB used to make it, the PNNL-prepared AB/MC samples were also "fair flowing" (38- to 40-degree measured angle of repose). Among the candidate surrogate materials tested, a wax sample flowed too freely (~29 degrees measured; "very free flowing" range, 25 to 30 degrees). On the other hand, a fine particulate form of low-density polyethylene (Microthene low-density polyethylene [LDPE]) was "fair flowing" (~42 degrees angle of repose measured), like Aviabor AB and the fresh AB/MC. As a result, it was used as a mechanical surrogate for conveyance tests in Section 2.2.6.3.

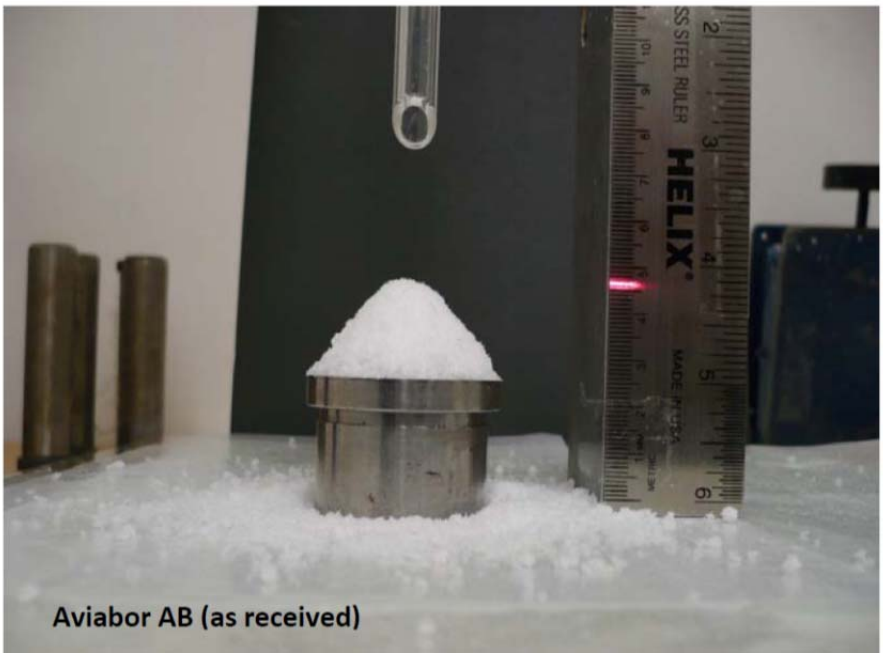

Figure 2.9. Measurement of Poured Angle of Repose of an As-Received Sample of Aviabor AB

To complement and extend the physical property testing (above), a contract was established with Jenike and Johanson, Inc. to assess the flow properties of three AB-containing particulate samples (as-received Aviabor AB, PNNL-prepared 80:20 AB/MC, and PNNL-prepared spent 80:20 AB/MC). Jenike and

Johanson, Inc.[1] is expert in flow property testing of solids, and they are renowned for their knowledge and experience in using a proven scientific approach based on the flow characteristics of powders and operating conditions to provide practical solutions that help customers avoid solids-handling problems.

For each of the three samples, the following tests were completed at ambient laboratory conditions:

- Cohesive strength
- Wall friction on two surfaces (i.e., 304 #2B stainless steel and a high-density polyethylene (HDPE) plastic, TIVAR 88-2)
- Compressibility
- Particle size distribution (not completed on neat AB because of problems with static charge).

In addition, permeability testing was completed on the spent AB/MC sample. The spent fuel was selected for the permeability test because it provides information on limiting discharge rates due to two-phase effects and removal of spent fuel from a vehicle storage tank may be at greatest risk for such a limitation.

In summary, the Jenike and Johanson, Inc. report noted the following: "Ammonia borane had the highest cohesive strength. All materials were found to be easy flowing, but each has the ability to form a stable rathole if stored in a funnel flow bin. The spent AB/MC blend had the highest wall friction on both 304 #2B stainless steel and TIVAR 88-2. The spent blend of AB and 20% MC was highly permeable to air, suggesting that limiting discharge rates should not be a problem. Visual observations of the powders after testing suggested that the materials are likely to gain strength when stored at rest. As the materials will likely be stored at rest for periods of time, time tests are recommended to determine appropriate outlet dimensions and mass flow hopper angles for these materials."

2.2.2 Solid AB/MC System Designs

In an effort to identify an acceptable design for using solid AB/MC to supply hydrogen to a fuel cell automobile, a variety of storage-system concepts were developed. All of these approaches require a means of heating a small amount of AB to initiate its reaction to produce hydrogen without allowing it to propagate throughout the entire storage container and over-pressurize the system. To control the amount of material reacting, the AB can be transported to a reactor for the thermolysis reaction. Another approach is to divide the material into separate insulated sections. In this way, only one section can be initiate reaction at a time. These alternative designs will be discussed briefly, describing the concept and its advantages and disadvantages.

2.2.2.1 Screw-Auger System

An auger is one means of moving solids from place to place. A heated auger would allow the solids to be reacted as they are transported. Augers can be designed to be independent of gravity, thus providing a low profile design that would be acceptable for an automobile. The screw-auger design also can provide good heat transfer for both adding heat to initiate the reaction and removing heat once the exothermic reaction has started. A process flow diagram for a possible design is shown in Figure 2.10. A combustor can be used to provide heat during startup. Once the reaction is initiated, the heat of reaction can be transferred via a heat transfer fluid flowing in a jacket outside the auger from the reaction zone to the preheat zone. A separate cooling zone will be used to reduce the temperature of the AB before it returned to the feed/product tank.

[1] http://www.jenike.com/Services/testing.html

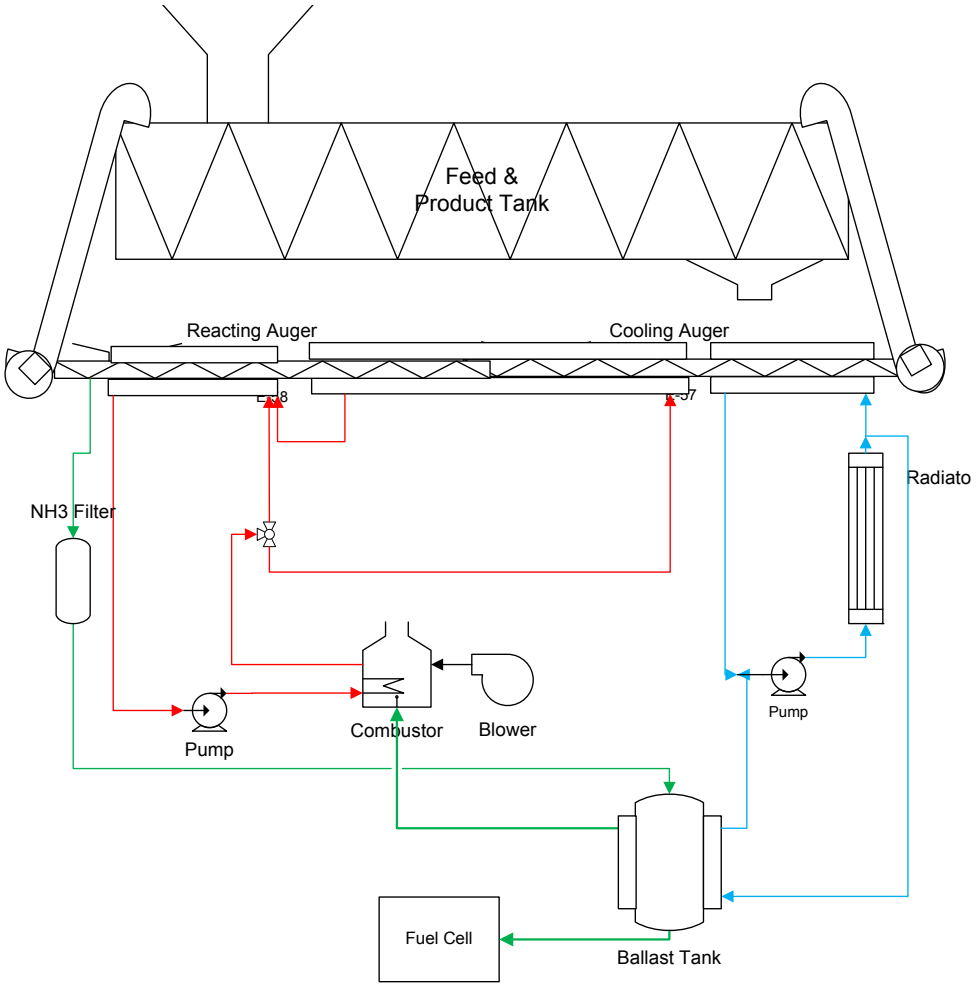

Figure 2.10. Screw-Auger Solid AB Storage-System Process Flow Diagram

The most significant problem with this design, as is the case for designs where the material is moving is sealing the high-pressure reaction zone from the low-pressure feed and product tank. Hydrogen losses associated with valving are a significant challenge. One alternative is to pressurize the feed and product tank to the level of the rest of the system. This eliminates the valving problem except during filling. However, it results is a much heavier storage tank, making it nearly impossible to meet the DOE gravimetric targets.

Validation of this design was performed with AB using an extruder for plastics. This auger-based extruder was outfitted for hydrogen generation by placing it in an inert enclosure. The purpose of the test was to determine if the AB could be moved through the auger during the reaction and if sufficient heat transfer could be achieved to react the AB. The result of this testing will be described in Section 2.2.6. In summary, although hydrogen was generated, the reactor clogged, and all auger-based designs were removed from consideration by HSECoE.

2.2.2.2 Other Reactors Requiring Material Movement

Various mechanical alternatives were investigated for movement and heating of a hydrogen storage material. Proposed approaches include transport of rods, balls, films, or blocks. The tape cassette and rod alternative designs are shown in Figure 2.11. In the case of the hydride tape cassette, a film made of some inert material containing AB is stored at low temperature in a spool. When hydrogen is needed, the film

passes through heated rollers that initiate the thermolysis reaction. Once the hydride tape cassette is spent, it can be removed and replaced.

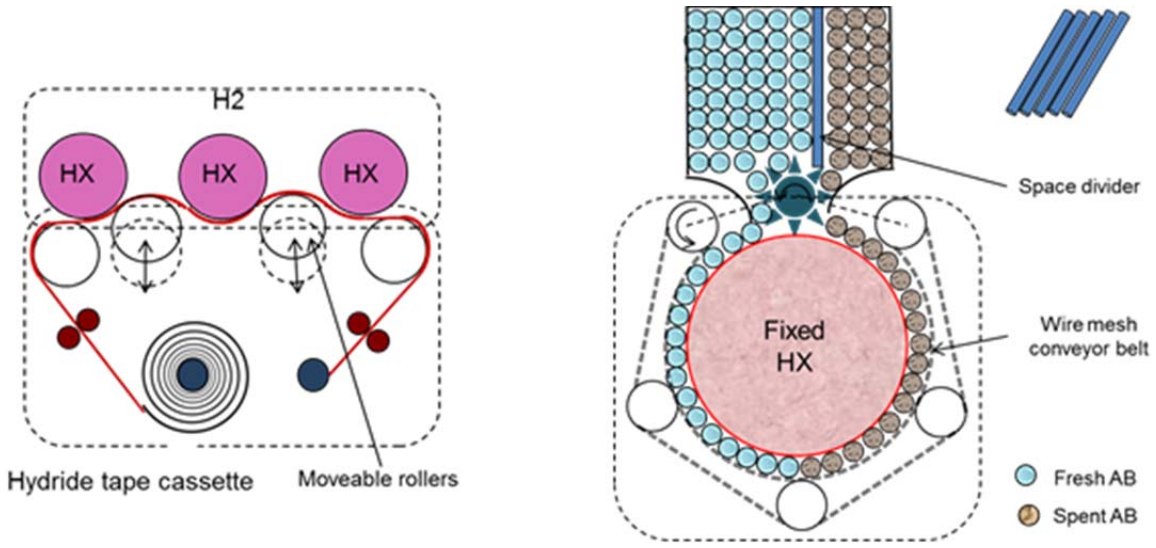

Figure 2.11. Two Possible Alternative Designs for a Flow-Through Reactor with Solid AB: (a) Hydride Tape Cassette and (b) Rod Conveyor

In another configuration, the hydride material is stored as rods or balls. These rods or balls roll out of a storage vessel and along a heat exchanger using a conveyor belt. They are rolled along a fixed heat exchanger to bring them to reaction temperature. Once heated, they react to produce hydrogen. Before the final product can then be returned to the same vessel or a separate storage vessel, it will be cooled along a similar heat exchanger.

All of these designs rely on the material maintaining its shape and not becoming sticky. This may not necessarily be the case unless additives such as MC are mixed with the AB. In addition, the packing factor of the material tended to be low, and the entire system needed to be pressurized with hydrogen. These factors resulted in the design being larger and heavier than would be acceptable to meet DOE gravimetric and volumetric targets.

2.2.2.3 Variable Concentration Reactor

An alternative design involves the use of high viscosity pastes rather than solids. If the paste can be made with high solids loading, the storage system will be smaller than the solid transport systems described above. In addition, using a paste provides a better seal between the high-pressure reactor and the low-pressure storage vessel. One such approach is shown in Figure 2.12. For this system, a high-pressure pump transfers the AB paste (assumed to be 60 to 70 wt%) into a reaction vessel where the paste could be mixed with a high-temperature slurrying agent. The slurrying agent would reduce the solids loading and reduce the viscosity. As a result, it would improve the flowability of the material. The hot slurrying agent also would heat the slurry to reaction temperatures and facilitate separation of the hydrogen from the solids, which may be difficult with a paste. Once the reaction is complete and the hydrogen gas is removed from the slurry, the slurrying agent would then be separated from the spent solids using something like a rotary fan press. The slurrying agent could then be recycled while the spent paste would be returned to a volume-displacement tank.

This approach required a paste pump and a press, both of which are considered heavy and energy intensive. The system mass was estimated at 225 kg based on a preliminary estimate with commercially available equipment. This is more than twice the 102 kg mass allowed for the DOE 2015 gravimetric target. As a result, this approach was eliminated from further consideration.

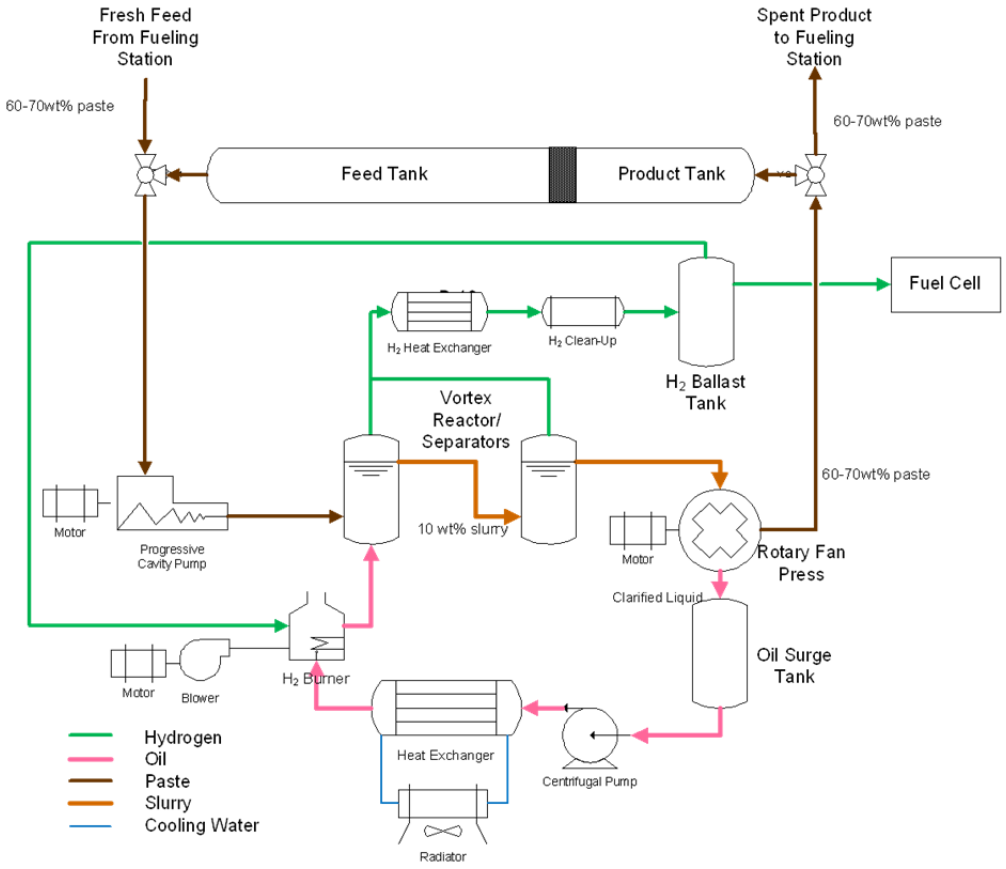

Figure 2.12. Variable Concentration Paste Reactor Process Flow Diagram

2.2.2.4 Fixed-Bed Storage-System Design

The fixed-bed storage system was an alternative to the systems that move the material through a reactor to produce hydrogen. This design consisted of eight thermally isolated sections in a single tank containing AB beads (see Figure 2.13b). Hydrogen gas can flow freely between sections to provide ballast for startup and drive-cycle transients. When the tank pressure drops below specified levels, the heating elements in a single section initiate the reaction at the bottom of the bed. Once a small layer of AB begins to react, the heat generated is sufficient to propagate the reaction through the entire section. The hot hydrogen flows through a heat exchanger where it is cooled before it is distributed to the other unreacted sections.

At refueling, AB beads are pneumatically conveyed out of each section of spent material. This pneumatic conveyance could be done with either hydrogen or nitrogen. Each section then is pneumatically refilled with fresh AB beads. After all spent sections are refilled with fresh AB, the tank is re-pressurized with hydrogen (see Figure 2.13a).

This system requires that 1) the reaction be exothermic and 2) the hydrogen-generation rate via propagation be greater than the usage rate. Validation testing was performed on the concept of reaction propagation through a bed of AB. The results indicated that the reaction will propagate successfully through a bed of AB as described in Section 2.2.6.2. In addition, both the feed and product must be flowable to allow pneumatic transport of the fresh and spent solids into and out of the reactor. The concept of pneumatic transport of an AB simulant into and out of a prototypical reactor section was performed and successfully demonstrated the concept. These validation tests will be described in Section 2.2.6.3.

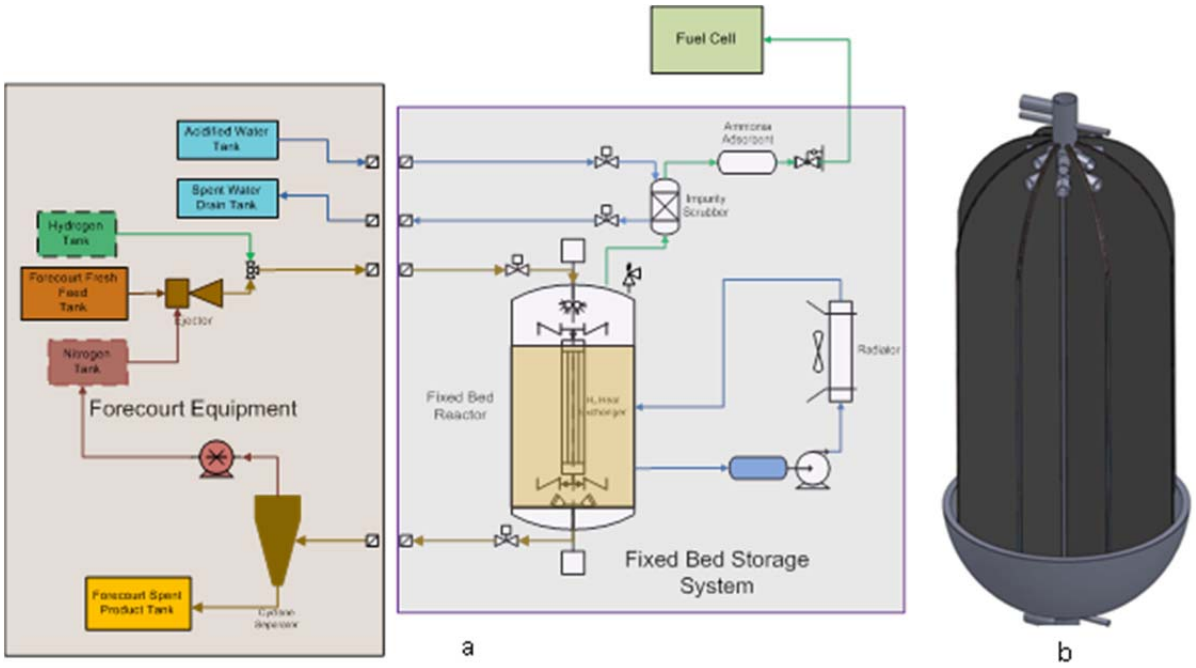

Figure 2.13. Eight-Section Fixed-Bed Storage System: (a) Process Flow Diagram and (b) Reactor Concept

This system was modeled using COMSOL® and Simulink® to demonstrate that it could meet the drive cycles selected by the HSECoE. Detailed modeling will be described in a subsequent section. The results of this modeling effort indicated that all transients could be met as well as meeting the 90% onboard efficiency target. Unlike other storage systems studied, it could meet a continuous 80-kWe hydrogen flow requirement (based on 0.02 g/s/kWe).

The mass and volume of the fixed-bed storage system also were estimated. The masses of all of the components are shown in Figure 2.14. As can be seen, the AB/MC media and pressure vessel accounts for the largest fraction of the mass (24% and 20%, respectively). To meet DOE targets, the AB/MC media must account for greater than 37% of the total mass. This design was found to be 65% and 60% of the DOE 2015 gravimetric and volumetric targets, respectively.

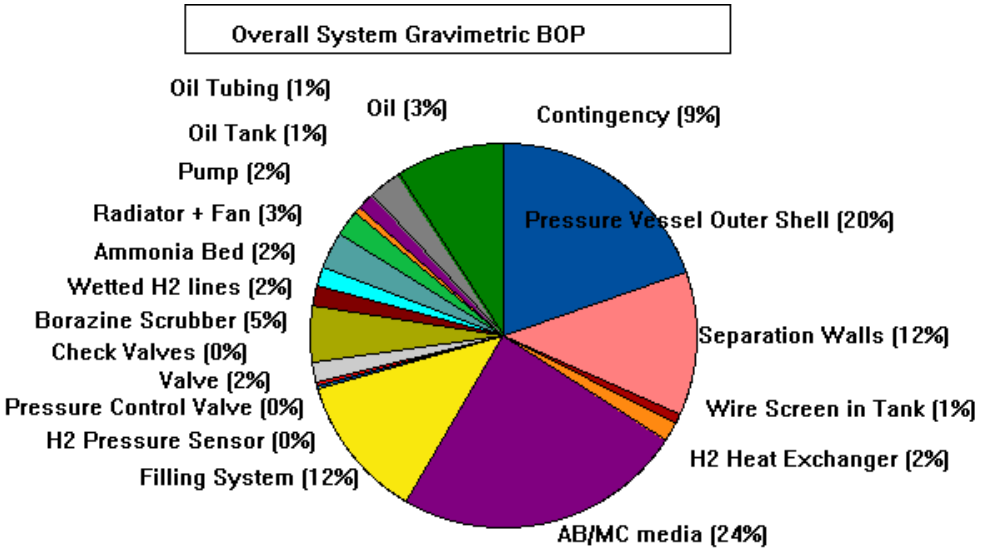

Figure 2.14. Mass Distribution of the Fixed-Bed Storage System

The fixed-bed reactor design looked the most promising of any of the solid AB storage system. It met most of the DOE technical targets and appeared to be a viable approach. The primary concern was the complexity of onboarding and off-boarding the material. While validation results were promising for simulant, testing needed to be performed with fresh and spent AB particles to ensure that they did not agglomerate and could all be removed within ultimate DOE target of 2.5 minutes for 5 kg of hydrogen.

2.2.3 Solid AB/MC System Models

The system designs described in the previous sections were implemented into computer models (Devarakonda et. al. 2012). A common modeling approach for various chemical hydrogen storage materials and for these various reactor configurations was developed using Simulink. The heat and mass-transfer equations for the reactor and heat exchangers are modeled using Simulink "S-functions" written in C-code and are then coupled with a Simulink fuel cell and vehicle-level model developed by other members of the HSECoE. These hydrogen storage system models predict the production rate of hydrogen that could be supplied from the storage system to a vehicle-based fuel cell during startup and drive-cycle transients and assist in sizing storage-system components. The approach uses a generic model that is independent of the reactor design. The generic model contains a reactor block for calculating the kinetics, rate and heat of reaction, a reaction heat exchanger block that models the reactor temperature based on heat transfer to the metal, a metal block that calculates the metal temperature based on heat transfer to the reactor and the heat exchanger, and a heat exchanger block that models the heat exchanger temperature based on heat transfer to the metal. The heat exchanger can either be a liquid (oil) or a gas (air). A feed materials block calculates the transport properties of the material such as bulk density and bulk specific heat based on the inert fraction considered in the chemical hydrogen storage.

2.2.3.1 Auger Reactor System Model

The auger reactor system developed in Section 2.2.2.1 and provided as a process flow diagram in Figure 2.10 was modeled. This design contains two augers (a reacting auger and a cooling auger) in which hydrogen is generated from the chemical hydrogen storage material. These augers are discretized into
10 cells along the axis. The reactor system is designed for an 80-kWe (i.e., 1.6 g/s of hydrogen flow) fuel cell.

The kinetics studies show AB conversion as a function of time as sigmoidal, which is characteristic of nucleation and growth phenomena in solids and is well described by Avrami kinetics (Avrami 1939). For solid AB, we use Kolmagorov-Johnson-Mehl-Avrami (KJMA) kinetics given by Equation 2.1.

$$\left.\frac{\partial \alpha_i}{\partial t}\right|_{kinetics} = n_i k_i (1-\alpha_i)\left[-\ln(1-\alpha_i)\right]^{(n-1)/n} \tag{2.1}$$

Here, i = 2 (for two equivalents of hydrogen from solid AB). The term α is the fractional conversion ranging from 0 to 1, and k_i is the rate constant calculated from the Arrhenius expression using the kinetic parameters shown in Table 2.3.

The global rate of change in fractional conversion (α_i) is given by Equation 2.2.

$$\frac{\partial \alpha_i}{\partial t} = -u\ \frac{\partial \alpha_i}{\partial z} + \left.\frac{\partial \alpha_i}{\partial t}\right|_{kinetics} \tag{2.2}$$

In Equation 2.2, 'z' is the spatial coordinate; u is the velocity of the chemical hydrogen storage material given by Equation 2.3, where ρ_{bulk} is the bulk density of the material, A_z is the area of the reactor, and $\dot{m}_{in}$ is the mass flow rate of the material calculated for a target hydrogen flow rate of 0.8 mol/s to the fuel cell.

Table 2.3. Kinetic Parameters for Solid AB, Liquid AB and Alane

Parameter	Units	Solid AB		Liquid AB		Alane
		First	Second	First	Second	First
A_i	s^{-1}	5.19E8	8.35E17	2.261E17	1.09E17	1.2E10
E_i	kJ/mol	85.3	170.1	142.0	146.0	102.2
β	-	1.1	1.4	1.0	1.35	1.5
n	-	3.0	1.0	1.5	2.5	2.0
ΔH	kJ/mol hydrogen	22	15	21	21	-11.4

$$u = \frac{\dot{m}_{in}}{\rho_{bulk} A_z} \tag{2.3}$$

A generic calculation for the mass flow rate into the reactor ($\dot{m}_{in}$ is defined in kg/s) is represented in Equation 2.4. MW_i is the molecular weight of the chemical hydride material, χ_i is moles of hydrogen produced per moles of chemical hydrogen storage material, and f_{inert} is the inert fraction, by weight.

$$\dot{m}_{in,i} = \frac{0.8 * MW_i}{\chi_i (1 - f_{inert})} \tag{2.4}$$

In this work, we used 15% MC as the inert material for solid AB, and the kinetics of solid AB-MC mixture are assumed to be the same as the kinetics of pure AB. The auger reactor is spatially discretized into 10 axial increments or cells along its axis. The overall hydrogen flow rate from the reactor is calculated by adding the flow rate from nine each of the individual cells in the reactor, given by Equation 2.5, and heat of reaction (Q_{rxn}) is calculated based on in Equation 2.6.

$$\dot{n}_{H2} = \frac{1000 A_x \rho_{bulk} (1 - f_{inert}) \Delta z}{MW} \sum \left(\beta_i \left. \frac{\partial \alpha_i}{\partial t} \right|_{kinetics} \right) \tag{2.5}$$

$$Q_{rxn} = \frac{1000 A_x \rho_{bulk} (1 - f_{inert})}{MW} \sum \left(\beta_i \left. \frac{\partial \alpha_i}{\partial t} \right|_{kinetics} \Delta H_{rxni} \right) \tag{2.6}$$

The temperature of the reacting material (T_{out}) is based on heat conduction along the length of the reactor and the convective heat transfer to the metal and is given by Equation 2.7.

$$A_z \rho_{bulk} C_{p,bulk} \left(\frac{\partial T_{out}}{\partial t} + u_{AB} \frac{\partial T_{out}}{\partial z} \right) + P_{metal} h_{metal} (T_{out} - T_{metal}) = Q_{rxn} \tag{2.7}$$

P_{metal} and h_{metal} are the perimeter and heat-transfer coefficient of the metal, respectively. The metal temperature (T_{metal}) is given by Equation 2.8. External heat from a burner (Q_{burner}) or an electrical element can increase the metal temperature. Based on the reactor design, one or more reactor heat exchanger blocks can heat the metal.

$$A_{metal} \rho_{metal} C_{p,metal} \left(\frac{\partial T_{out}}{\partial t} \right) + P_{metal} h_{metal} (T_{metal} - T_{out}) + P_{HX} h_{HX} (T_{HX} - T_{metal}) = Q_{burner} \tag{2.8}$$

A_{metal}, ρ_{metal}, Cp_{metal} are the cross-sectional area, density, and specific heat of the metal, respectively; P_{HX}, T_{HX}, and h_{HX} are the perimeter, temperature, and heat-transfer coefficient of the heat exchanger, respectively. The velocity of the heat exchanger fluid (u_{HX}) is given by Equation 2.9.

$$u_{HX} = \frac{\dot{m}_{HX}}{\rho_{bulk} A_z} \tag{2.9}$$

The term $\dot{m}_{HX}$ is the mass flow rate of heat exchanger fluid, A_{HX} is the heat exchanger cross-sectional area, and ρ_{HX} is the density of heat exchanger fluid. The temperature of the heat exchanger is calculated from Equation 2.10. The parameters used in the auger reactor model development and simulation are given in Table 2.4.

$$A_{HX}\rho_{HX}C_{p,HX}\left(\frac{\partial T_{HX}}{\partial t} + u_{HX}\frac{\partial T_{HX}}{\partial z}\right) + P_{HX}h_{HX}\left(T_{HX} - T_{metal}\right) = 0 \tag{2.10}$$

Table 2.4. Parameters used for the Fixed-Bed Reactor COMSOL Model

Parameter	Value	Units	Parameter	Value	Units
Solid Density	740	Kg/m3	β_1, β_2	1.1, 1.4	mol H_2/mol AB
Porosity (ε)	0.36	--	Molecular Weight AB (MW_{AB})	30.8	g/mol
Heat Capacity	2370	J/kg/K	Particle Diameter (d_p)	$1.58x10^{-4}$	m
ΔH_{rxn} (1st Eq)	22,000	J/mol H_2	Thermal Conductivity AB (k_{solid})		
ΔH_{rxn} (2nd Eq)	15,000	J/mol H_2	Fraction inert (f_{inert})	0.15	--

The objective of auger reactor simulations is to obtain a desired hydrogen flow of 0.8 mol/s with a representative set of parameters, feed material, and initial conditions. A fixed-step solver, ODE RK-4, was used to simulate the auger reactor with a time step of 0.01 seconds. The feed temperatures of solid AB and counter-flow heat exchanger fluid were set to 120°C and 200°C, respectively, and the initial condition for temperatures (T_{out}, T_{metal}, T_{HX}) was 120°C. For the solid AB simulation, an initial condition of 0.01 was chosen for α_i. Solid AB feed was calculated to be 0.018 kg/s (assuming an AB-MC mixture containing 15% inert material) for a hydrogen target of 0.8 mol/s to the fuel cell, and the heat exchanger fluid (oil) feed was chosen as 0.1 kg/s counter-flow to the flow of solid AB.

All other feed, initial, and simulation conditions remain the same for this case. Figure 2.15 shows the baseline plots from the auger simulation for solid with the main variables—hydrogen flow rate, χ, the materials (solid AB/liquid AB/alane), and heat exchanger temperatures.

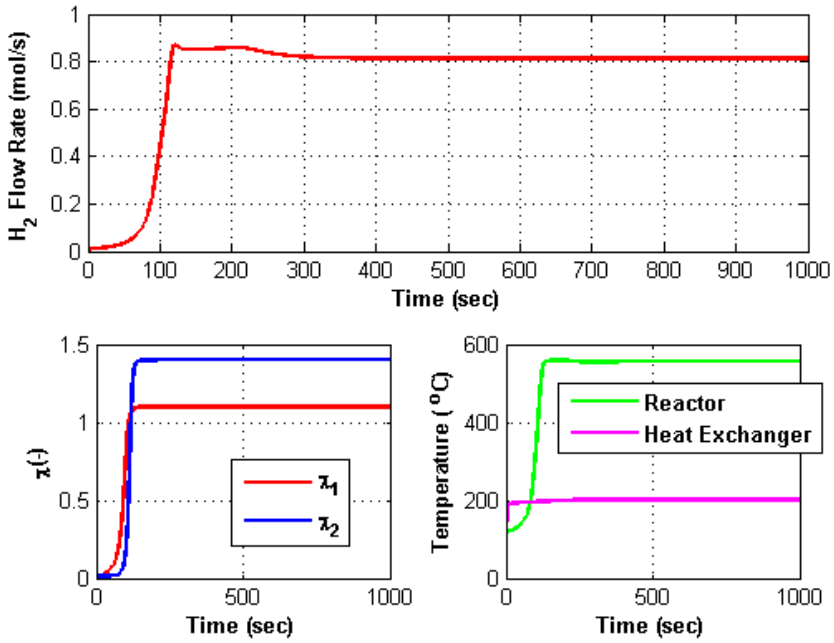

Figure 2.15. Screw-Auger Simulation Results for Solid AB

2.2.3.2 Fixed-Bed Reactor Model

The fixed-bed reactor is an alternative design to the auger system and other systems that require movement of the material into a reactor. In the fixed-bed reactor case, once the storage material is loaded in the eight thermally isolated sections of the single tank, the CHS material does not move until after it is reacted and system refueling is required again (see Section 2.2.2.4).

Modeling of a single section of the fixed-bed reactor was performed using COMSOL Multiphysics® to predict the reaction front propagation both with parallel and counter-flow of hydrogen. The model assumed a 33-inch-long, 4-inch-diameter reactor. The reaction is initiated at the bottom of the tube by heating AB pellets to 180°C. The remaining material had an initial temperature of 60°C. The reactions were solved assuming an axisymmetric system.

The computation assumed Avrami kinetics parameters developed previously. Heat transfer occurs between the solid AB and the hydrogen gas based on the energy equations for the two phases: solid (Equation 2.11) and gas (Equation 2.12):

$$\rho_{bulk} C_p \frac{\partial T_{solid}}{\partial t} - \nabla \cdot k_{solid} \nabla T_{solid} + h_{solid-gas}\left(T_{solid} - T_{H2l}\right) = Q_{rxn} \qquad (2.11)$$

$$\rho_{H2} C_p \frac{\partial T_{H2}}{\partial t} - \nabla \cdot k_{H2} \nabla T_{H2} + h_{solid-gas}\left(T_{H2} - T_{solid}\right) + \rho_{H2} C_p u \cdot \nabla T_{H2} = 0 \qquad (2.12)$$

where the ρ, Cp, and k are the density, heat capacity, and thermal conductivity, respectively, of the solid and hydrogen based on their subscripts (solid and hydrogen), and the $h_{solid\text{-}gas}$ is the heat-transfer coefficient between the two phases based on a Nusselt number expression (Equation 2.13).

$$Nu = (0.4Re^{1/2} + 0.06Re^{2/3})Pr^{0.4} \text{ for } Re > 50 \qquad Nu = 2 \text{ for } Re < 50 \qquad (2.13)$$

Hydrogen flow is calculated using Equation 2.14, with the assumption of Darcy's law for flow-through porous media:

$$\frac{\partial(\varepsilon\rho_{H2})}{\partial t} + \nabla\cdot\left(\rho_{H2}\left(-\kappa/\eta\nabla P\right)\right) = \dot{n}_{H2} \tag{2.14}$$

where η represents the kinematic viscosity of the hydrogen and κ is its permeability through the bed. For a packed granular bed of spherical particles, the kinematic viscosity can be calculated based on the porosity (ε) and particle size (d_p) using the Equation 2.15:

$$\kappa = \frac{{d_p}^2}{180}\left(\frac{\varepsilon^3}{1-\varepsilon^2}\right) \tag{2.15}$$

The hydrogen ($\dot{n}_{H2}$) and heat generation (Q_{rxn}) rates are calculated using Equations 2.16 and 2.17, assuming that β_i is the molar ratio of hydrogen produced in each reaction, f_{inert} is the amount of non-reacting solid present, and ΔH_{rxn} is the reaction enthalpy for each mole of hydrogen produced. The reaction kinetics expression is calculated using Equation 1.17.

$$\dot{n}_{H2} = \sum_{i-1}^{2}\left[\frac{(1-\varepsilon)\beta_i\rho_{AB}MW_{H2}\left(1-f_{inert}\right)}{MW_{AB}}\left.\frac{\partial\alpha_i}{\partial t}\right|_{kinetics}\right] \tag{2.16}$$

$$Q_{rxn} = \sum_{i-1}^{2}\left[\frac{(1-\varepsilon)\Delta H_{rxn,i}\rho_{AB}\left(1-f_{inert}\right)}{MW_{AB}}\left.\frac{\partial\alpha_i}{\partial t}\right|_{kinetics}\right] \tag{2.17}$$

The values for each of the parameters used in the model are shown in Table 2.4.

The model was run assuming the outlet was at the top of the tube and at the bottom to determine the impact of co- and counter-flow of hot hydrogen. In both cases, the initiation time was 50 seconds. The propagation rate of the reaction was much different: 16 mm/s for parallel flow and 2 mm/s for counter-flow. The results of the counter-flow simulation result are shown in Figure 2.16. In this figure, the colors represent the reaction temperature of the AB, and the arrows represent the downward flow of hydrogen.

Using the reaction initiation time and propagation rate results of the COMSOL model, a Simulink model was developed. As a result, as long as other transport parameters did not change, a simple expression (Equation 2.18) for the reaction rate in the bed was included in the Simulink model.

$$\frac{\partial\alpha_i}{\partial t} = -u_{\alpha_i} \tag{2.18}$$

In Equation 2.18, u_α represents the rate at which the reaction front moves through the bed. Using this approach, the kinetic expressions Equations 2.1 through 2.3 are replaced simply with Equation 2.18, thus significantly simplifying the model while providing a reasonable estimate of the reaction rate. Multiple runs of the COMSOL model were made to determine the sensitivity of u_α. Results indicate, for example, that the reaction propagation rate is a function of the bed initial temperature and could be modeled as shown in Equation 2.19.

$$u_\alpha = 7.0x10^{-6}T_{bed,ave} + 1.5x10^{-3} \tag{2.19}$$

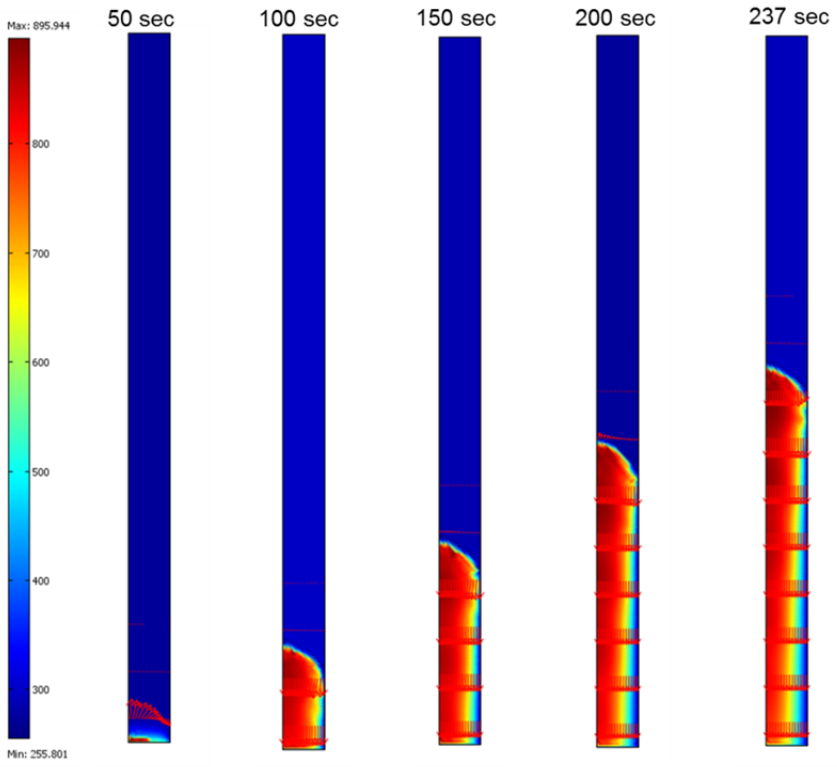

Figure 2.16. COMSOL Model Results from Simulations of the Fixed-Bed Reactor with Counter-Flow Hydrogen

The reaction propagation rate up the reactor was independent of the initiation heater temperature. There was, however, an initiation time before the constant reaction propagation rate began. This was found to be an Arrhenius function of the heat input as shown in Equation 2.20. Using these two parameters, the reaction rate in the fixed bed was quantified based on given AB bed parameters such as particle size and bed porosity.

$$\tau_{\alpha} = 1.3x10^{-6} \exp\left(\frac{65.0}{RT_{heater}}\right) \tag{2.20}$$

The ballast tank and hydrogen heat exchanger from the auger system were used to describe the temperature and pressure of the hydrogen in the fixed-bed tank. Unlike the COMSOL model, the Simulink model is a one-dimensional expression modeled as 10 differential elements in each reactor section. Based on the system hydrogen pressure, the reaction in a section could be initiated after the initial incubation period (τ_α) by setting $\alpha = 1$ at the base of the section. As long as there is enough pressure in the ballast tank, the tank provides hydrogen to the fuel cell as demanded. The cutoff pressure (p_{cutoff}) in the ballast tank is set as 10 atm. In an ideal scenario, whenever the ballast tank pressure falls below p_{cutoff}, the reaction in the subsequent section is triggered. Although extensive analysis on all four drive cycles has been done, we discuss only a two test cases here for brevity.

The reactor vessel was designed to be 1 m in height and 0.5 m in diameter with a pressure capacity of 112 bar. Each section contains 5.1 kg of AB/MC pellets in 10.8 L of section volume. The complete reaction of a single section required approximately 500 seconds to produce 0.71 kg hydrogen. This is equal to an equivalent electrical production rate of 71 kWe. The model successfully met the required demand for all four drive cycles. The hydrogen demand, delivered, and production are shown in Figure 2.17for Case 1 (UDDS + HWFET) and Case 2 (US06) for a single drive cycle.

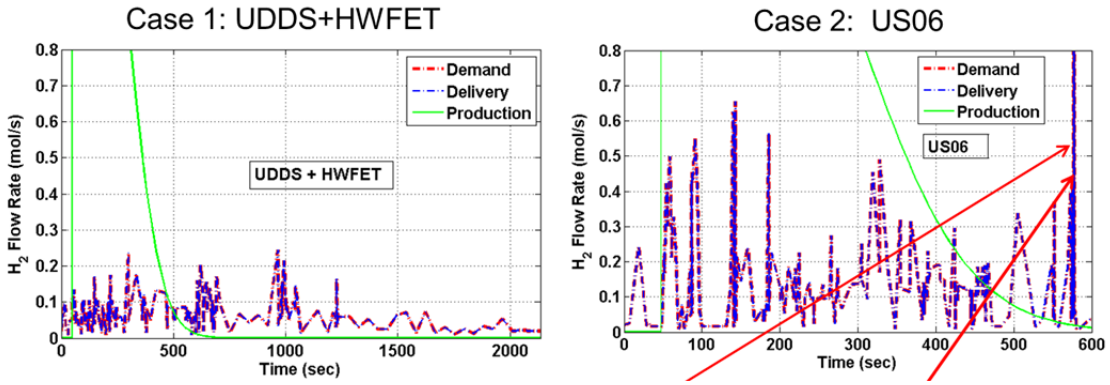

Figure 2.17. Comparison of the UDDS + HWFET and US06 Drive Cycles to the Production of a Single Fixed-Bed Section

2.2.4 Balance of Plant for Solid AB System Design

The BOP was evaluated to some degree for each of the solid system designs that were developed in Section 2.2.2. For each of the systems, the parts required were identified and their mass and volume estimated based on calculations. In most cases, these evaluations were cursory to determine parts upon which an estimate of system mass could be made. The fixed-bed system was the most developed solid AB system so it will be discussed in more detail here. Similar approaches were taken for other system designs.

2.2.4.1 Approach to BOP Component Identification

The BOP components were initially identified based on the development of a process flow diagram. Depending upon the level of rigor undertaken, the process flow diagram evolves through multiple versions as additional parts are added to flesh out the design and then parts are removed as the design is simplified. Once the parts are identified, simple calculations are performed to determine the operating parameters for each component. Such things as expected volume, mass flow, temperature, and pressure were estimated. For typical components, commercial vendors were contacted to identify components that meet the specifications. To assist in this process, a library of BOP components was developed for HSECoE use. This library included pumps, controllers, valves, filters, pressure regulators, tubing, pressure relief valves, and other components expected to be required for either the chemical hydrogen storage, metal hydride or adsorbent systems being evaluated by the HSECoE. Hydrogen compatibility, temperature, and pressure limits were considered as the library was developed. In the case of CHSs, these components require compatibility with high temperatures and pressures.

In some cases, the components required for a design are not available commercially. In this case, more detailed calculations are performed to develop a preliminary design. Thermodynamic properties, heat transfer, and pressure drop may be calculated to develop the design. The component is then sized and the weight and volume estimated.

2.2.4.2 Balance-of-Plant Component Description

The BOP components for the fixed-bed system along with their masses and volumes and whether they are an off-the-shelf design or custom are shown in Table 2.5. The BOP is divided into three major subcategories: 1) physical-storage BOP, 2) hydrogen BOP, and 3) oil BOP. The physical-storage BOP components consist of the reaction tank and the filling system. The hydrogen BOP components provide hydrogen cleanup and valves and sensors for hydrogen after it is generated. The oil BOP component is the cooling system reactor.

Table 2.5. List of BOP Components for the Fixed-Bed System

Subcategory	Component	Total Mass (kg)	Total Volume (L)	Design Basis
Physical Storage	Pressure Vessel Outer Shell	33.8	192	Custom Design
	Separation Walls	20.3		Custom Design
	Heater Elements	1.39		Watlow
	H_2 Heat Exchanger	2.7		Custom Design
	Plastic Pneumatic Pipe	3.9		US Plastic
	Stainless-Steel Pneumatic Pipe	9.1		Online Metals
	Pressure Relief Valve	0.1		Circor
	AB/MC Media	41.3		5.7 kg H_2
Hydrogen BOP	Pressure Control Valve	0.6	0.49	Emerson
	H_2 Pressure Sensor	0.11	0.03	American Sensor Tech
	Valves/Actuators	2.8	2.05	Assured Automation
	Check Valves	0.17	0.01	Circor
	Borazine Scrubber	7.9	7.2	Custom Design
	Wetted H_2 lines	3.1	6.94	Swagelok
	Ammonia Bed	2.73	3.3	Custom Design
Oil BOP	Radiator + Fan	5.3	2.3	AirTech
	Pump	3.9	13.9	Shurflo
	Oil Tubing	0.9	1.0	Swagelok
	Oil Tank	2.2	2.0	Swagelok
	Oil	9.5		Dow
Total System		152	231	

Reactor Vessel

The reaction vessel is a custom-designed system capable of providing 5.7 kg of usable hydrogen to the fuel cell. It is 1 m tall and 0.5 m in diameter and is constructed of carbon fiber with an aluminum liner. The tank is designed for 115 bar pressure with a 2.25 safety factor. The surfaces in contact with AB are insulated and covered with a thin layer of stainless steel. The walls also have aluminum microchannel heat exchangers to provide system cooling. The volume at the top and bottom heads and the pore space between particles provides the buffer volume for startup and transients. The eight sections are separated by insulated aluminum walls. These walls also have microchannel heat exchangers flowing oil to maintain the temperature of an unreacted section below 60°C.

Along the center of the reaction vessel is a hydrogen heat exchanger that removes most of the heat from the hydrogen before it flows to the unreacted sections. This custom built shell and tube heat exchanger cools the hydrogen to 80°C.

The filling system consists of electrically actuated 2-inch stainless-steel valves at the top and bottom of the column for filling fresh AB and draining spent AB, cable heaters at the bottom of the reaction vessel to initiate the reaction, high- and low-pressure pneumatic pipe, and a pressure relief valve. The pressure vessel and its associated valving must be designed for high temperature (200°C) and high-pressure (115 bar) hydrogen. All of these components are commercially available that were purchased from companies such as Assured Automation, Watlow, and Circor.

Hydrogen Handling Equipment

During the reaction of AB, borazine and ammonia are produced. To remove these impurities before they go to the fuel cell, a scrubber and adsorber are included in the design. The sizing of these

components is based on Los Alamos National Laboratory (LANL)/PNNL consensus values of 4 wt% borazine and 0.5 wt% ammonia in the hydrogen product. The borazine/ammonia scrubber removes the bulk of the impurities. Borazine reacts stoichiometrically with water to produce boric acid, while 90% of the ammonia is removed in the reaction with acid. As a result, the scrubber uses a water/ethylene glycol/phosphoric acid mixture. The ethylene glycol increases the boric acid solubility. Approximately 5 L of solution was required per fill. The scrubber has a 6 L volume, and is a plastic tank fabricated from fluorinated ethylene propylene and designed for 5 bar pressure.

Additionally there is an activated carbon bed to remove the remaining ammonia. With an adsorbent capacity of 2 wt% ammonia at breakthrough and an assumed replacement frequency of one bed changes per year, the bed is 0.6 kg of Kuraraycoal T-B in a fluorinated ethylene propylene plastic tank. The hydrogen BOP includes commercially available pressure control valve, hydrogen sensor, check valve, and electrically actuated ball valve. All process lines are assumed to be ½-inch in diameter.

Cooling Oil Handling Equipment

Heat generated from the reaction is removed through the heat exchangers inside the reaction vessel, both from the wall heat exchangers and the central hydrogen heat exchanger. This heat is removed with heat-transfer oil and sent to a radiator where the heat is rejected. This system consists of a commercial radiator, pump, tank, and tubing.

2.2.5 Solid AB System Cost

A cost estimate for a solid AB system including the cost of media, tanks, valves, other BOP equipment, and manufacturing and assembly were developed based on system models and a BOP developed to maintain system pressure and temperature. A cost estimate was developed for only one of the Phase I solid AB systems. Cost estimates, based on DOE requirements, were developed for 10,000, 30,000, 80,000, 130,000, and 500,000 units of annual production. The Phase I model was a top-down cost estimate using material quantities and projections of material costs from manufacturers' quotes for materials and BOP components. Progress ratios were used to adjust prices as quantities increased.

The cost model was used to develop an estimate of the system costs and the cost/kilogram of usable hydrogen stored to determine how close the system approached the cost target. During Phase I, the cost target became "to be determined," so there was no total cost or cost target on a $/kWh basis. The values for the system were used in the "well-to-wheels" analysis to determine the life-cycle cost of solid AB system and its impact on the total fuel cost for the solid AB system. The model only develops the system's first cost starting at the edge of the car and ending just before the fuel cell. As such, the cost estimate does not provide an average cost for AB over the lifetime of the system. Off-board regeneration costs for AB were not a part of the cost estimate. The regeneration costs were developed outside the HSECoE.

2.2.5.1 Cost-Determination Methodology

A schematic of the solid AB system was obtained, and a bill of materials was developed in conjunction with the system modeler and manager of the BOP components. For the solid AB cost model, the system model provided the volume, capacity, and weights of the tanks that were developed. The system modeler also identified the operating pressure, temperature, flow rates and types of valve, solenoids, pumps, etc., that are required to operate the system. Valves and other BOP components were identified that met the model requirements. The bill of materials provided a supplier and model number. The operating pressures, temperature ranges, and activity to be accomplished were provided, as well, because they were useful in discussing components with manufacturers as they sometimes would suggest components that were less expensive but could do the same job. If manufacturers suggested alternative components, other

team members reviewed the alternatives to ensure compatibility with temperatures, pressures, and hydrogen atmosphere.

Once components were identified, manufacturers were contacted to determine pricing. Manufacturers were asked to provide pricing at each level of production required, but often manufacturers/distributors would only provide pricing for limited numbers of units. The primary reason given was that currently the company did not have capacity to manufacture that many units per year. Some of the manufacturers contacted were very small and would require a significant expansion of their facilities to reach the annual quantities required to meet each of our annual production level requirements. Some manufacturers would give at least two quantities and associated prices. In addition, some manufacturers would not provide pricing as it was their policy to not to supply end-users directly or they were limited by their distribution agreements. In certain cases, prices were obtained from local suppliers because even the distribution warehouses would not provide pricing.

The analysis assumed that auto manufacturers would deal directly with manufacturers rather than through distributors to get the best price. The prices used in the analysis were adjusted to reflect manufacturer prices if the prices were obtained from distributors. For each level away from the manufacturer, a 30% price reduction was taken to account for the markup from the manufacturer price.[2,3]

A progress ratio is based on the ability to learn as manufacturing quantities and the number of units produced increase. The initial basis for establishing progress ratios emanated from labor learning, which commonly is called "the learning curve." As used in this estimating process, the progress ratio embodies cost reductions that are obtained from technological progress, economies of scale, and labor learning curves. The progress ratio is often stated as a fraction (NETL 2013). Tsuchiya and Kabayashi (2004) indicate that progress ratios range from 80 to 95% for mechanical products and 70 to 85% for semiconductors and electronic devices. The implication of a progress ratio is that, for every doubling of production volume, the cost of producing that volume is represents a progress ratio of 70 to 95% of the previous volume. However, progress ratios have a bottom limit for production costs, which is the cost of materials for the item being produced. In other words, costs can approach the cost of materials in production, but the progress ratio cannot cause production costs to go below the cost of materials. In addition, prices at different volumes, if available, were used to develop progress ratios. In other cases, where only one price was obtained, a progress ratio was developed based on how immature the market was, how small the current production capacity was, and the type of material or product for which a high-volume price was being forecast. The progress ratio is defined as shown in Equation 2.21.

$$P = (1\text{-}2^{-b}) \tag{2.21}$$

In Equation 2.21, P is the learning rate at which costs decline for doubling of output, and 2^{-b} is the progress ratio. All costs and prices were adjusted to 2005$ for Phase I, while for Phases II and III, they were adjusted to 2007$ using the Gross Domestic Product Implicit Price Deflator. Finally, the model estimates and pricing were examined by one of the OEM to determine whether any of our prices were out of line with their expectations based on their purchase records. If the prices were not consistent with the OEM values, the progress ratios were adjusted to reach the OEM suggested price.

2.2.5.2 Assumptions for the Fixed-Bed Reactor Costs

The system schematic for costing is the fixed-bed model described in Section 2.2.2.4. The primary material costs are shown in Table 2.6. Some of the most significant costs drivers for the solid AB tank system were the AB media itself and tank materials. The AB media costs were obtained from a

[2] Personal communication with Frank Hampshire, Motor and Equipment Manufacturers Association, January 26, 2011

[3] Personal communication with Ron Rossi, Automotive Aftermarket Industry Association, January 26, 2011.

Dow Chemical study that indicates AB material could be purchased in large volumes for $9/kg (Linehan et al. 2010). Small-quantity purchases were found in the $4,500 to $5,000 /kg range.

Table 2.6. Major Material Costs for the Solid AB Fixed-Bed Reactor System (2005$/system)

		Production Units				
	Progress Ratio	10,000	30,000	80,000	130,000	500,000
Ammonia Borane	0.670	88	47	27	20	9
Methylcellulose	0.89	8	7	6	5	4
Carbon Fiber+ Epoxy	0.975	27	26	25	25	24
Stainless Steel 304	0.950	6	5	5	5	5
Aluminum 6061-T6	0.950	12	11	10	10	10

Carbon fiber and resin added significantly to the cost estimate with prices for pre-impregnated carbon fiber ranging as high as $44.9/kg (Ahluwalia et al. 2009). Costs reported by Quantum were used for our large-volume fiber estimate, which was nearly $24/kg (Leavitt and Johnson 2010). The stainless steel 304 price was estimated from MEPS North American Steel website (MEPS 2010). Wastage was an additional cost that was added to component costs. In Phase I, a flat 15% wastage factor was assumed for all tank material components based on OEM feedback.

For BOP components, a significant amount of the components had progress ratios in the 0.90 to 0.95 range. Progress ratios in this range are removing the larger margins associated with small volumes. The progress ratios used were similar to those deduced from a fuel estimate by James et al. (2002). Note also that OEMs reviewed the pricing in the model to ensure that the values were approximately correct within their databases. In certain cases, such as filters and temperature sensors, OEMs said they could get a better high-volume price than the estimate obtained from the progress ratio provided. In those cases, the progress ratio was adjusted to reflect the better price given by the OEMs.

Heat exchanger costs are based on material costs plus a markup based on information from a proprietary model from Oregon State University (OSU). Several heat exchangers were estimated, and the results were summarized and provided to HSECoE. The results of the price examination found that the first 10 heat exchangers were 10 times more expensive per unit than units at 500,000 units of annual production. Based on the summary of results, a 45% markup was assumed at the 500,000-unit level. The progress ratio was back-casted to fit a price 10 times higher at the 10 unit level.[4]

Manufacturing costs and assembly costs were developed based on ratios of direct material costs to total costs based on information found for similar manufacturing. The use of analogy occurred because the maturity of the schema did not account for what types of equipment would be needed to manufacture or assemble the tank system. A markup of more than 100% was used because of the complexity of the multi-compartmented tank with many internal components including the custom-designed heat exchanger that included heating elements. This doubled the markup of the compressed hydrogen tank estimated by Quantum (Linehan et al. 2010). The assembly percentages were based on fuel cell assembly percentages from James et al. (2002).

2.2.5.3 Results and Discussion

The overall cost of the solid AB reactor and system was $4,400 at 500,000 units of output, approximately 40% of the cost at 10,000 units of annual production. The cost in terms of unit energy produced was $23.6/kWh. As shown in Table 2.7, the reactor tank comprises more than 41% of tank costs primarily because the manufacturing costs, the amount of aluminum in the tank components, and the carbon fiber around the outside of the multi-compartmented tank to contain the pressure inside the reactor. Similarly,

[4] Personal communications with Steven Leith, Pacific Northwest National Laboratory on January 20, 2011.

valves and the remaining BOP components comprise a similar percentage of the total system cost. Media accounts for about 8% of total costs at the 500,000 unit production level.

Table 2.7. Fixed-Bed System Costs for Solid AB at 10,000 to 500,000 Production Units

	Production Amount				
	10,000	30,000	80,000	130,000	500,000
Total Costs	10,866	7,951	6,289	5,640	4,400
$/kWh					23.6
Item	10,000	30,000	80,000	130,000	500,000
Tanks	2,459	2,168	1,954	1,861	1,813
Media	3,150	1,685	968	737	341
Media Cost/kg	76	41	23	18	8
Borazine Scrubber	97	81	69	64	52
Ammonia Bed	35	28	23	21	16
BOP	3,482	2,808	2,384	2,198	1,831
Assembly	1,643	1,180	890	759	348

The costs of AB could be a significant cost of the first costs for the solid AB tank and a significant risk factor for the cost estimate. Dow Chemical provided a cost at full-scale production of $9/kg (Linehan et al. 2010). The number is significantly below current small-quantity costs of $4,500 to $5,000/kg obtained from laboratory supply companies. No values for commercial quantities of AB could be obtained from chemical distributors or manufacturers. A progress ratio was developed based on the current small-quantity prices and the Dow Chemical estimate. The progress ratio was used to estimate the price at interim volumes of production. The estimated progress ratio was 0.67, which is somewhat below the range of values found in the literature. In addition, the technical team review of the AB cost per kilogram received some significant discussion around the validity of the Dow Chemical estimate. Table 2.8 depicts the cost breakdown for the reactor tank.

Table 2.8. Fixed-Bed Reactor Tank Component Costs

Item	Quantity or Wt	10,000	30,000	80,000	130,000	500,000
Tank Components						
Outer Shell						
Carbon Fiber	10 kg	302	290	280	275	267
Aluminum In Reaction Zone	9 kg	114	105	97	94	95
Aluminum non-Reaction Zone	8 kg	125	115	107	103	104
Insulation	19 square feet	12	10	10	10	10
SS304	7 kg	43	40	37	36	36
Separation Walls						
Aluminum	7 kg	96	88	82	79	80
Insulation	30 kg	19	17	17	17	17
Stainless Steel 304	12kg	76	70	65	62	63
Rough Screen	0.29 linear feet	2	1	1	1	1
Fine Screen	0.43 square feet	6	6	4	3	2
Heat Exchanger		382	295	234	209	193
Total Tank Costs		2,459	2,168	1,954	1,861	1,813

Note that there are 24 kg of aluminum 6061-T6 in the outer shell and separation walls heat exchangers as well as 19 kg of stainless steel 304 in the tank structure as described in Section 2.2.3.2. The aluminum and stainless steel comprise approximately 39% of the total tank cost so reducing the amount of these

materials could significantly reduce the cost of the tank. Note that the insulation and screen costs could double but not significantly affect the cost estimate. The heat exchanger estimate was compared with another heat exchanger cost and found to be similar for the amount of material involved in the device.

The ammonia and borazine cleanup systems were estimated based on the prices of two different sizes of commercial off-the shelf tanks (see Table 2.9). The prices for these tanks were significantly reduced because the supplier that provided the quote was not related to the manufacturer. Thus, two markups were removed from the quote. In addition, given the amount of materials used, the simplicity of design and ease of manufacture, a progress ratio of 0.89 and 0.85 were assigned to the borazine scrubber tank and the ammonia adsorbent tank, respectively, to forecast prices at different quantities. The prices of the media used in cleanup reactions and adsorption would not significantly change the cost estimate if the prices tripled.

Table 2.9. Media, Borazine, and Ammonia Cleanup Component Costs for the Fixed-Bed AB System

Item	Quantity	Wt	10,000	30,000	80,000	130,000	500,000
Media							
Ammonia Borane		35 kg	3,098	1,642	932	704	316
Methylcellose		6 kg	51	43	36	33	25
Media Subtotal			3,150	1,685	968	737	341
Borazine Scrubber							
Tanks	1		94	78	66	61	49
Water		2 L	0	0	0	0	0
Ethylene Glycol		2 L	3	3	3	3	3
Sulfuric Acid		0.4 kg	0	0	0	0	0
Scrubber Total			97	81	69	64	52
Ammonia Bed							
Tank	1		30	23	18	15	12
Ammonia Media		1 kg	5	5	4	4	4
Total			35	28	23	21	16

The most significant costs in the rest of the BOP are valve costs as shown in Table 2.10. At the low-volume prices quoted by manufacturers, the prices ranged from $100 to $400 each. Valve prices were compared with results from reports published by TIAX LLC to ensure that the values forecast were reasonable. The forecasted unit price for 500,000 units of annual production is shown in the right hand column of the table. Thus, the cost of valves represents a significant cost risk if our assumptions about how low the prices can be economically sustained are incorrect. Note, the 16 check valves are the valves in the multi-compartmented reactor that receive and dispose of the AB and outlet the hydrogen released during reaction. Thus, a significant area for cost reduction would be the development of a valve that could feed the eight compartments.

Table 2.10. Solid Ammonia Borane BOP for the Fixed-Bed System (2005$)

Item	Quantity	Wt	10,000	30,000	80,000	130,000	500,000	Each
Radiator + Fan	1		177	150	129	120	97	97
Heater Elements	8		234	198	170	158	129	16
Valve 2-inch SS316[a]	2		157	133	114	106	86	43
Valve ½-inch SS316[a]	2		97	82	71	66	54	27
Pump	1		881	501	302	235	118	118
Check Valves	16		818	754	702	677	613	38
Pneumatic Pipe	10	feet	7	6	6	5	5	0
Pneumatic Pipe	4	feet	24	20	17	16	13	3

Item	Quantity	Wt	10,000	30,000	80,000	130,000	500,000	Each
Oil Tubing	12	feet	36	33	31	30	27	2
Pressure Control Valve	1		145	145	145	127	127	127
Pressure Regulator	1		125	120	114	112	106	106
Pressure Transducer	1		171	157	146	141	128	128
Pressure Relief Valve	1		78	53	37	31	19	19
Pressure Gauge	1		21	20	20	19	19	19
Coolant Oil	0	6 L	27	25	23	22	20	3
Oil Tank	1		94	78	66	61	49	49
H_2 Pressure Sensor	1		50	43	37	34	28	28
Internal OiI Headers	5	feet	15	14	13	12	11	2
Internal OiI Headers	5	feet	12	11	10	10	9	2
Valve 2-inch SS316[a]	2		310	263	226	210	171	86
Internal Pipe/Seals	2	feet	3	3	3	3	3	1
Total BOP				3,482.5	2,808.3	2,383.8	2,197.9	1,831.4

[a] SS316 = 316 stainless steel

Another significant risk in the cost estimate is the pump. The original price for the pump was nearly $1,000 per unit at low-volume production. The manufacturer estimated their costs at high-volume production at nearly $400 per unit while we estimated the cost at just over $100 per unit based on team judgment and the application of a 0.70 progress ratio. Other relatively high cost items are the radiator and fan. The manufacturer quote for large-volume production of these items combined was $140 per unit and our estimate was $97 per unit. We discussed the estimating approaches with both of the manufacturers and felt that they were not taking advantage of economies of scale in the approach to estimating the costs.

2.2.5.4 Summary of Cost Analysis for the Fixed-Bed System

The Phase I cost estimate for the solid AB system at $4,400 per system was in the middle of two other Phase I cost estimates that were also performed by PNNL, one for a MOF-5 adsorbent system and the other for the metal-hydride system, sodium alanate (Motyka 2014). The MOF-5 estimate totaled $2,869 per system or $15.4/kWh while the sodium alanate system cost $8,008/system. All of the estimates are in 2005$. The solid AB system cost suffered from significant complexity to obtain the 5.6 kg of usable hydrogen while the sodium alanate system suffered from the volume and cost of two tanks needed to provide 5.6 kg of usable hydrogen. The two tanks also doubled the cost for each tank. The comparison of the three systems can be seen in Figure 2.18. The solid AB reactor tank was approximately 39% more expensive than the MOF-5 carbon fiber tank. The solid AB tank was significantly more complicated than the Phase I version of the Type-III tank developed by the adsorbent team during Phase I. The solid AB tank cost approximately 48% of the metal-hydride tank system with it twin tank concept. The cost of sodium alanate also contributed to the high cost of the metal-hydride tank. The significant cost of sodium alanante combined with the quantity required to provide 5.6 kg of usable hydrogen made the media cost almost seven times the cost for either MOF-5 or solid AB. The solid AB and metal-hydride systems were not close to previous DOE targets for system cost and cost per unit of energy produced, which became “to be determined” during Phase I.

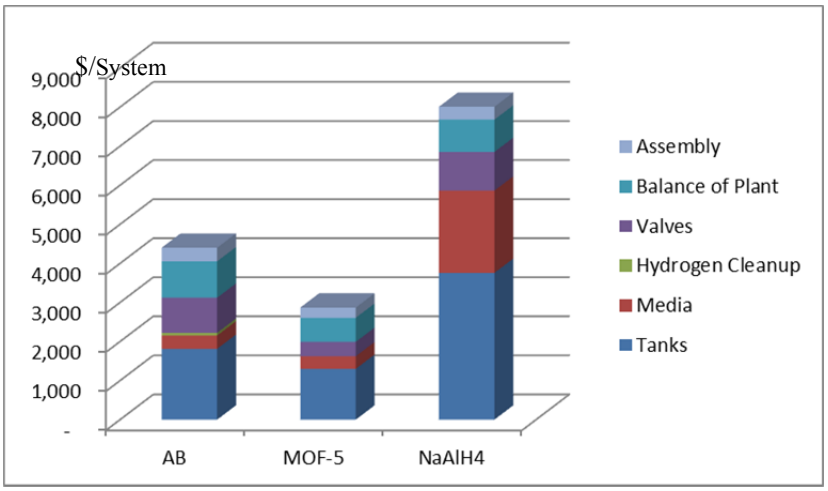

Figure 2.18. Cost Comparison of the Three Alternative Phase I Systems (2005$)

2.2.6 System Component Validation Tests

In addition to developing the system designs, models, and costs, experimental work was performed in an effort to validate the storage-system designs. The experimental work determined if the system would operate as expected and if DOE technical targets could reasonably be met. The primary concern for both the auger and fixed-bed based storage systems were the reactor design and the on- and off-boarding of the solid material. As a result of these concerns, experimental work was performed for these two areas.

2.2.6.1 Auger Reactor Testing

Testing was performed to investigate the feasibility of an auger (flow-through) reactor as a source of hydrogen generation from solid AB. The reactor, which is known as a plasticating single-screw extruder, is the most common piece of equipment in the polymer industry (Chambon and Winter 1985, Kollár and Springer 2003). For our work, it was outfitted for generating hydrogen in the present work. The purpose of experimental validation includes 1) validate the concept of flow-through reaction with an auger, 2) verify sufficient heat transfer to AB at required feed rate, and 3) measure hydrogen generation vs. AB feed rate. The experimental procedures are described below.

As shown in Figure 2.19, the extruder consists of a hopper, which holds the AB powder, and the extruder barrel, which can be conceptually divided into three sections on the basis of function—the feed, compression, and metering sections. In the feed section, the solid AB powder is conveyed by the rotating screw from the hopper to the compression zone where the AB is forced against the heated walls of the barrel. When the AB reaches the metering zone, it has finished dehydrogenating, and the shearing action of the screw rotating against the inner wall of the extruder barrel forces the spent AB out of the extruder and through a nozzle. During extrusion, cold water cooling lines were used to maintain the feed section of the barrel at room temperature, whereas the compression and metering zones were sustained at 150°C and 70°C, respectively. To neutralize sudden generation of hydrogen and undesired volatile byproducts throughout the thermal decomposition process of AB, the experiments were carried out in a shielding box under flowing nitrogen.

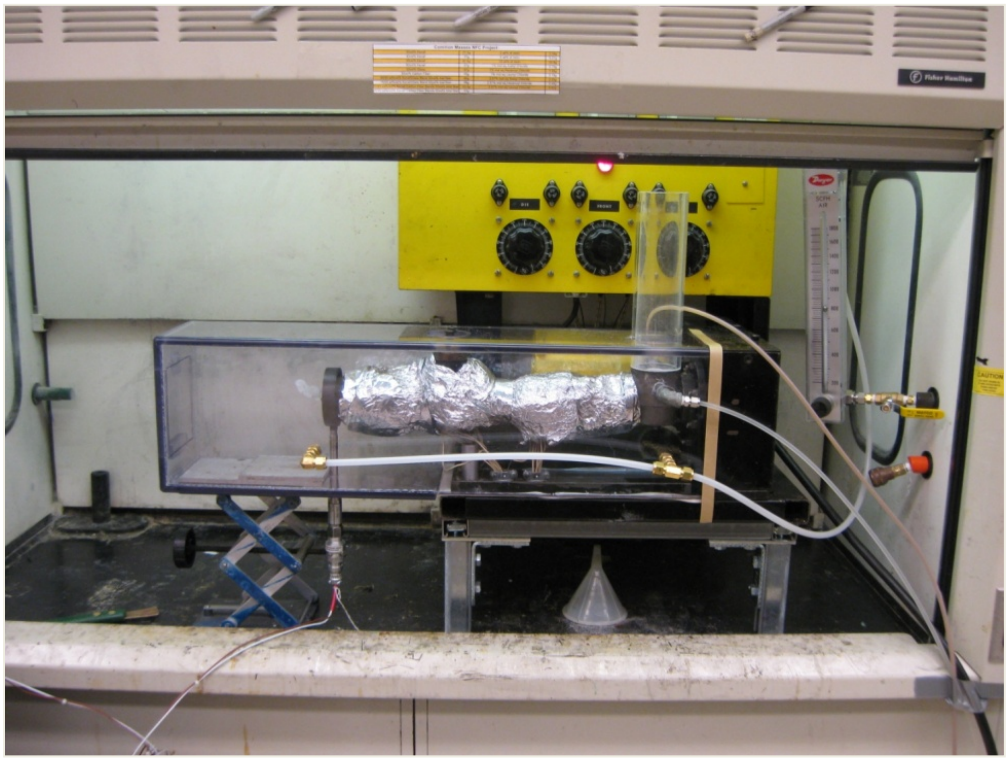

Figure 2.19. Auger (flow-through) Reactor for Concept Validation with AB

As the AB powder moved from the hopper to the screw channel and the screw rotated, the solid bed was compacted, transported down the channel, and then released hydrogen in the compression zone. However, because of the excessive pressures from the hydrogen-generation and frictional forces between the barrel and the AB powder, the barrel and screw in the extruder nozzle clogged. Therefore, with the current screw and nozzle design, we were not able to validate the flow-through reaction concept using an auger as a solid AB reactor. No additional experimental work was performed with the auger system since the focus of the HSECoE changed to the fixed-bed reactor design.

2.2.6.2 Fixed-Bed Reactor Validation Tests

The purpose of our experiments with a fixed-bed reactor validation tests was to better understand thermal heat propagation in AB and AB/MC composite needed to successfully operate the fixed-bed reactor. An experimental-scale, fixed-bed reactor was developed as shown in Figure 2.20. This system heated a sample from the bottom and then measured the reaction propagation by thermal imaging with an infrared camera. Testing was performed on 2.5 g of AB and AB/MC in a temperature range of 160°C to 400°C at 1 atm. The results indicate that neat AB chips foamed and did not propagate heat well in the current design. However, AB/MC composite powder did not foam, and heat propagated up the sample over time. Figure 2.21 shows the infrared camera images of this latter run. Heat propagation was not fast, and it took 4 minutes for the temperature to peak and that is with an initial point of 300°C. We believe the hot spot that develops within the 236- to 260-second period is a reflection and not real. The temperatures along the column of the bed were measured with an array of thermocouples as shown in Figure 2.22. By comparing the temperature profile of AB and AB/MC, one can see that heat is propagating in AB/MC.

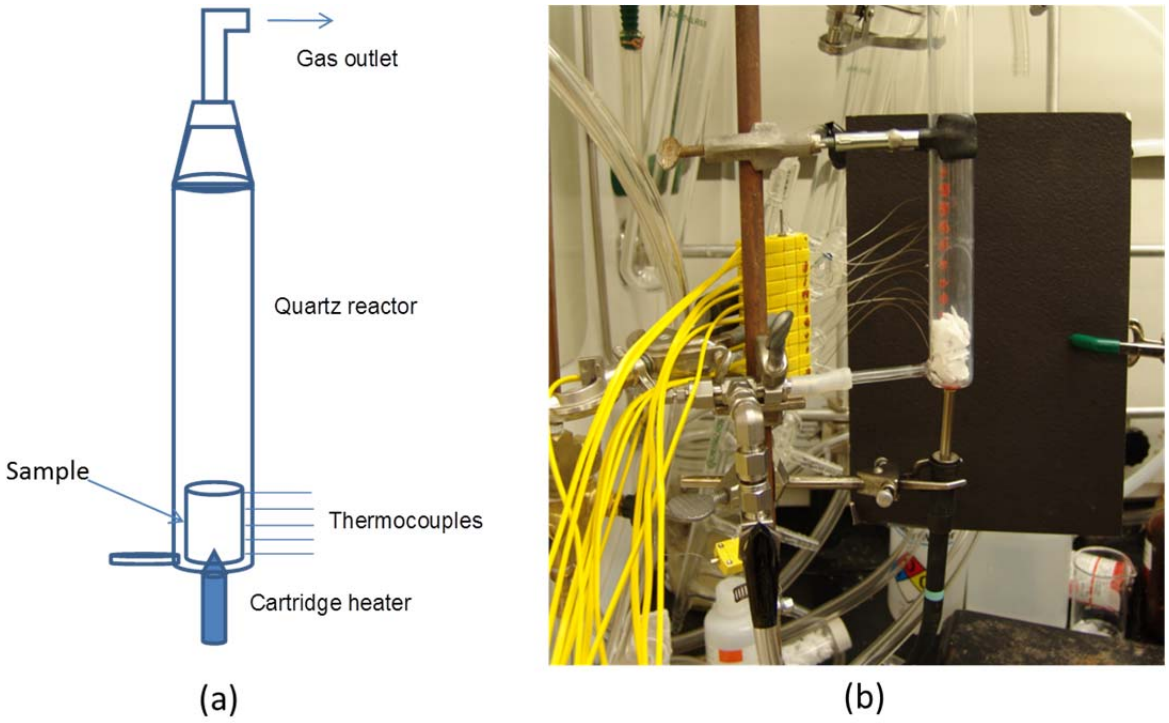

Figure 2.20. Fixed-Bed, Proof-of-Concept Testing: (a) Experimental Diagram and (b) Photograph of the Experimental Setup

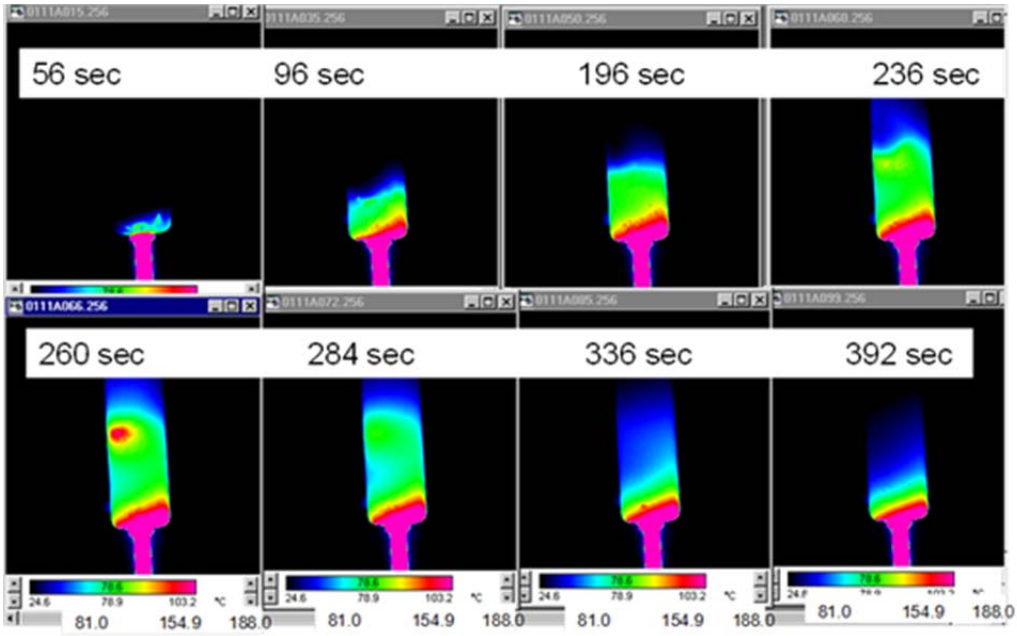

Figure 2.21. Thermal Imaging of the Fixed-Bed Reactor Tests Demonstrating Reaction Propagation Over Time

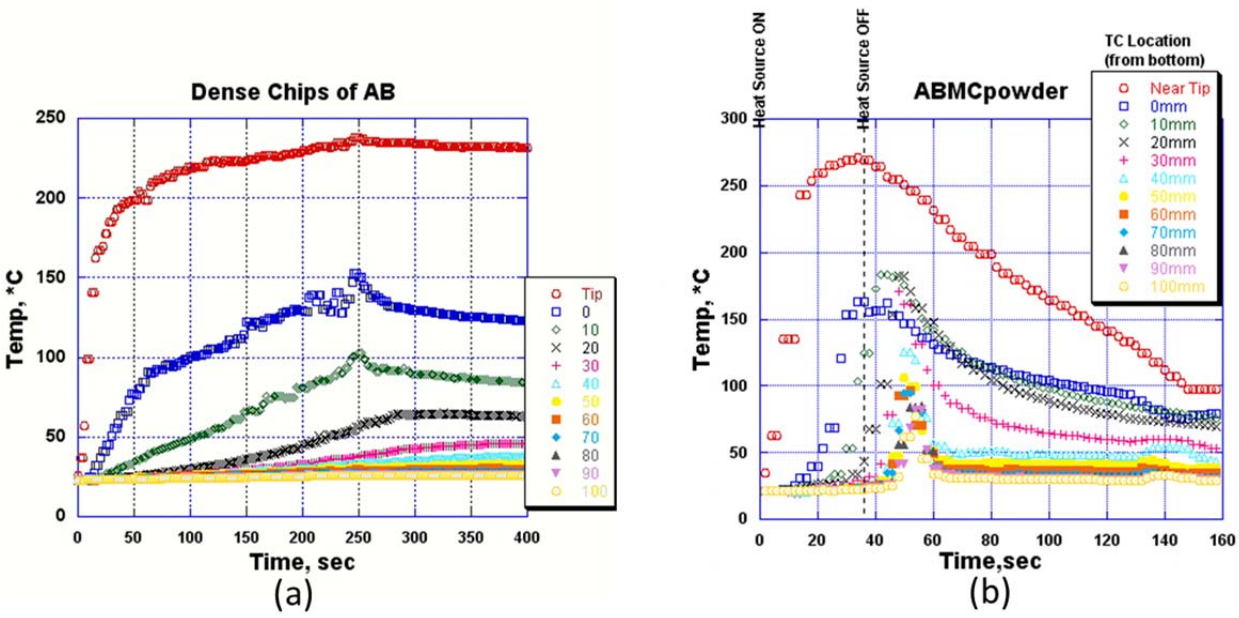

Figure 2.22. Axial Temperature Profile for the Fixed-Bed Reaction Propagation Experiments: (a) for AB Chips and (b) for AB/MC Powder

2.2.6.3 Pneumatic Conveyance Validation Tests

Pneumatic conveyance was chosen as the means for transporting bulk solids for the refueling concept validation testing. For delivering fresh fuel to a vehicle storage vessel, other conveyance approaches including augers and gravity feeding from overhead storage bins may be practical solutions. However, for removing spent solid fuel from a vehicle rapidly, gravity draining alone is not likely to be sufficient, and pneumatic conveyance is a relatively simple approach that can be implemented. A commercially available 2-inch Exair heavy-duty line vacuum apparatus was acquired for refueling concept testing (for both filling and draining) (Figure 2.23). The line vacuum device was placed near the middle of ~22 feet of 2-inch flexible hose. The vacuum device was operated with ~80 psig compressed air because the vendor specifies an air usage rate of ~75 scfm at this pressure. This system is capable of transporting rock salt over 100 feet at 4 kg/min. Because the conveyance rate depends on the material density, AB should be transportable being only 0.8 g/mL as compared to a density of 2.2 g/mL for rock salt.

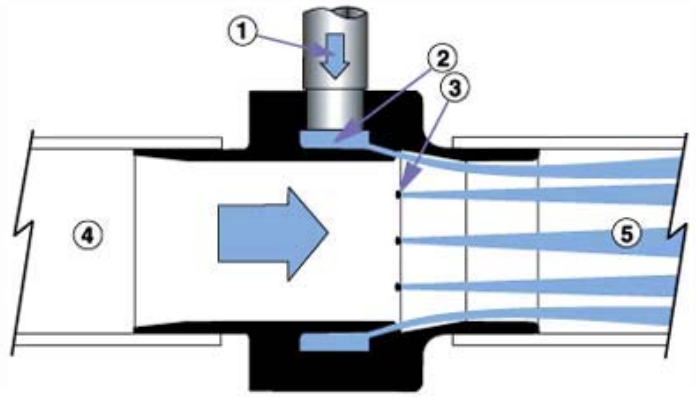

Figure 2.23. Exair Line Vac Design Principles (source Exair.com)

Based on this device, the concept for refueling would be as follows:

- Vent the hydrogen from the tank to ~1 atm pressure and saving it for Step 4
- Drain spent fuel sections (e.g., evacuate/remove pneumatically using air or nitrogen as the carrier)
- Refill empty sections (e.g., add fresh fuel pneumatically under a 1-atm hydrogen cover blanket)
- Recompress and add to the tank the "same amount" of hydrogen that was vented in Step 1.

Preliminary, open-ended flow tests were performed with this system to demonstrate total flow capability. Tests were performed with both fine particulate LDPE powder and LDPE beads because of the high cost of AB/MC and the large volumes required for these tests. The LDPE beads, which can be considered a surrogate for proposed AB or AB/MC pellets, were irregularly shaped with rounded surfaces and were 3 to 8-mm in diameter (as spheres). Assuming the fuel ratio is 80:20 AB/MC (and the 2.5 molar equivalents of hydrogen are released during onboard reaction), a refueling rate of 9.2 kg/min is required to meet the DOE 2010 target refill rate of 1.2 kg hydrogen/min. Transport rates of 9 kg and 20 kg were achieved for the powder and pellets, respectively. Therefore, the tests were successful in showing that solid materials could be transported fast enough to exceed DOE technical targets.

A one-eighth size section of the full-scale, fixed-bed storage vessel designed by PNNL and described in Section 2.2.2.4 was fabricated from Plexiglas to evaluate the onboarding and off-boarding of AB (Figure 2.24). In this system, the surrogate material is filled from the top and drained from the bottom. Both pellets and powder were tested. One of the drain tests is shown in Figure 2.24. In the design, the pellets gravity flow from the one- eighth section into a central tube. Then, the pellets are pneumatically vacuumed from the top of the central tube. For filling, the Line Vac is reversed and material is transported into the top of the central tube and then blown into a slot connecting the central tube to the top of the one-eighth section. The transport gas flows through a filter just below the top lid of the one-eighth section to prevent loss of material.

Figure 2.24. Draining Experiment of a One-Eighth Section of the Fixed-Bed System using Polyethylene Beads

The results of the fill and drain tests with both pellets and powder are shown in Table 2.11. Based on the results of these preliminary tests, pellets are recommended over powder for transport. Both the fill and drain rates of these pellets is >50% of the DOE 2010 target.

Table 2.11. Results of the Pneumatic Fill and Drain Tests for the Fixed-Bed System

Condition Tested	LDPE Type	Measured Rate	Comparison to DOE 2010 Target
System Fill	Pellets	5.4-6.9 kg/min	60-75%
System Drain	Pellets	4.8-9.2 kg/min	50-100%
System Fill	Powder	2.5 kg/min	27%
System Drain	Powder	4.5 kg/min	49%

Note that the estimated AB/MC transport rate assumes that fresh fuel would be added simultaneously with the removal of spent fuel, both at the same rate (neglecting the mass loss due to hydrogen release from the spent fuel). This could be accomplished, for example, using separate conveyance systems for filling and draining in parallel.

2.2.7 Summary of Solid AB Work

The use of solid AB was ultimately rejected in favor a fluid AB system. There were several challenges related to these systems, but the challenges generally are associated with solids handling. There were concerns about plugging and adequate flow in moving the material onboard and off-board the vehicle or in transporting it through a reactor onboard the vehicle. Of particular concern is that neat AB foams to nearly 10 times its original volume during reaction. As discussed above, additives can minimize this foaming but at a mass and volume penalty. In addition, the AB becomes sticky during reaction as the material reaches its melting point and begins to react. As a result, AB particles may agglomerate within the bed or reactor and prevent their flow.

2.3 Phase II: Evaluation of Slurry Chemical Hydrogen-Storage Materials

The fluid-like nature of slurry will provide a unique opportunity for storing, delivering, and distributing hydrogen. The use of slurry as a medium to carry CHS materials has advantages as alternative techniques in terms of pumping, transporting, and adapting to existing infrastructure. The spent fuel can be collected relatively easily at the regeneration station as well. Slurries provide an attractive option without significant reductions in gravimetric and volumetric densities of hydrogen if the weight percent of the CHS material is kept high. In addition, slurries potentially have the advantage of efficient heat transfer and heat management. In an effort to develop an advanced hydrogen storage technology, PNNL began investigating a slurry system composed of AB/high-temperature liquids in FY 2011.

For this work, we selected AB powder as a role model for CHS slurries and identified a liquid carrier to prepare slurries with a weight percent solid loading of AB as high as possible. The properties of these slurries were investigated, and they were tested relative to the system components, either with the fresh or spent slurries themselves or with surrogates with similar physical properties. This work will be described in Sections 2.3.1 to 2.3.3. Although most of the experimental work done at PNNL was with AB slurries, system development was performed with alane slurries as well. AB was the representative exothermic CHS material with a system design tailored to its properties while alane was the representative endothermic CHS material and a slightly different system was developed for it. The system designs will be described in Section 2.3.4.

The results of the system development and experimental validation were used to develop transient storage-system models that can be used to understand the performance of the storage system under a variety of operating conditions. These storage models can then be coupled with a larger vehicle-level model to predict the performance of a mid-size vehicle during four different drive cycles and three different ambient temperatures. The cost of these systems at production levels between 10,000 and 500,000 units can be estimated to provide a comparison to other storage systems being developed both inside and outside of HSECoE.

2.3.1 Material Operating Requirements

Material operating requirements identified by HSECoE have focused on supporting experimental validation activities and determining material engineering properties in cases where literature data are not available. During our material engineering work, we identified the need for material development to optimize performance of fluid AB to be successfully integrated in the CHS validation testing during Phase II.

In support of this work, our experimental efforts included:

- Prepare scale-up quantities of fluid chemical hydrogen for large-scale testing
- Characterize pre- and post-reaction materials properties.

For fluid-phase compositions, the MOR group provided input to the system modelers and transport phenomena studies by measuring the following parameters:

- Hydrogen capacity
- Thermodynamics
- Dehydrogenation kinetics
- Particle size
- Stability
- Viscosity
- Impurities
- Thermal conductivity.

Fluid AB was selected as a surrogate material by HSECoE for systems engineering of a CHS system. To aid in the down-selection process, HSECoE modeling results were used to create a set of criteria that are listed in Table 2.12.

Based on the outcome of material engineering, preliminary testing, properties of slurry AB were compared to the criteria. The following three areas require additional evaluation:

- We need to report on ability to develop a 40wt% liquid AB material that can be pumped both pre- and post-dehydrogenation and that has kinetics comparable to neat AB.
- Reactor testing is required to investigate if the fluid CHS candidate has potential to perform as desired with respect to reaction characteristics, impurity levels, and fouling.
- The CHS be must be able to be pumped without clogging, settling, or flocculation throughout the system. If settling or flocculation does occur, the feasibility of an engineering solution may be assessed.

Table 2.12. Acceptance Criteria for a Chemical Hydrogen-Storage Material in Comparison to AB Slurries

Selection Criteria	Minimum Criteria	Quantified Properties for AB Slurry
Hydrogen Content of the Chemical Hydrogen-Storage Material (includes slurrying agents and additives)	≥6 wt%	7.2 wt% obtained (45 wt% loading)
Phase change	No phase change that would result in material not being transportable	No phase change observed
Flowability before and after H-release at -20°C to 40°C	<1500 cP	~600 cP for 45% AB fresh and spent slurry
Thermal and chemical stability at -20°C to 40°C	Shelf life >6 weeks	Fresh AB slurry stable at r.t. for >4 months
Onboard Efficiency based on HSECoE drive cycles and up to eight startups per day	>90%	Modeling shows feasibility
Safety	Safety issues comparable to gasoline or Safety issues can be mitigated reasonably	Flammability test to be performed at the United Technologies Research Center (UTRC)
Kinetics	Similar to neat AB	Better than neat AB since no induction period
Settling/flocculation	Minimum mitigation/stirring to recover sample acceptable	Fresh AB good for >4 months. Spent AB settles within hours; stirring to recover acceptable
Heat of reaction	Similar to neat AB	Similar to AB
Impurities	Can be mitigated reasonably	UTRC investigated adsorbents as part of HSECoE
Scale up to larger quantities	≥1 L can be produced before Phase III	Achievable

2.3.2 Slurry Development

To develop stable slurry that remains in suspension, we explored preparation methods to obtain homogenous slurry with AB finely dispersed in a liquid carrier. These results are also documented in the literature (Choi et. al. 2015). Regarding preparation of hydrogen storage materials, milling is a method widely used for materials synthesis and particle size reduction. We investigated different methods of ball milling to decrease particle size; these methods included high-energy milling, jar rolling, and planetary milling. Ammonia borane was milled both dry and in the liquid carrier without achieving satisfactory results.

Another proposed method of AB particle size reduction is sonication, which is commonly used in the preparation of evenly dispersed nanoparticles in liquids. The primary advantage of sonication processes such as ultrasonic bath or an ultrasonic probe is that it yields materials with high level of homogeneity at the atomic level by breaking intermolecular interactions. We will here show how this technique will be applied not only to decrease the particle size of AB in the fluid-phase composition but also to achieve a homogeneous mixture of AB/liquid carrier/dispersant.

2.3.2.1 Carrier Fluid Selection

To obtain stable and fluidic AB slurry, the optimization of several variables is critical. The most important variables include: liquid media/stabilizing agents, particle size, and slurry homogenization systems/slurry stability. More specifically, when preparing slurries, it is important to achieve a distribution of the solid in the liquid in such a way that the solid does not settle or flocculate. In addition,

the liquid media and any dispersants need to be chemically stable not only by themselves but also with AB through its decomposition. To evaluate promising liquid carriers for stable and fluidic AB slurry, each candidate mixture of liquid carrier and a small amount of AB was mixed and categorized based on their wettability and suspension state for the first 24 hours. We have explored high-temperature liquids that are chemically compatible with AB and its dehydrogenation products. These liquids are 1) P-alkyl aromatics (HT), 2) synthetic hydrocarbons (HTR), 3) MK1 (a mixture of biphenyl and diphenyl ether), and 4) silicone fluids, many of which are stable up to 350°C.

To select a liquid carrier, we mixed the same amount of AB in the liquid carrier in a glass vial and observed if a suspension was formed. In the test of the liquid carrier MK1, an unacceptable odor that may be an environmental hazard was observed. Thus, MK1 was discontinued. To further investigate the wettability, suspension state, flowability and chemical stability of the remaining liquid media at 25°C, 10 ~ 40wt% of AB was added to HT, HTR, tetraglyme, and silicone fluids. The results indicated that AB powder slowly wetted in the liquids and would separate relatively rapidly because of the difference of densities between AB (0.78 g/mL at 25°C) and candidate carriers (0.89~1.075 g/mL at 25°C). The slurries were qualitatively evaluated for their ability to flow through a 12.7-mm tube. While all the fluids produced reasonable slurries the HT fluid was eliminated because it flowed quite slowly through the tube and appeared dense and nearly saturated. During testing, the 10% AB in HTR floated and agglomerated, while the 20% AB in tetraglyme solidified.

Thermogravimetic analysis was then performed on the remaining fluid carriers to determine if any mass loss occurred during a typical decomposition reaction. All but the silicone oil (AR 20) and HTR undergo mass losses greater than 2 wt% over the target temperature range. Based on the results of this test, the silicone fluid was selected as the fluid candidate of choice. Figure 2.25 represents the mixtures of AB/silicone oil under a variety of conditions. The 10 wt% slurry clearly separates from the silicone oil. In addition, the maximum loading capacity of neat AB to form slurry that flows readily in the respective liquid carriers has been found to be up to 30 wt%. Further increasing the AB loading over 40 wt% showed degradation in the degree of flowability, and most of the liquid carriers were absorbed by the AB powder as shown in Sample 6 in Figure 2.25, which is a 40 wt% AB/AR 20 slurry.

	Sample 1	Sample 2	Sample 3	Sample 4	Sample 5	Sample 6	Sample 7
Composition	10wt%AB/ silicone oil	20wt%AB/ silicone oil	20wt%AB/ silicone oil	20wt%AB/ silicone oil	30wt%AB/ silicone oil	40wt%AB/ silicone oil	40wt%AB/ silicone oil
Milling conditions	N/A	N/A	Planetary Milling 4h	Jar-roll Milling 16h	Jar-roll Milling 72h	N/A	Planetary Milling 24h
Color	opaque white & oil	opaque white & oil	opaque white & oil	opaque white & oil	opaque white & oil	opaque white & oil	opaque white & oil
Flow-ability[1]	4.5	4.5	3.5	3.5	3	1.5	2
Slurry stability	• Phase separation (AB & silicon oil)	• Phase separation	• Forming soft pack[2] • Phase separation	• Forming soft pack • Phase separation	• Forming soft pack • Phase separation	N/A	• Forming soft~hard pack[3] • Phase separation

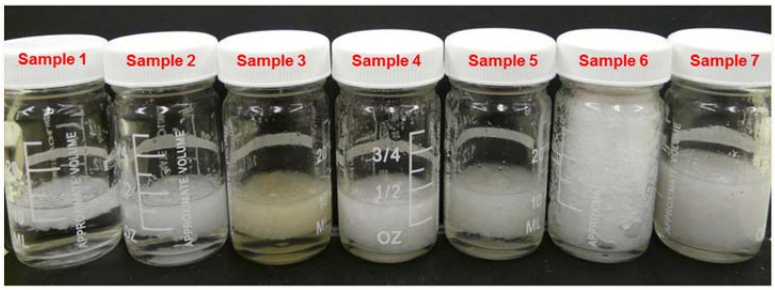

[1] In scale, 1: Very poor, 5: Very good
[2] Soft pack: diffuse & easily reincorporated
[3] Hard pack: dense & difficult to reincorporate back into slurry
* Density (g/mL at 25°C) : AB (0.78), Silicon oil (1.07)

11

Figure 2.25. Evaluation of Ball-Milled Samples of AB in Silicone Oil

2.3.2.2 Particle Size Reduction Techniques

To achieve higher loading of 40 to 50wt% AB solids, and above, it is necessary to have smaller AB particles in the AB/silicone fluid composition. Therefore, it is crucial to adopt an efficient tool to reduce particle size. As a result of the inability to dry mill the AB, an approach to obtain smaller particle sizes of the solid hydride while in the fluid phase was explored, and we selected two unique processes: 1) a wet milling/mixing method and 2) a sonication process. Starting at 30wt% AB/silicone fluid we strived to reach 50wt% while maintaining a flowable/pumpable viscosity.

Milling Techniques

To reduce particle size in an efficient way, low-energy ball-milling systems (i.e., jar roll and planetary mill) were applied to AB/silicone fluid slurries. A variety of milling times between 5 minutes and 72 hours were investigated. The container and grinding medium for milling were made of tungsten carbide, and the ball-to-AB slurry weight ratio was 10:1. Milling was performed at atmospheric pressure, and the milling speed was 200 rpm. Under these conditions, we obtained a 20~30 wt% AB/silicone oil composition that showed acceptable flowability after certain milling times.

Overall, the experimental results indicate that the maximum loading of AB slurry is up to 40 wt% because of the limitation of particle size reduction and the lack of flowability when using ball-milling methods. More specifically, most AB particles floated in the silicone oil after milling, and formed a dense AB layer that prevents the slurry from flowing readily. Loadings over 50 wt% could not be effectively achieved under these conditions. In conclusion, none of the employed milling techniques could effectively reduce particle size; therefore, these techniques were discontinued for slurry preparation.

Sonication Techniques

Sonication is commonly used in the preparation of evenly dispersed nanoparticles in liquids. The primary advantage of a sonication process such as ultrasonic bath or an ultrasonic probe is that it yields materials with high levels of homogeneity at the atomic level by breaking intermolecular interactions. Thus, the application of this technique could not only decrease the particle size of AB in the fluid phase but also achieve homogeneous and stable slurry. In the course of this study, we have found that sonication is highly beneficial for obtaining well-dispersed, significantly reduced particles, and slurries with acceptable flowability with up to 40 wt% solids.

We found that the morphology of the starting particles has proved critical in the development of quality AB slurries. Smaller more regular and uniform particles would generally lead to slurries with greater flowability. We obtained powder AB from three different sources—Sigma-Aldrich, Aviabor, and PNNL. The micrograph photos shown in Figure 2.26 reveal significantly different particle sizes and shapes for the three different batches. In the end, a fourth supplier, Weylchem Chemicals was used for AB slurry production. Weylchem produces an AB with a smaller range of particle sizes. While these other three sources produce AB with very few particles less than 40 μm, nearly 25% are in this size range.

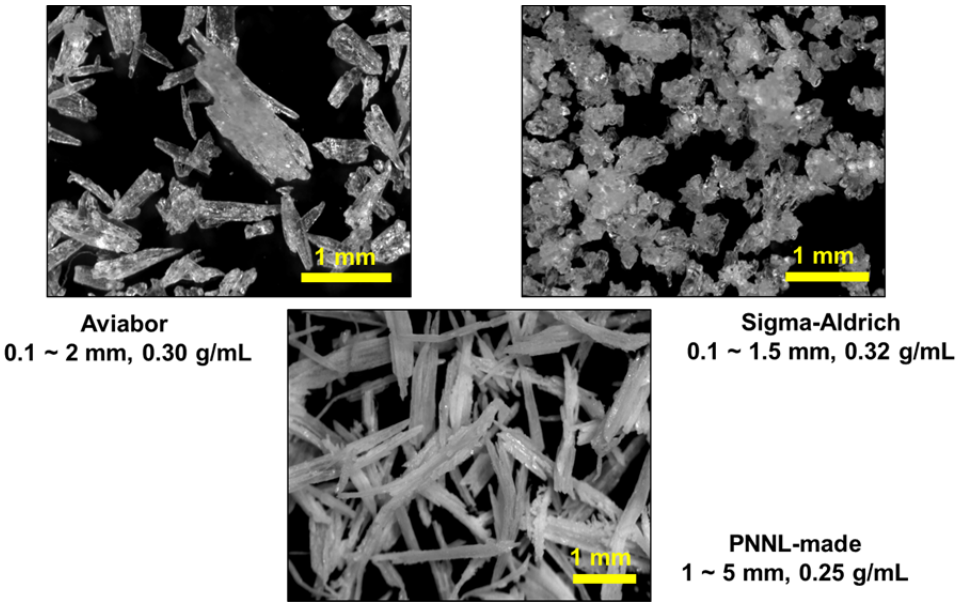

Figure 2.26. Microscope Analysis of Candidate Solid AB Materials

In the preliminary experiments, it was revealed that there is no beneficial effect to obtain better homogeneity using an ultrasonic bath regardless of the experimental variables/parameters. However, the preliminary experiments did reveal significant improvement in homogeneity and flowability using an ultrasonic probe (hereafter referred to as "tip-sonication"). Typical AB slurry was prepared using the following procedure. First, approximately 10 g of AB were added to a flask containing stirring silicone fluid. The flask then was submerged in an ice bath, and the sonicator tip was lowered into the flask just below the orifice of the vortex. During the sonication process, the flask was kept under a positive flow of nitrogen. The ice bath was changed every half hour or as needed.

Analyses of samples produced at 10, 20, 30, and 40 wt% AB after 1-hour of tip sonication indicate that there is substantial difference in the degree of homogeneity when compared to grinding. The samples show well-dispersed slurries without any noticeable AB particles. Although AB powder will float in the silicone oil because of the difference of densities in samples of <20 wt% AB slurry, there is no indication of such phase separation in higher AB loading over 30 wt%. This implies a significant improvement over the suspension state compared to the slurries after ball milling or ultrasonic bath processing. Finally, the slurries after tip-sonication show considerable improvement in terms of flowability compared to those after ball milling.

2.3.2.3 Screening of Particle Size Distribution

In addition to sonication, the AB was prescreened through an U.S. 35 (500 μm) mesh screen with the assistance of a marble pestle. The sieved AB powder was subsequently used for further optimization of slurry composition. The particles before sieving had angular shapes and sizes in the range of 0.1 to ~1.5 mm as estimated by spherical diameters. After sieving, the primary particle size was reduced to between 50 and 500μm. The sieved AB powder was subsequently used for further optimization of slurry composition.

Several size distributions were investigated to optimize the initial particle size distribution. Using this process, we determined that narrow particle size (i.e., <100μm) distribution produced very thick and viscous slurries at loadings as low as 35 wt%. In addition, sieving below 100 μm only produced thixotropic pastes. Ultimately, it was determined that a wide distribution of particles of less than 500 μm produced the most stable slurries with low viscosities. Subsequently, all slurries were prepared with AB that had been freshly passed through a U.S. 35 mesh screen.

2.3.2.4 Surfactant Addition – Mitigation of Foaming During Dehydrogenation

It is known that AB can foam up to 10 times its original volume during the release of the first two hydrogen equivalents. One of the desirable aspects of a slurry AB is the possibility of controlling this foaming through the use of surfactants or other anti-foaming agents (AFA). In many applications, silicone fluids often are used as AFAs as they have very low surface tension leading to small, fragile bubbles that rupture when they reach the surface. Unfortunately, the massive release of hydrogen during the first two equivalents (i.e., up to 19 wt%) exceeds the innate properties of the silicone fluids, and the slurry often foams up to 10 times its original volume. In addition to the excessive volume change, this foam tends to solidify if allowed to cool too rapidly. This poses a serious problem for automotive applications as the solidified AB foam is quite tough and rigid, and can easily plug tubing.

To help control this foaming, several nonionic surfactants were tested. Unlike the more conventional ionic surfactants, nonionic surfactants are neutrally charged long-chain alcohols. This type of surfactant was chosen because of concern with chemical incompatibilities. Surfactants with extremely low hydrophile-lipophile balance numbers were evaluated based on their flash points, viscosity, functionality, and chemical compatibility. Ultimately, three potential AFAs were selected from Dow Chemical's Triton line—X-15, X-35, and X-45, which are a series of octylphenol-ethoxylates.

These products were chosen based on low hydrophile-lipophile balance numbers, high flash points, and chemically compatibility with AB. To gauge the effectiveness of each AFA, a series of tests were conducted on 40 wt% slurries. Loadings of 1, 3, 5, and 7 wt% were tested for their ability to reduce the level of foaming in a typical thermal dehydrogenation reaction.

In this study, the ability of the AFA to control the level of foaming was characterized by a series of qualitative tests. Each respective AFA and loading concentration was added to 40 wt% slurry, and the mixture was mixed thoroughly for 1 hour. The slurries then were thermally reacted in the bench-scale reactor. Through the course of testing, it became clear that the X-45 surfactant had no beneficial effect on the level of foaming. Both the X-15 and X-35 surfactants show reasonable effectiveness at loadings as low as 1 wt%. In both cases, the surfactants were able to reduce the foam level by up 50%. Further testing demonstrated that the X-15 surfactant could reduce the foam level by 60% at 3 wt% loading in 40 wt% slurry. This equated to 2.87 wt% relative to the AB.

In addition to determining the optimum loading of AFA, several methods were investigated to determine an adequate method for applying the AFA—1) direct coating of AB with the surfactant; 2) dissolving both AB and surfactant, followed by rapid evaporation of the solvent; and 3) adding the surfactant to the slurry during processing. Ultimately, adding the AFA to already-prepared slurries was the most successful.

2.3.2.5 Slurry Preparation Scale Up

Two major challenges existed in producing both high loading and large volumes. It is common knowledge that the high-energy tip-sonication process used in slurry production results in localized temperature gradients. Without proper cooling, these localized gradients could produce a cascade thermal reaction resulting in a violent exothermic reaction. In addition to regulating the process temperature, providing adequate mixing also is essential. It has been observed that AB readily absorbs silicone fluid up to 50% of its mass. As with many slurry materials, increasing the solids content exponentially increases the viscosity. While AB slurries are shear thinning, the yield stress is quite high, and common laboratory mixing methods proved unable to thoroughly mix slurries with high solid loadings.

The first step in producing high solid loading slurries was to better regulate the temperature of the slurry while simultaneously reducing the minimum amount of time required to sustain the process. After testing multiple apparatuses and concepts, the use of a jacketed reaction vessel connected to a recirculating

chiller proved the most successful. In this configuration the slurry temperature could be easily regulated by controlling the bath temperature. A bath temperature of 5°C would keep the slurry temperature to <15°C throughout the sonication process. This application also proved to be highly modular as jacketed vessels could be used with volumes ranging from 50 to 2000 mL. With this method, only a single sonicator could be implemented. We discovered that, while regulating temperature gradients for a single sonicator was achievable, two or more probe sonicators proved too great a challenge to regulate safely.

Once the issue of temperature regulation was resolved, the mixing issues were addressed. While the use of a magnetic stir plate worked for small-scale, low-solid-level slurries, it was not practical or feasible for large volumes or slurries with high solids loadings. We tried several mixing methods including high-shear mixing, low-shear particle dissolution, and high-torque/high-speed mechanical mixing. Ultimately, a high-speed/high-torque overhead mixer was the key to adequately mixing slurries with high solids loadings. With this technique, a specialized overhead mixer equipped with a jiffy mixer could adequately provide the required agitation to produce "flowable" slurry. In this method, it was not uncommon for slurries above 40 wt% to require mixing speeds in excess of 800 rpm and torques as high as 30 lbf-ft. The improved large-scale mixing apparatus is shown in Figure 2.27.

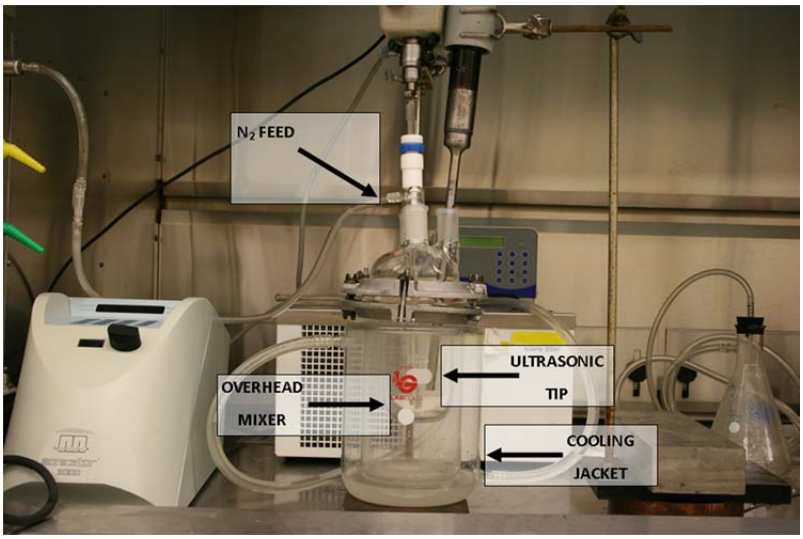

Figure 2.27. Scaled-Up AB Slurry Production Apparatus

2.3.3 Slurry Properties

Reaction kinetic rates for fresh AB slurries were measured, and the particle size distribution, settling rate, and rheology were measured for both fresh and spent AB slurries over a range of concentrations. The results of these analyses are discussed in the following sections. These results are also documented in the literature (Westman et. al. 2016)

2.3.3.1 Reaction Kinetics

Dehydrogenation kinetic properties of AB slurry were investigated with PNNL's Burette system. Two experiments on AB slurry were performed at 100°C and at 120°C and compared to solid AB. Solid AB is known to have a 20- to 30-minute induction period. It can be seen in Figure 2.28 that the slurry AB does not have any delay in hydrogen release, instead the release occurs immediately. Moreover, more hydrogen was released compared to solid AB. At one point, the temperature was increased to 160°C to finish the reaction and up to 2.5 equivalents of hydrogen, or about 16 wt%, was released. The reason for not observing a delay in onset of hydrogen release in AB slurry may be because of better heat transfer in the liquid carrier.

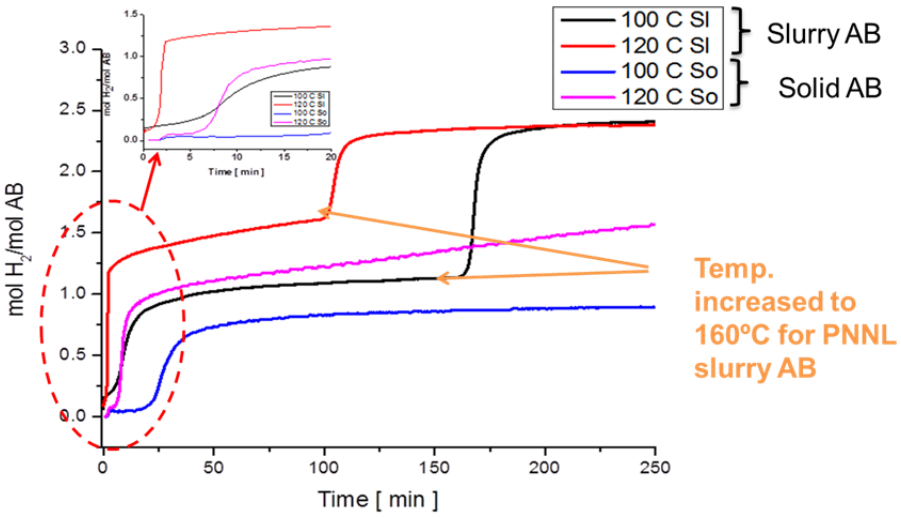

Figure 2.28. Dehydrogenation Kinetics of Slurry AB Compared to Solid AB

2.3.3.2 Particle Size

Using the data collected from the particle size analysis of multiple slurries, a series of size distribution histograms were produced. Distributions were developed for fresh slurries ranging from 20 to 50wt% and for spent slurries of 35, 45, and 50 wt%, respectively.

In comparing the neat AB particle distributions between the two suppliers, stark differences are observed (see Figure 2.29). The Sigma-Aldrich AB consists of no particles less than 50 µm and uneven distribution of particles throughout the measured range. In contrast, the Weylchem AB has a fairly consistent distribution across the measured range. We believe this is an additional benefit to the production of low-viscosity, highly solids-loaded slurries with the Weylchem AB.

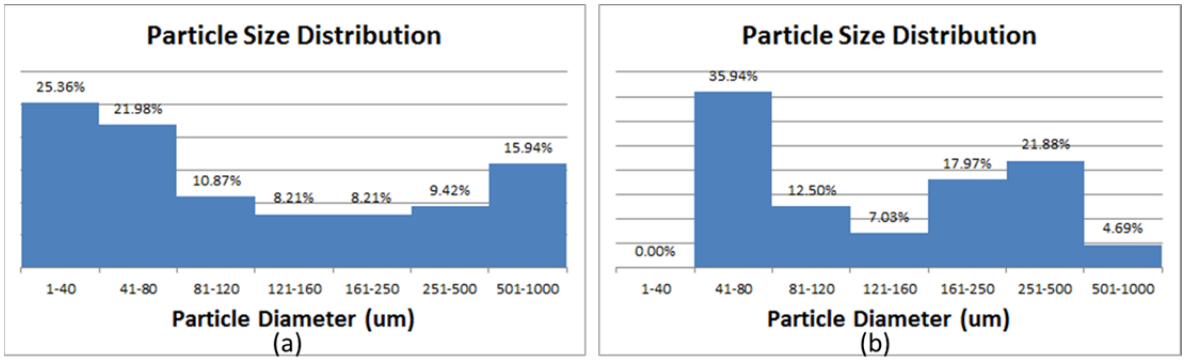

Figure 2.29. Particle Size Distribution of Neat AB: (a) Weylchem and (b) Sigma-Aldrich

Of note is the distribution change of spent AB relative to the fresh material. This distribution indicates a significant decrease in particle size and a narrowing of the overall distribution (see Figure 2.30). This observation corresponds to the measured decreasing in viscosity between fresh and spent AB as well and the significant increase in yield stress.

After the material is sonicated and mixed with slurrying agent, the distributions increase to >75% in the 1 to 40 µm bin. The overall distribution curves, however, appear unaffected by the increase in solid loadings from 20% to 50%. The distributions lean toward the small particle bin but a consistent amount, approximately 20% is in the remaining bins. This further demonstrates the effectiveness of the sonication slurry process in provide particle size reduction at all solids loadings.

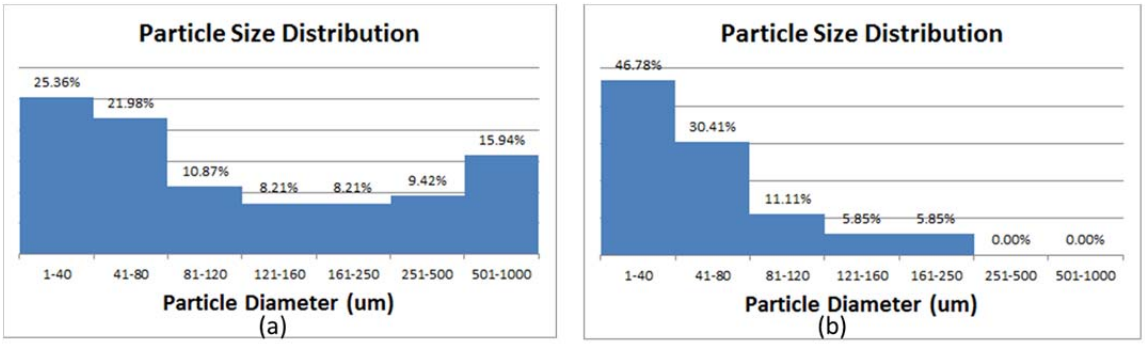

Figure 2.30. Particle Size Distribution of Neat Weylchem: (a) Pre-Reaction and (b) Post-Reaction

In the distribution histograms of the respective AB slurries when comparing fresh and spent material, a significant change in the particle distribution was observed. In all three cases as in the neat AB, with reaction the distribution had shifted significantly to the smaller bins (see Figure 2.31). This once again confirms the observations of decreased viscosity with increasing yield strength post-reaction.

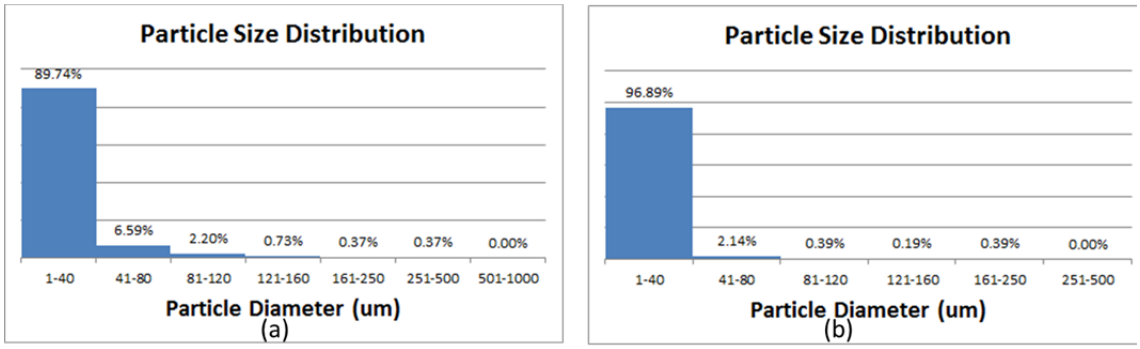

Figure 2.31. Particle Size Distribution: (a) Fresh and (b) Spent 45 wt% Weylchem Slurries

2.3.3.3 Settling and Flocculation Rates

AB like many suspensions will eventually separate into two phases without adequate agitation. In the fresh state, the density of the AB is much lower than the oil and phase separation results in flocculation of the AB. With spent AB, the phases are inversed and the AB tends to settle out of suspension. In an effort to fully characterize the properties of AB slurries the kinetics of this phase separation was determined.

A simple method of recording the extent of phase separation by monitoring the level of free silicone fluid was used to determine the settling and flocculation kinetics for 45 and 50 wt% slurries, respectively. With the 45 wt% samples, an overall flocculation rate for the fresh slurry was observed to be 26.3 vol% within 2 hours (see Figure 2.32). After 48 hours the flocculation had reached equilibrium. The spent 45 wt% slurry also had similar kinetics in that the bulk of settling occurred within the first 2 hours; 36.8 vol% and equilibrium was reached within 48 hours.

With the 50 wt% slurry (see Figure 2.32), a significant change in both the rate and extent of phase separation was observed. Even after 48 hours no visible separation of the fresh slurry was observed. Later observations even after 30 days has shown only minimal <1 vol% separation. We believe this indicates near saturation of the silicone oil with AB. Unfortunately, this trend did not hold with the spent AB. In this case, as with the 45-wt% slurry, the majority of separation occurred within the first 2 hours, 15 vol%. Unlike the 45 wt% slurry, the spent 50 wt% slurry continues to settle, and a final separation of 25vol% was recorded.

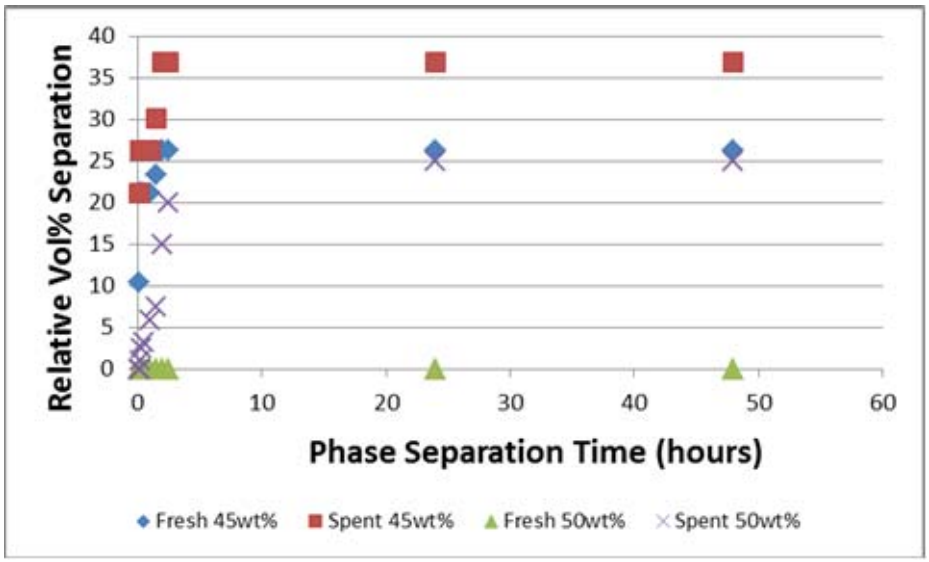

Figure 2.32. Phase Separation Kinetics of Fresh and Spent 45 wt% and 50 wt% Slurries

2.3.3.4 Slurry Rheology

While producing slurries with high solid loadings, the ability to readily flow was critical and driven by the ultimate application of these slurries. To that end, extensive rheological measurements were taken throughout process development. To maintain a reasonable level of flowability, slurry viscosities needed to be below 5000 cP. The original series of experiments was conducted using a cup-and-bob geometry to facilitate the low viscosity nature of the slurries. The commonly accepted Bingham model was used to determine dynamic viscosity and yield stress. Slurries were freshly stirred prior to measurement unless otherwise noted. All measurements were conducted at 25°C.

As seen in Figure 2.33**,** an increase in solid loadings had a subsequent increase in viscosity of fresh AB slurries. This increase in viscosity appears linear in solid loadings up to 35 wt% at which point the viscosity rise becomes exponential. Yield stress also exhibited this trend and almost mirrors the exponential slope of viscosity above 35 wt%. Under stress, the slurries exhibited shear thinning properties which were heavily influenced by the variation in the microstructure of solid aggregates upon shear. .

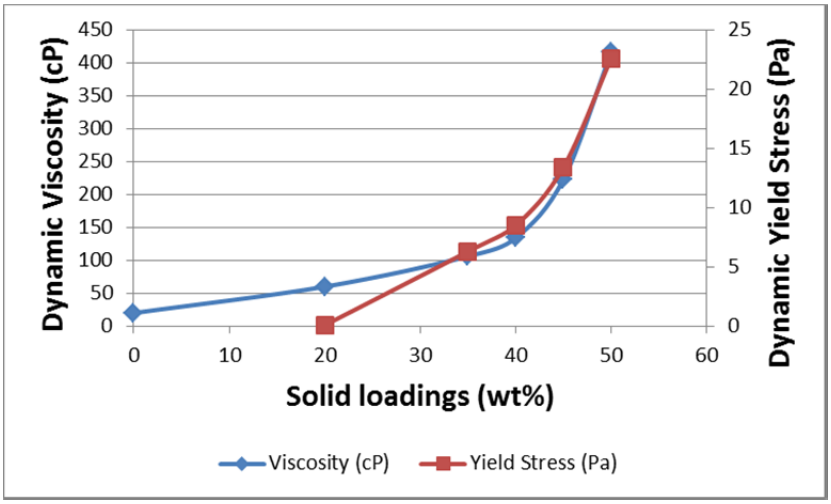

Figure 2.33. Dynamic Viscosity and Yield Stress of Various Solid Loadings of Fresh AB Slurries

While characterizing rheological properties of fresh slurries proved to be relatively easy, the spent slurries produced significant challenges. It has been observed that while thermally dehydrogenating AB in a slurry form, further reduction in particle size and a lowering of the slurry viscosity occurs. What was unexpected was that while the particles had reduced in size, their ability to be deformed or otherwise flow in the bob/cup geometry had significantly changed. We believe that through the release of hydrogen the individual crystalline structure is collapsed resulting in a material with a significant increase in modulus. As a result of this suspected increase in modulus, many of the spent slurries were unable to be measured accurately.

Summary of AB/Silicone Oil Slurry Testing

To optimize chemical hydrogen storage slurry for use as a liquid fuel to provide hydrogen for automotive fuel cell applications, we selected ammonia borane in silicone oil as a role model material. We investigated preparation methods and found that tip-sonication is the most beneficial method. The primary advantage of the tip sonication process is that it yields materials with a high level of homogeneity at the atomic level by breaking intermolecular interactions. This technique was applied to decrease the particle size of AB in the fluid-phase composition and also to achieve a homogeneous mixture of AB/liquid carrier. We found that sonication is highly beneficial for obtaining well-dispersed slurries. A test indicated that the slurry meets the stability requirements and do not decompose in several months.

Ammonia borane (AB) slurry with solid loadings up to 50 wt % (ca. 8 wt % theoretical H2) were produced with non-Newtonian plastic viscosities less than 1000 cPs. These slurries were produced through an ultrasonic process capable of producing slurries of volumes in excess of 2 L. An ideal slurry should be flowable and remain in suspension to facilitate fueling with hydrogen and to avoid re-stirring the slurry. Settling and flocculation were studied, finding that phase separation in a fresh <45 wt % AB slurry result in flocculation, but all concentrations of spent AB settle out of the suspension regardless of loading.

Optical microscopy revealed that AB slurry based on AB particles that do not agglomerate has lower viscosity, is more homogeneous, and can reach higher loadings. Particle size analysis revealed that AB slurry with a consistent particle size distribution and of low viscosity form a flowable slurry. After thermal treatment, particle size significantly decreases and the overall distribution narrows. This observation corresponds to the measured decrease in viscosity of spent AB relative to fresh AB slurry and a significant increase in dynamic yield stress after thermal decomposition. AB is known to foam upon decomposition and AB slurry with loadings of 35 wt % foamed 3 times its volume while slurries over 45 wt % formed a solid mass and were not flowable. The use of a non-ionic surfactant, Triton X-15, show significant promise in controlling the level of foaming produced during the thermal dehydrogenation of the AB.

Through the development of new and efficient processing techniques and the ability to adequately control the foaming, our results demonstrate that stable homogeneous slurries with high solid loading are a viable hydrogen delivery source.

2.3.4 Slurry System Designs

The initial design was based on using AB as the chemical hydrogen material, but it was developed to be flexible and adaptable to a wide range of fluid-phase CHS materials. With minor modifications to the exothermic system design (e.g., slurry-based AB), the system design can be recast for use with endothermic materials (e.g., slurry-based alane). The current system process flow diagram is shown in Figure 2.34. The system operation and the basis for its selection are described in this section and in the literature (Brooks et. al. 2014a).

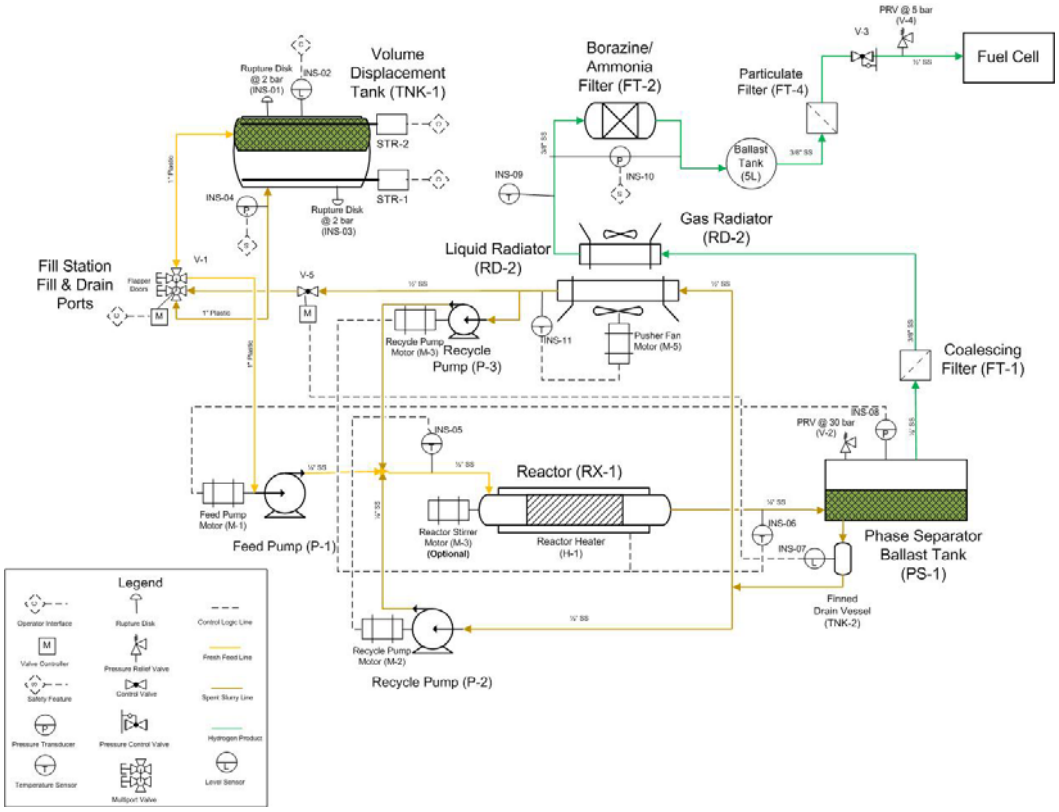

Figure 2.34. System Process Flow Diagram for an Exothermic Chemical Storage Material

The hydrogenated slurry/fuel is loaded on the vehicle where it is stored in a volume-displacement tank (TNK-1). The volume-displacement tank consists of a membrane separating the feed side of the tank from the product side. As fresh slurry is loaded into the tank, the membrane displaces spent slurry from the tank and back to the filling/transfer station for reprocessing. During system operation when hydrogen is being generated, the fresh slurry is transported from the feed side of the tank through the process and then back into the spent slurry side of the volume-displacement tank. The advantage of using a volume-displacement tank is that the overall tank volume is reduced by a factor of two. The volume-displacement tank is not under pressure (~1 atm) nor will it experience high temperatures (<60°C). As a result, it can be a conformable tank made of lightweight, polymeric materials.

Stratified, heterogeneous slurries result from density differences in the solids and the liquid carrier matrix. Stratification occurs when the solid-phase density is less than the carrier matrix, causing the solids to float or, when the solid-phase density is greater than the carrier matrix, causing the solids to settle. In both cases, stratification is undesirable so active mixing is required. Testing was performed to identify approaches that would homogenize the slurry with minimum equipment and effort while not impacting the tank design. The preferred alternative found was the perforated-plate approach. In this approach, a perforated plate nearly the size and shape of the tank is cycled up and down to produce a homogenous mixture. The plate creates vortices that quickly mix the stratified solids (Figure 2.35). Magnetically coupling the perforated plate with linear actuators on the outside of the tank may eliminate unnecessary feed-through connections.

Figure 2.35. Validation Test of the Perforated Plate for Active Mixing in the Volume-Displacement Tank

Ammonia borane dehydrogenation requires elevated reaction onset temperatures. Rather than heat the system quickly to meet the stringent startup time required by DOE technical targets, hydrogen gas is stored in a ballast tank. The ballast tank allows hydrogen to immediately flow to the fuel cell during cold startup while the storage system is warming to the required temperature to initiate the thermolysis reaction. A hydrogen ballast tank with an estimated volume of 20 L and pressurized to 25 bar can store enough hydrogen for the most aggressive drive cycles during the first few minutes of system heating. The ballast tank also provides hydrogen to accommodate the transients associated with the drive cycles described above. As a result, for a short duration, higher hydrogen flow rates are available to the fuel cell than can be provided by a storage system. By having a ballast tank, the system is not required to produce the full 80 kWe. In fact, even with the most aggressive US06 drive cycle that has shown requests for 80 kWe, the maximum hydrogen output for the system is slightly over 20 kWe.

The reactor is a modified plug-flow design. The dehydrogenation reaction is assumed to be a non-catalytic thermolysis. Small-scale, flow-through reactor experiments have shown that active mixing is required to prevent reactor fouling. The reactor design includes axial mixing elements that provide active mixing for the entire reactor volume. In addition, axial mixing also promotes gas-liquid separation, thus mitigating reactor slugging. The reactor is heated on the outer surface with electrical resistance heaters to bring it to temperature and initiate the reaction. Although alternative, possibly more efficient heat sources were considered for providing heat to the reactor, the AB efficiency is already high, and electrical resistance heaters are the lightest weight alternative.

During startup, the heater surrounding the reactor is turned on to raise the temperature of the reactants to the light-off temperature. The fresh feed in the volume-displacement tank is homogenized before feeding into the reactor. Upon reaching the required light-off temperature (~3 minutes), the feed pump begins to move fresh feed into the reactor. Hot product at ~250°C is recirculated to mix with the feed. The recycle stream preheats the feed to eliminate the need to heat the reactor once the reaction is initiated. The recycle also increases the heat capacity of the slurry, diluting the feed and reducing the high temperatures associated with exothermic reaction heat. To maintain the reactor exit temperature at <250°C to prevent volatilizing the slurry fluidizing agent, producing high levels of impurities, or damaging the reactor and downstream components, the recycle can also include a fraction of cold spent slurry exiting the radiator.

Hydrogen is separated from the three-phase mixture in a phase separator developed by Eaton Filtration design group and UTRC. The two-stage design comprises a coalescing demister pad (first stage) and the Cenpellar™ centrifugal separator (second stage). Hydrogen separation is performed using the following three principles: 1) gravity separation similar to a knockout pot, 2) impingement on a surface, and 3) the centrifugal flow generated as the some of the three-phase mixture passes through the centrifugal separator (Figure 2.36a). No slurry materials can be in the hydrogen, and no hydrogen can be in the remaining

slurry. As a result, the separation requirements for the phase separator must be nearly perfect. The gas passes through a coalescing filter to remove any aerosol droplets. The hydrogen gas then passes through a radiator to lower its temperature to that required for the fuel cell feed. The radiator uses a finned tube configuration based on ¾-inch outer diameter (OD) aluminum fins and a ¼-inch stainless-steel tube from Energy Transfer MDE (Figure 2.36b). Improvements in heat transfer were accomplished by inserting a turbulator™ inside the radiator tube. A turbulator™ is a twisted-tape that creates turbulence in the radiator and increases the heat-transfer coefficient between the hydrogen and the tube wall. Increasing the heat-transfer coefficient is corollary to decreased radiator volumes and masses.

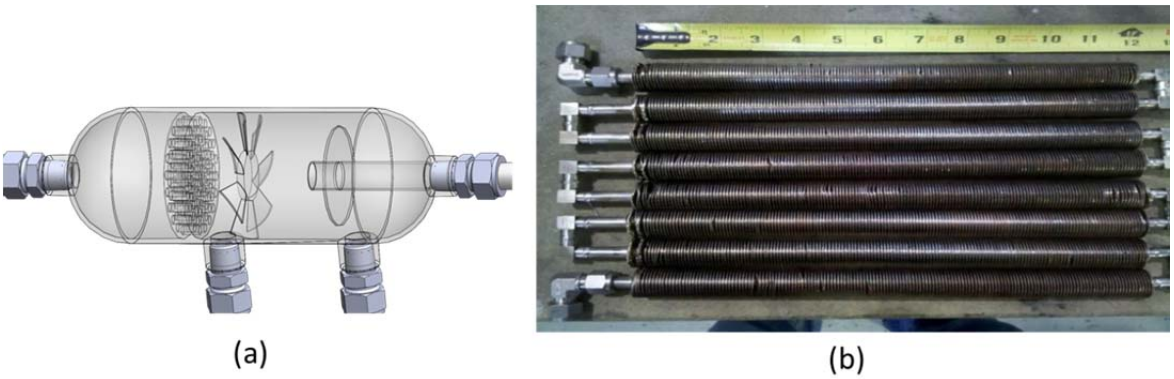

Figure 2.36. (a) Internal Design of the Eaton Filtration Phase Separator and (b) Energy Transfer MDE Finned Tube Slurry/Gas Radiator Design

Impurities generated from CHS media require removal prior to reaching the fuel cell. The hydrogen delivered to the fuel cell must be greater than or equal to 99.97%. The SAE J2719 hydrogen quality guidelines for fuel cell vehicles list a number of impurities and their maximum concentrations. Dehydrogenation of AB is known to produce fuelcell impurities; namely, ammonia, borazine, and diborane. Doped activated carbon adsorbent beds were demonstrated to adsorb these impurities and produce fuel cell grade hydrogen (Graetz and Reilly 2005).[5] Based on our system design, the size of these adsorbent beds is based on the amount of impurities anticipated and an 1800 mile replacement frequency. The fuel cell grade hydrogen (T = 80°C and 25 bar) is then fed to the fuel cell at 5 bar via a pressure regulator.

The slurry from the phase separator enters a collection vessel where the hydrogen gas in the slurry can coalesce and gravity separate from the condensed phase. This additional separation is required based on the experimentally observed foam that has been produced in the validation studies with UTRC. Once this final separation is complete, a fraction of the slurry is recycled back to the reactor and the remaining hot material passes through the slurry radiator with 1-inch OD aluminum fins and a ⅜-inch stainless-steel tube. The slurry radiator has a similar design to the gas radiator, using finned tubes and a turbulator™. The radiator lowers the slurry temperature to a safe handling temperature of less than 60°C, thus eliminating the premature, uncontrolled hydrogen release from the fresh fuel located in the adjacent storage volume. A valve controls the flow of the cooled slurry returning to the volume-displacement tank to maintain a constant overall system pressure near the set point of 25 bar. Because the volume-displacement tank has a limited volume and is maintained at atmospheric pressure, we assumed that any hydrogen remaining in the slurry as it returns to the volume-displacement tank would be vented to the atmosphere.

All slurry piping is designed with tubing of at least ½-inch diameter to prevent plugging. The high-pressure hydrogen gas lines were sized to ⅜-inch diameter. The system is instrumented as required with thermocouples, pressure transducers, and level gauges to provide adequate system control.

[5] Personal communication with Dr. S-Y Liu, University of Oregon.

The system design described above and provided in Figure 2.34 is for an exothermic reaction such as AB dehydrogenation. For a mildly endothermic reaction (e.g., alane dehydrogenation), the system design is modified slightly (see Figure 2.37). For the endothermic system design, the recycle stream is replaced with a recuperator that allows heat transfer from the product to the feed without diluting the feed stream with spent product, thus, minimizing unnecessary heating requirements. Its design is a ½-inch tube within a ¾-inch tube, and flow is countercurrent. The reactor heater for endothermic materials operates during startup (as is the case of an exothermic reaction) and continuously during reactor operation. One additional change in the system design is that the adsorbent beds employed to remove fuel cell impurities have been eliminated because alane does not produce fuel cell impurities during dehydrogenation.

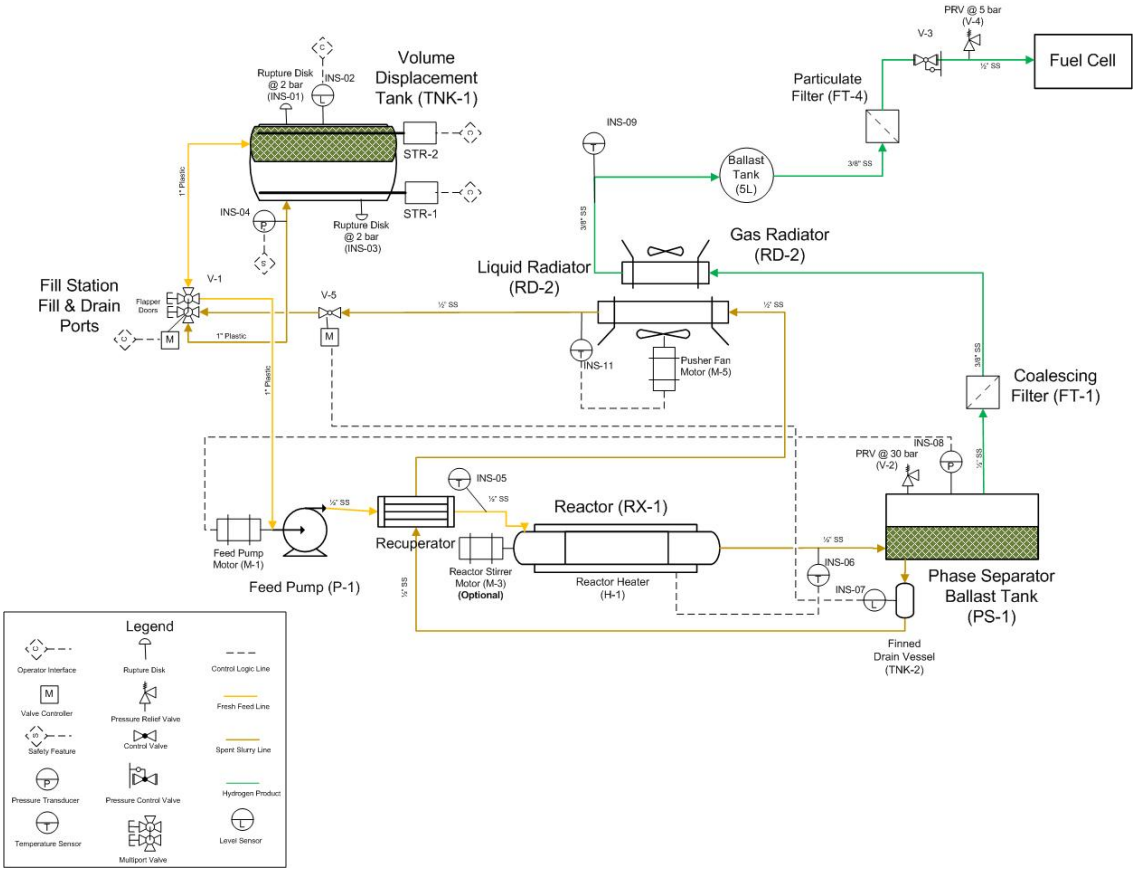

Figure 2.37. System Process Flow Diagram for an Endothermic CSM

The original design is based on the properties of AR 20 (polyphenyl-methylsiloxane from Sigma-Aldrich). While this oil was reasonably good for preliminary validation testing, there is a need for improved slurrying agents with even lower vapor pressures to minimize the need to remove them in the onboard hydrogen purification process. Oils such as those used for diffusion pumps are good candidates. Silicone oils like pentaphenyl trimethyl trisiloxane have a very high-temperature stability and very low vapor pressure, both of which are highly desired when trying to minimize onboard hydrogen purification requirements. Additional work is required in this area.

2.3.4.1 System Design Relative to DOE Technical Targets

These systems have been developed to meet most of the DOE technical targets for AB and alane as shown in the spider charts in Figure 2.38 and Figure 2.39, respectively. The primary target that has been the focus of this work is the gravimetric capacity. It has been determined that, if the system mass can be reduced to meet the gravimetric density, the volumetric density also will be met.

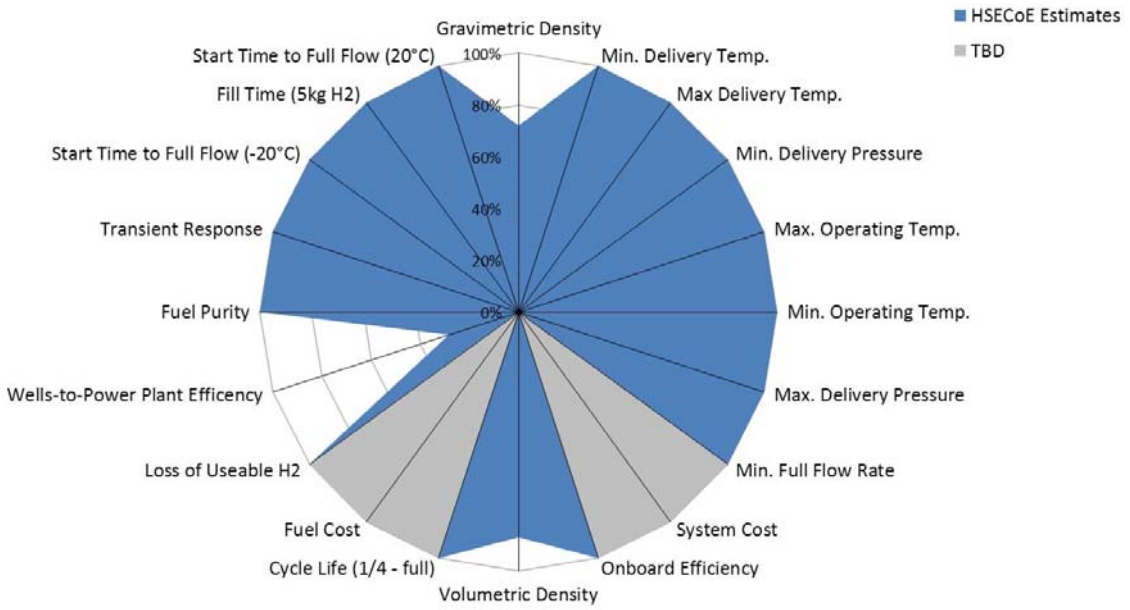

Figure 2.38. Spider Plot Comparing DOE Technical Targets to AB System Design

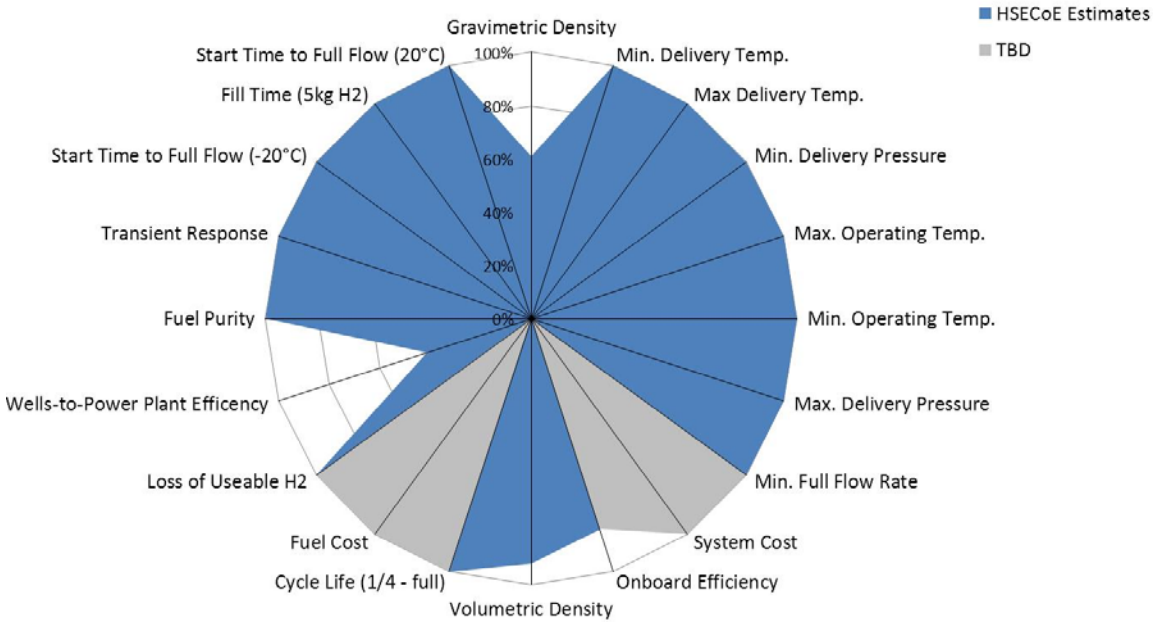

Figure 2.39. Spider Plot Comparing DOE Technical Targets to Alane System Design

Unlike most of the other targets that have been met by the design or are outside the scope of the system design, the system mass is a variable that system designers have worked to reduce. The system mass for AB was estimated to be 122 kg, and the volume was estimated to be 136 L. The distribution of the weight and volume for this system are shown in Figure 2.40. Assuming 5.6 kg of usable hydrogen is produced, the total system volume would be less than 140 L, thus meeting the 2017 DOE technical target for volume. In contrast, the mass is greater than the 102 kg maximum allowable to meet the technical target of 5.5 wt% hydrogen. This figure illustrates that the majority of the mass is in the slurry itself. Other large contributors are the tanks, hydrogen purification system components, valves, and piping.

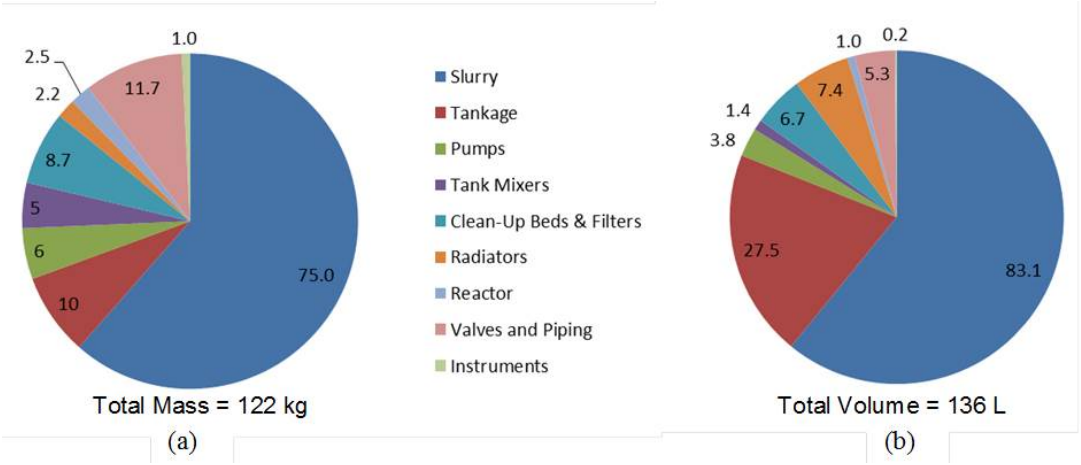

Figure 2.40. Distributions of System Components for an AB Hydrogen-Storage System: (a) Mass (kg) and (b) Volume (L)

As part of this study, efforts were made to determine how the overall mass could be reasonably reduced to meet DOE targets. One possible pathway to reduce the system mass and meet the DOE gravimetric target is shown on the waterfall plot in Figure 2.41. Although some reductions in system mass could be achieved by using smaller components than can be found commercially or by combining two or more components into a single, multi-functional unit, these reductions in system mass would be relatively minor. Similarly, a 25% reduction in the phase-separator, volume-displacement, and ballast tanks achieves only modest reductions in system mass. Increasing the solids loading or the hydrogen content of the slurry would result in the most significant improvement.

An increase in the slurry hydrogen can be achieved by either increasing the current AB material from a solids concentration in the slurry from 50 to 58 wt% or by increasing the hydrogen content of the storage material itself from 15.2 to 17.8 wt% with a 50 wt% loading. Both of these improvements would be a significant challenge because the AB slurry at 50 wt% is near the limit of its loading capacity.

Higher AB solids at higher loadings tend to remain on top of the slurry rather than in a homogeneous mixture. Ammonia borane is a material with one of the highest hydrogen contents so identifying materials with higher concentrations will be challenging.

In the case of alane, the system is 42 kg heavier than the AB system and 162 kg heavier than allowed by the DOE gravimetric target. Furthermore, the system volume is 11 L more than the DOE volumetric target. While no recycle pump or hydrogen purification components are required, the primary mass contributor results from the lower hydrogen loading of alane in a 50 wt% slurry compared to that of AB. Rather than being slightly over half of the total mass of the system, the alane slurry is almost three-quarters of the total system mass as shown in Figure 2.42.

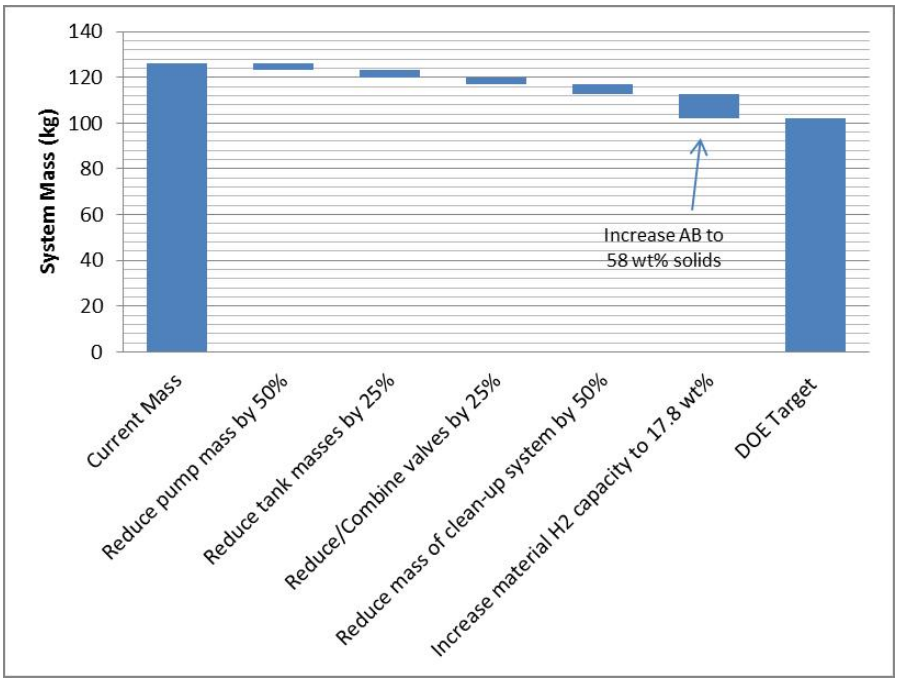

Figure 2.41. Waterfall Plot of an Approach to Reaching DOE Technical Targets with an AB-Based Storage System

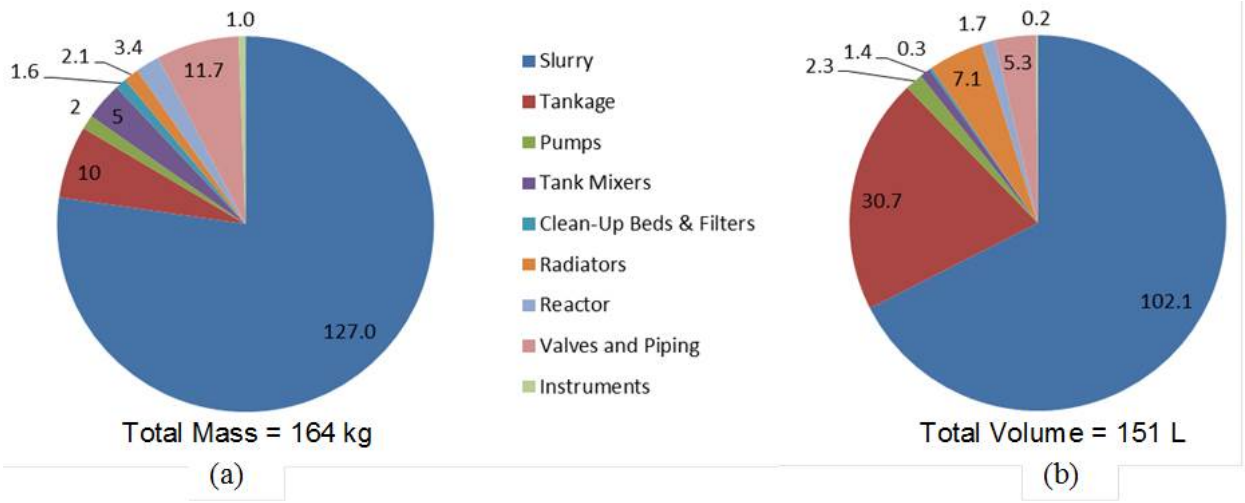

Figure 2.42. Distributions of the System Components for an Alane-Based Hydrogen-Storage System: (a) Mass (kg) and (b) Volume (L)

Using similar reduction factors for the size of the system BOP components, meeting DOE targets would require increasing the solids loading from 50 wt%, which is the current basis, to 88 wt% (Figure 2.43). Alternatively, the hydrogen content of the solids would have to be increased from its current value of 10-wt% to 17.6-wt% hydrogen with a 50-wt% solids loading of the slurry. As with AB, increasing either the solids loading of the alane or the hydrogen content of the CHS material would be challenging.

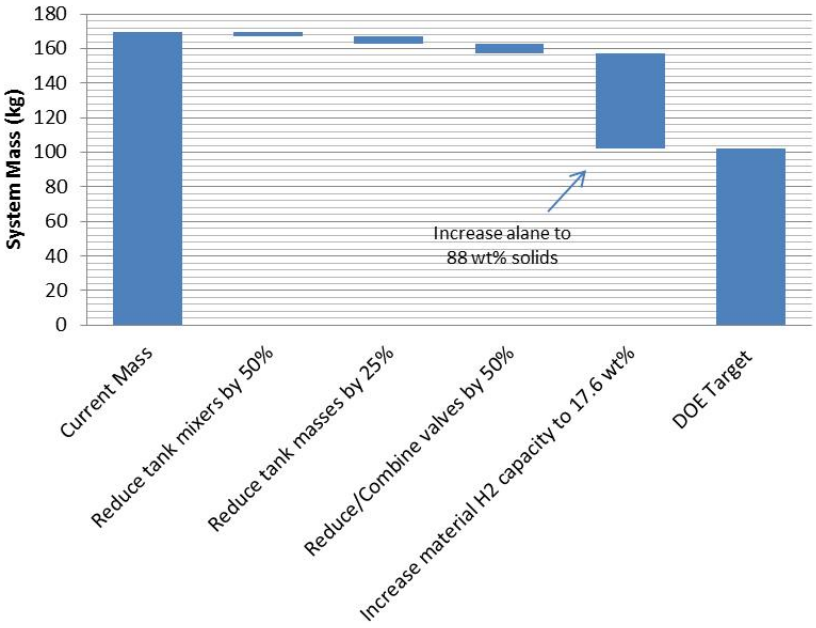

Figure 2.43. Waterfall Plot of an Approach to Reaching the DOE Targets with an Alane-Based Storage System

2.3.5 Slurry System Model Development

The mass and energy balances of the entire storage system described in the previous section were modeled in Simulink simulation software using a similar approach as described in Section 2.2.3. This software provides an understanding of the operational dynamics of the storage system under simulated drive-cycle scenarios. The components that are modeled are described below and in the literature (Brooks et. al. 2014b).

2.3.5.1 Reactor Model

The reactor for the AB slurry is a tubular reactor with an internal stirrer or auger to prevent agglomeration of the solids during reaction while allowing the gas to flow through the reactor center. The parameters used for the reactor model are provided in Table 2.13. For the purposes of modeling, it is assumed that the slurry is pushed to the walls of the reactor while the gas flows down the reactor center.

Table 2.13. Reactor Parameters Used in the Reactor Model

Reactor Parameters	Value	Units	AB Parameters	Value	Units
Reactor Outer Diameter (d_{out})	$4.44x10^{-2}$	m	AB Bulk density (ρ_{bulk})	780	kg/m^3
Reactor Inner Diameter (d_{in})	$4.11x10^{-2}$	m	Molecular weight AB (MW_{CH})	30.8	g/mol
Reactor Stirrer Diameter (d_{stir})	$4.76x10^{-3}$	m	Heat of Reaction 1st Eq. (ΔH_1)	15	kJ/mol H_2
CH fraction in slurry (x_{CH})	0.5	wt frac	Heat of Reaction 2nd Eq. (ΔH_2)	22	kJ/mol H_2
Startup Heater (Q_{heater})	8	kW/m	Heat capacity slurry (C_{pbulk})	2694	J/kg/K
Density Metal (ρ_{metal})	8000	kg/m^3	Alane Parameters	Value	Units
Heat capacity metal ($C_{p,metal}$)	480	J/kg/K	Slurry bulk density (ρ_{bulk})	1486	kg/m^3
Slurry Thermal Conductivity (k_{CH}')	2.0	W/m/K	Molecular weight AB (MW_{CH})	30	g/mol
Silicone Oil Density	1070	kg/m^3	Heat of Reaction (ΔH_1)	-7.6	kJ/mol H_2
Silicone Oil Heat Capacity	1846	J/kg/K	Heat capacity slurry (C_{pbulk})	1000	J/kg/K
Reactor Length (AB)	1	m	Reactor Length (Alane)	2	m

The fractional conversion of the CHS material to hydrogen in the slurry down the length of the reactor is given by α and is calculated as shown in Equation 2.22.

$$\frac{\partial \alpha_i}{\partial t} = -u_{slurry}\frac{\partial \alpha_i}{\partial z} + \left.\frac{\partial \alpha_i}{\partial t}\right|_{kinetics} \tag{2.22}$$

In the case of AB, Equation 2.22 consists of two equations (i = 2) for the two separate polymerization reactions that correspond approximately to the first equivalent and the second and a fraction of the third equivalent for a total hydrogen production of 2.35 equivalents. In the case of alane, Equation 2.22 is a single equation producing 1.5 equivalents. The velocity of the slurry (u_{slurry}) is calculated based on Equation 2.23.

$$u_{slurry} = \frac{\dot{m}_{slurry}}{\rho_{slurry} A_{slurry}} + C_{auger}\upsilon_{auger} \tag{2.23}$$

where C_{auger} is the axial displacement of the auger per rotation, υ_{auger} is the rotational speed, and A_{slurry} is the area of the gas/slurry interface in the reactor where the slurry channel is estimated to be 75% of the total area of the reactor ($A_{reactor}$) calculated as $A_{reactor} = \pi\left(d_{in}^2 - d_{slurry}^2\right)/4$. As hydrogen is generated, the slurry density, ρ_{slurry}, decreases to create a foamy mixture of solid, liquid, and gas with a density given in Equation 2.24.

$$\rho_{slurry} = \frac{\dot{m}_{slurry} + \dot{m}_{H2}}{\frac{\dot{m}_{H2}}{\rho_{H2}} + \frac{\dot{m}_{slurry} f_{inert}}{\rho_{inert}} + \frac{\dot{m}_{slurry} f_{CH}(1-\alpha_i)}{\rho_{CH}} + \frac{\dot{m}_{slurry} f_{CH}\alpha_i}{\rho_{CHP}}} \tag{2.24}$$

The parameters f_{inert} and f_{CH} are the fractions of inert and chemical hydride, ρ_{H2}, ρ_{inert}, ρ_{CH}, and ρ_{CHP} are the densities of hydrogen, slurrying agent, chemical hydride, and its product, respectively. A minimum value of the slurry density, $\rho_{slurry,min}$ is set, and as more hydrogen is generated, it then goes into the gas phase rather than the slurry. This foaming of the slurry mixture has been seen experimentally.

The rate of change of α due to kinetics is given by Equation 2.1, following KJMA approach where k_i is the rate constant of the dehydrogenation reactions calculated by the Arrhenius expression as shown in Equation 2.25.

$$k_i = A_i' e^{-E_{a,i}/RT} \tag{2.25}$$

The hydrogen generation rate is shown in Equation 2.26. In this expression, the hydrogen coefficients (β_i) correspond to the molar ratio of hydrogen generated in each dehydrogenation reaction (x_{CH}), ρ_{slurry} is the fraction of CHS material in the slurry, A_{slurry} is the cross-sectional area of slurry flow, Δz is the length of a differential reactor section, and MW_{CH} is the molecular weight of the CHS material.

$$r_{H2} = \frac{A_{slurry}\rho_{slurry}x_{CH}\Delta z}{MW_{CH}}\sum_i \beta_i \left.\frac{\partial \alpha_i}{\partial t}\right|_{kinetics} \tag{2.26}$$

The exothermic heat generated from the reactions is critical to the calculation of reactor temperature and is calculated based on the reaction kinetics as shown in Equation 2.27.

$$Q_{rxn} = \frac{A_z x_{CH} \rho_{bulk}}{MW_{CH}} \sum_i \beta_i \left. \frac{\partial \alpha_i}{\partial t} \right|_{kinetics} \Delta H_i \tag{2.27}$$

An energy balance across the reactor is used to calculate the reactor temperature ($T_{reactor}$), reactor wall temperature (T_{metal}), and hydrogen gas temperature (T_{gas}) as shown in Equations 2.28. The model assumes convection of mass and heat but no axial conduction of heat or diffusion of mass. The source term Q_{loss} is the heat losses calculated from the metal to the ambient through the reactor insulation. During reactor startup, heaters on the outer surface of the reactor walls conduct heat into the reactor (Q_{heater}).

$$\begin{aligned}
&A_{slurry}\rho_{bulk}C_{pbulk}\left(\frac{\partial T_{reactor}}{\partial t} + u_{slurry}\frac{\partial T_{reactor}}{\partial z}\right) + d_{out}\pi h_{metal}\left(T_{reactor} - T_{metal}\right) + d_{in}\pi h_{gas}\left(T_{reactor} - T_{H2}\right) = Q_{rxn} \\
&A_{metal}\rho_{metal}C_{p,metal}\left(\frac{\partial T_{metal}}{\partial t}\right) + d_{out}\pi h_{metal}\left(T_{metal} - T_{reactor}\right) = Q_{heater} - Q_{loss} \\
&A_{H2}\rho_{H2}C_{H2}\left(\frac{\partial T_{H2}}{\partial t} + u_{gas}\frac{\partial T_{H2}}{\partial z}\right) + d_{in}\pi h_{H2}\left(T_{H2} - T_{reactor}\right) = 0
\end{aligned} \tag{2.28}$$

The cross-sectional areas of the metal and gas are calculated based their corresponding diameters. The heat-transfer coefficients between the metal, the slurry, and the gas ($h_{metal/gas/slurry}$) are calculated based on the appropriate thermal conductivities, diameters, and the Nusselt numbers. The Nusselt number for the slurry at the gas and metal interface were fitted from graphs provided for fully developed laminar flow in concentric annular ducts for uniform temperatures at both surfaces from Rohsenow et al. (1998) as shown in Equations 2.29 and 2.30. The Nusselt number for the gas phase was equal to 4.36 when laminar and Equation 2.31 when turbulent (Incropera and DeWitt 1985).

$$Nu_i = 3.75 r^{*-0.436} \tag{2.29}$$

$$Nu_o = 3 + r^* \tag{2.30}$$

$$Nu_{H2} = 0.023 \mathrm{Re}_{H2}^{0.8} \mathrm{Pr}_{H2}^{0.4} \tag{2.31}$$

The value of r* is the ratio of the inner and outer diameter of the slurry. Re_{H2} and Pr_{H2} are the Reynolds and Prandtl numbers for the hydrogen gas based on a gas velocity calculated from its mass flow and the area between the gas/slurry interface and the stirrer based on Equation 2.32.

$$u_{gas} = \frac{4\dot{m}_{gas}}{\rho_{gas}\pi\left(d_{slurry}^2 - d_{stir}^2\right)} \tag{2.32}$$

A variable step solver named "ode23tb," which is available in Simulink, is used for all the simulations conducted in this work. To avoid algebraic errors in the model resulting from reactor outputs feeding back to the controller, unit delays are used. Simulink solves the temporal components of the equations. The spatial components are solved by a series of 10 differential reactor length elements coupled together.

2.3.5.2 Reactor Parameter Development

The Arrhenius values used were based on those previously developed by Graetz and Reilly (2005) for α-AlH3 polymorphs. The Arrhenius values for AB were fit based on batch reactor data. Batch reactor data of 35 wt% AB slurries in AR 20 silicone were performed at the University of Oregon.[6] The hydrogen

[6] Personal communication with Dr. S-Y Liu, University of Oregon.

production as a function of time over the range of 120°C to 150°C is shown in Figure 2.44. These data were fit to obtain the rate constants as described in Equation 2.4 and hydrogen coefficients (β_i) described in Equation 2.5 that would be used in the Simulink reactor model. The best fit with this experimental data was achieved when β was found to vary as a function of temperature in the form shown in Equation 2.33.

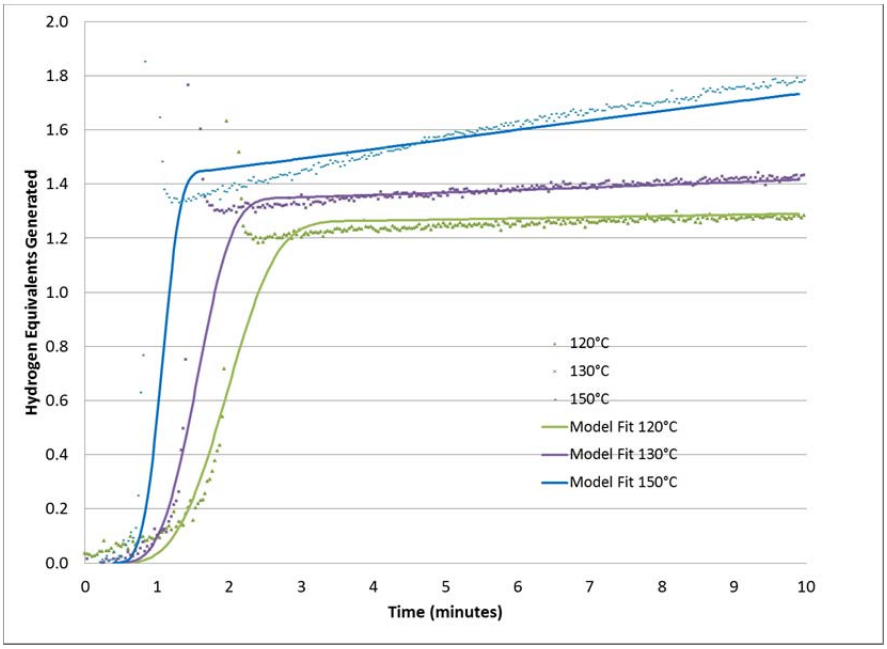

Figure 2.44. Batch Kinetic Results for a 35wt% AB Slurry with Model Fits

$$\beta_i = \beta_i' e^{-k''_i T^{n_i}} \tag{2.33}$$

where k'' and n' are constants to best fit the temperature dependence of the hydrogen coefficient.
The rate constant and hydrogen coefficient parameters for the AB and alane slurry model are shown in Table 2.14. In the case of alane, the β value was assumed to be a constant with temperature. As a result, no exponential fitting was required.

Table 2.14. Reaction Parameters Developed from Experimental Data

		AB		
Parameter	Units	First Equivalent	Second/Third Equivalent	Alane
Arrhenius Factor (Ai)	s^{-1}	$9.6x10^{3}$	$8.8x10^{7}$	$1.2x10^{10}$
Activation Energy (Ei)	kJ/mol	45.0	89.1	102.2
H_2 Coefficient Constant (β_i')	mol H_2/mol AB	1.45	0.905	1.5
Beta Constant (k_i")	$(1/°C)^{ni'}$	$1.29x10^{-6}$	$1.62x10^{-7}$	0
Beta Temperature Exponent (n'$_i$)	unitless	2.98	3.84	1
H_2 Coefficient Exponent (n_i)	unitless	3.1	1.2	2

2.3.5.3 Gas and Slurry Radiators

The radiator models used for both gas and slurry product cooling are based transient heat losses from the process to the radiator and from the radiator to ambient. The radiator is assumed to have finned tubes with ambient air blowing across them. The temperature distribution in the fin is assumed to be constant, while the base metal temperature varies. The model assumes transient thermal mass of the radiator with convection between the process stream (T_{slurry}) and the radiator metal (T_{metal}). Axial conduction is considered negligible. The equations used to model the process and metal temperatures are shown below in Equation 2.34.

$$A_{\text{interior}}\rho_{bulk}C_p\left(\frac{\partial T_{slurry}}{\partial t}+u_{slurr}\frac{\partial T_{slurry}}{\partial z}\right)+h_{\text{interior}}D_{\text{interior}}\pi\left(T_{metal}-T_{slurry}\right)=0$$
$$A_{exterior}\rho_{metal}C_{p,metal}\left(\frac{\partial T_{metal}}{\partial t}\right)+h_{\text{interior}}D_{\text{interior}}\pi\left(T_{metal}-T_{slurry}\right)+h_{exterior}D_{exterior}\pi\delta_{fin}\eta_{fin}\left(T_{metal}-T_{ambient}\right)=0 \quad (2.34)$$

The increased surface area associated with the fin δ_{fin} can be calculated using Equation 2.35:

$$\delta_{fin} = [(D_{fin}^2 - D_{exterior}^2)+ 2D_{exterio}\, p_{fin}] /(2D_{exterior}\, p_{fin}) \quad (2.35)$$

where D_{fin} is the OD of the fin, $D_{exterior}$ is the OD of the heat exchanger tube, $D_{interior}$ is the inner diameter of the heat exchanger tube, and p_{fin} is the fin pitch. The fin efficiency (η_{fin}) was calculated for a circular fin as described by Rohsenow et al. (1998). The heat-transfer coefficient for a cylinder in cross-flow is calculated based on the method reported by Incropera and DeWitt (1985) as shown in Equation 2.36:

$$h_{exterior}=\frac{k'_{air}}{D_{exterior}}\left(0.3+\frac{0.62\,\text{Re}_d^{1/2}\,\text{Pr}_{air}^{1/3}}{\left[1+\left(0.4/\text{Pr}_{air}\right)^{2/3}\right]^{1/4}}\left[1+\left(\frac{\text{Re}_d}{28200}\right)^{5/8}\right]^{4/5}\right) \quad (2.36)$$

where $\text{Re}_d=\frac{\rho_{air}v_{air}d_{hxOD}}{\mu_{air}}$ and Pr_{air}, k_{air}, v_{air}, μ_{air}, and ρ_{air} are the Prandtl number, thermal conductivity, velocity, viscosity, and density of air at the film temperature, respectively. The value of $h_{interior}$ is calculated based on the Nusselt number is for the interior of a tube with a swirl flow device for laminar flow in a uniformly heated tube as described by Rohsenow et al. (1998) and shown in Equation 2.37:

$$Nu_{interior} = 5.172(1+0.005484*Pr^{0.7}(Re_d/y)^{1.25})^{1/2} \quad (2.37)$$

where y is the twist ratio of the turbulator inside of the heat exchanger tubes. The parameters used in the radiator models are shown in Table 2.15. The fin is constructed from aluminum, and the tube from stainless steel.

Table 2.15. Parameters Used in the Heat Exchanger Models

Slurry Parameter	Value	Units	Gas Parameter	Value	Units
Fin Diameter (d_{fin})	0.025	m	Fin Diameter (d_{fin})	0.016	m
Heat Exchanger Tube Diameter (d_{hxOD})	0.0095	m	Heat Exchanger Tube Diameter (d_{hxOD})	0.00635	m
Fin Thickness	0.00046	m	Fin Thickness	0.00046	m
Fin Pitch (p_{fin})	0.00254	m	Fin Pitch (p_{fin})	0.00254	m
Twist Ratio (y = diameters/180° twist)	9.84		Twist Ratio (y = diameters/180° twist)	9.84	
Slurry HX Length AB	2	m	Gas HX Length AB	1.25	m
Slurry HX Length alane	1.5	m	Gas HX Length alane	1.25	m

As with the reactor model, Simulink solves the temporal components of the equations while the spatial components are solved using a series of 10 differential elements.

2.3.5.4 System Controller

The amount of material that needs to be recycled, in addition to the material that needs to be pumped to the reactor, is governed by a control system. The overarching goal of the controller is to control the flow rate of fresh slurry into the reactor based on requested hydrogen from the fuel cell and ballast tank pressure. Control of the reactor inlet and outlet temperatures is achieved by adjusting the fraction of spent product that is recycled.

The feed flow rate is based on the hydrogen requested and the hydrogen capacity of the storage material based on complete conversion as shown in Equation 2.38:

$$\dot{m}_{feed} = \frac{\dot{n}_{H2,required} MW_{CH}}{(\beta_1 + \beta_2) x_{CH}} + \dot{m}_{PI}\left(P_{ballast} - P_{setpoint}\right) \tag{2.38}$$

Where $\dot{n}_{H2,required}$ is the molar flow of hydrogen requested from the fuel cell. To maintain the system pressure, the total hydrogen required is adjusted up or down by a proportional-integral controller. The ballast tank set point is 25 bar.

The flow of hot slurry product as recycle with the feed was adjusted to ensure that the target temperature (T_{target}) was met and the reaction could be initiated without requiring external heating. The flow rate of this recycle stream was calculated using Equation 2.39.

$$\dot{m}_{recycle} = \frac{\dot{m}_{feed} Cp_{feed}\left(T_{target} - T_{ambient}\right)}{Cp_{prodcut}\left(T_{product} - T_{target}\right)} \tag{2.39}$$

With large exothermic heat release of AB, the temperature of the product exiting the reactor in some cases was unacceptably high. To address this problem, a fraction of the cold product from the radiator is mixed with a fraction of hot product exiting the phase separator to produce an overall larger recycle stream at the same target temperature as before. The amount of recycle flow from the radiator and phase separator is calculated using Equations 2.40 and 2.41, respectively.

$$\dot{m}_{productrecycled} = \frac{\dot{m}_{feed} Cp_{feed}\left(T_{target} - T_{ambient}\right) + \dot{m}_{recycle} Cp_{product}\left(T_{target} - T_{radiator}\right)}{Cp_{prodcut}\left(T_{product} - T_{radiator}\right)} \tag{2.40}$$

$$\dot{m}_{radiator} = \dot{m}_{recycle} - \dot{m}_{productrecycled} \tag{2.41}$$

In this way, both constraints for a sufficient preheat and adequate dilution for maximum temperature maintenance could be met. The feed temperature target temperature is 120°C and the product maximum temperature is 250°C.

The endothermic reaction requires that heat be added to the reactor continuously. As a result, a slightly different controller for heat flux to the reactor exterior surface was implemented. Rather than just being a constant used only during startup, as is the case for the AB reactor, the heater for the alane system controller is based on the hydrogen requested and the heat of reaction of the storage material and the heat required to achieve the target temperature. Equation 2.42 is used to model this.

$$Q_{heater} = \frac{\dot{n}_{H2,required}\left(\beta_1 \Delta H_{rxn,1} + \beta_2 \Delta H_{rxn,1}\right)}{\left(\beta_1 + \beta_2\right)} + \dot{m}_{feed} C_{p,feed}\left(T_{target} - T_{feed}\right) + Q_{PI}\left(T_{reactor} - T_{target}\right) \tag{2.42}$$

To maintain the reactor temperature near the target value, the heat is adjusted up or down by a proportional-integral controller based on the difference between the reactor and target temperature.

2.3.5.5 Recuperator for Alane Slurry

In the case of alane, a recuperator is used to provide heat to the reactor. The recuperator is assumed to be a counter-flow, tube-in-tube heat exchanger. It is modeled by a series of four differential equations representing the slurry feed (T_{feed}) and product temperatures ($T_{product}$), inner temperatures (T_{inner}), and outer

(T_{outer}) wall temperatures. Heat convection is accounted for as if flows from the hot product to the inner wall to the cooler product using Equation 2.43.

$$
\begin{aligned}
&A_{inner}\rho_{feed}C_p\left(\frac{\partial T_{feed}}{\partial t}+u_{feed}\frac{\partial T_{feed}}{\partial z}\right)+h_{inner}D_{inner}\pi\left(T_{feed}-T_{inner}\right)=0\\
&A_{innerwall}\rho_{metal}C_{p,metal}\left(\frac{\partial T_{inner}}{\partial t}\right)+h_{inner}D_{inner}\pi\left(T_{inner}-T_{feed}\right)+h_{innerwall}D_{innerwall}\pi\left(T_{inner}-T_{product}\right)=0\\
&A_{tubeannulus}\rho_{product}C_p\left(\frac{\partial T_{product}}{\partial t}+u_{product}\frac{\partial T_{product}}{\partial z}\right)+h_{innerwall}D_{innerwall}\pi\left(T_{product}-T_{inner}\right)+h_{outer}D_{outer}\pi\left(T_{product}-T_{outer}\right)=0\\
&A_{outer}\rho_{metal}C_{p,metal}\left(\frac{\partial T_{outer}}{\partial t}\right)+h_{outer}D_{outerwall}\pi\left(T_{outer}-T_{product}\right)=0
\end{aligned}
\tag{2.43}
$$

In these equations, the cross-sectional areas (A) and diameters (D) represent the inner tube (tubecenter) and tube annulus (tubeannulus) and the inner and outer of the metal tubes. The heat-transfer coefficient for the feed is based on the laminar, fully developed flow Nusselt number of 4.36 for constant heat flux. The heat-transfer coefficients for the annulus are provided in Equations 2.39 through 2.41. As with the reactor and the radiators, Simulink solves the temporal components of the equations while the spatial components are solved by creating a series of 10 differential elements. The parameters used for the alane recuperator are shown in Table 2.16.

Table 2.16. Parameters Used in the Recuperator Model

Slurry Parameter	Value	Units
Inner Tube Diameter ($D_{innerwall}$)	0.0127	m
Outer Tube Diameter ($D_{outerwall}$)	0.0196	m
Wall Thickness	0.00056	m

2.3.5.6 Ballast Tank

The pressure of the ballast tank varies based on the tank temperature and the number of moles in the tank assuming ideal gas law. Its temperature is calculated based on the temperature of the hot gases entering the ballast tank from the radiator using Equation 2.44.

$$
n_{H2total}C_{p,H2}\left(\frac{\partial T_{BT}}{\partial t}\right)+\dot{n}_{H2in}C_{p,H2}\left(T_{radiator}-T_{BT}\right)=0 \tag{2.44}
$$

The number of moles in the tank is based on the number of moles entering the tank from the reactor and the number of moles leaving to meet the drive cycle as shown in Equation 2.45.

$$
\frac{\partial n_{H2total}}{\partial t}=\dot{n}_{H2in}-\dot{n}_{H2FC} \tag{2.45}
$$

To maintain hydrogen pressure above 5 bar during startup, the ballast tank volume must be 30 L.

2.3.5.7 Parasitic Power

The parasitic power includes power required to operate system pumps, heaters, blowers, and mixers. These system components require electricity either continuously or periodically based on the system operations (see Table 2.17). This parasitic power is calculated and summed throughout the model run and is used to determine storage-system onboard efficiency.

Table 2.17. Parasitic Power Requirements

Component	Value/Equation (Watts)	Operation
Volume-Displacement Tank Mixers	20	Startup Only
Pumps	5.04×10^5 ΔP (bar)* $\dot{m}_{slurry}/\rho_{slurry}$	Variable
Radiator Blower	91	Constant

The model also predicts the storage-system mass and volume based on user inputted dimensions such as mass of the chemical hydride (CH), radiator length, ballast tank volume, and the reactor design. These values were estimated based on simple system designs and the weight and volume of commercial components. They are provided in Table 2.18. The total system mass and volume can then be used during trade-off studies to study impacts of the system parameters.

Table 2.18. Parameters used to Calculate Overall System Mass and Volume

Component	Mass Coefficient (kg)	Volume Coefficient (L)	Determining Dimension
CH Material	M	0	M=mass of CH, kg
Volume Exchange Tank	51.9*M/ρ+1.75	M/ρ*1000	M=mass of CH, kg ρ= slurry density, kg/m^3
Reactor	Based on stainless steel and dimensions		
Gas Radiator	0.32*L	0.2*L	L=radiator length, m
Slurry Radiator	0.54*L	0.87*L	L=radiator length, m
Ballast Tank	0.17*V	V	V=tank volume, Liters
Ammonia Scrubber	0.0032*C	0.0068*C	C=concentration, ppm
Borazine Scrubber	0.0017*C	0.0015*C	C=concentration, ppm
Recuperator	Based on stainless steel and dimensions		
Balance of Plant	32.1	26.8	

2.3.5.8 Model Validation Experiments

Once the model was developed, the reactor piece of the model developed as described above was then compared to the preliminary experimental results obtained by LANL using a prototypical flow-through reactor scaled down from the design anticipated for automotive application. The reactor design consisted of a 1 cm inner diameter tube with a 19.1-cm-long heated section. A McMaster Carr deep-hole drip bit rotated at 40 rpm inside of the tube as a means of mixing and moving the slurry through the reactor as shown in Figure 2.45. The reactor temperature was controlled on the outer surface over a range between 150°C to 235°C. Alane and AB slurries between 20 and 60 wt% in AR 20 silicone oil flowed through the reactor. The auger speed was adjusted between 12 and 40 rpm and the residence time between 2.4 and 7.6 minutes. For each condition, the reactor was allowed to equilibrate and the hydrogen-generation rate was measured using a calibrated flow meter. The hydrogen flow rate was then compared to the flows predicted by the model.

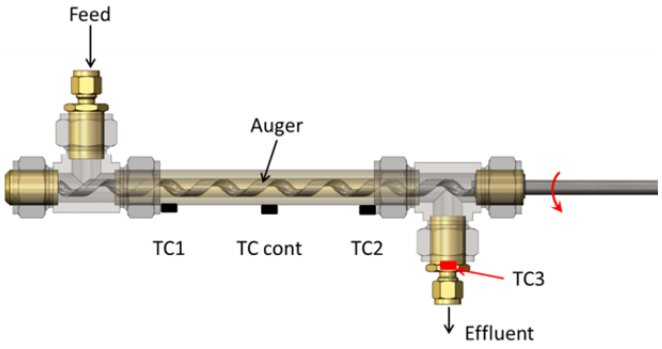

Figure 2.45. Flow-Through Reactor Design used to Validate the Model

The automotive dimensions and flows used in the model were scaled down to those used in the LANL experiment. The temperature within the small-scale reactor was assumed to be constant at the controlled value rather than including reaction enthalpies and heat losses as assumed in automotive case. The tanks, heat exchangers, and other BOP components used in the automotive storage-system model were removed to predict the reactor behavior. Only the minimum slurry density ($\rho_{slurry,min}$) was adjusted to fit the experimental data. The value of 34 kg/m^3 for alane was fit to the data using a least squares regression analysis. Using this minimum density value, the coefficient of determination was calculated to be 90% for 12 data points fit in Table 2.19.

Table 2.19. Comparison of Measured and Model Predicted Alane Conversion

Solids Loading (wt%)	Reactor Residence Time (min)	Auger Speed (rpm)	Average Reaction Temperature (ºC)	Measured Alane Conversion (mol/mol)	Model Conversion Values (mol/mol)
50%	7.6	12	185	16%	11%
50%	7.6	40	185	11%	4.6%
50%	4.2	12	187	7%	6.6%
50%	7.6	12	214	88%	80%
50%	7.6	40	214	74%	53%
50%	4.2	12	214	38%	49%
20%	6.8	40	188	10%	7.1%
20%	6.8	40	212	38%	50%
20%	6.8	40	235	84%	100%
60%	7.2	12	180	5%	6.5%
60%	7.2	12	194	20%	21%
60%	7.2	12	208	48%	55%

These data include a range of solids loadings, residence times, auger speeds, and reaction temperatures. There is reasonably good fit between the model and the experimental results over the range of conditions. Using the parameters obtained from the data set modeled in Table 2.19, a separate set of alane data was fit with the model. These data were obtained for 20-wt% slurry, residence time of 6.8 minutes, and an auger speed of 40 rpm over a temperature range of 150°C to 275°C. The results of this data fit are shown in Figure 2.46. While the fit is reasonably good, the model does tend to slightly under-predict hydrogen-generation rates at the low temperatures and over-predict them at the higher temperatures.

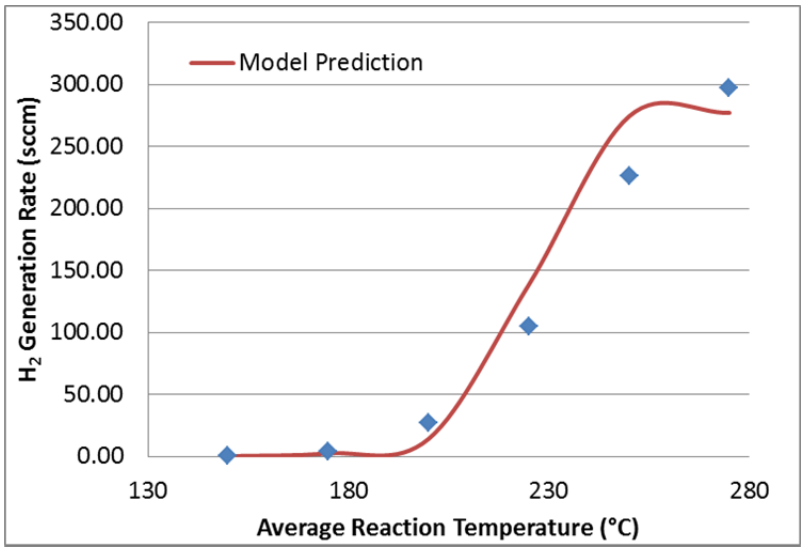

Figure 2.46. Comparison of Model Predicted Hydrogen Flow Rate to that Measured Experimentally for 20 wt% Alane Slurry

This same model was also used to fit the experimental data developed for AB. Only three data points were measured experimentally because of difficulties in pumping the AB slurry. In this case, the density of the slurry product of 370 kg/m^3 was measured and used in the model as the minimum slurry density ($\rho_{slurry,min}$). The model predicted the experiment accurately at 150°C, the maximum temperature of the batch data, but did not extrapolate well to higher temperature values (Figure 2.47). As a result, the kinetic parameters were adjusted to fit these three experimental data points. These updated kinetic parameters are shown in Table 2.20 and are used for all subsequent analysis.

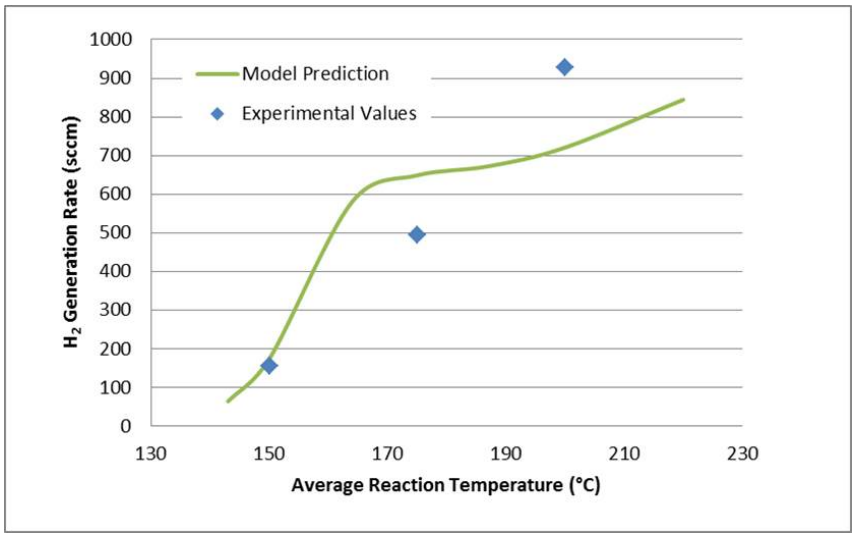

Figure 2.47. Comparison of Model Predicted Hydrogen Flow Rate to that Measured Experimentally for 20 wt% AB Slurry

Table 2.20. Updated Kinetic Parameters Based on Measured AB Values

		AB	
Parameter	Units	1st Equivalent	2nd/3rd Equivalent
Arrhenius Factor (Ai)	s^{-1}	2.81 x 10^2	4.18 x 10^{15}
Activation Energy (Ei)	kJ/mol	29.9	149

Validation of the radiator models was performed using eight finned heat exchangers in series assembled into a rectangular configuration as shown in Figure 2.36b. These finned tubes produced by Energy Transfer MDE were made from 0.95 cm diameter stainless-steel tubes with a total length of 2.43 m.

Because of the cost of both the raw materials and the preparation of CH slurries, a simulant was developed to be used in the radiator test instead of using reacted CH materials. A 40-wt% polyimide (P84-N, 10 to 59 microns) slurry in AR 20 silicone oil was selected. It proved to be a good physical simulant and modeled reasonably well spent slurry from a 40-wt% AB. The simulant slurry concentration was selected because it matched the viscosity of the product—both being approximately 200 cP with a shear stress of 1 pascal. The simulant slurry had a higher wt% and vol% solids than the AB slurry, but it bound both of these values, and the two-phase system was selected to tolerate the elevated temperatures and pressures required for the validation testing.

The polyimide slurry was electrically heated in a stirred feed vessel to between 150°C and 230°C. The model results then were compared to the experimental results as shown in Figure 2.48. The good fit between the model and experimental results adequately validated the model. Additional detail on the experiments performed with the radiator is provided in Section 2.3.8.1.

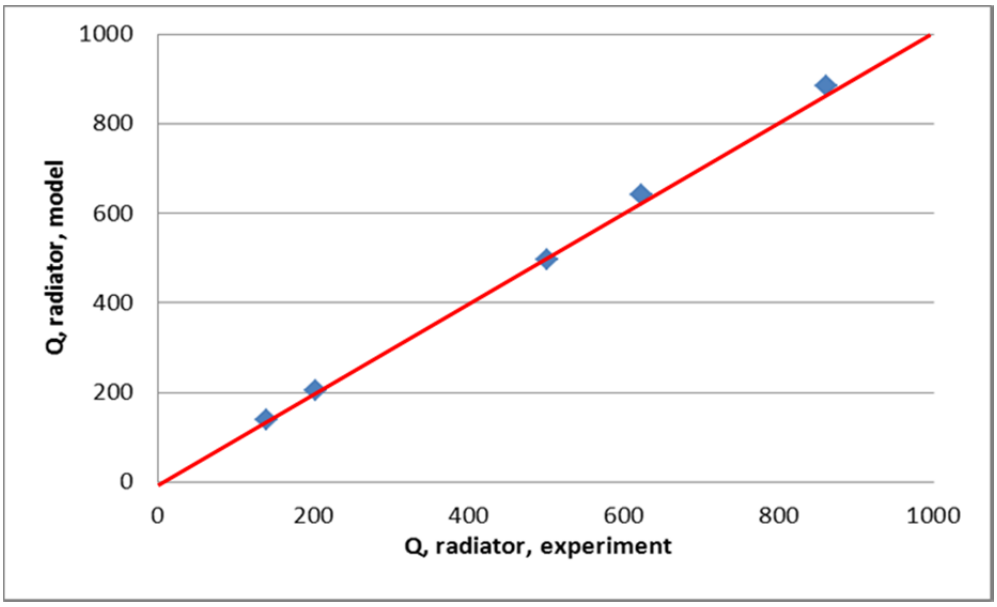

Figure 2.48. Comparison of Experimental and Modeling Results for the Heat Exchanger

In addition to the reactor and radiator, other components were validated as part of this project. These components include the volume-displacement tank, the phase separator, and the impurities cleanup system. These components require validation as part of the system development, but are not critical to the modeling effort. As a result, their validation will not be described here.

2.3.5.9 Simulation Results

The ode23tb variable step solver in Simulink was used to solve the model for all studies performed in this work. To avoid algebraic errors in the model resulting from reactor outputs feeding back to the controller, unit delays are used. To demonstrate the usefulness of the simulation for real vehicle driving scenarios, transient simulations using various drive cycles were run. The test matrix was provided by our HSECoE partners to test various storage-system models developed by team partners and includes 1) a highway cycle [UDDS + HWFET], 2) an aggressive driving cycle [US06], 3) a cold-start cycle [Cold FTP], and 4) a hot cycle [SC03-Hot]. Hydrogen demand data from the fuel cell were provided by the National Renewable Energy Laboratory, a HSECoE partner.[7] All the drive-cycle simulations were successfully implemented into the model but only important simulation results are shown in this paper for conciseness. All the drive cycles are repeated until the DOE required 5.6 kg of usable hydrogen were produced.

The US06 drive cycle, the most aggressive drive cycle considered in this study, was used as the hydrogen requirement input to the model. As is consistent with all drive cycles, the pressure in the ballast tank shows an initial decrease with no hydrogen being generated while the reactor is being heated to temperature as shown in Figure 2.49. This first ~2 to 3 minutes of the US06 drive cycle determines the size of the ballast tank. It must be large enough to maintain the hydrogen pressure above 5 atm during startup. Once the reaction is initiated, the hydrogen pressure in the ballast tank varies only slightly around the 25 atm set point until the slurry is consumed and ballast tank pressure is lost.

[7] Personal communication with K. Day, 2010, National Renewable Energy Laboratory.

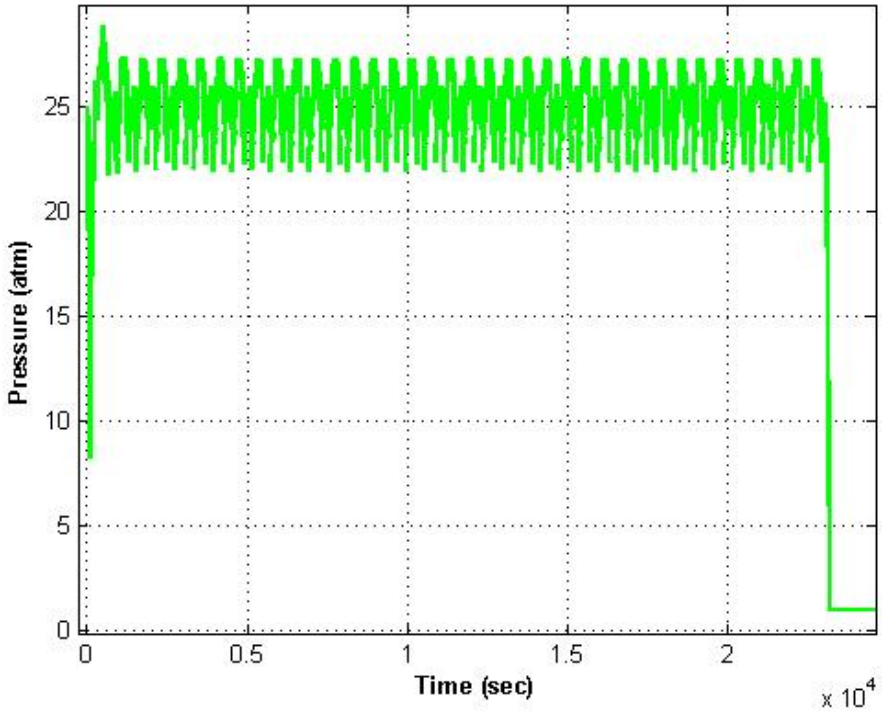

Figure 2.49. Ballast Tank Pressure as a Function of Time for 50 wt% AB with the US06 Drive Cycle

Although the US06 drive cycle reaches hydrogen usage of up to 0.8 moles hydrogen/second (80 kWe), the storage-system ballast tank provides a buffer. As a result, for 50 wt% AB, the storage system is required to produce a maximum of only 0.43 moles hydrogen/second (30 kWe) as shown in Figure 2.50.

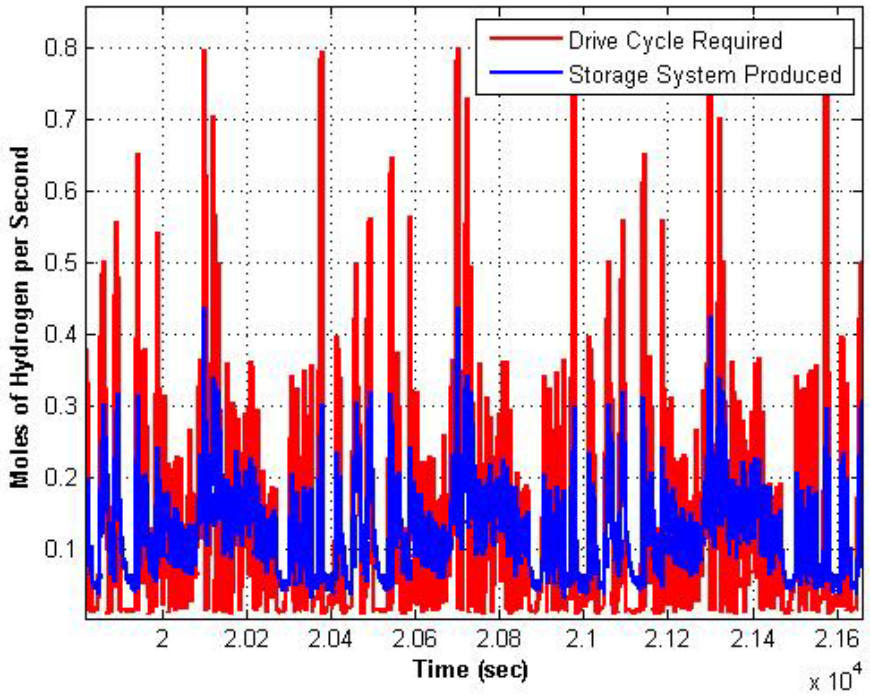

Figure 2.50. Comparison of Hydrogen Required by the Drive Cycle and Hydrogen Produced by the Storage System for 50 wt% AB with a US06 Drive Cycle

This significantly reduces its size and capacity requirements. During startup, an electric heater brings the reactor to temperature prior to initiating the reaction. During the entire operation, electric pumps and mixers are used to maintain the flow and ensure homogeneity of the slurry mixture. All of these electrical components contribute to parasitic hydrogen losses that detract from primary automotive propulsion. The DOE has given the requirement for 90% onboard efficiency. Based on the amount of electrical power required and using 0.02 g hydrogen/s/kWe conversion of hydrogen to electrical power, the onboard efficiency was calculated using Equation 2.46:

$$Efficiency = \frac{m_{H2,total} - m_{H2,parasitics}}{m_{H2,total}} \tag{2.46}$$

where $m_{H2,total}$ is the mass of hydrogen generated by the system and $m_{H2,parasitics}$ is the amount of hydrogen that must be converted to electrical power to account for parasitic losses. For the US06 drive cycle as well all other drive cycles studied with 50 wt% AB, the onboard efficiency is predicted to be >95%. In contrast, the onboard efficiencies for 50% alane is predicted to be 87 to 93%. The alane reaction is endothermic and, as a result, requires reactor heating throughout operations. In contrast, AB produces enough heat that no reactor heating is required. Reactor heating is the major parasitic loss in the system.

The high hydrogen requirement of the US06 also results in the most stringent case for the storage-system radiators. As shown in Figure 2.34, there is one radiator to cool the separated hydrogen and one for the spent slurry. The DOE targets require that the hydrogen going to the fuel cell be maintained at a temperature less than 85°C. There is not a specific target for the cooling required for the slurry, but at sustained temperatures >60°C, the fresh CH that is in contact with the spent CH through only a membrane in the volume-displacement tank will begin to generate hydrogen. As a result, the slurry radiator has been sized to maintain the spent slurry temperature <60°C. The temperatures of the hydrogen and slurry for both AB and alane are shown in Figure 2.51. As can be seen from these results, the highest gas temperature occurs shortly after the storage system begins producing hydrogen. In the case of the slurry product temperature, the highest temperature occurs at the beginning of the run for the 50 wt% AB system and at the end of the run for the 50 wt% alane system.

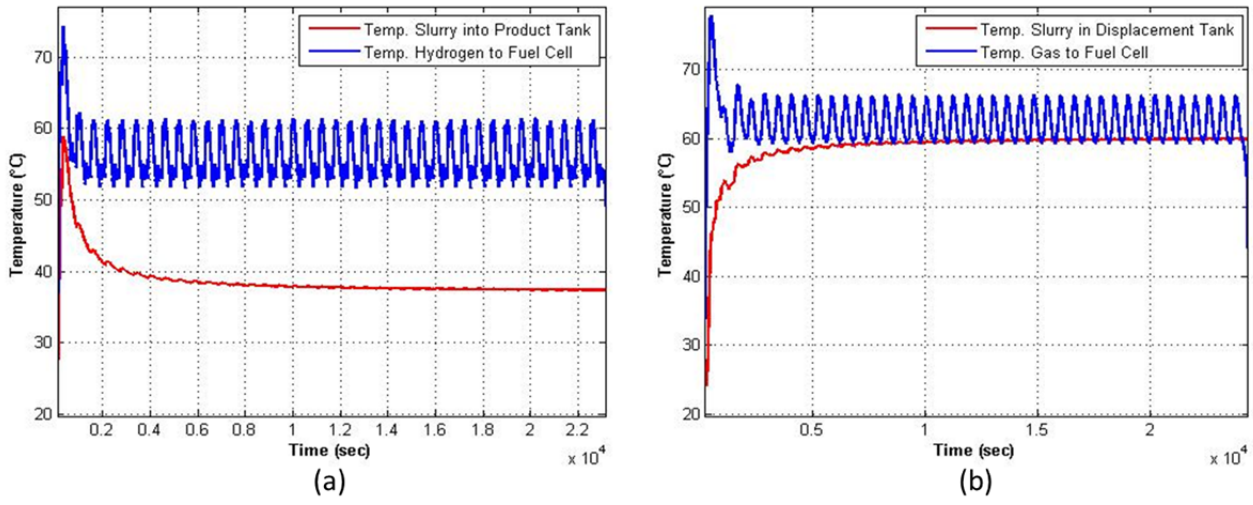

Figure 2.51. Temperature of Gas and Slurry Radiator Products: (a) 50 wt% AB and (b) 50wt% Alane with the US06 Drive Cycle

The model demonstrated that the storage system as designed could meet the drive-cycle requirements for both alane and AB for the other three drive cycles as well. Similar results were obtained for the other drive cycles but are not provided here.

2.3.5.10 Sensitivity Analysis

The DOE does not assume that AB or alane slurries will be the materials ultimately used in the vehicle. Rather, it is assumed that additional CHS material discovery and development will be performed. As a result, one of the purposes of the model is to help guide potential material developers as to the range of material properties that could successfully be implemented into a chemical storage system similar to what was developed here. To this end, the model also was used to perform a sensitivity analysis with a goal of better understanding the impact of the properties of materials that would be able to meet DOE targets. The models were run for 3000 seconds using five US06 drive cycles back-to-back. Key material properties were varied individually around the values used in the model described above until one of the DOE targets was not met or the model could not successfully run.

Key parameters of a hydrogen storage material are heat of reaction, hydrogen capacity, and reaction rate. These parameters were explored for both alane and AB as surrogates for possible future hydrogen storage materials. The heat of reaction was varied for these two materials and the results evaluated. For either exothermic or endothermic materials, as the heat of reaction moves further from zero, the reactor temperature increases. This temperature increase results in higher temperatures in the ballast tank and product tank. At some point, the temperature may become excessive. Additionally, as the reaction heat becomes increasingly exothermic, onboard efficiency and conversion decrease as well. Based on the results of the model, onboard efficiency drops below the DOE technical target value of 90% at approximately 11 kJ/mol hydrogen as shown in Figure 2.52.

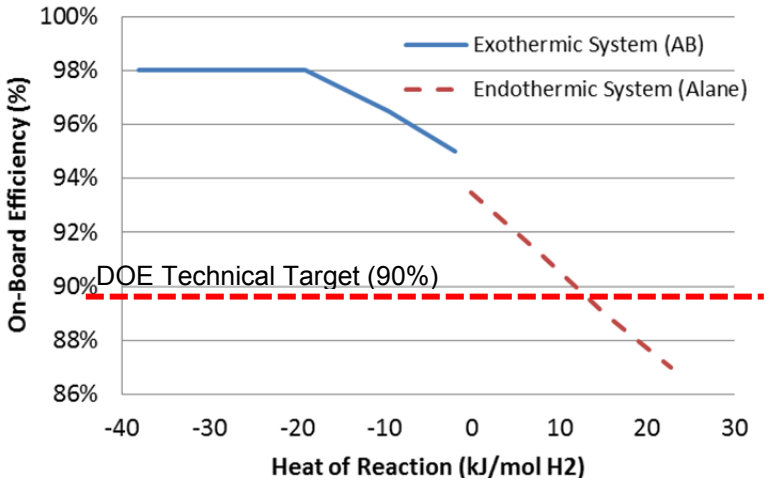

Figure 2.52. Sensitivity Analysis Comparing Heat of Reaction to the Predicted Onboard Efficiency for an Endothermic and an Exothermic System

The hydrogen capacity of the material impacts the onboard efficiency and gravimetric and volumetric capacity. Lower hydrogen capacity decreases the onboard efficiency, similar to the heat of reaction. Values of ~3.75 wt% hydrogen for endothermic slurry and 2.7 wt% hydrogen for exothermic slurry yield an onboard efficiency of less than 90%. More significantly, the gravimetric density is decreased with low hydrogen capacity. For both AB and alane, the DOE gravimetric factor target of 0.055 can be met at hydrogen capacities of >11.4% (see Figure 2.53). The system mass was similar for both systems in spite of differences in their component makeups. For 50 wt% slurry, this would require 125% and 50% increases in hydrogen capacity for alane and AB, respectively, relative to their current values. Previous sensitivity analyses indicate the volumetric capacity would be met when the gravimetric capacity is achieved.

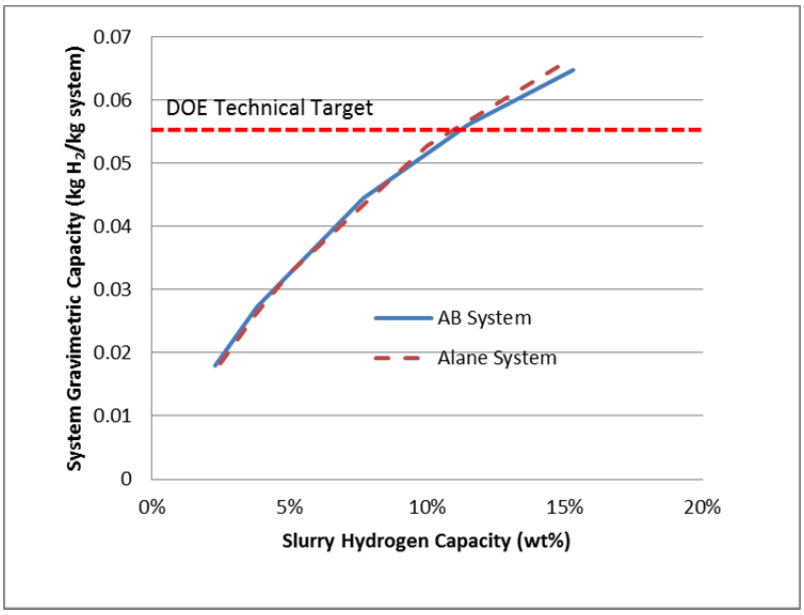

Figure 2.53. Sensitivity Analysis Comparing the Slurry Storage Capacity to the Predicted System Gravimetric Capacity for an Endothermic and an Exothermic System

An increase in reaction kinetics above their current values has little effect on the drive-cycle performance or the system parameters. Similarly, decreasing the reaction kinetics has little impact as well up to the point that conversion becomes so poor that the drive cycle cannot be met. This point occurs at approximately 50% of the reaction rate of AB and 2% of the reaction rate of alane.

2.3.6 Slurry System Cost

A Phase-II cost model was used to develop an estimate of the system costs and the cost per kilogram of usable hydrogen stored to be compared with DOE targets for system cost and cost per kilowatt-hour. The model develops only the first cost of the system, and does not provide an average cost for AB or alane over the lifetime of the system. Off-board regeneration costs for AB and alane were not a part of the cost estimate. The Phase-II model was a combination of a top-down cost estimate and bottoms-up estimates using material quantities and projections of material costs from manufacturer's quotes and progress ratios to determine prices as quantities required for the manufacturing process increased. Unlike the solid AB cost estimate, the Phase-II work estimated manufacturing costs based on the levelized costs of capital, labor, and operations and maintenance (O&M) costs and electricity costs, rather than using the analogy approach. Electricity costs were broken out if the equipment consumed significant electricity. A bill of materials and schematics were used similar to that used in Phase I. All costs and prices were adjusted to 2007$ for Phases II and III using the Gross Domestic Product Implicit Price Deflator.

2.3.6.1 Manufacturing Costs

Manufacturing costs are based on the levelized costs of capital, labor, and operations, and costs for maintenance and electricity. Electricity costs were broken out if the equipment consumed significant electricity.

2.3.6.2 Capital Costs

Major capital costs for each manufacturing step were estimated based on quotes from manufacturers. Buildings were assumed to provide a 30-year life while equipment was based on a 7-year life. The cost of installing equipment was assumed to be 65% of the Free-Onboard price. The cost of the major equipment was multiplied by 4.55 to obtain an estimate of the total capital cost of the manufacturing facility, including the cost of the building and auxiliary equipment (Peters and Timmerhaus 1991).

Annualized capital costs were separated into building and equipment costs and estimated separately using a 10% after-tax rate of return. The cost recovery factors are outlined in assumptions section. The cost factors for equipment and buildings are based on the following formulas. A cost recovery factor was developed separately for equipment and buildings. Equation 2.47 provides a factor that can be used to annualize capital to a before tax rate of return, and Equation 2.48 adds a factor to the first factor to account for taxes adjusted for tax depreciation to reach an after-tax rate of return:

$$CRF = (i * (1 + i)^n / (((i * 1)^n) - 1) \quad (2.47)$$

where *CRF* is the capital recovery factor, *i* is the discount rate, and *n* is the life of the asset

$$FCRF = CRF * (1 - t * NPV)/(1 - t) \quad (2.48)$$

where *FCRF* is the fixed charge recovery factor after taxes, *t* is the effective tax rate, and *NPV* is the net present value of depreciation over life of the asset.

Multiplying the appropriate fixed charge recovery factor by the investment cost of equipment and buildings provides the annualized cost of capital per piece of equipment and buildings. Dividing the annualized costs of capital and equipment by the number of power systems produced per year provides the cost per power system.

Electricity Cost

For equipment with significant electricity requirements, the cost of electricity was estimated separately. Electricity costs for each piece of equipment with known energy requirements was estimated using expected operating hours and the industrial rate of electricity from the EIA ($0.0644/kWh).

Operations and Maintenance and Labor

Operations and maintenance costs include labor costs. Operations and maintenance costs excluding labor cost was assumed to be 2% of total installed capital costs. Labor was estimated based upon the number of people required to operate each piece of equipment. A burdened labor rate of $50/hour was used for all process labor. A three shift basis was assumed.

2.3.6.3 Global Assumptions for the Cost Estimate

During Phase II, HSECoE worked with Strategic Analysis, Inc. (hereafter referred to as Strategic Analysis) to determine primary material costs such as aluminum, stainless steel, and carbon fiber that would affect all analyses by all estimators. The motivation behind the materials price agreement was that the amount of material needed to develop the system cost estimates should be the primary difference, not differences in prices of the materials used. The primary material costs in the model, including those agreed upon with Strategic Analysis, are shown in Table 2.21. Some of the most significant costs drivers in the solid AB tank system were the AB media itself plus tank materials. Similarly, alane was a

significant contributor to the first costs of the alane system. The AB media costs were obtained from a Dow Chemical study, which indicated that AB material could be purchased in large volumes for $9/kg (Linehan et al. 2010). Small-quantity purchases were found in the $4,500/kg to $5,000/kg range.

Table 2.21. Major Material Costs (2007$) used with AB and Alane Slurries

Item/Number of Units	10,000 $/kg	30,000 $/kg	80,000 $/kg	130,000 $/kg	500,000 $/kg
Ammonia Borane	92.41	48.41	27.18	20.42	9.24
Alane	178.00	103.90	64.25	50.65	26.17
Silicon Oil AR 20	11.66	9.01	7.16	6.39	4.66
Aluminum AI 6061-T6	7.48	6.89	6.41	6.18	4.45
Stainless Steel 316	9.15	8.44	7.85	7.57	4.92
Stainless Steel 304	6.28	5.79	5.39	5.20	3.55

Unlike AB, there are no studies for the costs of first production of alane. There are studies for regenerating alane from spent alane, but not for first production. Those estimates place the cost at about $4/kg hydrogen, assuming 10 wt% hydrogen produced from the alane (James et al. 2013). In discussions with Savannah River, the production process for the initial production cost of alane is costly because it must be completed in an oxygen-free environment. We developed a draft placeholder cost for alane by including materials and adding processing costs from regeneration. The value estimated was approximately $26/kg of hydrogen from the alane. The value was evaluated by calculating the progress ratio connecting the large-volume estimate and the small volume estimate. The ratio was approximately 0.71, which is at the bottom end of the range for progress ratios estimated by van Sark (2008) for bio-ethanol. In the early phases of bio-ethanol manufacturing (i.e., 1980 to 1985), the progress ratio was 0.93, but the progress ratio declined to 0.71 for the 1985 to 2002 period, indicating that early progress was slow but technological progress increased as more production occurred.

An additional check evaluated a regeneration pathway that includes a chemical for which estimates are available, sodium alanate (Zidan et al. 2009). Using an estimate of sodium alanate provides a lower bound on the initial production cost of alane. Sodium alanate can be electrolytically converted to alane in the presence of the catalyst tetrahydrofuran. The electrochemical cell in the conversion process has an aluminum anode (which is expected to be consumed as the alane is produced) and a platinum cathode. TIAX estimated the cost for large volumes of sodium alanate to be approximately $10/kg (2005$) (Lasher and McKenney 2007). Thus, the high-volume cost would be somewhere in this range. Small-quantity costs were found from laboratory supply companies with alane prices in the range of $5,500 to $6,000/kg. The results are shown in Table 2.21.

Silicone oil prices are based on price quotes from a distributor. During Phase II, the modeling approach switched from high-pressure systems to low-pressure systems in which the maximum pressure was in the 45 to 60 bar range. Therefore, the system design did not include carbon fiber and resin. The prices for stainless steel were estimated from MEPS North American Steel website (MEPS 2010).

Progress ratios for materials reflect an approach to show the quantity discounts that would be expected between small quantities and large mill or manufacturer prices. In all the cases, we had large-volume prices, and we found that small quantities often could contain a 100% markup over the large-volume prices. In the case of AB, a small-quantity price and the Dow Chemical cost estimate were obtained. The progress ratio is the fraction that fit the small-quantity price to the large-volume cost.

Prices for BOP components were based on prices from manufacturers or distributors. The preference to get the price from manufacturers reflects the case that OEMs most likely purchase directly from the manufacturer. Sometimes because of either the inability to get a quote from a manufacturer or because distribution agreements prohibited the manufacturer from providing a price quote, quotes were obtained from distributors or local supply houses.

Progress ratios were then applied either by estimating the progress ratio from quotes from different volumes or by evaluating the size of production, maturity of the technology and the method of manufacture. For BOP components, the vast amount of components had progress ratios in the 0.90 to 0.95 range. Unless we changed BOP components from Phase I to Phase II, progress ratios remained the same. Progress ratios in this range are based on simply removing the larger margins associated with small volumes. The progress ratios used were similar to those deduced from a fuel cell estimate by James et al. (2002). Note also that OEMs reviewed the pricing in the model to ensure that the values approximately corresponded with information in their databases. In certain cases such as filters and temperature sensors, OEMs said they could get a better high-volume price than the estimate obtained from using the chosen progress ratios. In those cases, the progress ratio was adjusted to reflect the better price given by the OEMs.

Equipment costs are shown in Table 2.22. Prices were obtained from manufacturers and, when possible, from the number of workers needed to operate the machinery. Equipment pricing is based on available equipment that meets the requirement for producing the specified volume in the estimates.

Table 2.22. Equipment Prices for CH Manufacturing and Assembly Steps

Equipment Type	Unit Cost ($)
Sonicator	5,260
Stamping	320,000
Neck-Forming Equipment	800,000
Ball Mill	15,000
BOP Assembly and Inspection	377,000

In the case of the sonicator for producing the AB/silicone oil slurry, no large pieces of equipment could be found that would meet the requirements for any volume. The sonicator was scaled to produce the estimates required at the different levels of production. The size of the sonicator used to develop the price estimate would only produce enough slurry for about 18 systems. At the largest volume, sonication was only adding approximately $10/system to the costs. At 10,000 units, sonication was adding about $49/system. Thus, an error of double the costs for producing slurry for 500,000 systems would not significantly impact the system costs.

Stamping mill costs were used to evaluate the costs of the stirrers in the bladder tank. Neck-forming equipment was used to manufacture the reactor from tubing. The ball mill was used to determine the costs of the mixing the super-activated carbon with the manganese chloride in the ammonia and borazine cleanup system. The square footage required to assemble the system was based on team estimates of the assembly area required. Based on the costs of a facility, machinery requirements were extrapolated using an equipment-to-facility factor of 4.55 (Peters and Timmerhaus 1991). Miscellaneous machinery includes welders and other tools required to assemble the system.

Assumptions used in estimating manufacturing and assembly costs are shown in Table 2.23. The rates are standard assumptions for building and equipment lifetimes. The approaches used to determine cost recovery factors are described in the Section 2.2.5.1. The manufacturing cost estimates are supposed to provide for a full economic recovery of the asset in the specified lifetime. The estimation methodology provides a 10% after-tax recovery rate for capital.

2.3.6.4 Exothermic System Cost

The system schematic for costing is shown in Figure 2.34 and described in Section 2.3.4. The bill of materials for this system is provided in Table 2.24. The bill of materials is divided into the media, tanks and tubing, feed loop, return loop, recycle loop, and hydrogen discharge loop. Each component was priced, and costs were developed to represent the cost in the system.

Table 2.23. Major Economic Assumptions for Estimating Manufacturing Costs

Economic Assumptions	
Building Lifetime	30 years
Equipment Lifetime	7 years
MACRS Building Life	20 years
After-Tax Rate of Return	10.0%
Federal Tax Rate	35.0%
State Tax Rate	6.0%
Effective Tax Rate	38.9%
Property Tax Rate	0.01
Insurance Rate	0.01
O&M Rate	0.02
Weighted Labor Rate	$49.69/hour
Cost Recovery Factors (percentage of the investment value)	
Building Cost Recovery Factor	10.6%
Value of Building Depreciation	44.8%
Building After-tax Recovery Factor	14.34%
Equipment Cost Recovery Factor	20.5%
Value of Equipment Depreciation	73%
Equipment After-tax Cost Recovery Factor	24.1%

The media is comprised of 38 kg of AB that is mixed with 38 kg of silicone oil. The process used to combine the solid AB and the silicone oil required sonication to induce the slurry. The time required to make the slurry at very low quantities was approximately 3 hours per tank. That value was the basis for developing an estimate of the added manufacturing costs of producing the slurry AB.

Tanks and tubing contained the volume-displacement tank with a linear actuator and stirrers to keep the fresh and spent slurries from settling. In addition, there were two rupture disks, a level sensor, pressure sensor, fill and drain lines, and high- and low-pressure lines. The feed loop contains the valves and valve controller that manages the fresh AB to the bladder tank and the spent fuel being drained back to the filling station.

Assumptions Specific to Slurry AB

The costs of the super-activated carbon were assumed to be similar in nature to AX-21, another super-activated carbon. The patent to produce AX-21 was used as the process to produce the estimated costs per kilogram of super-activated carbon (Wennerberg and O'Grady 1978). The process was input into ASPEN™, and the capital, labor, materials and O&M costs for the process was provided by the model to produce 18 million kilograms of super-activated carbon. The results of that modeling are depicted in Table 2.25 and Table 2.26. Table 2.25 shows the total equipment and capital cost scaled from the original quantities to those quantities required by the ammonia and borazine cleanup system.

Results and Discussion

The slurry AB onboard storage system total cost was approximately $3,000 or approximately $16/kWh at the 500,000 unit production level (see Table 2.27). Costs declined from almost $9,500 at the 10,000 system production level. The table provides a breakdown of system costs by major component system.

The feed loop, hydrogen discharge, media, and the return loop components comprise the bulk of the system costs containing approximately 81% of the total. The tank, recycle loop, and the manufacturing and assembly cost are a relatively small portion of total cost—approximately 4% to 8% each for a total of 19% of the system costs.

Table 2.24. Bill of Materials with Operating Pressures, Temperatures, and Flow Rates for Slurry AB

							Design Operating Limits			Extreme Operating Limits				
Item #	Description	Material	Wt (kg)	Vol (L)	Cost ($)	Dimensions (mm)	Pmax (bar)	Tmax (°C)	Flow Max (L/min)	Pmax (bar)	Tmax (°C)	Flow Max (L/min)	MAWP (bar)	Temp (C)
Media														
AB1	AB Chemical	AB Chemical to mix into slurry	38	0										
SIL1	AR20 Silicone Oil	Silicone Oil	38	0										
	Slurrification													
Tanks and Tubing														
TNK-1	Volume Displacement Tank	High Density Polyethylene	5.7	76		16"dx22"	2	50	NA	3	70	NA		
STR-1	Linear Actuator for Stirrer		4.44	1.39		635 mm x 73 mm x 30 mm each	2	50	NA	3	70	NA		
STR-2	Stirrers in Top and Bottom	6061 Aluminum Perforated	0.9	0		0.063" thick, 40% open , 1/8" holes	2	50	NA	3	70	NA		
NA	Fill and Drain Lines	Plastic	0.44	1.5		1" x .083 and 2.5 feet long each	2	50	35	3	70	70		
NA	Low T and P Lines	Stainless Steel	0.1	0.3		3/8" x 0.035 5 feet	30	85	0.5	45	150	0.75		
NA	High T and P Lines	Stainless Steel	0.8	0.4		1/2" x .035 10 feet	30	300	0.5	45	400	0.75		
INS-01	Rupture Disk		0.6	0.16			2	50	35	3	70	70	43.5	
INS-02	Level Sensor for Volume Displacement Tank					Hummingbird® PiranhaMax™ 150 Fish Finder	2	50	35	3	70	70		
INS-03	Rupture Disk		0.6	0.16			2	50	35	3	70	70		
INS-04	Pressure sensor	316L SS	0.1	0.001			2	50	NA	3	70	NA		
Feed Loop														
V-1	Multiport Valve		2	1			2	40	35	3	70	70	28	160
V-1	Flapper Valves		0.56	0			2	40	35	3	70	70	28	160
V-1	Valve Controller		2	1			NA	50	NA	NA	-20	NA	NA	
P-1	Feed Pump		1	1			30	120	0.5	45	150	0.75		
M-1	Feed Pump Motor		1	1.3			NA	35	NA	NA	50	NA		
INS-05	Temperature sensor	M8MJSS-18-U-6 and M8C-SIL-JI-S-F-	0.2	0.02			30	60	0.5	45	90	0.75		
RX-1	Reactor	SS tubing	0.3	0.1		1.75"OD X 0.065 wall s 39" length 304 SS	30	250	0.5	45	300	0.75		
M-3	Reactor Motor		1	0.2		18VCD DeWalt Drill Motor	30	250	0.5	45	300	0.75		
H-1	Reactor Heater		1.6			.5" Diameter, 39" heater length								
	Manufacturing													
	Insulation					Kaowool-- 1 inch thick								
	Shaft	2" X1/2"	0.202			1/2 Shaft welded to Stirrer								
	Stirrer	1/16 x 39" X 1.7" wth	0.53289			1/16" thick X 39" long X 1.7" wide								
	Pump Shaft Seal					McMaster Carr 9281K66								
INS-06	Temperature sensor	M8MJSS-18-U-6 and M8C-SIL-JI-S-F-	0.2	0.02			NA	250	NA	NA	300	NA		
INS-07	Level Sensor for P/S		0.216	0.139			30	250	NA	45	300	NA		

Table 1.24. (continued)

Return Loop														
PS-1	Gas Liquid Separator	347/347L SS	5.8	2.7		88.9 dia X 302 long (1/2" inlet/outlet/drain	35	200	1200 (gas) 1.4 (liquid)	37	260	600 (gas) 0.75	37	260
TNK-2	Drain Vessel	1/16" wall, 304L SS	0.6	1										
INS-08	Pressure sensor	316L SS	0.1	0.001			30	100	NA	45	150	NA		
V-2	Pressure Relief Valve		0.6	0.1		31.8 Diameter 100 Length	45	250	NA	45	300	NA		
RD-2	Liquid Radiator	304 SS	1.2	1.3		1 tubes, 3/8" diameter, 52 inches long, 1" OD w fin	30	250	0.5	45	300	0.75		
M-5	Liquid Radiator Fan Ultra Thin Line 12V Electric Fan (Puller)	Nylon	1	5.9		12" x 14" Radiator Fan size 280 diameter x 75.7 thick	NA	35	6 m/s	NA	50	6 m/s		
	Fan Pig Tail			1										
	Fan Feet													
INS-11	Temperature sensor		0.2	0.02			30	60	0.5	45	90	0.75		
V-5	Control Valve	Brass	2.0	1		1.68 dia. X 3.37 tall	2	60	0.5	45	90	0.75		
Recycle Loop														
P-2	Feed Pump and Motor	SS	1	0.2		120 x 337 x 83	30	250	0.5	45	300	0.75		
M-2	Feed Pump Motor	Misc	1	1.3			NA	35	NA	NA	50	NA		
Hydrogen Discharge														
FT-1	Coalescing Filter	SS	1.4	0.5			30	250	27	45	300	29	30	
RD-2	Gas Radiator and Header	304 SS	0.47	0.3		1 tube, 1/4" diameter, 39 inches long, 3/4" OD w fin	30	250	27	45	300	29	30	
M-4	Fan for Gas Radiator	Nylon	1	5.9		12" x 12" Radiator Fan size 280 diameter x 75.7 thick	NA	35	6 m/s	NA	50	6 m/s		
INS-09	Temperature sensor		0.2	0.02			30	60	NA	45	90	NA		
INS-10	Pressure Switch		0.1	0.001			30	60	NA	45	90	NA		
FT-2	H2 Clean-Up System Borazine		3.9	15.5			30	60	17	45	90	19		
	Super Activated Carbon		14.6	0										
FT-3	40% MnCl2		0.6	0			30	60	17	45	90	19		
	Additional Ballast Tank	Aluminum	1.30	13										
FT-4	Particulate Filter		0.25				5	60	84	30	90	19		
V-3	Pressure Regulator Gas		1	0.5		1.68 dia. X 3.37 tall	5	60	84	30	90	19	5-30	
V-4	Pressure Relief Valve		0.6	0.1		31.8 Diameter 100 Length	5	60	84	30	90	19	30	204

Table 2.25. Super-Activated Carbon Equipment Costs (000$ in 2007$)

Production Units	10,000	30,000	80,000	130,000	500,000
Total Equipment Cost	1,164	2,512	4,992	7,012	18,003
Equipment Capital Recovery	239	516	1,025	1,440	3,698
Equipment After-Tax Capital Recovery Factor	0.205	0.205	0.205	0.205	0.205
Present Value of Depreciation	$0.73	$0.73	$0.73	$0.73	$0.73
Fixed Charge Recovery Factor	0.241	0.241	0.241	0.241	0.241
Annualized Equipment Cost	$280.24	$604.67	$1,201.43	$1,687.70	$4,333.25
Total Building Cost	930	2,006	3,986	5,600	14,377
Equipment Capital Recovery	99	213	423	594	1,525
Equipment After-Tax Capital Recovery Factor	0.1061	0.1061	0.1061	0.1061	0.1061
Present Value of Depreciation	$0.49	$0.49	$0.49	$0.49	$0.49
Fixed Charge Recovery Factor	0.1434	0.1434	0.1434	0.1434	0.1434
Annualized Building Cost	133	288	572	803	2,061
Annualized Capital Cost	414	892	1,773	2,491	6,395
Insurance	21	45	90	126	324
Property Tax	21	45	90	126	324
Total Annualized Capital Cost	$455.44	$982.70	$1,952.53	$2,742.81	$7,042.29

Table 2.26. Super-Activated Carbon Costs per Kilogram Different Production Volumes

		10,000	30,000	80,000	130,000	500,000
Capital Cost	$/kg	3.1	2.2	1.7	1.4	1.0
Labor		4.5	2.4	1.3	1.0	0.4
Materials						
Coconut Char		2.7	2.7	2.7	2.7	2.7
KOH 50%		0.1	0.1	0.1	0.1	0.1
Electricity		0.1	0.1	0.1	0.1	0.1
Other Materials Allowance		0.2	0.2	0.2	0.2	0.2
Maintenance Costs		0.2	0.2	0.2	0.2	0.2
Total	$/kg	10.9	7.9	6.2	5.7	4.7

Table 2.27. Summary of System Costs for Slurry AB at Volume of Production Levels

Item \ # of units	10,000	30,000	80,000	130,000	500,000
			$/System		
Media	4,004	2,216	1,330	1,040	539
Tank	384	327	287	271	232
Feed Loop	1,369	1,098	923	852	695
Return Loop	1,396	1,057	829	736	534
Recycle Loop	632	461	348	303	206
Hydrogen Discharge	1,311	1,008	843	783	663
Manufacturing And Assembly	357	276	219	195	142
System Cost	9,454	6,444	4,779	4,181	3,011
$/kWh	50.70	34.56	25.62	22.42	16.15

The media, tank, and reactor costs are detailed in the Table 2.28. Media accounts for about 18% of the slurry AB system costs. The media section also provides a cost for creating the AB/silicone oil slurry. The ability to scale the costs for creating the slurry are a significant risk as the ability put AB into the oil solution has not been demonstrated at quantities greater than a few kilograms.

Table 2.28. Detailed System Costs for Media Tank and Feed Loop for Slurry AB at Different Volumes

		Costs at Levels of Production (2007$)				
	Units	10,000	30,000	80,000	130,000	500,000
Media Total		4,004	2,216	1,330	1,040	539
AB Chemical	38	3,512	1,839	1,033	776	351
AR 20 Silicone Oil	38	443	342	272	243	177
Slurry Production		49	34	25	22	10
Tank		384	327	287	271	232
Volume-Displacement Tank	1	107	107	106	105	104
Linear Actuator for Stirrer	1	22	17	14	12	9
Stirrers in Top and Bottom	1	57	46	38	34	26
Fill and Drain Lines	2	8	7	7	7	7
Low T and P Lines	5	7	7	7	7	7
High T and P Lines	5	9	8	8	8	8
Rupture Disk	1	20	14	10	9	6
Level Sensor for Volume-Displacement Tank	1	43	36	31	29	24
Rupture Disk	1	20	14	10	9	6
Pressure Sensor	1	90	70	56	50	36
Feed Loop		1,369	1,098	923	852	695
Multiport Valve	1	166	141	121	112	92
Flapper Valves	2	72	67	62	60	54
Feed Pump	1	632	461	348	303	206
Temperature Sensor	1	31	30	30	30	29
Reactor	3	30	28	26	25	23
Reactor Motor	1	18	18	17	17	17
Reactor Heater	6	169	190	185	183	177
Manufacturing		52	20	9	6	3
Insulation	3	6	5	5	5	4
Shaft	0	2	2	2	2	1
Stirrer	1	5	5	5	4	3
Pump Shaft Seal	1	11	11	11	11	11
Temperature Sensor	1	31	30	30	30	29
Level Sensor for P/S	1	117	90	72	64	47

The AB material costs also present an unknown risk as there was significant discussion about the original estimate for AB. The price, at about $9/kg, for 500,000 tanks is significantly below the $5,600 price quote for AB procured in small quantities. Economies of scale can provide for most of the decline in costs.

The tank costs were priced based upon the major component parts, and assembly of the items was included in the overall assembly cost. The feed pump and motor was the most expensive item priced at $4,800 per unit. A progress ratio of 0.82 was applied to this item. The resulting price at high volume was approximately 10 times the high-level estimate of the cost of materials in the pump. The pressure sensors in the tank were significantly expensive when procured in small quantities with a price of $495. A progress ratio of 0.85 was applied to both items. The rupture disks were relatively expensive when procured in small volumes, priced of $245 each. A progress ratio of 0.80 was applied because of the simpler construction available.

The reactor, which is composed of a tube, motor, and heater, would have been relatively inexpensive except that there were six heaters. The heaters were a well-established product with little room left for technological growth. As such, little cost reduction was expected. The low-volume price was $55 each. Neck-forming equipment was used to bring the reactor entrance and exit to an appropriate size. The level sensor was priced at $790 each, and a progress ratio of 0.85 was applied to the price.

The gas-liquid separator was priced by the manufacturer at all levels of production. The gas-liquid separator was priced at approximately $8,500 each for the first one and $4,500 each for 500,000 units per year. In discussions with the team, the design and construction was analyzed and a determination was made that the price/cost should be much less expensive than estimated by the manufacturer. A progress ratio of 0.82 was applied that still left the cost of the gas-liquid separator above the high-level estimate of the cost of materials by two times (a 100% markup).

The liquid radiator was priced by the manufacturer at approximately $350 per unit. They also priced the radiator at about $35 each for 500,000 units. The resulting progress ratio was about 0.86. The radiator also contained a fan that was priced separately from the main body of the radiator. The use of the fan was explained to the manufacturer, and they recommended that a fan pigtail for connecting the fan to the power supply and mounting brackets be added. The manufacturer priced them at 1 unit and 10,000 units, dropping the price from $103 per unit to approximately $36 per unit. The progress ratio of 0.95 was calculated.

Costs of the return loop, the recycle loop, and the hydrogen discharge system are detailed in Table 2.29. The return loop contains the gas-liquid separator, liquid radiator, radiator fans, a pressure sensor, a relief valve, a control valve with actuator, and a drain vessel.

The drain vessel estimate was created based on manufacturing and materials costs. In work for the adsorbent system estimate, a Type-I tank manufacturing process was estimated. The values from manufacturing the tank were applied to the tank plus the cost of materials. The recycle loop contained only a feed pump and motor. The same pump and costs for the feed pump were used for the recycle loop.

The hydrogen discharge system contains the coalescing filter, radiator, temperature sensor, pressure switch, ammonia and borazine cleanup system, an additional ballast tank, a particulate filter, backpressure regulator, and a pressure relief valve.

The most expensive element in the system is the pressure switch. The item was priced at one unit and 10,000 units. At one unit, the price was $750 while it was approximately $490 at 10,000 units. The switch was priced at a supply house where two markups were removed. The resulting progress ratio was 0.95. The gas radiator was priced by the same manufacturer as the liquid radiator at the same sets of volumes. The prices were somewhat lower than the liquid radiator but the same progress ratio was calculated for the resulting pricing.

Two quotes were provided for the coalescing filter for the same specifications. One quote was for $710 while the second quote was for approximately $440. A progress ratio of 0.85 was applied to the lower quote. The particulate filter was priced at $1,769. A review by an OEM found that they were purchasing the same quality and specification of filter for much less at high volumes. The price for the particulate filter was adjusted down to the high-volume value suggested by the OEM.

The ammonia and borazine cleanup system was estimated based on its parts. The tank was quoted at approximately $105 each at small quantities and $100 at 10,000 units. A progress ratio of 0.95 was used. The super-activated carbon quantity was discussed previously. A ball mill was used to provide the desired the product.

Table 2.29. Detailed System Costs for Return Loop, Recycle Loop, and Hydrogen Discharge System for Slurry AB at Different Volumes

		Cost at levels of Production (2007$)				
	Units	10,000	30,000	80,000	130,000	500,000
Return Loop		1,396	1,057	829	736	534
Gas-Liquid Separator	1	1,043	762	575	501	340
Pressure Sensor	1	90	70	56	50	36
Pressure Relief Valve	1	56	51	48	46	42
Liquid Radiator	1	73	57	47	42	31
Liquid Radiator Fan Ultra -Thin Line 12V Electric Fan (Puller)	1	34	31	29	28	25
Fan Pig Tail	2	0	0	0	0	0
Fan Feet	1	2	2	2	2	2
Temperature Sensor	1	31	30	30	30	29
Control Valve Actuator and Valve	1	62	48	38	34	25
Drain Vessel	1	5	5	4	4	3
Recycle Loop		632	461	348	303	206
Feed Pump and Motor		632	461	348	303	206
Hydrogen Discharge	-	1,311	1,008	843	783	663
Coalescing Filter	1	62	48	38	34	25
Gas Radiator and Headers	1	48	35	27	24	16
Fan for Gas Radiator	1	34	31	29	28	25
Fan Pig Tail	2	0	0	0	0	0
Fan Feet	1	2	2	2	2	2
Temperature Sensor	1	31	30	30	30	29
Pressure Switch	1	320	295	274	264	239
H_2 Cleanup System Borazine and Ammonia Combined	1	47	43	40	39	35
Super-Activated Carbon	15	160	115	91	83	68
40% MnC12	1	2	2	2	2	2
Mixing		1	4	1	1	0
Additional Ballast Tank	1	47	43	40	39	35
Particulate Filter	1	359	182	99	73	32
Backpressure Regulator Gas	1	134	127	122	119	113
Pressure Relief Valve	1	56	51	48	46	42
Manufacturing and Assembly	40	357	276	219	195	142
Total		9,454	6,444	4,779	4,181	3,011

Assembly time for the system was based on the hours required to assemble the cryo-compressed system divided by the number of parts. The time estimated on a per part basis was multiplied by the number of parts in this system to get an estimate time required at 500,000 units estimated. A progress ratio of the 0.85 was used to backcast the number of hours per system, and the value estimated was very close to the value estimated by the individual that assembled the laboratory version.

Figure 2.54 provides further breakdown of the other BOP in the system at 500,000 units of annual production. The largest component is the valves in the system followed by the pumps. Thus finding ways to reduce the cost of valving by using fewer valves would be appropriate. In addition, three individual items contribute 36% of the system's other BOP costs. The two pumps and the gas-liquid separator could be examined to understand their cost drivers and determine whether there are any pathways for reducing their costs.

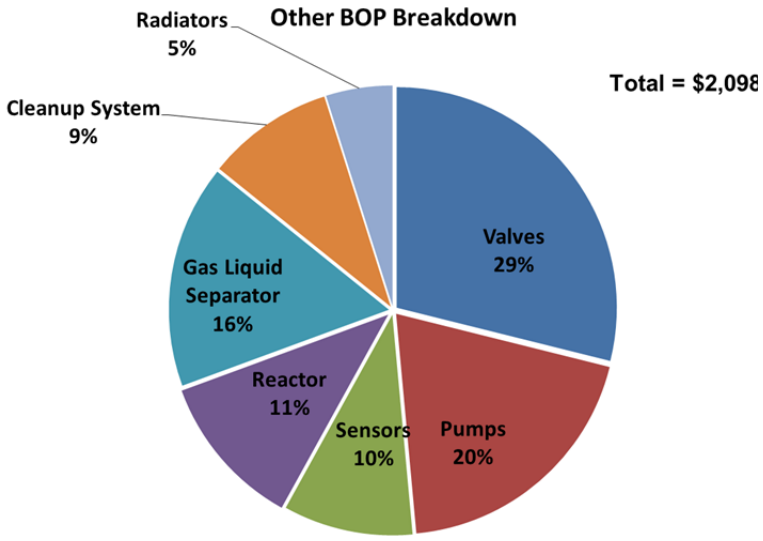

Figure 2.54. Breakdown of Other BOP Components for AB Slurry

Figure 2.55 examines the risks in the cost estimate. The values beside each bar of the graph indicate the range in dollars per item. The graphic indicates that the risks are primarily to the upside. We reviewed our estimates to determine whether the approach left more upside or downside risk. Most items were forecast to have a bottom range of 90% of the midpoint. The exceptions are the feed pump and silicone oil for which we believe there may still be some downside potential; therefore, they were forecast to be 50% of the median. Forecasting progress ratios has been shown to have significant upside risks. The previously mentioned case of bio-ethanol is one those cases, while photovoltaics are another. There were two distinct phases for both of these technologies where progress ratios in the early phase of the technology were much higher than they were in later phases of commercial production. (The smaller a progress ratio is the faster cost declines as production doubles.) The gas-liquid separator was forecast to potentially be three times the average because of the significantly different estimates from the manufacturer. Manufacturing and assembly was multiplied by approximately five because manufacturing estimates are so dependent on the knowledge of the process and that was still somewhat unknown, especially for sonication of the media and the assembly. Because of the progress ratio risk, the feed pump, pressure switch, silicone oil, and backpressure relief valve were multiplied times two. The reactor heater, the volume-displacement tank and multiport valve all were mature technologies with little upside risk and 10% was added to the average.

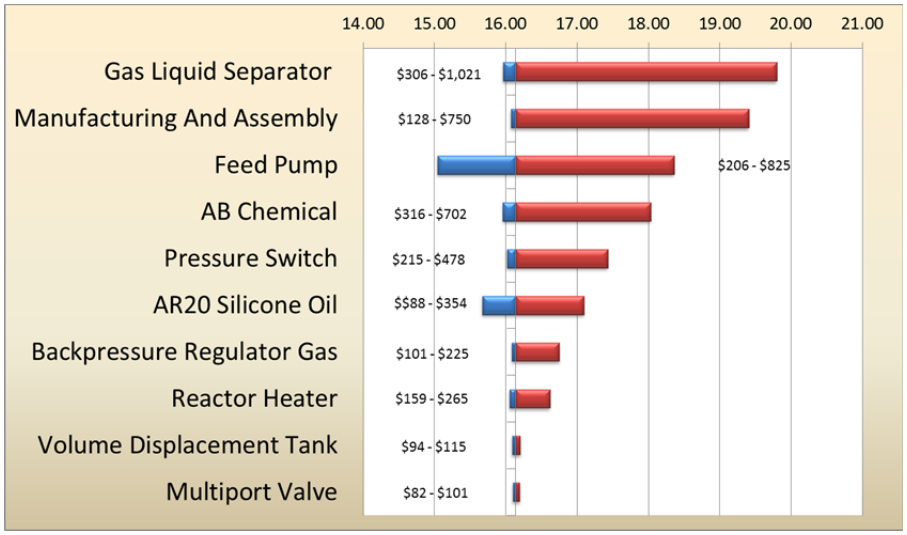

Figure 2.55. Tornado Chart for Slurry AB By Major Components

The gas-liquid separator, manufacturing and assembly, feed pump, and the AB chemical are the largest four risk contributors to the cost estimate. The gas-liquid separator and the feed pumps have small-quantity prices that are significantly above their prices at 500,000 units. In the case of the gas-liquid separator, the price quoted per unit by the manufacturer at 500,000 units of annual production was above the cost estimate for the entire system as estimated. The difference in forecast prices needs a more a thorough investigation. Similarly, the price for the pumps requires a significant reduction in price from the quoted small-volume price. Manufacturing and assembly costs need to decrease from approximately 40 hours per system to be in the range estimated for the system.

Results and Discussion

The total cost of the onboard storage system for the slurry alane was estimated to be approximately $4,100 or about $22/kWh at a 500,000 unit production level (see Table 2.30). Costs declined from almost $16,400 at the 10,000 system production level. The table provides a breakdown of system costs by major component system.

Table 2.30. Slurry Alane Onboard Storage Costs by Major System Component (2007$)

Item \ # of units	10,000	30,000	80,000	130,000	500,000
			$/Systems		
Media	11,740	6,995	4,427	3,538	1,915
Tank	472	412	370	352	311
Feed Loop	1,399	1,127	951	879	721
Return Loop	1,396	1,057	829	736	534
Hydrogen Discharge	1,032	794	664	617	522
Manufacturing And Assembly	326	251	199	178	129
System Cost	16,364	10,636	7,440	6,300	4,133
$/kWh	87.75	57.04	39.90	33.78	22.16

2.3.6.5 Endothermic System Costs

A cost estimate for a slurry alane onboard hydrogen storage system was developed from the slurry AB system previously discussed. The approach and the methodology were identical. There were five differences between the slurry alane system and the slurry AB system as estimated. Only the differences and the impact on the cost per system and cost per kWh will be discussed. The major differences between slurry alane system and the slurry AB system were that the hydrogen carrier was alane rather than AB. The recycle loop was removed because there was no need to recycle the material to extract more hydrogen. The media storage tank was approximately 30% larger than for slurry AB. However, more than 61 kg each of alane and silicone oil were required to obtain 5.6 kg of usable hydrogen, more than 60% greater than the weight of the AB and silicone oil. The ammonia and borazine cleanup systems have been removed as there are no ammonia and borazine byproducts from alane. A recuperator was added to condition product entering the reactor added. All the remaining components of from the slurry AB system remain unchanged.

The system estimated is shown in Figure 2.37 and described in Section 2.3.4. The bill of materials for the alane system can be seen in Table 2.31.

Table 2.31. Bill of Materials with Operating Pressures, Temperatures, and Flow Rates for Slurry Alane

								Design Operating Limits			Extreme Operating Limits					
Item #	Description	Specified?	Material	Wt (kg)	Vol (L)	Cost ($)	Dimensions (mm)	Pmax (bar)	Tmax (°C)	Flow Max (L/min)	Pmax (bar)	Tmax (°C)	Flow Max (L/min)	MAWP (bar)	Temp (C)	Manufacturer/Model
Tanks and Tubing																
AB1	Alane	Yes		61.6	0											
SIL1	AR20 Silicone Oil	Yes	Silicone Oil	61.6	0											Dow
	Slurrification															
TNK-1	Volume Displacement Tank	Yes	High Density Polyethylene	6.8	99		15" tall x18"wide (square) with 6" cone for draining	2	50	NA	3	70	NA			
STR-1	Linear Actuator for Stirrer	Yes		4.44	1.39		635 mm x 73 mm x 30 mm each	2	50	NA	3	70	NA			Firgelli Automations FA-35-TR-20"
STR-2	Stirrers in Top and Bottom	Yes	6061 Aluminum Perforated	1.1	0		0.063" thick, 40% open , 1/8" holes, 2 plates (top and bottom)	2	50	NA	3	70	NA			McMaster-Carr , 9967T5
NA	Fill and Drain Lines	Yes	Plastic	0.44	1.5		1" x .083 and 2.5 feet long each	2	50	35	3	70	70			
NA	Low T and P Lines	Yes	Stainless Steel	0.1	0.3		3/8" x 0.035 5 feet	30	85	0.5	45	150	0.75			Swagelok SS-T6-S-035
NA	High T and P Lines	Yes	Stainless Steel	0.8	0.4		1/2" x .035 10 feet	30	300	0.5	45	400	0.75			Swagelok - SS-T16-S-083-6ME
INS-01	Rupture Disk	Yes		0.6	0.16			2	50	35	3	70	70	43.5		BS&B Safety Systems via NW fluids
INS-02	Level Sensor for Volume Displacement Tank	Yes					Humminbird® PiranhaMax™ 150	2	50	35	3	70	70			Humminbird® PiranhaMax™ 150 Fish Finder
INS-03	Rupture Disk	Yes		0.6	0.16			2	50	35	3	70	70			BS&B Safety Systems via NWFluids
INS-04	Pressure sensor	Yes	316L SS	0.1	0.001			2	50	NA	3	70	NA			Omega PX600-2006V
Feed Loop																
V-1	Multiport Valve	Yes		1.8	1			2	40	35	3	70	70	28	160	
V-1	Flapper Valves	Yes		0.56	0			2	40	35	3	70	70	28	160	
V-1	Valve Controller	Yes		2	1			NA	50	NA	NA	-20	NA	NA		
P-1	Feed Pump	Yes		2	0.5			30	120	0.5	45	150	0.75			**Using Mahr Pump as a placeholder**
INS-05	Temperature sensor	Yes	M8MJSS-18-U-6 and M8C-SIL-JI-S-F-	0.2	0.02			30	60	0.5	45	90	0.75			
RX-1	Reactor	Yes	SS tubing	1.76	1.54		1.75"OD X 0.065 wall 39" length 304 SS	30	250	0.5	45	300	0.75			Mixer Inside of 1/2" tube
M-3	Reactor Motor	Yes		1	0.25		18VCD DeWalt Drill Motor	30	250	0.5	45	300	0.75			Drill Motor similar to Mahr pump motor
H-1	Reactor Heater	Yes		1.6			.5" Diameter, 39" heater length									Rope Heaters (3 x 10' long @ 500 W each) Omega FGR-100
	Manufacturing															
	Insulation						Kaowool– 1 inch thick									2300 Deg. Kaowool Blanket #8 Premi
	Shaft		Stainless steel	0.1544			6" long 1/2" diameter Shaft welded to Stirrer									
	Stirrer		Stainless steel	0.2588			1/16" thick X 39" long X 1.62" wide 50% voids									
	Pump Shaft Seal						McMaster Carr 9281K66									McMaster Carr 9281K66
RD-3	Recuperator	Yes	316L SS	0.12	0.15		1/2" tube inside of a 3/4" tube	45	250	NA	45	300	NA			Tube inside a tube 0.5 m long
INS-06	Temperature sensor	Yes	M8MJSS-18-U-6 and M8C-SIL-JI-S-F-	0.2	0.02			NA	250	NA	NA	300	NA			
INS-07	Level Sensor for P/S	Yes		0.216	0.139			30	250	NA	45	300	NA			

Table 1.31. (continued)

								Design Operating Limits			Extreme Operating Limits					
Item #	**Description**	**Specified?**	**Material**	**Wt (kg)**	**Vol (L)**	**Cost ($)**	**Dimensions (mm)**	**Pmax (bar)**	**Tmax (°C)**	**Flow Max (L/min)**	**Pmax (bar)**	**Tmax (°C)**	**Flow Max (L/min)**	**MAWP (bar)**	**Temp (C)**	**Manufacturer/Model**
Return Loop																
PS-1	Gas Liquid Separator	Yes	347/347L SS	3.2	2.7		88.9 dia X 302 long (1/2" inlet/outlet/drain connections)	35	200	1200 (gas) 1.4 (liquid)	37	260	600 (gas) 0.75 (liquid)	37	260	2" Type "31LR-CLC" (Eaton Filtration)
INS-08	Pressure sensor	Yes	316L SS	0.1	0.001			30	100	NA	45	150	NA			
V-2	Pressure Relief Valve	Yes		0.6	0.1		31.8 Diameter 100 Length	45	250	NA	45	300	NA			
RD-2	Liquid Radiator	Yes	304 SS	1.79	2.66		1 tubes, 3/8" diameter, 3 meters long, 1" OD w fin	30	250	0.5	45	300	0.75			Energy Transfer MDE
M-5	Liquid Radiator Fan Ultra Thin Line 12V Electric Fan (Puller)	Yes	Nylon	1	5.9		12" x 14" Radiator Fan size 280 diameter x 75.7 thick	NA	35	6 m/s	NA	50	6 m/s			Fluidyne 11" Pusher 12 Volt 9.3 amps fan 1075 cfm- Part # FHP34211
	Fan pig tail				1											
	Fan feet															
INS-11	Temperature sensor	Yes	M8MJSS-18-U-6 and M8C-SIL-JI-S-F-	0.2	0.02			30	60	0.5	45	90	0.75			M8MJSS-18-U-6 and M8C-SIL-JI-S-F-3
V-5	Control Valve Actuator and valv	Yes		2.4	1											
TNK-2	Drain Vessel	Yes	SS304 tank	0.6	1											
Recycle Loop																
Hydrogen Discharge																
FT-1	Coalescing Filter	Yes		1.4	0.34			30	250	27	45	300	29	30		Looked at Parker-Hannafin Coalescing
RD-2	Gas Radiator and Headers	Yes	304 SS	0.32	0.16		1 tube, 1/4" diameter, 0.5 meters long, 3/4" OD w fin	30	250	27	45	300	29	30		Energy Transfer MDE Quote
INS-09	Temperature sensor	Yes	JSS-18-U-6 and M8C-SIL-JI-S	0.2	0.02			30	60	NA	45	90	NA			M8MJSS-18-U-6 and M8C-SIL-JI-S-F-
INS-10	Pressure Switch	Yes		0.1	0.001			30	60	NA	45	90	NA			Ashcroft D-Series
	Additional Ballast Tank	Yes	Aluminum @ 37 atm	4.70	27											Sherwood
FT-4	Particulate Filter	Yes	Taken from D. Tamberello 12/13/12 (3/4" 0.062" wall seven 9" elements ~ 1.1 kg)	0.2	0.001			5	60	84	30	90	19			
V-3	Backpressure Regulator Gas	Yes		1	0.5		1.68 dia. X 3.37 tall	5	60	84	30	90	19	5-30		Swagelok
V-4	Pressure Relief Valve	Yes		0.6	0.1		31.8 Diameter 100 Length	5	60	84	30	90	19	30	204	Generant HPRV-500B-V-450

Figure 2.56 provides a share breakdown between the major sub-components of the alane system and compares them with the same AB system sub-components. Note that the recycle loop has been removed in the alane system. Also note that the alane, silicone oil, and manufacturing costs are 35% of costs for the alane system compared with 18% for the AB system. The hydrogen discharge sub-system decreases from 22% of the AB system to 15% of the alane system primarily because of removal of the ammonia and borazine cleanup systems. The feed loop, hydrogen discharge, media, and the return loop components comprise the bulk of the system costs containing approximately 87% of the costs as compared with 81% of the total costs for the AB system. The tank, manufacturing, and assembly costs account for just 13% of the alane system costs, very similar to the same components of the AB system.

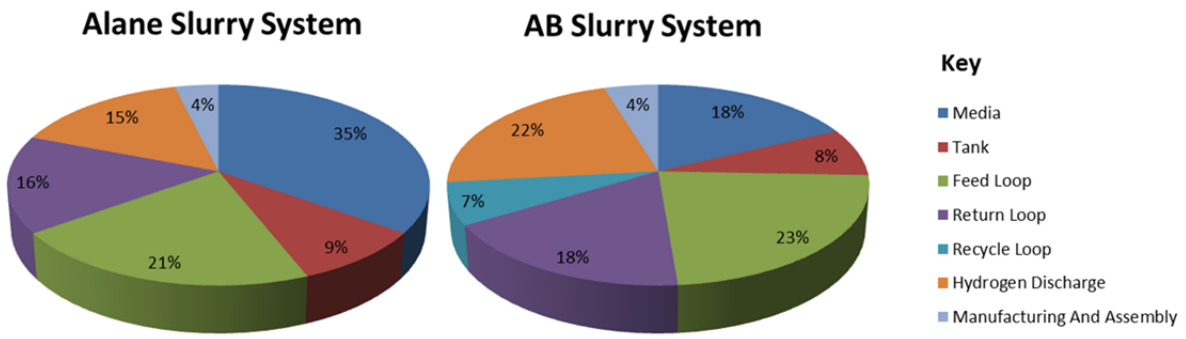

Figure 2.56. Comparison of Major Components for Onboard Storage of Slurry Alane and Slurry AB

The primary difference between alane and the AB slurry systems was the change to alane media, which although it was only 30% more volumetrically, it was 62% more in weight. Table 2.32 shows the costs for the items that changed in the slurry alane system. The added weight for both alane and the silicone oil increased the cost of media to more than three times the AB media cost. The cost of alane, $26/kg was almost triple the estimated price of AB, $9/kg. The other component whose cost increased was the tank. The original price was $270 for the alane volume-displacement tank as compared with the $159 for the AB tank. The recuperator was estimated as a ½-inch stainless steel 316 tube inside a ¾-inch stainless steel 316. The assembly costs for the recuperator are included in the assembly cost. Assembly cost decreased to $129 for the alane system from $142 for the AB system because fewer items had to be assembled.

Table 2.32. Slurry Alane Onboard Storage Cost Detail Component for Media, Tank, And Feed Loop (2007$)

		Cost at levels of production (2007$)				
	Units	10,000	30,000	80,000	130,000	500,000
Alane Chemical	62	10,965	6,400	3,958	3,120	1,612
AR 20 Silicone Oil	62	718	555	441	393	287
Slurry Production	-	57	40	29	25	16
Volume-Displacement Tank	1	182	181	180	179	177
Recuperator	2	15	14	14	14	14
Manufacturing And Assembly	40	326	251	199	178	129

Figure 2.57 compares the other BOP components for the two systems. Valving becomes more important to the alane system as it increases to 34% from 29% for the slurry AB system. Pumps decline as a percentage as there is one less pump. Hydrogen discharge also declines as the ammonia and borazine cleanup is removed.

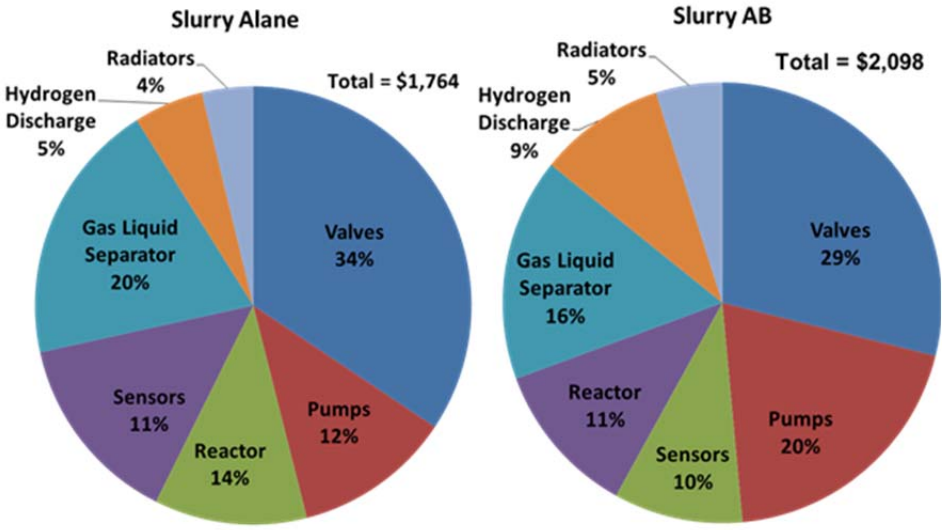

Figure 2.57. Comparison of Major Components needed for Onboard Storage of Slurry Alane and Slurry AB

Figure 2.58 shows the risks in the slurry alane cost estimate in a one-at-a-time basis. There are only two differences in the alane system tornado chart from slurry AB—manufacturing and assembly cost and risk in the hydrogen carrier media. As there were fewer items manufactured and assembled, the range declined. Alane costs reflect as much upside risk as downside risk. Even at a very low alane cost of $14/kg, the system cost is still more than $18/kWh, substantially above the $12/kWh target.

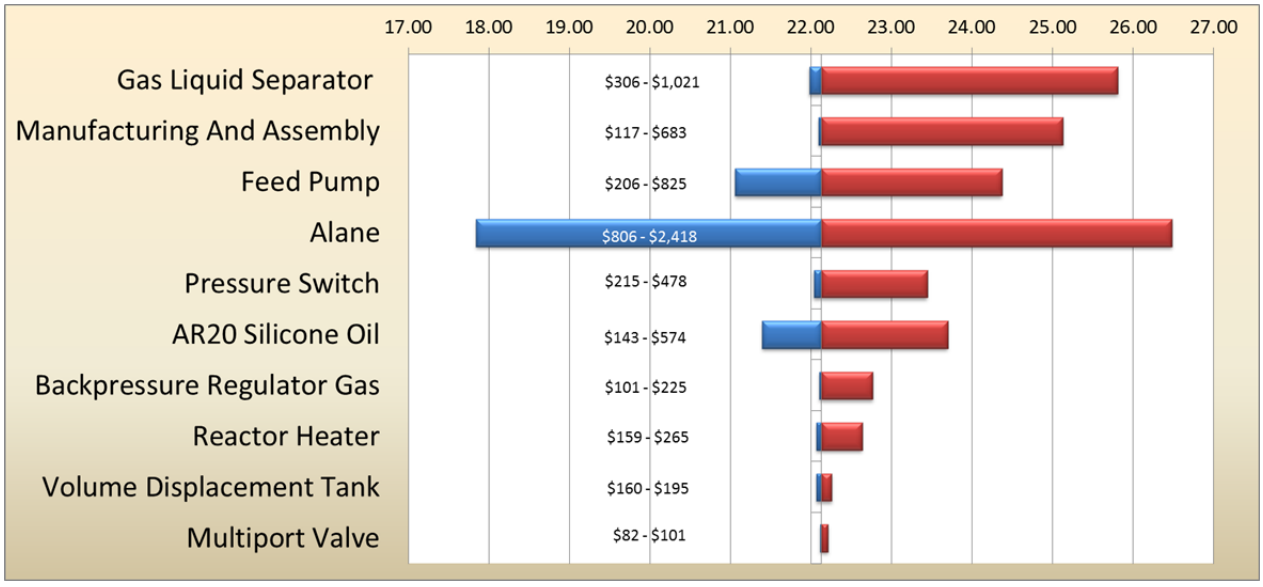

Figure 2.58. Tornado Chart of Major System Risks for the Alane Slurry System

2.3.6.6 Summary of Cost Estimates

The slurry alane onboard storage-system cost just over $22/kWh or 83% above hydrogen storage targets for 2017. The total system costs for the slurry alane system were slightly under the solid AB system at just under $24/kWh. Figure 2.59 indicates how the slurry alane system compares with the two AB tanks as well as other tank types. The slurry alane system cost is approximately 10% less than the solid AB system cost, $24/kWh, but is more than one-third more costly than the slurry AB system, at $16/kWh. Even at a very low alane cost (i.e., $14/kg), the system cost is still more than $18/kWh, which is substantially more the $12/kWh target. The offset for slurry alane is in off-board regeneration where it is substantially less costly than the AB. The regeneration cost of alane is estimated at $4/kg hydrogen compared with $10.46/kg hydrogen for AB indicating the life-cycle costs will be less. Figure 2.59 indicates the significant change in cost from the Phase I tank to the Phase-II tank. The graphic also indicates that the slurry AB cost is still somewhat above the Phase-II system estimated—a MOF-5 absorbent system. No system estimated to date has come under the $12/kWh or approximately $2,200 per 5.6 kg hydrogen system estimated despite using fairly aggressive cost estimating parameters.

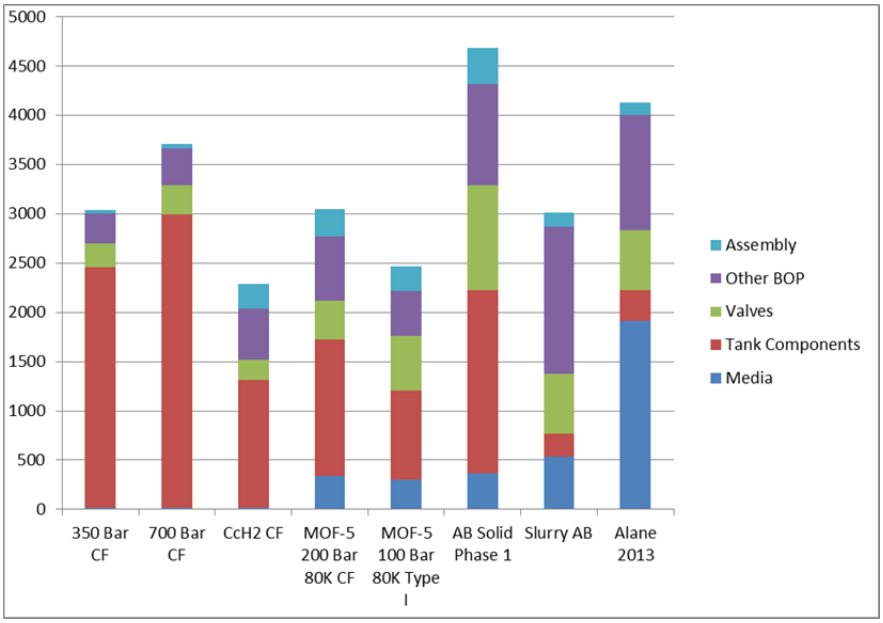

Figure 2.59. Comparison of Major Component for Slurry Alane and Slurry AB

2.3.7 Balance of Plant for the Slurry System Design

The BOP components were initially identified based on the development of a process flow diagram. Depending upon the level of rigor, the process flow diagram evolved through multiple iterations as additional parts are added to flesh out the design and then parts are removed as the design is simplified. Once the parts were identified, simple calculations were performed to determine the properties of each component. Such things as expected volume, mass flow, temperature, and pressure were estimated. For typical components, commercial vendors were contacted to identify components that would meet the specifications. To assist in this process, a library of BOP components was developed as part of the HSECoE. This library includes information on pumps, controllers, valves, filters, pressure regulators, tubing, pressure relief valves, and other components expected to be required for the CH, metal-hydride, or adsorbent systems being evaluated by HSECoE. Hydrogen compatibility, temperature, and pressure limits were considered as the library was developed. In the case of CHs, these components require compatibility with high temperatures and pressures.

In some cases, the components required for a design are not available commercially. In this case, more detailed calculations were performed to develop a preliminary design. Thermodynamic properties, heat transfer, and pressure drop may be calculated to develop the design. The component then was sized and the weight and volume estimated.

2.3.7.1 System Design Progression

At the beginning of Phase 2, the slurry system contained only the major system components (see Figure 2.60). This level of detail was developed sufficiently for modeling the major components. The system consisted of only 12 parts and the estimate of the system mass and volume was very rough. As a result, the estimate included a 10% contingency to cover for the bulk of the minor BOP components.

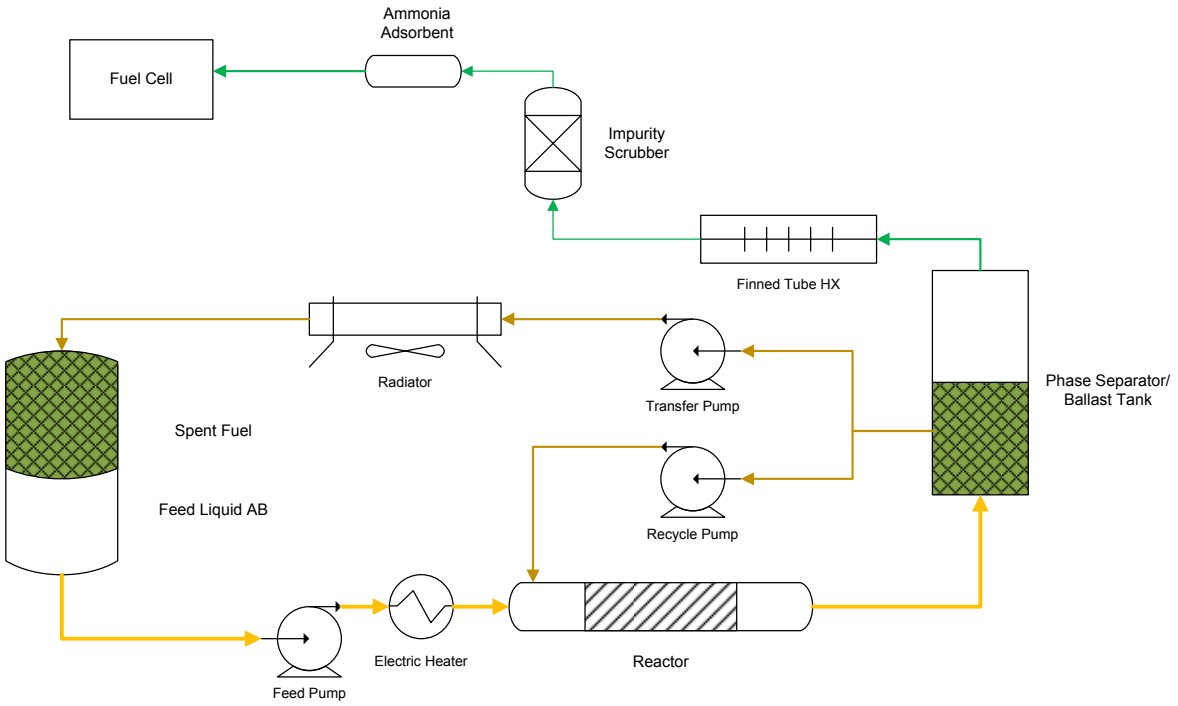

Figure 2.60. Draft Phase-II Process Flow Diagram for the Slurry System

As part of the Phase-II scope, details to this initial design were added to include expected instrumentation and valving. The part count rose from only 12 to more than 35 parts as details of the design began to be addressed (see Figure 2.61). With this new update, the scope of HSECoE was changed to include identifying and validating components. Specific commercial vendors for the pumps, radiators, phase separator, and valves were identified, and in some cases, components were tested with either actual AB or with a plastic simulant in silicone oil. The components were generally sized for maximum design operating limits of 250°C and 30 bar and extreme operating limits of 300°C and 45 bar. The total system mass was estimated at 127 kg for this system.

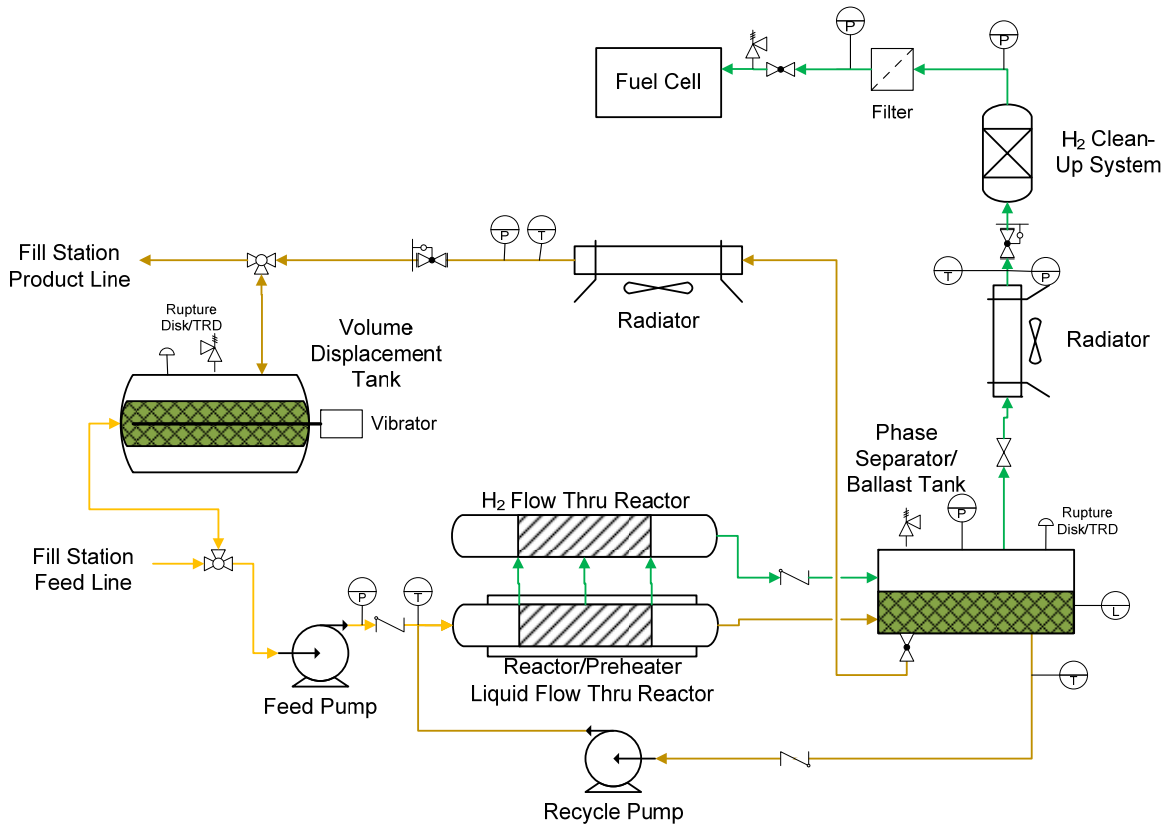

Figure 2.61. Phase-II Process Flow Diagram for the Slurry System Updated from the Initial Draft

In January of 2013, a "deep dive" evaluation was performed in which PNNL and the other HSECoE partners examined the design to identify instruments that could be removed, control logic required, and components that could be combined. This design became the basis for the cost analysis and Phase 2 modeling and design. The updated design was based on additional validation of components such as the volume-displacement tank and its mixers, radiators, check valves, reactor, phase separator, borazine, and ammonia cleanup filters. The Mahr pumps that were included in the design were purchased and validation tests attempted with fresh slurry AB. The results were that the fresh AB could not be pumped using Mahr pumps. Additional detail of this is described in Section 2.3.8.3. No other pump was identified that could pump the slurry at the conditions required. In spite of this discovery, Mahr pumps with their respective mass and volume remained as placeholders in the design.

The updated design is shown in Figure 2.34. In this design, the mass and volume did not change significantly, but the number of instruments required was reduced to the minimum required. The reactor was redesigned based on experimental work to have the slurry mixed as it reacted. The phase separator developed by UTRC had a drain vessel that is included in the design Based on additional work, it was recognized that a coalescing filter was required. A ballast tank of approximately 15 L also was required. The BOP components along with their mass, volume, and design basis are shown in Table 2.33.

Table 2.33. List BOP Components after the "Deep Dive" Design

Subcategory	Component	Total Mass (kg)	Total Volume (L)	Design Basis
Tanks and Tubing	AB/Silicone Oil Slurry	77		50 wt% AB
	Storage Tank	6.2	86	Custom HDPE Tank
	Three Linear Actuators	4.44	1.39	Firgelli Automations
	Two Perforated-Plate Stirrers	0.9	0	PNNL Design
	Fill/Drain Lines	0.44	1.5	1 in. × 2 ft Plastic
	Slurry/Gas Lines	0.9	0.7	½ inch & 3/8 inch SS
	Rupture Disk	0.6	0.16	Estimate
	Level Sensor	0.1	0.1	HawkEye
	Pressure Sensor	0.14	0.001	Estimate
Feed Loop	Pump/Motor	2	1.3	Mahr/TC-1251
	Flapper Valve	0.56	0	Custom
	Reactor	1	0.13	1-3/4" x 3 ft
	Reactor Heater	0.7	0.05	Omega
	Reactor Stirrer	1	0.2	Dewalt
	Pressure Sensor	0.1	0.001	Estimate
	Temperature Sensor	0.2	0.02	Estimate
	Valve	3.8	1	Assured Automation
Recycle Loop	Pump/Motor	2	1.5	Mahr/TC-1251
	Pump/Motor	2	1.5	Mahr/TC-1251
	Slurry Radiator	1.36	1.36	Energy Transfer MDE
	Radiator Fan	1	5.9	Fluidyne 11"
	Phase Separator	3.2	2.7	UTRC Design
	Level Sensor	0.18	0.14	Omega
	Drain Vessel	0.6	1	Custom
	Backpressure Regulator	1	0.12	Parker Veriflo
	Pressure Relief Valve	0.6	0.16	Estimate
	Control Valve	2.4	1	Assured Automation
	Pressure Sensor	0.1	0.001	Estimate
	Temperature Sensor	0.2	0.02	Estimate
Hydrogen Discharge	Coalescing Filter	1.4	0.34	Parker
	Gas Radiator	0.47	0.133	Energy Transfer MDE
	Radiator Fan	1	5.9	Fluidyne 11"
	Backpressure Regulator	1	0.5	Parker Veriflo
	Pressure Relief Valve	0.6	0.08	Generant
	Pressure Switch	0.1	0.001	Ashcroft
	Temperature Sensor	0.2	0.02	Estimate
	Ballast Tank	6.9	15	PNNL Design
	Particulate Filter	0.2	0.001	Savannah River National Laboratory (SRNL) Design
	H_2 Cleanup	19.1	16.4	LANL/UTRC Design
Total System		145.7	146.3	

A final evaluation was performed called an "elevated schematic." In this study of the BOP, components were combined together wherever possible to minimize the mass and further simplify the system. A reduction in system reliability was not considered during this evaluation. The consolidated components have not been developed and have not been validated, but are considered a bounding design to reduce the mass (see Figure 2.62). In this design, a small pump and jets are used to mix the material in the volume-displacement tank rather than the perforated-plate design that requires three linear actuators. The three pumps are combined into single system. With the appropriate gearing, we believe that it would be

possible to have a single motor drive both the feed and recycle pumps. The phase separator, ballast tank, drain vessel, and coalescing filter combined to a component with reduced mass and volume. A single radiator fan can drive both gas and liquid radiators. Finally, the particulate and impurities filters are combined into a single component as well. Using this design the number of components is reduced and the system mass decreased to 114 kg, which is 89% of the 2017 DOE target for mass.

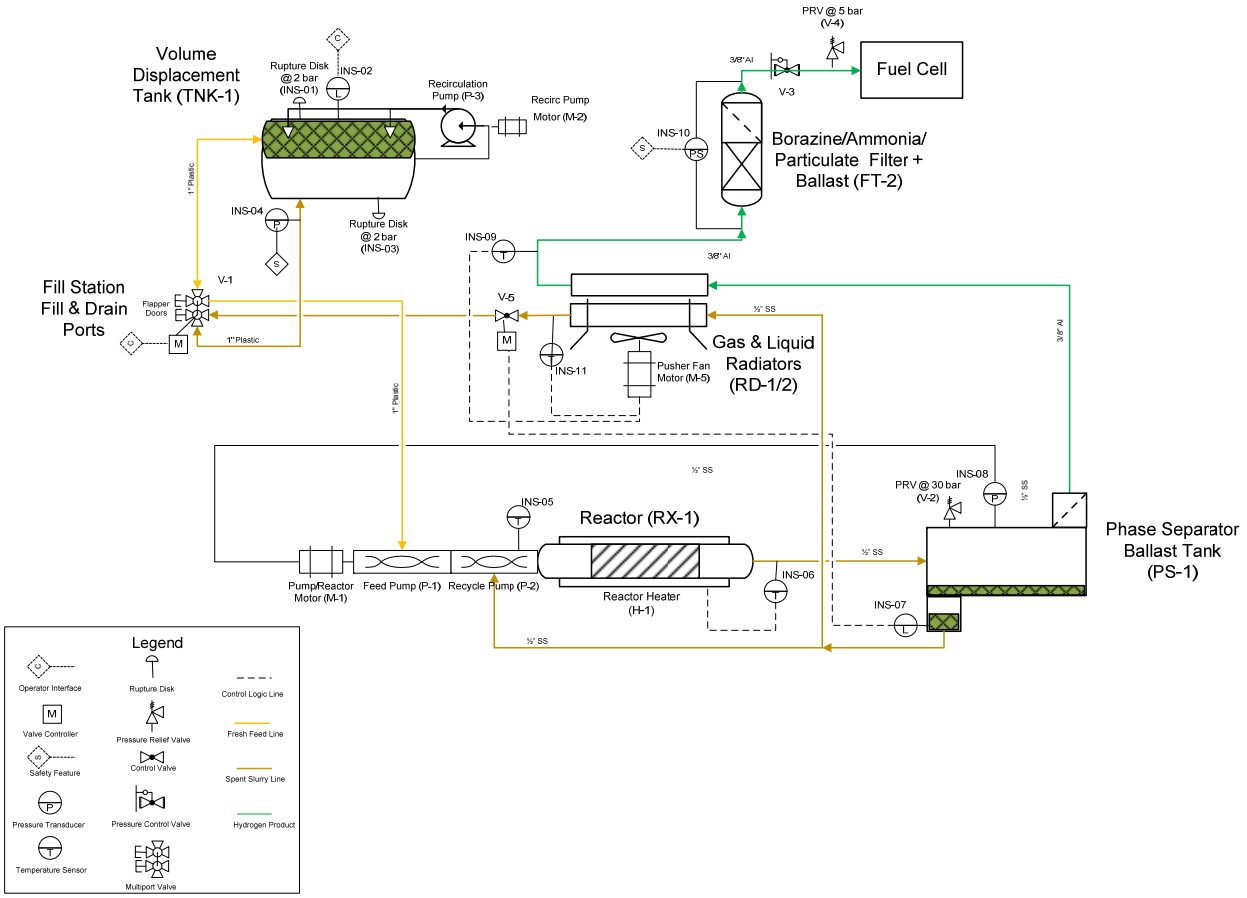

Figure 2.62. "Elevated Schmatic" of the Slurry Process Flow Diagram

2.3.8 Slurry System Component Validation

The scope of PNNL's work was to validate the radiator design, the volume-displacement tank design, and slurry flow through the system (heat exchanger, valves, tubing, pumps, etc.) at expected temperature and pressure conditions. To assist LANL, PNNL also developed a reactor for evaluating techniques that could be employed to prevent plugging during reaction. This reactor was instrumented to measure the exothermic heat produced during the reaction of AB slurry. A discussion of these tests follows.

2.3.8.1 Slurry Radiator Validation Testing

The exothermic AB reaction results in a high-temperature discharge from the reactor. This material has to be cooled prior to storage. The air-cooled finned tube heat exchanger described in Section 2.3.4 was used for validation testing. The validation approach was to heat a surrogate simulant with similar thermal

(latent heat) and rheological[8] properties capable of withstanding relatively high-temperature testing conditions. The surrogate simulant was heated, and the temperature change across the near prototypic air-cooled radiator was determined. The results of these validation tests then were compared to results from the model described in Section 2.3.5.3.

For design purposes, the discharge from the AB hydrolysis reactor was estimated to be at 525K with a flow rate range of 100 mL/min to 900 mL/min (4 to 36 kWe equivalent of hydrogen) per the modeling validation drive cycle. This discharge stream was to be cooled to 360K using forced air with an effective[9] velocity of 6 m/s (13.4 miles per hour). The cooling requirement was increased to cool a slurry flow rate of up to 1.0 L/min. The greater than maximum model demand slurry flow cooling requirement plus the use of relatively low velocity air cooling capabilities were conservative requirements for the radiator design.

The mass and volume restrictions on the heat exchanger and the relatively low simulant and cooling air velocities imposed design challenges that became additional requirements early in the review process. These requirements are listed below:

- The upper target simulant flow rate inside the cooling heat exchanger resulted in a relatively low internal average velocity and a Reynolds number (Re) of less than 50. The simulant flow was therefore in the laminar regime over the entire regime of testing conditions. To increase total material in contact with the internal surface of the heat exchanger tubing and to combat potential settling of solids, twisted-tape inserts were inserted in all straight lengths of the heat exchanger tubing.[10]
- To save on weight restrictions, lighter weight aluminum fins were selected over more conductive copper fins on the outer surface of the radiator tubing.
- System and heat exchanger tubing would remain stainless steel, and internal twisted-tape inserts also would stainless steel.
- The heat exchanger fins were positioned to maximize thermal loss, as provided by the air pusher used to simulate air flow at up to 6 m/s.

The resulting cooling heat exchanger consisted of eight 30-cm-long sections of 0.95 cm OD stainless-steel tubing with 0.79-cm-tall aluminum fins. The fins had a uniform thickness of 0.045 cm and were supplied with 4 to 5 fins per linear cm of 0.95-cm tubing. The eight sections were welded to 90° "Micro-Fit" weld fittings after the 30-cm -long sections of twisted-tape were chamfered at both ends to limit slurry plugging in the bends and then inserted. This resulted in closely spaced sections of finned tubing in a fixed parallel configuration, as illustrated in Figure 2.36. This configuration was chosen over a bulkier modular approach to minimize the overall weight of the heat exchanger.

[8] The surrogate simulant was designed to match the flowability and settling performance expected from the spent AB slurry The surrogate was therefore designed to have solids of similar average particle size and density to the spent AB, to be miscible in silicone oil, to withstand the elevated temperature and pressure testing conditions, and for the slurry to match the viscosity of the spent AB.

[9] Forced air flow was generated by mounting an 11-inch off-the-shelf pusher fan to a shroud attached perpendicularly to the heat exchanger. The average velocity of the air, measured at various locations at the discharge of the shroud at 10.3VDC, was the effective air flow (reported as velocity) available for cooling.

[10] There is a considerable body of evidence to suggest passive devises such as twisted-tape inserts would enhance heat transfer, but this use is not typical for two-phase systems consisting of liquid and solids; therefore, testing the heat exchanger performance with respect to plugging became of critical importance to the validation of the design.

An off-the-shelf DC powered automotive pusher fan was purchased to supply cooling air. The pusher fan was round and larger than the resulting rectangular cooling heat exchanger. As a result, a shroud was fabricated to support the pusher fan and to direct all the discharge air across the surface of the cooling fins. The shroud discharge area was rectangular in shape, to fit the profile of the eight parallel finned tubes.

A test loop was fabricated to validate the cooling heat exchanger by circulating a surrogate simulant (silicone oil plus polyimide solids) in an open test loop. Slurry was pumped from a feed vessel equipped with an agitator through a prototypic feed pump, check valve, three-way valve, cooling heat exchanger, and needle valve before discharging into a surge pot on a balance (Figure 2.63). Slurry was heated in the feed reservoir prior to diversion through the three-way valve and the cooling heat exchanger. The slurry then was cooled on the way to a discharge reservoir downstream of the heat exchanger. The discharge reservoir was positioned on a balance, and the change in mass was used to estimate the flow rate through the test loop. A gravity drain was used to transfer the slurry in batches from the discharge reservoir back to the feed reservoir. The model and manufacture of the prototypical equipment is shown in Table 2.34.

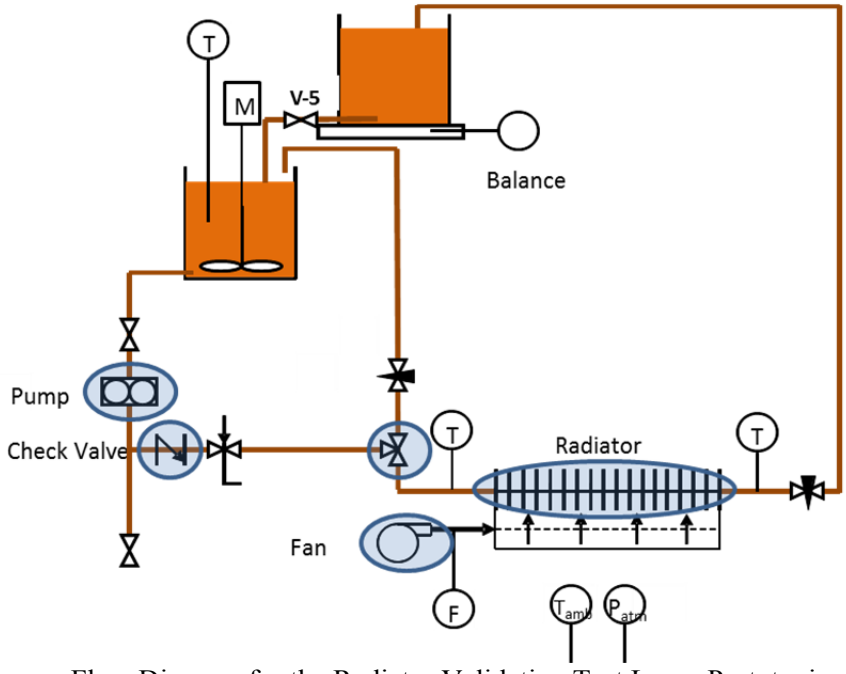

Figure 2.63. Process Flow Diagram for the Radiator Validation Test Loop. Prototypic equipment (transfer pump, check valve, three-way valve, pusher fan, and heat exchanger) highlighted in blue.

Table 2.34. Prototypical Equipment used in the Radiator Validation Test Loop

Equipment	Manufacture	Part Number	Properties
Three-way valve	Assured Automation	B33DAXV4B	⅜-inch automated valve
Check valve	Watts Wye	CVY, order code 0700530	½-inch pattern check valves
Pusher Fan	Fluidyne	FHP34211	11-inch pusher fan, 12 VDC, 9.3 amps, 1,075 cfm
Pump	Mahr	TC-1251	Round pump, 6 cc/rev, 24 V motor

Forty weight-percent polyimide (P84-N, 10 to 59 microns [10 to 90%] from Evonick Industries) in 20 cP polyphenylmethyl-siloxane (Sigma-Aldrich, AR 20) was the slurry used for the cooling heat exchanger validation testing. The slurry was selected to match the properties of the reacted product of 40 wt% AB. The simulant slurry concentration was selected because it matched the viscosity of the product: both were approximately 200 cP with a shear stress of 1 pascal. The simulant slurry had higher weight percent and volume percent solids than the AB slurry, but it bound both of these values and the two-phase system was selected to tolerate the elevated temperatures and pressures required for validation testing.

The flow loop was designed to allow the cooling heat exchanger to be heated by flowing slurry that was heated by heat tape on the validation loop tubing and feed reservoir. Once the slurry reached the appropriate testing temperature and the cooling heat exchanger was at a steady temperature, the cooling fan was started, and the flow was either discharged back into the feed vessel or discharged into a surge reservoir on the balance to determine the average slurry flow rate. The pump flow rate was varied over a range of flow rates and the temperature difference measured across the heat exchanger to obtain the cooling heat exchanger duty.

The cooling fan (an 11-inch pusher fan) performance was evaluated by measuring the air velocity (in miles per hour) at various locations on the discharge end of the fan shroud at different voltages. The voltage and current associated with air flow near 6 m/s (the air flow velocity associated with the assumed available cooling supply) was 10.3VDC and 4.9 A. This fan setting was used for subsequent cooling validation tests.

High temperatures and low-flow rates resulted in solids buildup in areas of direct heating (i.e., the location of heat tape on tubing and base of feed reservoir). In spite of these difficulties, a set of experimental data was collected, and the key parameters from this analysis are shown in Table 2.35. Steady-state temperatures within the cooling heat exchanger were achieved relatively quickly, but the heaters (heat tape) could not maintain the feed tank temperature as the cooled discharge reduced the feed temperate to lower temperatures than could be maintained by the heat tape with single-pass operation. Therefore, as the test proceeded, the inlet temperature to the cooling heat exchanger steadily decreased. The cooling heat exchanger had to be bypassed and the slurry loop reheated to bring the temperature back up to set point.

Table 2.35. Results of Cooling Heat Exchanger Loop Testing

	Mass Flow (g/min)	Pump Level (%)	Ambient T (°C)	Tin (°C)	Tout (°C)	ΔT (°C)
Day 1, Condition 1	246	25	29	160	45	114
Day 1, Condition 2	50	15	29	152	31	122
Day 2, Condition 1	119	20	29	218	35	183
Day 2, Condition 2	263	25	29	201	54	147
Day 2, Condition 3	44	16	29	232	32	200

The model calculated values were compared to the experimental values in Figure 2.48. As can be seen in the figure, the cooling heat exchanger model fits the experimental data very well.

2.3.8.2 Volume-Displacement Tank Validation Testing

The volume-displacement tank is a volume exchange tank designed to store both fresh and spent AB slurries in as small a volume as possible. The proposed design was to store both slurries in the same large tank, separated by a flexible and impermeable membrane, and to discharge one side with simultaneous charging of the other. In this way, the flow into the tank from one side of the membrane would cause the membrane to expand and discharge the contents of the other side.

The volume-displacement tank development work focused on two areas: 1) design and testing of the membrane that separates the feed and product slurries and 2) development of methods for mixing both the feed and product prior to transfer. This volume-displacement storage and mixing is designed to provide homogeneous feed slurry to the process after two weeks of inactivity.

Charging (on-loading) of fresh AB slurry (or surrogate) into the fresh side of the tank was to take the same time as the average time to fill a gasoline tank, and therefore, the transfer requirement was for feed on-loading and product off-loading to be completed in 2.9 minutes (2017 goal for 5.6 kg hydrogen equivalent).

Membrane Design

Three candidate materials for the membrane were evaluated for physical properties and chemical compatibility: nitrile, ethylene propylene diene monomer (EPDM), and Viton. The tensile strength and elongation were measured for each of these materials with no contact, 200 hours of contact, and 1000 hours of contact with fresh AB slurry at ambient temperature. In addition, the material was measured for weight and dimensional changes. The results of these tests are shown in Figure 2.64 to Figure 2.66. The Viton has a high tensile strength, but has poorer elongation than the other materials. None of the materials showed significant changes in tensile strength of elongation over time. The EPDM however, showed significant weight loss over time in the fresh AB. Based on the results of these compatibility tests, the best material appeared to be nitrile, which showed only a slight decrease in weight over time and maintained good strength and elongation after 1000 hours immerged in the fresh AB silicone oil mixture.

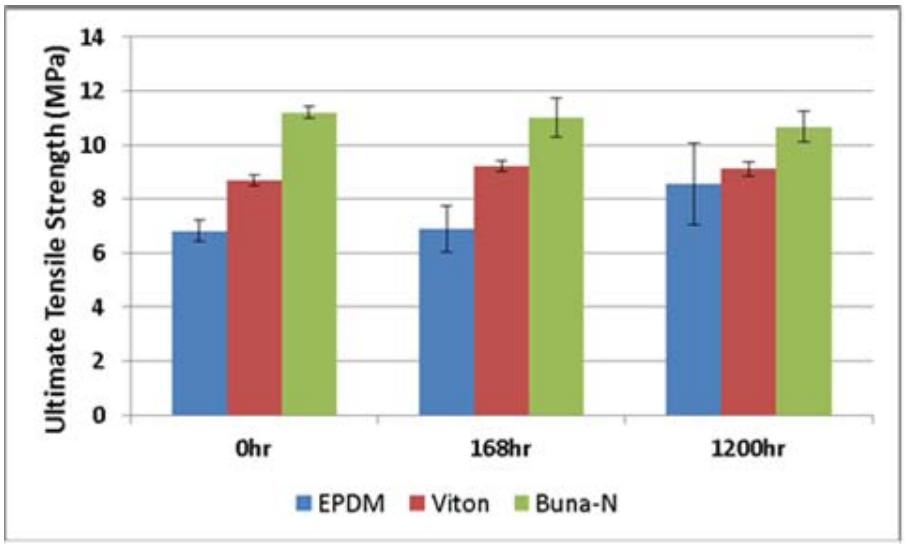

Figure 2.64. Membrane Material Tensile Strength Change in Fresh Ammonia Borane with Silicone Oil

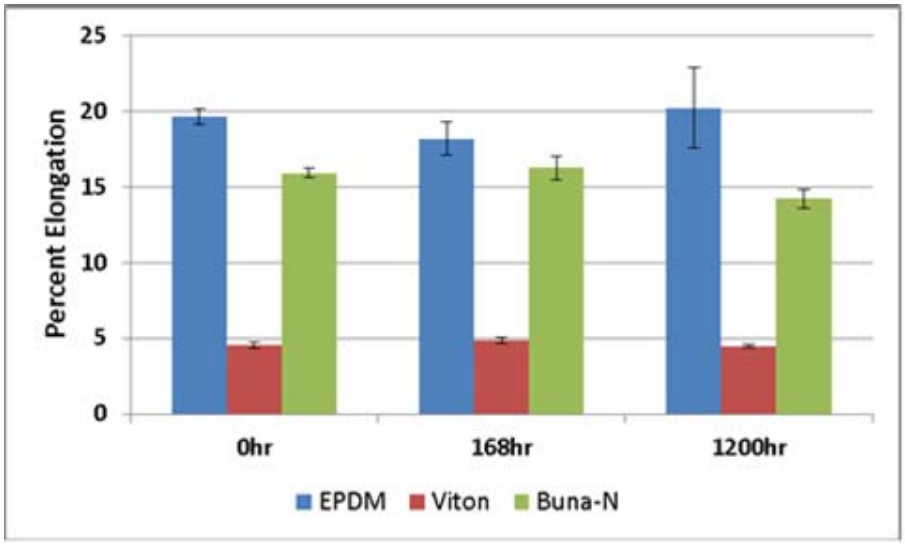

Figure 2.65. Membrane Material Elongation Change in Fresh AB with Silicone Oil

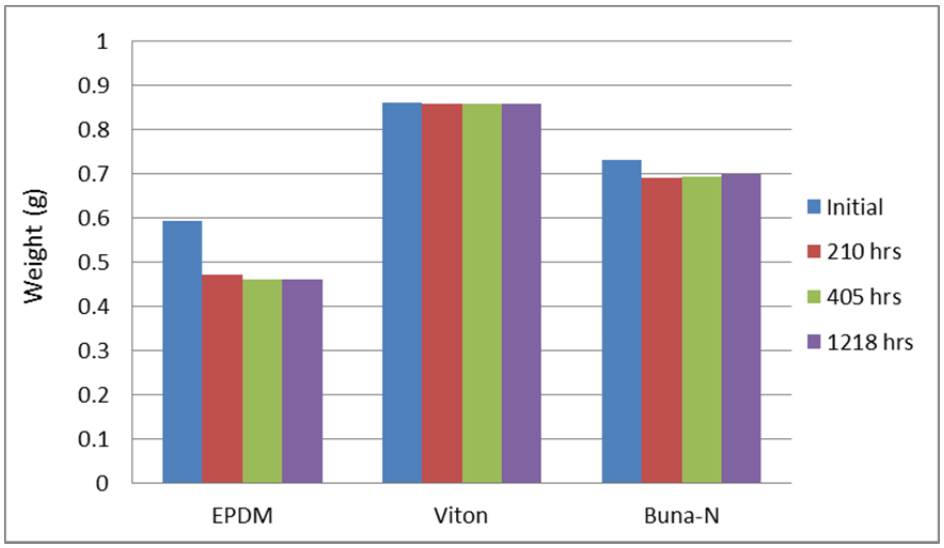

Figure 2.66. Membrane Material Compatibility Testing Weight Change from Fresh AB with Silicone Oil

To minimize the amount of stretching required of the membrane, a silicone membrane was fabricated with pleats to allow it to expand without significant stretching, thus improving its life

Figure 2.67). The membranes were evaluated in a 2-L polymethyl methacrylate volume-displacement tank with both water and air as the motive fluid. The results indicated that a pleated membrane will work and very low pressures would be required to move it from fully expanded on one side to the other (~1.5 psid).

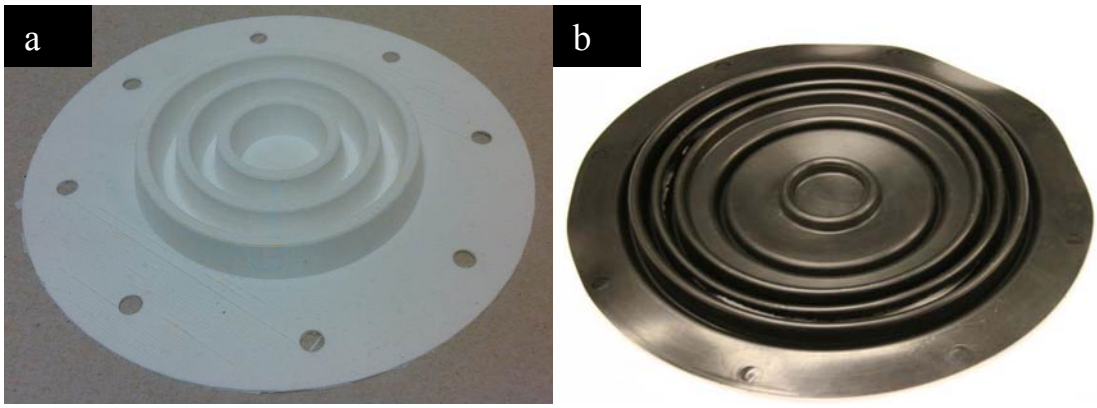

Figure 2.67. Volume-Displacement Pleated Test Membranes: 10-cm Proof-of-Concept Membrane Illustrated in (a) and Large Scale and 30-cm Diameter Illustrated in (b)

Select small-scale proof-of-concept displacement test results are illustrated in Figure 2.68. A 10-cm diameter acrylic test chamber was fabricated to test slurry storage and volume displacement. Two equal volume sections with flanges were bolted together with the test membrane inserted between the center flanges. Ports in the blank flanges were used to on-load or off-load test fluids (air, water, silicone oil, surrogate simulants, etc.). In photograph (a), both chambers were open to the atmosphere and no elongation of the membrane was observed. In photograph (b) the upper chamber was pressurized to ~1.5 psig and all the pleats were unfolded, but elongation of the sections was minimal. In photograph (c), the pressure was increased to ~2.5 psig and all the pleats were unfolded, and the sections elongated to the extent that the membrane filled the cavity of the bottom chamber. The pressure in the upper chamber was released and the bottom chamber pressurized to ~1.5 psig to demonstrate identical membrane performance in the opposite direction.

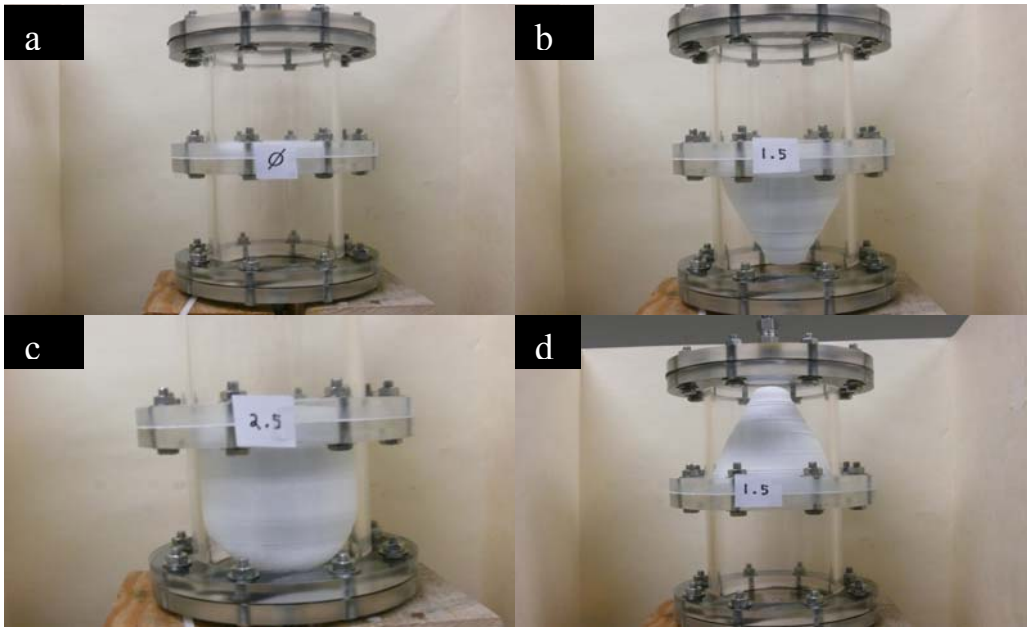

Figure 2.68. Scoping Studies for the Pleated Membrane in the Volume-Displacement Tank

Scoping Studies for Slurry Mixing

The proposed volume-displacement tank was designed to store and transfer feed slurries (to the hydrolysis reactor) and product (from vehicle) separated by a flexible and impermeable membrane. Equally significant was the re-suspension of solids or local (short-term) suspension of high solids concentration conglomerates prior to transfer.

The feed material requires homogenization prior to transfer to the hydrolysis reactor, especially when the vehicle has been parked for an extended period of time and the feed slurry has been sitting idle. The feed material (fresh AB in silicone oil) naturally separates into a two-phase system of very low solids concentration silicone oil on the bottom and a high solids concentration flocculation product on top. Attempts to pump the separated system resulted in no transfer of material from the flocculation phase and the transfer of the oil (carrier fluid) from the bottom liquid phase, leaving the less dense solids matrix behind.

Small-scale scoping tests were performed to determine the most promising methods for remixing the feed and product materials. A 50:50 ratio of fresh AB/spent AB slurry and simulants for both fresh and spent AB were evaluated. The simulant for fresh AB was polyethylene powder (Microthene G, MN71120) in a mixture of 68%/32% glycerin and water. This simulant had a similar difference in density and was found to have a yield stress of 100 Pa as compared to 50 Pa for the actual fresh AB. The simulant for the spent AB was polyimide powder (P84-N, 10 to 59 microns) in silicone oil. It did not have as high a density difference as the actual spent AB slurry, but post-settling analysis resulted in a yield stress of 20,000 Pa after sitting over a weekend as compared to 5000 Pa for the spent AB, thus it was considered bounding.

Small-scale tests were performed using a wide range of possible mixing techniques for the material after settling. These techniques included localized ultrasound (tip inserted into test beaker), ultrasound bath, both low- and high-frequency vibration, a flexible internal expansion chamber, stirring with an agitator, extrusion with the membrane, and a perforated plate driven through the fluid column.

Ultrasound. A variable-frequency, flat-tip ultrasonic probe was inserted into test media after allowing the test slurry to settle in the test container for up to a week. None of the test media mixed to the extent required (i.e., homogenization for fresh simulant and re-suspension of the bottoms for spent). The 50:50 mixture of fresh and spent AB and the polyimide slurry test samples demonstrated limited mixing, but only in close proximity to the probe tip. Frequency adjustments affected localized mixing with higher frequencies resulting in excessive localized heating that did not dissipate due to the lack of fluid flow and resulted in significant temperature stratification within the test containers. The ultrasonic probe had no mixing effect on the fresh surrogate (polyethylene in glycerin/water). The probe was tested in the flocculate and fluid phases and in the two-phase interphase. Material was observed moving near the probe surface, but not sufficiently for mixing to take place.

Test containers were placed in water-filled bench-top ultrasonic baths to evaluate mixing effectiveness. Enhanced separation was observed with the fresh surrogate and no apparent change was observed for the spent surrogate. We determined that the ultrasonic methods would require an extensive slurry volume to probe surface area ratio with significant mass and volume (support equipment) requirements to adequately mix the slurries. No further ultrasonic testing was performed.

Vibration. Vibration table tests were performed on both actual materials and simulants using high-frequency/low-amplitude and low-frequency/high-amplitude tables. The high-frequency tests were performed on a re-purposed bench-top solids transfer table. Test slurries were allowed to settle for up to a week and secured to the test bed in an upright orientation to maintain the container orientation and to keep

the containers from moving along the transfer bed. Low-frequency tests were performed on a 2 × 2-inch VDC driven vibrator with an insert attached to secure the test containers. These experiments demonstrated that vibration increased the phase separation rather than providing mixing. No further vibration testing was performed.

Flexible Expansion Chamber. A flexible membrane was secured to the bottom of an acrylic test tank, between the test slurry and the blank flange. A port in the flange allowed the flexible membrane to be inflated and deflated from an external air supply. Test slurry was allowed to settle on the membrane for up to a week before the membrane was pulsed with rapid slugs of low-pressure air. The result was that the entire slug of settled polyimide slurry moved up and down without re-suspension of the high solids concentration layer at the bottom. No further testing was performed using a flexible expansion chamber.

Extrusion. Removal of settled product slurry does not require homogeneous re-suspension of the solids. Of greater value is the removal of a significant fraction of the material in the product chamber within the same time frame allotted for feed on-loading. In an effort to focus product discharge requirements, polyimide surrogate slurry was allowed to settle in the test tank for up to a week and a flexible Buna-N membrane was used to drive (from above) the material through a port in the bottom. The test objectives were to establish the pressure range needed to extrude the material, and very importantly, to determine the amount of material extruded out of the tank and the amount of solids retained. The test demonstrated that a large fraction of the slurry could be removed in this way, but the approach was relatively slow as the undisturbed paste (high solids concentration bottoms) extruded from the bottom of the tank.

Agitators. Stirring with several mixer blade configurations was performed on simulant materials. The results were strongly dependent on the shear strength of the high solids concentration bottom layers; therefore, agitation was most effective, in terms of mixing power and impeller size, on simulants with lowest shear strength. The best mixing results were achieved with fresh AB simulants, although high impeller velocities were required to drive the fluid phase upwards into the flocculated upper solids layer. Additional investigations into optimal impeller designs would be required for optimization, but impellers would require a high-angle pitch to drive the fluid phase up rather than out as the flocculate matrix required significant upwelling to achieve sufficient homogenization.

The spent AB surrogate, with a yield stress of 20,000 Pa after several days of settling demonstrated the greatest power requirement for re-suspension. The slurry was allowed to settle on and around the test impellers located at the bottom of the test container and the mixer initiated after several days. This test condition resulted in excessive torque required to move the blade(s). None of the tested blades were effective at starting in undisturbed high solids concentration layers. No further testing of agitators was performed.

Perforated Press. The most promising scoping test results for feed simulant homogenization and product simulant re-suspension at the bottom of the test container were achieved using a perforated plate. A perforated plate made of aluminum is cut to the same diameter (and geometry) as the test container inside diameter, attached to a drive shaft, and then pressed through the test media. The pressing action was always in the vertical direction, perpendicular to the surface layer, because this was the shortest path of travel to mechanically compress the separated layers. A press cycle was defined as the travel from one end of the fluid column, through the entire fluid column, and back to the starting location.

In the case of feed simulant, the most practical starting location was above the flocculated solids layer, resulting in the press driving the solids matrix into the silicone oil fluid below. This method was highly effective at mixing the solids and liquid phases with a relatively low number of press cycles. By driving the lower density solids into the higher density fluid an unstable condition is forced on the separated phases that respond with highly turbulent flow jetting through the perforation and up the space between

the outer edge of the plate and the test container. The scoping test conditions were sufficient to re-suspend the separated feed simulant layers in <10 press cycles.

In the case of product simulant, the perforated-plate press was placed on the bottom of the test container with fully suspended polyimide solids in silicone oil. The solids were allowed to settle on the device for several days before driving the press through the concentration gradient. The initial action was to pull the press through the slurry and to repeat the cycle until the high solids concentration layer on the bottom was sufficiently disturbed that the material could be poured (with suspended conglomerates of high solids) with minimal solids residue remaining in the container. This investigation resulted in sufficient mixing within <10 press cycles, and the methodology was selected for larger scale testing.

Jet Mixing. Because feed and/or product material transfer pumps were design components required for AB slurry transfer, a jet-mixing methodology taking advantage of the existing capabilities was tested. Slurry material was pumped from the settled storage chamber and discharged at selected location and orientations depending on the material type targeted. For feed surrogate slurry testing, bottom layer low solids concentration silicone oil was recirculated and jetted onto the flocculate solids layer using different jet geometries. Mixing effectiveness was enhanced with increased flow (momentum) of the jet fluid. Relatively large volumes were required to drive the solids into the liquid layer. For the product surrogate test, the upper- to mid-height slurry was recirculated and jetted into the bottom layer. Small profile jets, with significant flow and time were successful in clearing large areas of heavily caked bottom layers.

A summary of the results of the tank mixing scoping studies is shown in Table 2.36. Based on the results of the scoping tests, it was determined than only the jet-mixing and perforated-plate approaches should be evaluated further on a larger scale.

Table 2.36. Summary of Volume-Displacement Tank Mixing Scoping Testing Results

Scoping Test	Fresh AB/ Fresh AB surrogate (polyethylene in water/glycerin)	Spent AB/ Spent AB surrogate (polyimide in silicone oil)	Large Scale Test (Y/N)
Ultrasound (probe)	Not mix separated layers Susceptible to high-temperature zones	Localized re-suspension of solids Susceptible to high-temperature zones	N
Vibration	No mixing Enhanced separation	No mixing	N
Expansion Chamber	No mixing	No mixing	N
Extrusion	--------	Slow Effectiveness dependent on shear strength of high solids layer	Y*
Agitator/Mixer blade	Requires high velocity and turbulent upwelling of liquid phase	High-torque motor required	N
Tea Press	Worked well	Worked well[a]	Y
Jet Mixing	Adequate re-suspension of solids into liquid phase	Adequate re-suspension of high solids bottom layer	Y

Y* Selected for large-scale testing in conjunction with other methods. Not considered as a standalone method.
(a) Worked well in terms of re-suspension of the bottom layer sufficient to pour contents out of container. Homogeneous re-suspension was not required.

Large-Scale Volume Exchange Tank Mixing Studies

A quarter-scale (19 L) volume-displacement tank was designed for final validation testing of mixing after settling and transfer of feed and product materials. The volume-displacement tank design goals were:

- For mixing of fresh AB surrogate (polyethylene in glycerin/water), demonstrate complete homogenization in less than 2 minutes.
- For mixing of spent AB surrogate (polyimide in silicone oil), demonstrate fluidization and draining of simulant in less than 2 minutes.
- Transfer fresh AB surrogate into the storage tank with a flow rate commensurate to the target of 76 L in 2.9 minutes.
- Transfer spent AB surrogate out of the storage tank using the feed on-loading transfer system and thus transfer at the same flow rate, with >90% of material removed.

A cylindrical acrylic 19-L validation platform with two chambers of equal volume (~9.5 L) was fabricated and outfitted with multiple jet nozzles, instruments, and inlet and outlet ports. The tank had an inner diameter of 24 cm, a height (including offset feet) of ~58 cm and a conical bottom with a pitch of 35.5°. The sections and flat top plate were assembled with flanges that allowed test membranes to be secured between the two chambers. The chambers were assembled and fittings attached as indicated in Figure 2.69.

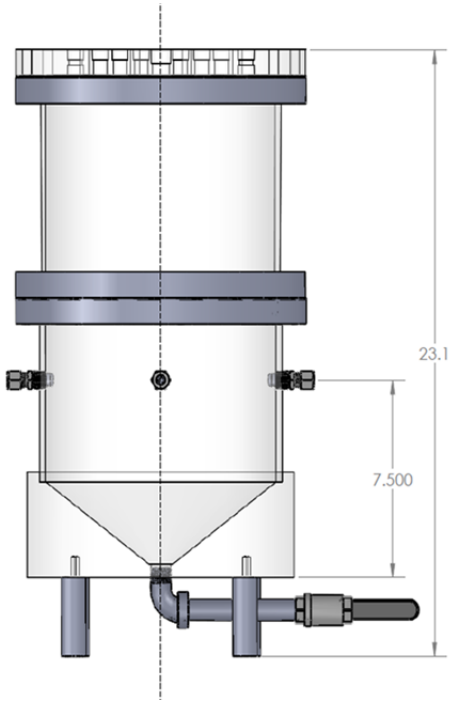

Figure 2.69. Side View of the Quarter-Scale Volume Displacment Tank

The upper section was designed to receive the fresh AB surrogate slurry that separated into a two-phase system with a low solids fluid bottom layer and the high solids flocculate upper layer. The upper chamber was cylindrical with flat ends and multiple (nine) ports in the upper blank flange for the transfer of material, for jetting onto the test slurry, and for placing pressure gauges.

The lower chamber was designed to receive the spent AB surrogate in which the solids are of greater density than the silicone oil and the solids settle in high solids concentration layers on the bottom surfaces. The bottom of the lower chamber was designed with a conical bottom to facilitate extrusion and/or transfer of simulant out of the chamber while minimizing the amount residual material. Four jet nozzles were mounted midway up the sides of the cylindrical section of the chamber. The nozzles were fanned out and directed down along the inner surface with the intent of flushing the bottom surface all way down to the drain port.

A conical perforated press was fabricated to be inserted into the bottom chamber with the push handle inserted through the discharge port at the end of the cone and secured with a rubber ferrule compression fitting. A corresponding, but flat, perforated press was fabricated for the upper chamber to be used with fresh AB surrogate testing.

Fresh AB Surrogate Testing in the Upper Chamber. The upper chamber testing was divided into two major testing objectives—mixing the slurry after settling by jetting and perforated-plate pressing and transferring homogeneous slurry within the required time constraint.

The test chamber was assembled with the flat nitrile membrane installed between the two chambers and six jet nozzles plumbed to the upper blank flange. The jet nozzles were downstream of the recirculation manifold and downstream of a recirculation diaphragm pump. The test chamber was charged with ~9.5 L of test slurry, and the media was allowed to settle for ~24 hours. The glycerin/water liquid was suctioned from the bottom of the test chamber and jetted onto the upper flocculate layer. Two jet nozzles designs were investigated—conical and focused (solid stream). The jetted streams were able to mix locally in vertical columns of influence, but the method was not effective at mixing the entire test volume.

The same charge of fresh AB surrogate was allowed to settle for ~24 hours prior to the perforated-plate test, and the recirculation plumbing and blank flange with jet nozzles were removed to expose the upper surface of the slurry for insertion of the perforated-plate press. The stroke length was limited to the depth of the membrane, and the stroke velocity (2-in./s) was approximated to match the travel of a typical linear actuator. The perforated-plate press was cycled through the simulant, from the top-down, and samples were collected after five and eight cycles to evaluate mixing effectiveness. A standard sample of homogeneous slurry also was collected. All samples were allowed to settle, and the relative effectiveness of mixing gauged by the fraction of solids relative to the homogeneous standard.

Figure 2.70 illustrates the mixing of lower density solids into the low solids concentration liquid phase below. In image (A) the flat perforated press is observed driving into the solids, while compressing most of the flocculate layer into the fluid layer and causing a fraction of the solids to be driven up through the gap between the press and the inside surface of the slurry. Within ~5 cm of travel, material is displaced from below the press and driven up and spilled over the upper surface of the plate (B). In image (D), the solids layer is seen to be driven by a significant volume of the fluid layer displaced from below, and the resulting “roll” of a significant fraction of the layers is demonstrated in the side view in image (C). The turbulent fluid flow up the sides and through the perforations continues throughout the full perforated-plate press cycle as the motion of the press continues to drive and displace fluid. By the end of the first cycle, significant portions of the layers have been inverted.

The extent to which the solids layer had been fluidized is illustrated in images (E) through (G) of Figure 2.70. In image (E) the solids holdup after the first full downward and upward cycle is compared to the holdup after five full cycles (F) and eight full cycles (G). The amount of holdup decreases as the cycled number increases, thus correlating the relative amount of solids fluidized and therefore re-suspended in the fluid.

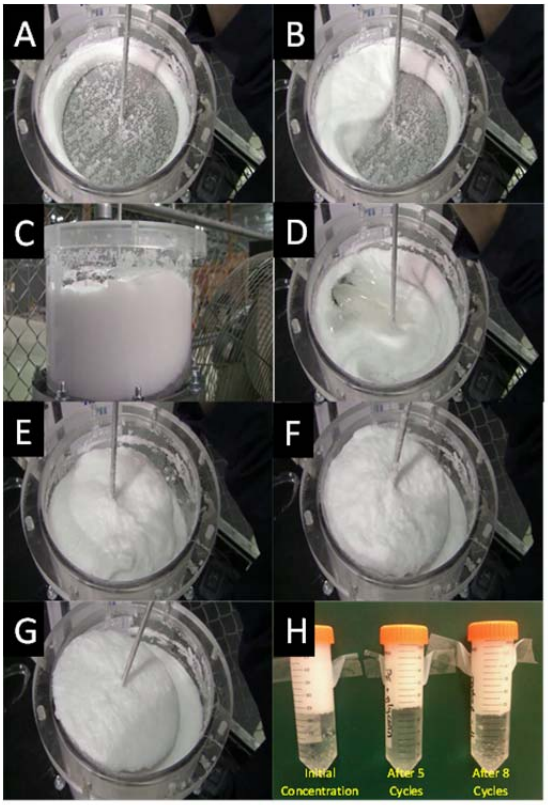

Figure 2.70. Perforated-Plate Mixing Evaluation with Quarter-Scale Volume-Displacement Tank

The samples collected at five cycles and eight cycles were allowed to settle with a sample of homogeneous surrogate slurry (control). The fraction of separated solids in the eight-cycle sample closely matched the homogeneous control and the fraction after five cycles was slightly less. Eight cycles were sufficient for homogeneous mixing of fresh AB surrogate at this scale and configuration.

Spent AB Surrogate Testing in the Lower Chamber. The lower test chamber, designed for spent AB simulant testing, was assembled with four downward facing fan-shaped jet streams designed to spray low solids concentration slurry along the inside surfaces of the test chamber. The objective of this configuration was to fluidize the high solids concentration layer settled on the bottom of the chamber. The nozzle tips were located at half the height of the straight walls of the cylindrical section above the conical bottom. Jetting with a relatively high recirculation flow rate had good sweeping of the surface along the cylindrical wall and over much of the conical area. The sweeping action was effective at fluidizing the solids layer after 60 seconds of recirculation flow and >98% of the slurry (9.5-L test batch) was discharged in 40 seconds by filling the upper chamber with water.

The second fluidization and discharge test of the spent AB simulant was a combination of cycled perforated-plate press mixing and membrane extrusion. A conical perforated-plate press was fabricated and inserted through a modified discharge port, enabling the shaft of the press to pass through a compression fitting and modified polytetrafluoroethylene gland such that the press could be actuated (up and down) and the slurry could be drained through the same port without leaking around the press shaft. The entire test assembly with test slurry contents was positioned on a balance to determine the maximum mass force required to drive the press through the settle simulant.

Spent AB surrogate was allowed to settle on the press and the bottom of the test chamber for ~64 hours before the perforated-plate press was cycled (upward and then downward) eight times in 30 seconds, followed by filling of the upper chamber to discharge the contents of the bottom chamber. The perforated-plate press was cycled without extending beyond the height of the membrane for eight full cycles while recording the weight readout on the balance. The highest mass recording was 7 kg.

After eight perforated-plate press cycles, the press was secured the discharge valve opened and drive liquid was added to the top chamber at a maximum of 10 psig, causing the bottom test simulant to be discharged. More than 97% of the 9.5 L test volume was discharged in 70 seconds. Figure 2.71 illustrates the test setup prior to solids fluidization in (image A), water fill into the upper chamber after eight press cycles (image B), and the extended membrane into the lower chamber cavity at the end of the test simulant discharge (image C).

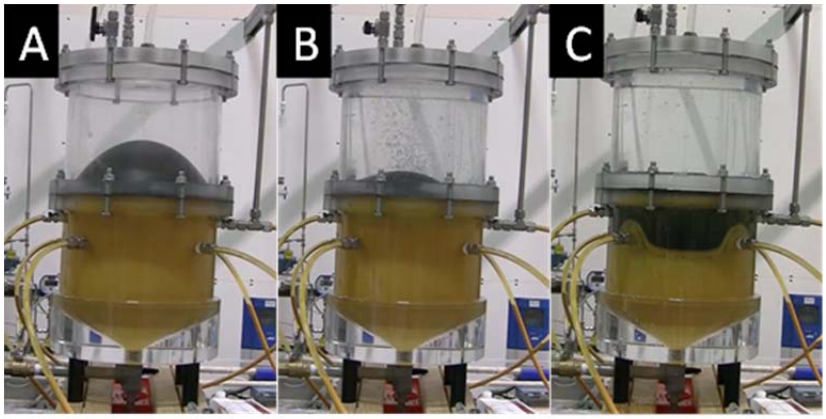

Figure 2.71. Spent AB Surrogate Mixing Results after Using the Perforated Plate to Fluidize Solids and Discharging with the Flexible Separation Membrane. Image (A) illustrates the setup prior to solids fluidization, (B) water fill into upper chamber after eight perforated-plate cycles, and (C) the extended membrane post discharge.

The test configuration was optimized for the 19 L scaled test condition and successfully demonstrated the fluidization and discharge of 9.5 L in 1.7 minutes. At full scale (i.e., a 76 liter tank and fill rate of 2.5 minutes), a force of 23 kg would be required to drive the perforated-plate press, and with larger discharge ports (e.g., 1 inch instead of ¾ inch), 76 L could be removed within the specified requirement.

2.3.8.3 Slurry Settling and Pumping Studies

The purpose of the flow-through system validation effort was to evaluate the prototypic components and to report on the performance of the flow system with respect to fouling and plugging because of the liquid-solid system operating over a large range of fluid velocities, temperatures and settling periods. The test loop that was used for the radiator validation study also was used to evaluate slurry settling and flowability during pumping. The prototypical components shown in Figure 2.63 were used for this test loop.

AB slurries (AB solids in silicone oil), both fresh and spent, were not available in sufficient quantities for component validation testing so surrogate simulants were needed. As a result, surrogate materials were used. Fresh AB in silicone oil was simulated with polyethylene beads in a water-glycerin (68 wt% glycerin) mixture. The polyethylene solids were Microthene G, MN71120, with a density of 0.915 g/cc and irregular shapes with an average particle size of U.S. 35 screen mesh. Testing simulants had solids

fractions from 35 to 50 wt%. The spent AB was simulated using polyimide solids at fractions ranging from 35 to 40 wt% depending on the level of conservatism required. Table 2.**37** summarizes the slurry properties of the AB slurries and of the corresponding surrogate simulants.

Table 2.37. AB Slurry Properties with Corresponding Surrogate Properties

	AB Material		Simulant	
	Fresh AB	Spent AB	Polyethylene	Polyimide
Slurrying Agent	Silicone Oil		Water/Glycerin	Silicone Oil
Mass Fraction (%)	40%	36.1%	40.3%	32.5%
Volume Fraction (%)	46.3%	24.8%	46.4%	24.8%
Solids Density (g/cc)	0.74	1.64	0.92	1.4
Density of Slurrying Agent (g/cc)	0.96	0.96	1.17	0.96
Density Difference (g/cc)	0.22	0.68	0.25	0.44
Yield Stress of Settled or Flocculated Material (Pa)	50	5000	130	20000

Experimental work was performed to evaluate the ability to pump the CHS materials after a period of settling, at cold conditions, and with key prototypical components in the slurry test loop. This testing was performed with both simulants and actual chemical hydrogen materials. The heat exchanger was encased in a dry ice bath, and the contents in the loop were cooled to approximately −20°C (the DOE target minimum operating temperature). Once this temperature was reached, the pump was restarted, and the slurry was pumped through the flow loop until the entire system was ≤-20°C. The results of these tests showed that both simulants and the spent AB were pumpable at <-20°C.

Table 2.38 summarizes the slurries evaluated and the tests performed. The gear pump was evaluated for flow rate and pressure as a function of temperature using both fresh and spent AB surrogate simulants. The pump was able to dispense the slurries at the flow rates and pressures required and even demonstrated good performance at temperatures higher than recommended. At higher temperature (>150°C), the performance of the pump declined, and the flow was reduced because of an increase in air in the loop. The pump housing components were optimized for ambient conditions, and we postulated that different expansions within the tight tolerance components may have contributed to suction of air into the pump housing. The pump was inspected after the cooling heat exchanger validation testing activities and function testing. The housing was disassembled and inspected for fouling and wear. This inspection indicated minimal wear of the gears on the housing endplate.

The slurries were allowed to settle in the flow loop (tubing and all components) for 3 hours, followed by a test overnight (18 hours), and finally over a weekend (>70 hours). In all cases, the pump was able to restart, and the pumpability of the slurry in the system was verified. The only area of difficulty in the pumpability tests was that the pump was not capable of pumping at very low-flow rates and high pressures (irrespective of the material processed). In a comparison between the simulant of spent AB (polyimide) and the actual spent AB material, flowability was more challenging with the simulant after restart than the spent AB. The polyimide material experienced some slugging initially upon pump restart, especially on the pump suction side.

Table 2.38. Slurries Evaluated with the Settling and Pumping Study

Solid Material	Solids Loading (wt%)	Slurrying Agent	Solid Density (g/cc)	Particle Size (μm)	Tests Performed
Simulants					
Polyethylene (fresh AB simulant)	50	Silicone oil (50 cP polydimethylsiloxane)	0.92	5–50	Pumpability Settling (70 hrs) Cold Start
Polyimide (spent AB simulant)	40	Silicone oil (20 cP polyphenylmethyl-siloxane	1.4	10–59	Hot Operation Pumpability Settling (100 hrs) Cold Start
Ammonia Borane					
Fresh AB (Weylchem)	20 & 35	Silicone oil (20 cP polyphenylmethyl-siloxane	0.74	1–1,000	Pumpability[(a)] Settling (3 hrs)
Spent AB (Weylchem)	40		1.6	NA	Pumpability Settling (70 hrs) Cold Start

(a) Pumpability was determined with a peristaltic pump because the gear pump could not pump fresh AB.

In contrast to the positive results obtained with the simulants and spent AB, the fresh AB developed at both 20 and 35 wt% was not pumpable with the Mahr pump. Ammonia borane slurry was compressed inside the gears of the pump, forming a solid piece that could not easily be dislodged within the teeth of the gears (see Figure 2.72). This buildup eventually prevented the gears from turning and stopped the pump. Changing to lower initial concentration or the pump speed did not remedy the problem. Testing with a peristaltic pump also identified another problem. With tubing sized at 0.32-cm inner diameter, the AB formed a plug downstream of the pump inside the tubing resulting in system stoppage. During subsequent tests with larger tubing, elbows, bends, and even a needle valve, these plugging problems did not reoccur, but there does appear to be a limit on the diameter of constrictions (~0.32 cm) that will not create plugging with the fresh AB. A short settling test with fresh AB did not produce any significant plugging problems; however, further testing is required to address the pumping and plugging issues with fresh AB.

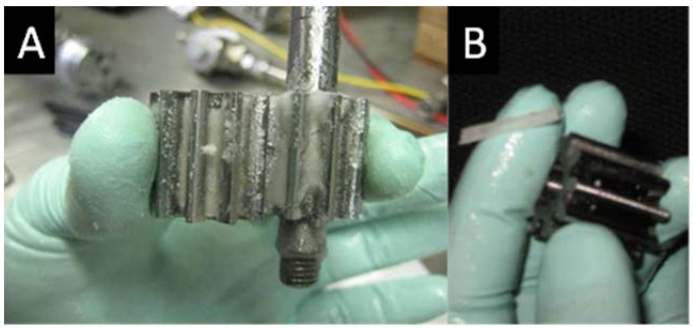

Figure 2.72. Slivers of Fresh Ammonia Borane Solids Compressed by the Interlocked Gears of the Mahr Gear Pump Caused the Pump to Stall

2.3.8.4 Reactor Testing

Reactor testing was performed using a stirred plug-flow reactor. The purpose of this testing was to identify and quantify the temperature increase as a result of the exothermic reaction. The process flow diagram is shown in Figure 2.73. Fresh AB slurry was added to the feed vessel (nominally 180 to 200 mL was required per run). The feed vessel was typically a large 200 mL syringe, as the most

consistent metering pump for driving the fresh AB slurry into the reactor was a modified syringe pump positioned vertically directly above the reactor inlet. The target flow rate of the AB slurry in the reactor was 15 mL/min. This flow rate was maintained for all thermal profile tests.

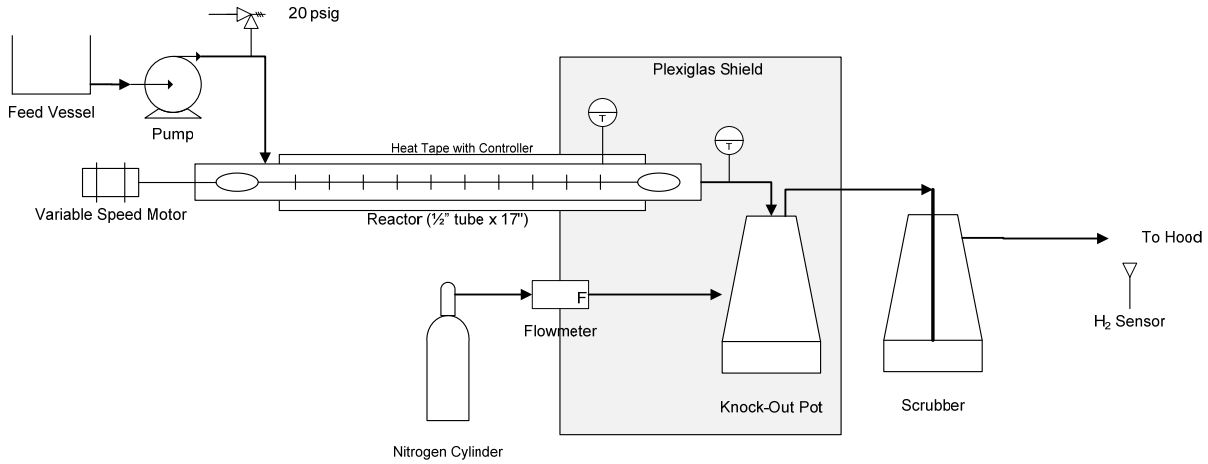

Figure 2.73. Stirred Plug-Flow Reactor Test Stand Process Flow Diagram

The reactor was a 1.27-cm stainless-steel tube with a 0.05-cm wall and an overall length of 43 cm, including the inlet and stirrer drive line compression assemblies. A stirrer was inserted along the full length of the reactor, such that the material entering the plug-flow reactor was stirred from the point of entry to the point of exit. The stirrer was attached to a variable speed motor that was used to slowly increase the stirrer speed in revolutions per minute during heating and to react the AB at ~100 rpm.

The product discharged from the reactor into a glass knockout pot where the gases and slurry products were separated. A relatively low flow of nitrogen gas (14 to 25 slpm) was supplied to the hydrogen, and to provide a carrier fluid to drive the gaseous products to the scrubber. The off-gas products were passed through a diffuser submerged in silicone oil in the scrubber container. Impurities were removed and the hydrogen gas was vented into the back of the hood near the vent port.

The stirred reactor, which was 43 cm long, was designed to heat the AB slurry from ambient temperature to an elevated temperature (measurable parameter) slightly greater than the energy required to initiate the exothermic hydrogen gas release. Heat tape was installed along the final 29 cm. of the external reactor surface, leaving about 10 cm of reactor without heating between the inlet and the edge of the heat tape (see Figure 2.74). Excessive heating of the reactor by the heat tape was avoided so internal thermal changes resulting from reaction thermodynamics could be differentiated from the hot initiation temperature conditions. Ten internal fast-response thermocouples were inserted through the reactor wall and located near the reactor inner surface in a straight line along the length of the heating zone without interfering with the stirrer (see Figure 2.74). The thermocouple tips were secured 2 to 3mm into the bottom of the reactor tube, deep enough to be submerged in the test slurry, with high-temperature epoxy adhesive. Three additional thermocouples were placed on the outside of the reactor—"FV" near the slurry inlet, "Hin" about midway along the length of the reactor, and "Hout" 2.5 cm from the discharge. The heat tape controller thermocouple was placed adjacent to "Hin" (midway along the full length of the reactor). The heat tape and thermocouples were insulated to protect operators from hot surfaces.

The stirrer diameter was fabricated to fit and was slightly smaller than the inside diameter of the reactor. The stirrer blades were designed without pitch to provide a surface cleaning sweeping action as the blade rotated and, therefore, did not impart motive force on the test material. The metering pump was the primary driver for the transfer of material into and through the reactor.

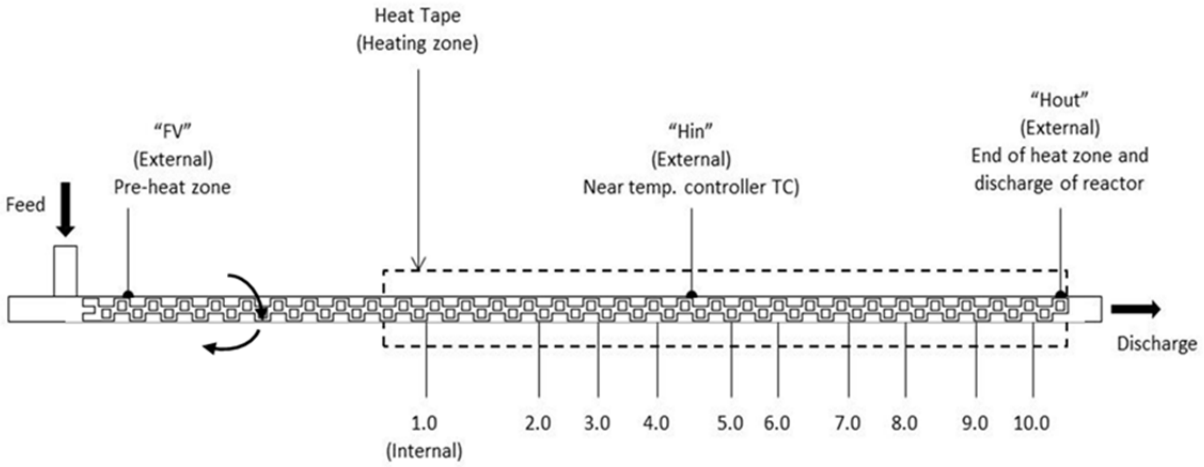

Figure 2.74. Stirred Plug-Flow Reactor Thermocouple Placement

A 50:50 wt% spent AB:fresh AB slurry with~50 wt% AB solids as tested with this reactor. The carrier fluid was 20-cP silicone oil. A test batch of ~140 mL of 50:50 wt% spent:fresh AB slurry was successfully de-hydrogenated with a slurry feed rate of 15 mL/min and a pre-feed steady reactor temperature of 170°C (as measured by the controller thermocouple on the exterior surface of the reactor). An increase in temperature (exotherm) was observed on the external thermocouple located at the discharge of the reactor and on the last five internal thermocouples (TC10 through TC14). The test slurry was fed at ambient temperature and upstream internal thermocouples (TC05 through TC09) predictably decreased in temperature, with the change in temperature decreasing as the test media traveled along the length of the heated reactor. Figure 2.75 illustrates the thermal profiles of the 10 internal thermocouples with TC05 at the beginning of the heating zone and TC14 at the end of the heating zone and ~2.5 cm from the reactor outlet.

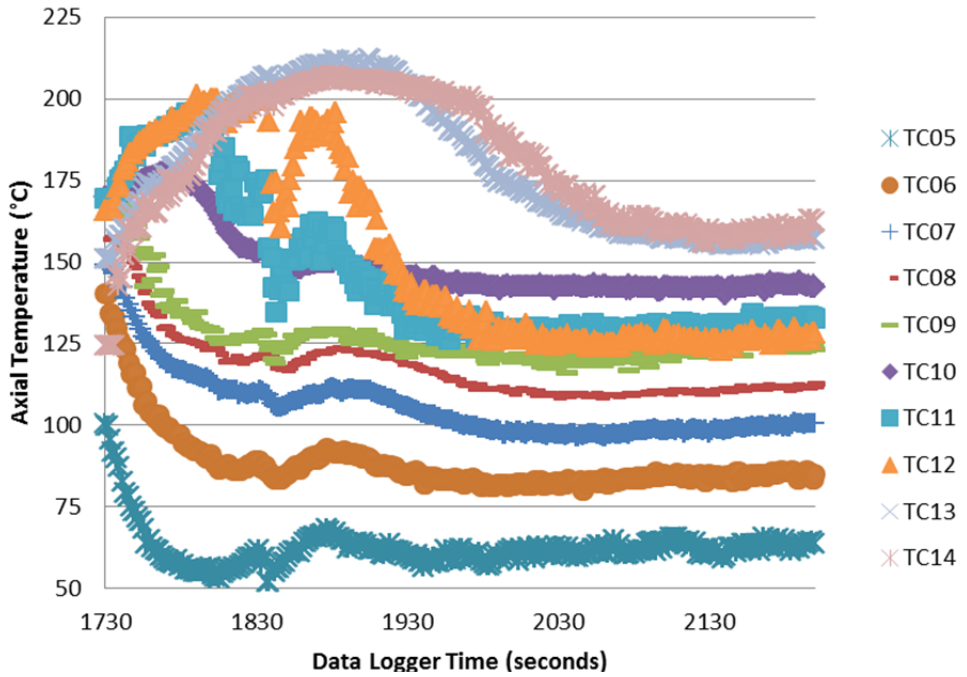

Figure 2.75. Thermal Profile of 50:50 Fresh:Spent AB Slurry

The highest reactor temperatures, which occurred during hydrogen release, were detected at the discharge of the reactor with the largest increase from pre-feed steady state (a difference of 81.2°C) recorded by the thermocouple nearest the reactor outlet(TC14), indicating that the high temperatures progressed down the reactor. The rate of temperature increase appeared to be steady over this range of thermocouples, suggesting that the maximum reaction temperatures were not detected in this test setup and that additional thermal release may have been present in the knockout pot.

The increase in reactor temperature, presumably from the exothermic thermal release, was first detected by thermocouple TC10 (about 13.7 cm from the reaction outlet). Because the internal thermocouples were confined to the heating zone and the heating zone covered the final 26.7 cm of the reactor, the slurry appeared to reach activation energy upstream of thermocouple TC10, about midway along the heating zone. Reaction temperatures and the increase in temperature from pre-feed steady state continue to increase along the length of the reactor.

Overall, reaction testing demonstrated a measureable heat release from the exothermic reaction.
It appears that preheating the feed and heat losses from the tube dominated the reactor sufficiently that an exotherm could not be maintained. Instead, the increased temperature moved down the length of the reactor over time and out the end of the reactor tube.

2.4 Conclusions and Recommendations for CHS Materials

Chemical hydrogen storage materials have significant benefits relative to neat hydrogen storage, adsorbents and metal hydrides. The CHS materials can be stored and reacted at modest temperatures and pressures. Their high hydrogen capacity allows them to better meet the DOE targets for gravimetric and volumetric capacity. Finally, many of these materials are relatively inert for handling. As a result, the CHS materials should continue to be considered as viable alternatives for the storage of hydrogen in automotive as well as non-automotive applications.

In this work, designs for the use of CHS materials in an automotive application have been developed that attempt to address many of the issues with these materials. While many of these designs were evaluated and ultimately not selected for a full analysis, both solid and slurry systems have been developed with sufficient detail to provide estimates of system mass and volume, cost, and performance relative to a set of drive cycles. This work not only addressed the immediate issues of AB and alane materials, but the tools and techniques can also be used for future development work.

For solid materials, the fixed-bed reactor system has merit as a reasonable approach to providing hydrogen for exothermic CHS materials. It was modeled for performance and the cost of the system estimated. In addition, propagation of the reaction front through a packed bed of AB/MC has been experimentally demonstrated. The primary issue with a fixed-bed reactor is the movement of the material onboard and off-board during refueling. This has been demonstrated with a surrogate material assuming a non-agglomerating bed. Although not selected by the HSECoE for continued study, it may be that this approach will be useful elsewhere. One possible application is its use with replaceable cartridges in non-automotive applications where connection and public acceptance issues are less daunting.

For slurries, a flow-through system was developed and demonstrated. At its core was a novel design for mixing the slurry during reaction to prevent agglomeration. A volume-displacement tank was developed that used a pleated membrane to allow the use of a conformable tank. The slurry could be homogenized using a perforated-plate approach that quickly can mix the entire contents of the tank. These concepts were tested successfully with surrogates with a range of properties. These designs may find applicability in the design of other CHS materials or for unrelated system designs.

Although AB may be a simulant for another yet undiscovered CHS material, it did demonstrate kinetic properties that, when extrapolated to higher temperature, are fast enough for the production rates and reactor sizes conducive to an automobile. These kinetic properties have been modeled in several different configurations and validated with experimental data. The versatility of AB as a CHS material was demonstrated as it reacts at wide ranges of temperatures and pressures to produce hydrogen. Cleanup of impurities is still required, but AB as a CHS material can provide hydrogen under reasonable conditions.

Both the solid and slurry models that were developed can be used beyond the scope of this current work to evaluate other potential CHS materials. Once researchers identify new materials, with rather minor changes, the model can be used to demonstrate the performance of these new materials in a fuel cell vehicle simulation under a variety of drive-cycle conditions. The model also was used to perform a sensitivity analysis and better understand the impact of the material properties being able to meet the DOE technical targets.

As this or other similar work moves forward, several items must be considered. Although not evaluated, there continues to be concern about phase separation of the gas products from the slurry. The testing performed here elucidated the issue by demonstrating that a foamy material is produced during reactor testing. The hydrogen must be removed from the slurry before it is returned as a spent material into the volume-displacement tank or a significant amount of hydrogen could be lost. The need for well-behaved slurry materials also was elucidated. The slurry needs to be pumpable, and verification tests to ensure that they can be remobilized must be performed, especially at the low temperatures tested as part of this work.

Future work with CHS materials should identify new materials with higher hydrogen storage properties. If a fixed-bed system is acceptable for the reactor, tests to verify propagation need to be performed. It is imperative that heat transfer from one reaction section does not initiate another section prematurely. Testing should be performed to move the material to and from the fixed bed. Pneumatic conveyance showed promise, but other approaches, such as augering and gravity feed should be considered.

If a fluid system is selected for testing, materials that maintain as a liquid both pre- and post-reaction would have significant advantages and would minimize system complexity. If slurries are considered, materials should be identified with better behavior when produced in the slurry form, especially at the very high concentrations required to meet the DOE gravimetric targets. Foaming and system plugging were both challenges for the AB slurries.

As new materials are selected, how the material is regenerated will be critical to its acceptance as a hydrogen storage material. The DOE has set an ambitious target of 60% “well-to-wheels” efficiency. In addition, its production at large scale must be considered. Both of these factors will impact material costs and ultimately the system cost.

3.0 Hydrogen Storage using Cryo-Adsorbent Materials

3.1 Introduction and Objectives

Because of their high hydrogen capacity, cryo-adsorbent materials are one focus area of HSECoE efforts to develop systems using solid-state hydrogen storage materials. Cryo-adsorbent storage materials use physical adsorption of hydrogen on a substrate as means of increasing the gravimetric and volumetric capacity over using compressed hydrogen. The metal hydrides and chemical hydrogen storage materials studied as part of the HSECoE use chemical bonds to store the hydrogen in a solid state. This section contains the work that has been performed by PNNL for the HSECoE in developing cryo-adsorbent storage materials.

Cryo-adsorbent hydrogen storage materials are high-surface-area organic materials in which hydrogen molecules adhere to the material surface due to van der Waals forces. The level of adsorption depends on the adsorbent material and the system temperatures and pressures. Adsorbent materials include activated carbons and MOFs. To achieve reasonable hydrogen capacities, the hydrogen must be stored on these materials at cryogenic temperatures (~80 K) and at elevated pressures (100 to 200 bar).

Because of their low densities, these materials can meet the gravimetric capacity targets, but meeting the volumetric targets is more challenging. Several approaches have been undertaken to improve their volumetric capacity. Compressing the powdered adsorbent into pellets and pucks increases the material density that, in turn, can increase volumetric loading up to a point. At some point, surface area is lost, and hydrogen capacity decreases.

A second issue with these materials is their low thermal conductivity, which results in challenges to removing the heat produced during hydrogen adsorption. Two designs that address these issues have been chosen. The *Hexcel design* uses an aluminum honeycomb structure filled with powdered adsorbent within the tank. Heat is removed during refueling by flowing cold hydrogen gas through the porous bed. Heat is added to the bed to desorb the hydrogen during operations with cartridge heaters. Heat transfer is enhanced by the aluminum fins of the Hexcell material.

The second design is the *Modular Adsorbent Tank Insert (MATI)*. MATI uses compressed pucks of adsorbent material interleaved between microchannel heat exchangers. Before the pucks of adsorbent are compressed, thermally conductivity enhancing materials are added. These thermal enhancements could include mixing expanded natural graphite with the adsorbent or insertion of aluminum pins longitudinally within the puck. During hydrogen refueling, liquid nitrogen flows through the microchannel heat exchangers to remove the heat of adsorption, while during operation, warm hydrogen is used to desorb the hydrogen. The design, experimental validation tests, and cost estimates of these two systems were performed in parallel.

The adsorbent initially selected as the baseline material for both the MATI and the Hexcell systems was MOF-5, which is a crystalline microporous material with the chemical formula $Zn_4O(BDC)_3$ (BDC = 1,4-benzene dicarboxylate). Compared to the AX-21 adsorbent that also was evaluated, MOF-5 has higher hydrogen capacity and thermal conductivity, better availability, and better ability to be densified. MOF-5 also is a member of a large class of framework materials where improved properties are likely to be identified.

The HSECoE partners developed storage-system designs for both the MATI and Hexcell systems and worked to develop areas of deficiency where the systems did not meet the DOE 2020 technical targets for a light-duty vehicle. Major areas of deficiency included the volumetric capacity of both the material

and the storage system, heat transfer in and out of the bed during refueling and operation, challenges associated with high-pressure cryogenic operation, and the high system cost as shown in Table 3.1. The purpose of this work was to develop engineering solutions to overcome these deficiencies and find ways to reduce the system mass, volume, and cost. In the process of developing these system designs, engineering methodologies, analysis tools, designs, and components have been identified that can be applied to other materials beyond MOF-5 as they are identified.

Table 3.1. Challenges with Cryo-Adsorbent Hydrogen-Storage Materials

Challenge Topic	Challenge Description
Hydrogen Loading	Heat removal during hydrogen loading is challenging due to material poor thermal conductivity and low temperature requirements.
Volumetric Capacity	Low density of cryo-adsorbent results in a large system
Dormancy	Difficulty in maintaining cryogenic temperatures and preventing hydrogen loss during system dormancy
System Cost	Minimize cost while maintaining its functionality
Material Compatibility	Determine impact of cryogenic temperature and hydrogen pressure on system materials
Refueling Rate	Address the heat removal requirements on the tank during refueling

While the HSECoE has addressed a wide range of issues with these two cryo-adsorbent hydrogen storage systems, PNNL's work has focused on

1. Tank development
2. Improved refueling rate
3. BOP mass and volume reduction
4. System cost
5. Material hydrogen compatibility.

In terms of tank development, PNNL assisted in determining the best type of tank for this application. Types-I, -III, and -IV tanks were evaluated both in terms of mass and cost of materials. A model was developed to assist researchers in identifying the appropriate tank. This work is discussed in Section 3.2. Computational modeling identified heat removal from the tank wall itself during refueling to be a major challenge. Large amounts of cold hydrogen would be required to reduce its temperature to a level that would minimize dormancy issues. An alternative approach to wall cooling using LN2 in the annulus between the tank and its insulation reduces this issue. This work is described in Section 3.3. Although the BOP represents less than 15% of the overall system mass and 12% of its volume, the HSECoE worked to reduce the number of components and their mass and volume. A consolidated valve block was developed wherein the bodies of 11 valves and instruments were combined into a single structure. Not only did this reduce volume and mass, it also reduced the number of fittings, resulting in a significant cost reduction. A description of the development of this part is provided in Section 3.4. The MATI and Hexcell system costs were estimated using both a top-down and a bottom-up manufacturing analysis. Where possible, off-the-shelf items were identified, and a progress ratio was used address the price declines between 10,000 and 500,000 units per year. With non-commercial items, manufacturing costs were estimated by determining the processing steps and the material and labor costs required from a Design for Manufacture and Assembly model. The cost effort is discussed in Section 3.5. The impacts of low temperatures and high-pressure hydrogen for polymeric materials used as seals, pistons, seats, and piping containment were evaluated. Results of both tensile and compressive testing are described in Section 3.6.

3.2 Pressure Vessel Development

The pressure vessel is an important piece of the overall hydrogen storage system because it represents a significant fraction of the cost, mass, and volume, which are three key performance metrics. Knowledge of the operating and refill cycles and of the efficiency of the adsorbent system is required to properly size the pressure vessel for the desired operational capacity. The larger the necessary capacity, the larger the pressure vessel needs to be, with thicker walls, larger mass and volume, and higher cost. The efficiency and operational requirements of the adsorbent material are the foundation of the system efficiency, while the need to add a pressure vessel around the system causes a net reduction in efficiency. This drives the need to minimize the size of the pressure vessel, and a number of vessel configurations and materials were considered to find the best candidate.

The cryogenic operating cycle was a major factor in designing the pressure vessel. The ability to operate at low temperatures requires added volume and material, and special care in selecting materials that have compatible thermal expansion properties. Carbon fiber expands at low temperatures instead of contracting, thus, carbon fiber's thermal expansion behavior is the opposite of typical materials, and this behavior has to be accounted for in the design of Type-III and Type-IV pressure vessels for cryo-adsorbent systems. The consequences of temperature and the effect on each type of tank design are discussed in Section 3.2.1.

The need to maintain cryogenic temperatures to meet dormancy targets was another critical factor in the design of the pressure vessel. A vacuum layer was identified as a key feature early in the design process, which added an extra shell layer around the main pressure vessel. The final technical challenge for the pressure vessel design was to cool the contents fast enough during refueling to meet the DOE refueling time target. The vacuum layer and the cooling rate challenge are discussed in Section 3.3, which covers the final prototype design.

3.2.1 Design and Assessment of Types-I, -III, and -IV Pressure Vessels

Because of the large volume of required adsorbent material, the largest impact on volume and cost of the system is the tank holding the adsorbent and its operational parameters. As a result, PNNL and its partners at Hexagon Lincoln and Savannah River National Laboratory were tasked with determining the type of tank that should be used. Type-I all-metal tanks tend to be heavier, especially at high pressures. They also are less expensive than composite tanks. Type-III and Type-IV tanks are composite tanks with a metal and polymeric liner, respectively. These tanks are much lighter, but are more expensive. PNNL developed models for these different types of tanks that could be used to down-select the most appropriate one based on conditions that would minimize the mass and cost.

3.2.1.1 Objectives

Three types of pressure vessels, Types I, III and IV, were considered for use in a prototype tank design. The goal was to investigate the possibilities for meeting the DOE target goals and select one candidate system for development into a prototype.

3.2.1.2 Tank Design: Results and Discussion

The three types of pressure vessels, Types I, III and IV, were evaluated using numerical modeling and in some cases material testing. The code developed and used for modeling to estimate the mass and material cost of the pressure vessels was named *Tankinator*. Ultimately, the Type-I tank was chosen for

development into a prototype system, as explained below. Each system is discussed briefly in the following sections.

Type-I Tank Design

The Type-I tank is a common type of pressure vessel that forms the pressure boundary with a single layer of material with a wall thickness that may vary by location. In terms of construction, Type-I tanks can be made from two formed end domes welded to a straight section of pipe. Other joining methods like friction stir welding may be employed to provide greater strength where the pieces are joined. We considered a number of materials (i.e., aluminum, steel, titanium, and magnesium). Aluminum was chosen as the most practical material because of its cost and strength/weight ratio.

The stress analysis of a Type-I pressure vessel is straightforward, and closed-form solutions exist in the *Tankinator* model for both thin-walled and thick-walled pressure vessels. Designing a pressure vessel with known volume capacity and approximate desired shape comes down to solving the closed-form solution equations for the wall thickness, as described in more detail in Section 3.2.2.

Because the Type-I tank wall consists of a single material, thermal stresses are not a concern. Unlike the Type-III and Type-IV tanks, there are no major complications in the function of the tank at cryogenic temperatures. Because of this and its relatively low cost, the Type-I tank was selected for development into a prototype system.

Type-III Tank Design

The Type-III tank uses a metal liner and a carbon fiber overwrap to form the pressure boundary. Because hydrogen permeates through carbon fiber, one key function of the metal liner is to act as an impermeable barrier. The metal liner typically contributes strength to the composite wall, reducing the necessary wall thickness of expensive carbon fiber. Initially, this hybrid structure was considered to be a viable compromise between the high cost of carbon fiber in a Type-IV tank and the high mass of a Type-I tank. However, finite-element analysis of the Type-III tank identified a complication caused by the differing thermal expansion characteristics between carbon fiber and aluminum.

A finite-element model representing a ring section of the cylinder section of the Type-III pressure vessel was constructed to test the response to the cooling, heating, and pressure cycle, as shown in Figure 3.1. The aluminum liner was assigned nonlinear temperature-dependent elastic-plastic material properties. The key physical phenomenon is the carbon fiber naturally expands when the temperature is reduced, which is the opposite of most engineered materials which contract. This behavior is manageable, but it requires special manufacturing steps and a must be considered in the design.

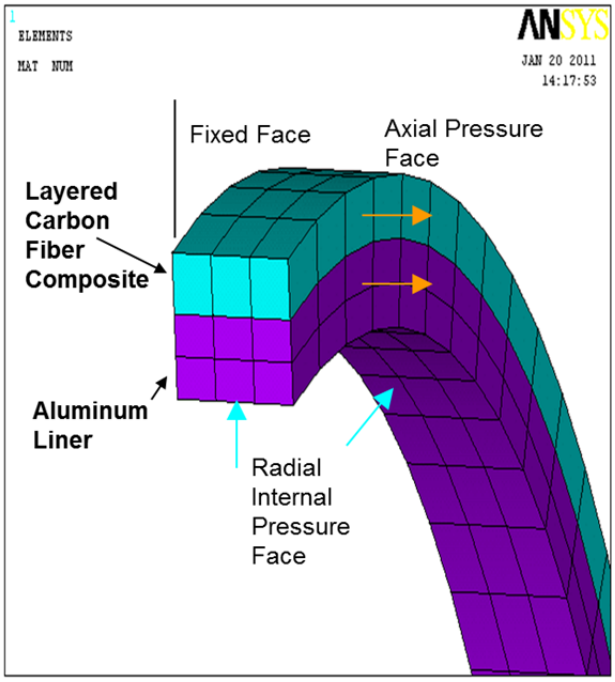

Figure 3.1. Finite-Element Model Representing a Ring Section of a Type-III Pressure Vessel

Figure 3.2 shows the plastic hoop strain response of the liner for two similar designs. Load steps 0 through 3 represent the manufacturing and initial cool down to operating temperatures. Load steps 4,5 and 6 are the regular pressure and temperature cycle. The normal cycle is 4,5,6,4,5,6,4,5,6…. Step 7 represents an accidental overpressure, while Step 8 is an unpressurized return to room temperature. The liner hoop stress is in a state of high tension in steps 4 and 6, but is in a state of high compression at Step 5. The difference between the two designs in shown in Figure 3.2 is the relative thickness of the inner aluminum liner and the outer carbon fiber overwrap.

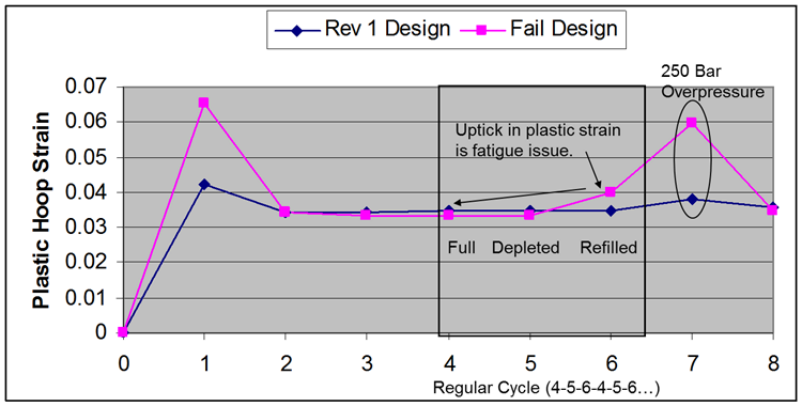

Figure 3.2. Type-III Liner Plastic Strain Cycles: Plastic Hoop Strain Response of the Liner for Two Similar Designs

Ultimately, the Type-III tank configuration was dismissed from consideration because it does not effectively share the load between the liner and the composite shell. Ideally, both layers would be loaded near their material strength capacity, but the thermal and pressure load cycle the tank is subjected to in the cryo-adsorbent case makes it physically impossible to divide the load efficiently. In the example designs shown in Figure 3.2, the aluminum liner is loaded to capacity, but the carbon fiber composite is nowhere

near its limit. The only design choices are the thicknesses of the liner and shell, and there is no practical combination of thicknesses that can shift the load to a more favorable distribution. In addition, a prototype Type-III pressure vessel was tested for rapid cooling performance, and it was found that the Type-III vessel could not meet the DOE targets for refueling times because of poor thermal conductivity in the carbon fiber overwrap. The cooling behavior is discussed in more detail in Section 3.3.

Type-IV Tank

Type-IV tank uses a polymeric permeation barrier liner wrapped in carbon fiber composite material. The carbon fiber composite provides the main structural strength. Designing Type-IV tanks is complicated by the end-boss geometry, which affects the carbon fiber tow winding angle, and with phenomena such as translation efficiency, which can be thought of as a practical reduction in the established strength of the carbon fiber material. Designing a practical carbon fiber pressure vessel that could be manufactured is appropriately a task for our experienced industrial partners (Lincoln Composites). For analytical purposes, a method for estimating Type-IV tank sizes was developed and implemented in the *Tankinator* code (Section 3.2.2), and this estimation model was compared against actual Lincoln Composites designs and found to be in the ±20% range. This level of agreement is sufficient for the purposes of this study, but it is worth noting that the estimate is not a replacement for a practical design effort.

Because of its relatively low mass, the Type-IV tank configuration was considered to be a serious candidate for selection for the prototype system. Through computer modeling, PNNL determined that the polymer liner needed to be limited to 2.55 mm to meet the volumetric and gravimetric BOP targets. Cryogenic material testing of candidate liner materials was performed by PNNL and Hexagon Lincoln (Section 3.6.) to choose the best liner. However, testing performed by Hexagon Lincoln revealed that, even when using the best materials, the liner would separate from the carbon fiber composite shell when the hydrogen pressure dropped below 35 bar at cryogenic temperatures. Because liner separation is not acceptable, a 35-bar minimum pressure would need to be maintained within the tank at all times, which would severely limit the amount of usable hydrogen in the system. This undesirable characteristic eliminated the Type-IV pressure vessel from consideration.

3.2.1.3 Summary

Type-I pressure vessels are the only practical tanks that can meet the needs of the cryo-adsorption system. Type-III tanks were considered, but the specific thermal and mechanical loading cycle makes it impossible to share the load between the liner and the carbon fiber shell effectively. Type-IV tanks were also considered, but the separation of the liner at cryogenic temperatures in the absence of 35 bar pressure is not acceptable. This leaves the Type-I pressure vessel as the only practical tank solution.

3.2.2 Approach to Modeling of Tank Designs

Because of the significant impact of the pressure vessel design to overall cryo-adsorbent system efficiency, it was necessary to consider a wide range of tank design options. The DOE volumetric, gravimetric, and cost targets were such that typical pressure vessels were not sufficient to meet the goals, and demanding temperature and pressure cycles were a challenge to more expensive lightweight pressure vessels. We needed a tool to compare and evaluate the potential of various combinations of material and tank configurations. Therefore, the spreadsheet tool named *Tankinator* was developed.

Tankinator was created to estimate the mass, volume, and material cost of Type-I, Type-III, and Type-IV pressure vessels of any size or material. Real pressure vessel design is a much more complicated process that is beyond the scope. Instead, *Tankinator* uses the fundamental closed-form solution for thin-walled

pressure vessels to solve for the wall thickness required to withstand a chosen pressure. This approach offers an approximate estimate of the size and mass of the pressure vessel. Practical pressure vessel designs may be more or less efficient than the *Tankinator* estimate in their use of material, but the general size and shape is expected to be relatively close.

Tankinator was set up to have separate worksheets for each type of tank (Types I, III, and IV) with similar inputs. All cases require two out of three of the following pressure vessel geometric parameters to be defined: length, radius, or volume. Specifying any two parameters provides enough information to determine the third. All cases make the assumption that the pressure vessel geometry is a cylindrical section capped by two hemispherical ends. This assumption is made to simplify the geometry and eliminate a degree of freedom. In realistic pressure vessel designs, the end cap rarely are near perfect hemispheres, and this treatment of the end caps by *Tankinator* is an expected source of disagreement between *Tankinator* estimates and practical designs.

Regarding the end cap geometry, it can be pointed out that *Tankinator* assumes that the hemispherical end cap geometry has the same wall thickness as the cylindrical portion of the tank, even though the stresses caused by internal pressure are lower in a hemisphere than in a cylinder of equal wall thickness. This is an indication that *Tankinator* may overestimate the amount of material that is needed in the pressure vessel end cap regions, but this is offset by the fact that the hemisphere is the most theoretically efficient geometry for an end cap. In practical pressure tank design, the transition from the cylinder section to the end cap geometry is a complex region where stresses and strains need to be carefully managed in the design process. Finite-element analysis of Type-I tanks has demonstrated that this treatment of the end region results in an acceptable stress state in the hemisphere-to-cylinder transition region, so this hypothetical pressure vessel shape works as a benchmark. Practical pressure vessel designs will be more or less efficient than the *Tankinator* benchmark.

Each of the three *Tankinator* spreadsheets performs a calculation of the necessary wall thickness in the cylindrical section of a thin-walled pressure vessel. The full design criteria for each type of tank and the implementation of the wall thickness calculation are discussed in more detail in Section 3.2.2.2. All tanks are designed to withstand a burst pressure of 2.25 times the operating pressure, but some additional considerations apply for each type of tank. Once the wall thickness is calculated, the geometry of the tank is fully defined, and the volume and mass of the tank material are calculated.

A cost prediction is incorporated into *Tankinator,* but this is a raw material cost estimate and not a full manufacturing cost estimate. The calculated mass of the tank wall materials is multiplied by the cost per kilogram assumed for each material. The first page worksheet of the *Tankinator* file contains an overview of the code and identifies the material costs assumed on a per kilogram basis. The intent of this feature of the code was merely for approximate, informational, cross-comparison purposes. It does not attempt to include manufacturing costs or the cost of BOP items, which will be performed in a separate, detailed cost analysis.

3.2.2.1 Objectives of Modeling

The purpose of the *Tankinator* code is to estimate mass, volume, and material cost for Types I, III, and IV pressure vessels. The code was used to estimate the performance of tank designs for comparison against DOE target goals. It also was used for cross-comparison of different pressure vessel types to determine viable pressure vessel configurations. The *Tankinator* code was provided to the members of the HSECoE for internal use and was ultimately made available to the public via the download site.

3.2.2.2 Results and Discussion of Modeling of Tank Designs

The three types of tanks covered by the *Tankinator* code follow slightly different logic to estimate minimum wall thicknesses. The calculation methods and key assumptions are discussed in separate sections below. For each type of tank, practical limitations are discussed.

One common feature in all three worksheets is the material cost assumption. These values are based on 2007$ prices and shown in Table 3.2.

Table 3.2. Material Cost Assumptions (2007 Dollars)

Carbon Fiber	$30.65/kg
HDPE (high-density polyethylene)	$2.06/kg
Aluminum 6061-T6	$4.45/kg
Type 316 Stainless Steel	$4.92/kg
4130 Chromoly Steel	$2.55/kg
4340 Steel	$3.01/kg

Type-I Tank Design

The Type-I tank is designed to meet two criteria: 1) a proof load and 2) a burst load. The proof load is 1.5 times the operating pressure, and the tank wall must not yield under this pressure. The burst load is 2.25 times the operating pressure, and the tank must not exceed the peak von Mises stress under this pressure load. These criteria were selected by the HSECoE team to ensure that a reasonable, competitive pressure tank design was estimated by the *Tankinator* code.

These design criteria do not account for the consequences associated with welded construction. A standard for compressed natural gas tanks—49 CFR 571.304 (Standard No. 304; Compressed natural gas fuel container integrity)—specifies a burst pressure of 3.5 times the operating pressure to be applied to welded Type-I tanks. This pressure is 56% higher than the burst pressure of non-welded tanks, so the minimum required wall thickness is proportionally increased. This places a 56% penalty on the mass of a welded Type-I compressed natural gas (CNG) tank compared to a non-welded CNG tank. If the same regulation is applied to Type-I hydrogen tanks, it can make welded tanks noncompetitive and incapable of meeting DOE target goals. The *Tankinator* code essentially assumes 1) the welded construction penalty will not apply to the hydrogen tanks or 2) alternate construction or design methods can be employed to circumvent the welded construction penalty.

Operating temperature is one of the inputs of *Tankinator*'s Type-I tank estimation. Material strength increases at lower temperatures and decreases at higher temperatures for most metals. For cryogenic applications, the use of room-temperature material strength is conservative. If the analyst wishes to account for the increased strength, an appropriate temperature can be identified.

Operating pressure is the single load that the tank wall must support. In a system where the pressure varies with the operating cycle, the pressure should be defined as the maximum normal pressure experienced under normal conditions. The proof load and burst loads are derived from multipliers placed on the specified operating pressure, and physically represent excursions from the normal pressure.

The spreadsheet contains information for four metals: 1) 6061-T6 aluminum, 2) 316 stainless steel, 3) 4130 chromoly steel, and 4) 4340 steel. The key properties are yield strength, ultimate strength, and density. The material properties included in the code are considered representative. The code will look up temperature-dependent strength from tabulated temperature-strength data. Two metals, 6061-T6

aluminum and 316 stainless steel, are coded with temperature-dependent properties, but the 4130 and 4340 steels assume constant strength over a range of temperatures. This type of material data is intended to be replaced by the user or expanded with additional materials as necessary.

The last input parameters are the *internal radius, length, or volume of the tank*. Defining any two of the three finalizes the design and the spreadsheet can complete the calculation of the minimum wall thickness. As discussed in Section 3.2.2, *Tankinator* makes assumptions about the end cap geometry that simplifies the shape.

The thin-walled pressure vessel hoop stress equation (hoop stress = pressure × radius ÷ wall thickness) is the basis of the wall thickness calculation. This equation is rearranged to solve for wall thickness (wall thickness = pressure × radius ÷ hoop stress). Pressure and radius are fixed by user inputs, although if the radius is an unknown, length and volume capacity can be defined to solve for radius. For the proof load criteria, the hoop stress is set at 1.5 times the operating pressure. For the burst load criteria, the hoop stress is set at 2.25 times the operating pressure. The maximum wall thickness is chosen from the two criteria to be the initial wall thickness estimate, and mass, volume, and material cost of the tank are calculated.

This hoop stress method offers a first estimate of the tank properties, but a number of additional steps are made to check and refine this estimate. One issue with the initial estimate is that it does not recognize when the geometry of the tank can no longer be considered a thin wall. A second issue is that the hoop stress calculation considers stress in just one dimension. The use of a three-dimensional stress analysis has demonstrated that the use of hoop stress alone to define wall thickness can be conservative. Both of these issues are dealt with by implementing a von Mises stress evaluation to consider the full three-dimensional stress state. The von Mises stress is calculated for the initial estimate of wall thickness, and three iterations are made to refine the wall thickness to drive toward the von Mises stress limits. The iterative process was used for its simplicity compared to solving the von Mises equation for wall thickness due to its complexity. Three iterations has been sufficient in testing to arrive at a wall thickness that is within 1% of the von Mises criteria limit for most practical cases up to 700 bar. *Tankinator* reports the von Mises error (in cell C190) to confirm that the iterative process has converged to the ideal minimum wall thickness. The difference in mass between the initial hoop estimate and the final von Mises estimate is reported in cell C189.

The spreadsheet calculations of von Mises stress have been validated against three-dimensional finite-element models to ensure the formulas were correctly implemented. The mass prediction capability of this spreadsheet has been compared against two sets of existing Type-I CNG tank designs: 1) 4130 Chromoly tanks at 250 bar and 2) 4340 steel tanks at 200 bar. Both of these sets of practical data show that the PNNL tank mass estimation is reasonable with errors on the low side. More detailed and specific examples of *Tankinator*'s ability to predict tank properties are provided below.

Example 1. The American CNG Type-I chromoly steel tank designated TYPE1-CP1459 is described on their website with engineering drawings. The working pressure of 248 bar matches the operating pressure input in *Tankinator*, and the test pressure of 372 bar matches the 1.5 times operating pressure proof load, and the burst pressure of 559 bar matches the burst load of 2.25 times operating pressure. The approximate specifications are 14 in. diameter, 59 in. length, 297 lbs for a 120 L capacity tank. Entering the rough information into *Tankinator* (149.86 cm length, 17.18 cm radius, 248 bar operating pressure) results in a mass prediction of 307 lbs, which is 3.4% higher than the actual tank mass. While this is a satisfactory prediction of mass, it should be noted that *Tankinator* predicts the tank volume to be 137 L rather than 120 L, or 14% higher than the actual volume. This discrepancy is due to the actual tank geometry, which takes advantage of increased wall thickness at the ends and has a 25-mm neck on one end.

Example 2. A second way to estimate the mass of the tank using *Tankinator* is to determine from the engineering drawings that the internal radius of the cylinder section is 338.2 mm and the nominal water capacity is 120 L. This changes the mass estimate to 272 lbs, which is below the mass target by 8.4%.

Example 3. A third way to estimate the mass of the tank using *Tankinator* is to use the target volume of 120 L, and then use the internal length of the pressure vessel, minus the neck length, to estimate the main mass of the tank, which is a length of 1461 mm. This provides an estimate of the non-neck region of a tank of 267 lbs. Add to this a 2.5 cm long neck with an approximate OD of 4.8 cm and inner diameter of 2.86 cm and a density of .008 kg/cm3, and the neck region adds approximately 0.5 lbs. The adjusted mass estimate of 268 lbs is still low by 9.8%.

These three attempts to match the real design of a Type-I pressure vessel help illustrate some of the difficulties in estimating a realistic tank. Designers have the flexibility to vary wall thickness throughout the design and use end cap geometry to suit their needs. However, this exercise demonstrates the *Tankinator* tool has the ability to predict the mass of a real Type-I tank with error bands of +3.3% and -9.8%. This tool provides researchers with a mass estimate of the tank without having to go through the effort of fully designing a tank.

The *Tankinator* cost estimate is another point of interest. The cost estimate feature assumes a raw material price of $2.55/kg for 4130 Chromoly, which is in the range of $307 to $356. The actual tank has a regular price of $1,950 and a sale price of $1,586. The code only calculates the raw material cost, so the predicted material costs are only a fraction of the total retail cost, in this case about one-fifth the sale price. *Tankinator* mass estimates are incorporated into more detailed cost models that include manufacturing and BOP components.

Type-III Tank Design

The Type-III tank estimator assumes that an aluminum liner with a carbon fiber overwrap comprise the tank. This estimator is designed specifically for the case of a cryogenic operation cycle with minimum temperatures reaching 80 K or lower. The tank wall components (liner and composite) are sized to withstand 2.25 times the operating pressure burst test at both cryogenic and room temperatures, so the mass estimates can be applied to room-temperature cases as well. However, the estimator uses a fixed relationship for the liner thickness to avoid a potential fatigue issue under cryogenic service conditions, which is a design restriction that does not apply for ambient temperature tanks. Because the aluminum liner and composite overwrap share the pressure load, designers have some flexibility to choose how much aluminum and carbon fiber is used, which will affect the gravimetric efficiency and cost.

The same pressure and geometry inputs as in the Type-I case are required. The temperature input is removed, and the calculations assume potentially conservative room-temperature strength properties for the aluminum liner and the carbon fiber. A new user input is called fiber translation efficiency, which is a "catch-all factor" that modifies the carbon fiber's effective strength to account for practical difficulties in achieving ideal carbon fiber strength in a practical tank design. Translation efficiency is a function of both the manufacturing process and the fiber lay-out, and in effect the phenomenon means more carbon fiber is required for use in a design to achieve a specified burst pressure than would be expected based on ideal stress calculations. Anecdotal examples of translation efficiency have been in the range of 63 to 90%. The carbon fiber composite strength currently coded into *Tankinator* (i.e., Revision 3) includes a reduction in carbon fiber material strength based on 90% translation efficiency. The translation efficiency input further adjusts the material strength. Because this treatment of translation efficiency is not intuitively obvious, any future revisions of *Tankinator* will revise the way translation efficiency is implemented. Until a new revision is released, Table 3.3 provides recommendations for translation efficiency input based on operating pressure.

Table 3.3. *Tankinator* Recommended Translation Efficiency Values

Pressure (bar)	Recommended Translation Efficiency	Translation Efficiency Input
20	90%	100%
200	90%	100%
300	85%	94%
400	80%	89%
500	74%	82%
600	68%	76%
700	62%	69%

The determination of the liner thickness and overwrap thickness are the two key calculations of the spreadsheet. The liner thickness is assumed to be constant throughout the cylinder and hemispherical end domes. The overwrap thickness also is assumed to be constant throughout the pressure vessel. The Type-III tank design characteristics are estimated for upper- and lower bound cases that are explained below.

The liner thickness is determined based on the burst pressure calculation (2.25 times the operating pressure) using the thin-wall hoop stress equation, as used in the Type-I tank calculation. However, Type-III liners in the lower bound case are only sized to carry 21% of the total burst pressure load. The carbon fiber composite layer is sized appropriately to carry the rest of the pressure load. This 21% division of the pressure load was determined based on finite-element analysis of the cryogenic operating cycle as discussed in Section 3.2.1.2. This fixed division of the load and its implications for the thickness of each layer of the Type-III tank is an important distinction between *Tankinator* Type-III estimates and other Type-III tanks that appear on the market. The calculated liner thickness is adjusted to a minimum value of 3 mm, which represents a practical manufacturing limit for a thin liner.

The wall thickness of the carbon fiber overwrap section is determined for upper- and lower bound cases. The lower bound thickness calculation assumes the carbon fiber overwrap has to be thick enough to carry the fraction of the burst load that is not already carried by the liner (79% of the burst pressure). The upper-bound calculation conservatively assumes that the liner carries none of the load, so the overwrap has to be thick enough to carry the entire pressure load.

In both cases, the necessary carbon fiber wall thickness is determined using the hoop stress equation, but note that the axial stress is also considered. In metals with isotropic strength the axial stress in a thin-walled pressure vessel can be neglected because hoop stress in a cylinder wall is double the axial stress. A metal wall that is thick enough to support the hoop stress can also support the concurrent axial stress. In a carbon fiber composite, the carbon fibers need to be oriented such that some of the fibers support the hoop load and others support the axial load. The ideal ratio for these fibers is 2:1, with twice as many fibers oriented in the hoop direction as the axial direction.

The carbon fiber composite is assumed to be Torayca T700S with a unidirectional composite strength of 2550 MPa that assumes a 60% fiber volume fraction. A factor of 0.9 is applied to this strength to represent a maximum 90% translation efficiency (2295 MPa). An additional factor of two-thirds is applied to the unidirectional laminate strength to represent the ratio of fibers aligned in the hoop direction to the fibers aligned in the axial direction. This is how the basic composite design strength of 1530 MPa (15,306 bar in *Tankinator*) was determined. The user can modify this design strength using the translation efficiency input as described above. The translation efficiency input offers the opportunity to scale the material strength of the composite up or down, as required.

The final modified hoop strength is used to determine the composite wall thickness for two pressure conditions. In the lower bound case, the composite wall must carry 79% of the burst pressure. In the upper-bound case, the composite wall must carry 100% of the burst pressure. Calculated wall thickness is rounded up to a whole number of layers. It is assumed that three layers of composite is the minimum practical wall thickness.

This treatment of the carbon fiber assumes that a practical winding strategy exists to achieve this effective fiber distribution, which is not always the case. This is one of the limitations of the *Tankinator* code: the estimates of wall thickness are based on treating the carbon fiber composite as a homogenized material that has an ideal orientation of fibers. The finite-element models that were used to determine the 21%/79% load share with the aluminum liner also assumed an ideal fiber orientation. This is sufficient for an approximate estimate of tank properties, but a significant design effort would be necessary to design a realistic Type-III tank that can function under the cryogenic cycle of an adsorbent system.

A validation comparison case is available through American CNG website. Their tank is designated Type-III – AME1945E, with dimensions of 19 inches OD, 45 inches length, 140 L, and 151 lbs, and a retail price of $3,300. In *Tankinator* units, the outer radius is 24.13 cm, outer length is 114.3 cm, and the total mass is 68.6 kg. The operating pressure is not listed, but a GGE value (presumably, gallons of gasoline equivalent) of 12 GGE is listed for the 140-L tank. The 120-L Type-I tank example used above was listed at 8.4 GGE, at a pressure of 248 bar. If we assume the GGE scales linearly with pressure (as in the ideal gas law), the estimated operating pressure of the Type-III tank is 304 bar. For this pressure, the translation efficiency is recommended to be entered as 94%, which represents a total translation efficiency of 85%. The initial estimate uses inputs of 24.13 cm for the internal radius and 140,000 cm^3 to estimate the wall thickness in order to estimate an internal radius from the given outer radius. This initial estimate estimates a mass of 68.4 kg (lower bound) and 75.5 kg (upper bound), but the outer radius of the estimated tank is 26.25 cm, which is 2.12 cm too large, and the exterior length of the tank is estimated to be 94.86 cm, which is nearly 20 cm too short.

A better estimate of the geometry is made when the internal radius is set to 22.2 cm, which was determined through iteration. The final estimate of tank mass is 65.2 kg, with an outer radius of 24.14 cm and an outer length of 109.11 cm. Further refinement is possible, but is not expected to make a significant difference. The 65.2 kg is labeled as the lower bound estimate in *Tankinator*, but it represents the best estimate of mass for a Type-III tank that designs the liner to support 21% of the total pressure load. The upper-bound estimate represents the mass of a Type-III tank that is designed such that the carbon fiber can carry the entire burst pressure load without any assistance from the liner. Compared to the actual mass of the AME1945E tank, the *Tankinator* prediction is low by 5%. This is a reasonably good agreement, and the actual tank mass falls between the upper and lower bounds established by *Tankinator*. The ratio of carbon fiber to liner mass is not available, but because of the close agreement with the *Tankinator* estimate, it is assumed that the real ratio and estimated ratio are similar. The raw material cost of the *Tankinator* estimate is $912, compared to the retail price of $3,300.

Type-IV Tank Designs

The Type-IV tank calculation is similar to the Type-III calculation in regards to sizing the composite wall thickness. The carbon fiber composite hoop strength is based on a two-thirds orientation of the Torayca T700S lamina with an assumed 90% translation efficiency. Higher or lower translation efficiencies can be defined using the translation efficiency input per Table 3.3. See Section 3.2.1.2 for more discussion of the material and wall thickness calculation procedure.

For Type-IV tanks, the liner is assumed to carry no load, and the liner wall thickness is a user input. The liner is assumed to be HDPE material, and 3 mm or 6 mm are common assumptions. The purpose of the

liner is to keep the hydrogen from permeating through the carbon fiber. Testing has demonstrated that HDPE liners, which function adequately at room temperature, are problematic for cryogenic applications because they delaminate from the carbon fiber composite overwrap due to differences in coefficient of thermal expansion. This delamination causes the liner to fail under normal operating loads, which allows hydrogen gas to permeate through the carbon fiber composite layer and makes typical Type-IV tanks unsuitable for cryogenic operation. *Tankinator* determines the mass for a standard HDPE liner, which is appropriate for ambient temperature operation, but not cryogenic service. The mass and material cost estimate provided by *Tankinator* might still be reasonable for a Type-IV tank used in cryogenic service, but the liner delamination issue remains a currently unresolved technical challenge.

American CNG provides a comparison case for ambient temperature Type-IV tank design. Their tank is designated Type-IV - QT2540, has a 234 L capacity, and has a 63.5 cm OD and a 101.6 cm length. The mass is 53.2 kg and cost is $4,934.50. The 20.5 GGE for a volume of 234 L suggests a pressure of 311 bar, using the GGE over volume capacity ratios from the Type-I and Type-III tank examples as a reference.

The *Tankinator* input assumes the liner is 3 mm in thickness, the pressure is 311 MPa, and the translation efficiency input is 94% (to achieve a total translation efficiency of 85%, see Table 2.2). The external radius of 31.75 cm is used as the internal radius input in an initial estimate with 234,000 cm^3 specified for the capacity. This initial estimate predicts a tank mass of 60.0 kg, but the external radius is 33.7 cm and the external diameter is 98.9 cm, indicating the geometry needs more refinement.

After some iteration, the internal radius is reduced to 29.9 cm to achieve a 234-L capacity tank with a 31.8 cm outer radius and a 107.0 cm outer length. This estimate of tank mass is 58.1 kg, which is 9.2% too high. Dropping the operating pressure to an even 300 bar lowers the mass estimate to 54.9 kg, which is just 3.2% off, and illustrates the sensitivity of the calculations to design pressure. The material costs for the 311 bar case and the 300 bar case are $1,668 and $1,572, respectively. Both material cost estimates are about one-third the retail cost.

American CNG has another Type-IV tank that has a similar appearance and designation on their site, Type-IV - QT2560, that is 50.8 cm longer and has a mass of 75.9 kg with a capacity of 392 L. Using the same internal radius of 29.9 cm and a 300 bar operating pressure, the mass estimate from *Tankinator* is 83.7 kg, an error of 10.2%. This illustrates the level of uncertainty associated with the *Tankinator* code's ability to predict realistic tank masses, 3.2% to 10.2% error in this example. The main difference in these two cases is the length/depth (L/D) ratio, which affects the overall fraction of material assumed to be in the cylindrical portion and the end cap portions of the tank.

Tankinator assumes that the composition of the Type-IV tank is a HDPE liner plus carbon fiber laminate. Type-IV tank designs can include other material that is not accounted for in *Tankinator*, such as the inclusion of fibers other than carbon or end-boss components. BOP components are not included in the estimate.

The estimation process that *Tankinator* uses is based on classical mechanics and the assumption of a homogenized carbon fiber laminate. A different approach to estimating the tank properties is to perform a netting analysis, which is an established analytical method for designing Type-IV tanks. Netting analysis is more about designing a Type-IV pressure vessel, and includes considerations such as fiber winding angle. This is a level of detail that is a step beyond the *Tankinator* estimate, but a netting analysis could be added to *Tankinator* if that feature is desired by the user community.

3.2.3 Summary of Pressure Vessel Development

Because of the low operating temperatures of cryo-adsorbent materials, special care should be taken in selecting the materials of the pressure vessel. Type I, III and IV pressure vessels were evaluated as part of the HSECoE using an internally developed model named *Tankinator*. Because Type-I tanks are relatively low cost and have low thermal stresses, they were selected for development into a prototype system.

Tankinator was created to estimate the mass, volume, and material cost of Type-I, Type-III, and Type-IV pressure vessels of any size or material. The *Tankinator* calculations were validated against three-dimensional finite-element models to ensure the formulas were correctly implemented. The *Tankinator* tank masses were also compared to commercially available tanks. The masses were correctly estimated within less than 10% error. Although *Tankinator* provides estimated cost for materials it does not include fabrication costs and as a result the costs estimated by *Tankinator* are significantly less than the retail cost of the commercial tanks.

3.3 LN2 Cooled-Wall Tank

To solve a technical problem associated with flow-through cooling, the LN_2 Cooled-Wall Tank concept was developed. The cryo-adsorbent system is expected to operate with a temperature cycle between 160 and 80 K. The amount of energy required to cool the adsorbent material from 160 K to 80 K is manageable using a cold hydrogen gas stream, but the energy required to cool a pressure vessel tank wall is significantly greater, such that any practical refueling stream of hydrogen would take too much time to cool the system down to 80 K. The concept is to use a separate stream of LN2 to cool the massive pressure tank wall and to use flow-through cooling on the inside of the vessel to cool down the adsorbent material.

Proof-of-concept testing demonstrated the feasibility of the concept using an aluminum pipe system. A 2-L prototype system was designed using an actual aluminum Type-I tank and a custom fabricated vacuum jacket. The prototype was tested in two test series and the data was analyzed to project the cooling efficiency of a full-scale tank system.

3.3.1 Evaluation of the Concept

The proof-of-concept testing and the prototype testing were developed to demonstrate the ability of a flow of LN2 to cool a thick-walled aluminum pipe that had the thickness of a realistic full-scale Type-I tank. The proof-of-concept test series is described in Section 3.3.1.1 below. A key finding was that the LN2 mass flow rate needed to be increased to achieve cooling times that would meet the DOE target goals. The prototype testing is described in Section 3.3.1.2.

A key concern that drove the design of the prototype was the potential pressure buildup within the vacuum jacket cavity caused by boiling nitrogen. The proof-of-concept test configuration was not designed to maintain a pressure boundary, so no information on pressure buildup within the LN2 cavity was gained in the test series. The only available information related to pressure was the exhaust stream, which went through a number of distinct phases. The conclusion was that the exhaust became a rapidly flowing, mixed-phase steam containing droplets of LN2. Rapidly flowing steam indicated a net pressure buildup within the LN2 cavity, but its magnitude remained unknown. Hexagon Lincoln staff worked with the vacuum jacket manufacturer to design a safe and functional vacuum jacket for testing, with sufficient customizable vent ports to accommodate a variety of test configurations. The safety considerations

resulted in a prototype that was not well suited to long-term dormancy testing, but it proved to be adequate for a time scale that covers a fill-up scenario**.**

The first test series using the 2-L Type-I prototype tank demonstrated that the pressure buildup within the LN2 cavity was negligible. It also demonstrated that a typical LN2 supply line does not provide sufficient LN2 mass flow rate to cool the 2-L prototype fast enough to meet DOE target goals. Much higher mass flow rates were achieved using a reservoir system that was filled from the LN2 supply before each test. The reservoir tests provided cooling rates that are projected to cool a full-scale system to meet the DOE target goals. The second test series increased the maximum LN2 mass flow rate by using a larger reservoir to achieve the maximum cooling rates. A final test was run on a Type-III prototype tank. This series demonstrated very low cooling rates that do not meet DOE target goals**.**

3.3.1.1 Proof-of-Concept Testing – Type-I Prototype Tank

Tank Wall System Configuration

The proof-of-concept testing was performed on a simulated tank wall system with a configuration shown in Figure 3.3. The central aluminum pipe wall represents the wall of a Type-I aluminum tank. The wall thickness was 6.5 mm in the first series and increased to 17 mm in the second series, with 17 mm being the estimated wall thickness necessary in a full-scale system (ca 200 L). Thermocouples were attached to the inside wall of the aluminum pipe. The LN2 cavity is an annular void that runs along the pipe between the inlet and the vent. Three different configurations were tested to vary the annulus radial width: 3 mm, 6 mm, and 9 mm. Larger annulus sizes provide more empty volume for the LN2 to fill while smaller sizes are more preferable to meet the DOE volumetric goal. The size of the outer jacket defined the annulus width, so three different sizes were constructed. In early cases, the system was tested as pictured in Figure 3.3. In later cases the outer jacket was wrapped in insulation to reduce energy losses to the environment. While the additional insulation helped, it was still not representative of a realistic system, which uses a vacuum jacket and multilayered insulation to achieve highly effective thermal barrier. Because of this, the cooling rates achieved during testing were expected to be conservative compared to a realistic system.

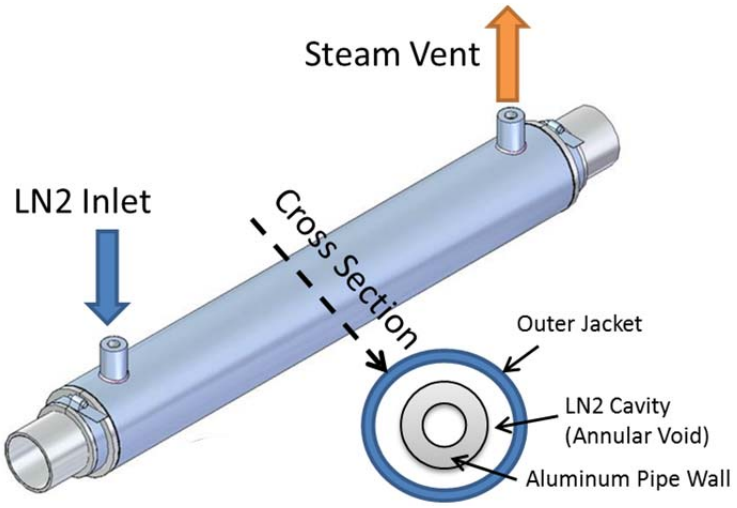

Figure 3.3. Proof-of-Concept Test Configuration of LN2 Cooled-Wall Type-I Prototype Tank

Experimental Setup for Testing of LN2 Cooled-Wall Type-I Prototype Tank

The experimental setup is shown in Figure 3.4. In this test case external insulation was not used. The LN2 supply is connected to a load cell, which measures the mass of the tank and provides information on the amount of LN2 used during the test. To start the test, the valve on the LN2 tank is turned to the full open position. The LN2 tank is pressurized to approximately 21 psig (1.5 bar), so nitrogen starts to flow into the LN2 cavity immediately, but the test data reveals a significant time lag before cooling begins. In cold-fill test cases (that start with aluminum wall temperatures near 160 K), a distinct warming of the aluminum pipe wall occurred. While this is known to be a consequence of the test configuration, this phenomenon needs to be considered when practical LN2 delivery methods are considered at the filling station.

Figure 3.4. Proof-of-Concept Test of LN2 Cooled-Wall Type-I Prototype Tank

The tests were conducted until a temperature saturation limit was achieved, which was usually below 90 K for all locations. Liquid nitrogen boils at 77 K at atmospheric pressure, and some thermocouple locations near the inlet reached temperatures below 85 K, but 90 K (-183°C) is a more practical goal because of the heat-transfer physics between LN2 and an aluminum tank wall. Figure 3.5 shows an example of the thermocouple data and the LN2 mass data for a cold-fill case with a 3-mm annulus. The temperature curves all have a distinct shape that consists of a slow cooling phase followed by a rapid cooling phase. While the rapid cooling knee occurs at a slightly different temperature for all thermocouples, this phenomenon can be traced back to the physics of LN2 surface boiling regimes. When the difference in temperature between the surface and the LN2 is relatively high (film boiling, $\Delta T > 55$ K) the heat transfer from the surface to the liquid is severely impeded by bubbles of nitrogen gas. Heat transfer from the surface to the LN2 becomes much better in the transition boiling and nucleate boiling regimes until the ΔT gets below about 10 K. This explains why testing shows rapid cooling from 130 K down to 90 K, and slower cooling outside this temperature band.

Data Analysis – Test of LN2 Cooled-Wall Type-I Prototype Tank

An early analysis of this data that relates cooling to mass flow rate is presented in Figure 3.6. The useful energy transport is defined as the amount of energy removed from the aluminum test pipe in one time step (0.5 second) divided by the LN2 mass flow rate (kg/s). For comparison, the heat of vaporization of LN2 is

199,000 J/kg, and in a half-second time step would cool 99,500 J. This indicates that the mass of LN2 flowing into the system has a lot more cooling capacity than is being used by the aluminum pipe wall. While energy losses to the environment are expected to be relatively high, the outer jacket of the test article and other items of hardware also deplete cooling energy. Figure 3.6 also shows photos of the steam vent and notes that by 235 seconds liquid nitrogen droplets are visible in the exhaust stream, so some LN2 cooling capacity is lost while passing through the system without boiling. Aside from these losses and system inefficiencies is the fact that LN2 boiling at a surface is limited by heat-transfer physics. Excess LN2 entering the system that does not boil will collect within the annulus. As more liquid collects within the annulus, more surface area is contacted, leading to increased cooling performance. While the test series does not have any way of determining how much LN2 was present within the annulus at any time, there are indications in the test data that surface area coverage is responsible for increased cooling efficiency. This leads to the design goal of flooding the LN2 cavity with LN2 as quickly as possible to achieve the greatest surface area coverage in order to achieve the fastest cooling.

If eliminating the mass flow rate component, Figure 3.7 shows the average surface cooling flux for the thick-walled test series in cold-fill cases. The theoretical limit of the film boiling phase is calculated assuming complete surface coverage of the aluminum pipe. The first 2 minutes of each of the three tests shows significant room to achieve greater cooling heat flux if more surface area is covered by LN2. This figure shows that surface area coverage is the key because the test starts with an empty LN2 cavity. In all three cases, the LN2 flows down onto the aluminum pipe surface, which ramps up to a steady value in the first 10 seconds. At about 70 seconds, the 3-mm annulus case starts to increase its cooling flux. At about 90 seconds, the 6 mm case starts to ramp up. Then, at 100 seconds, the 9-mm annulus case begins to ramp up. This sequence indicates that with an approximately equal mass flow rate the more shallow geometry in the 3-mm annulus case is the first to expose more of the aluminum pipe wall with LN2, followed by the middle 6-mm case and finally the deepest 9-mm case. It is not clear why the 6-mm annulus reaches peak cooling fluxes before the 3-mm and 9-mm annulus cases at approximately 240 seconds.

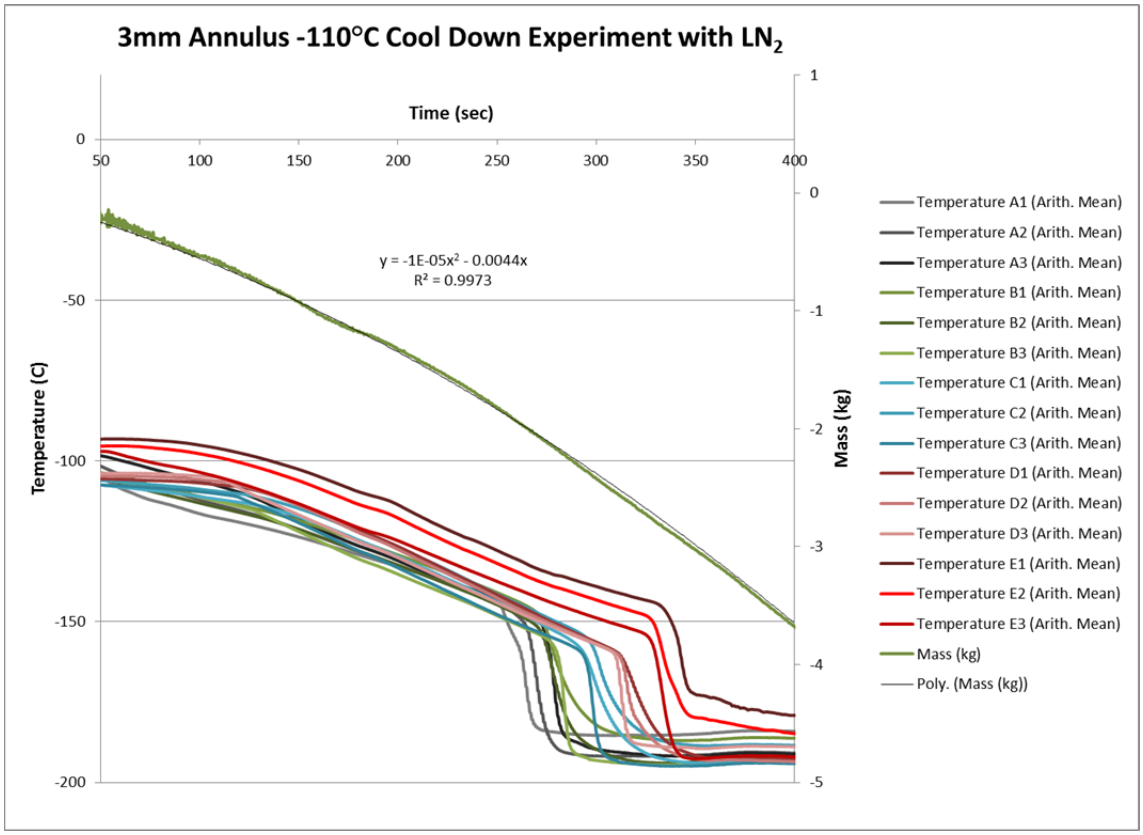

Figure 3.5. Example of Proof-of-Concept Test Data from the LN2 Cooled-Wall Type-I Prototype Tank

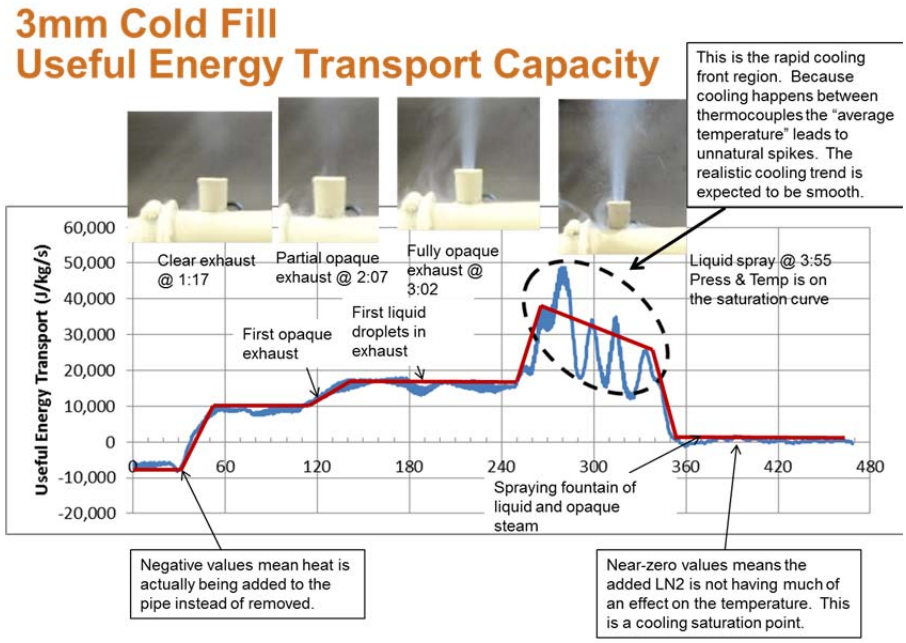

Figure 3.6. Example Proof-of-Concept Test Data Analysis of LN2 Cooled-Wall Type-I Prototype Tank

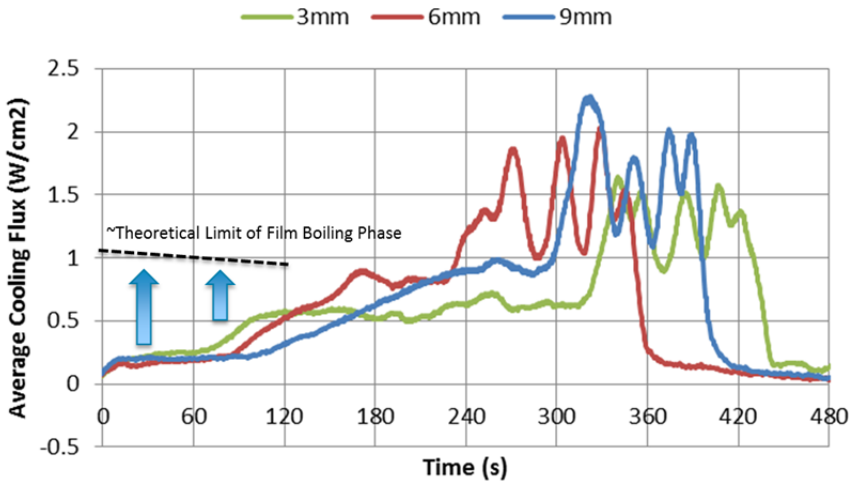

Figure 3.7. Average Cooling Flux for a Test Series of Three Annuli Sizes

The concept of filling the annulus space with LN2 to achieve maximum cooling is also supported by the analysis of test data for the 9-mm room-temperature and cold-fill test cases. The bounding limit data plotted in Figure 3.8 is digitized data from Jin et al. (2009), which is from full-immersion tests. The idea is that full immersion in LN2 offers the greatest possible surface heat transfer and so forms a natural limit of cooling rate. The room-temperature case shows that the average surface cooling flux starts off well below the bounding limit, but as the test continues it eventually starts to reach the theoretical limit. The cold-fill case behaves the same way. In the rapid cooling range between 10 K < ΔT < 50 K there are significant local effects affecting the average surface heat-flux calculation (as Figure 3.7 shows, there can be a 50 K difference in temperature along the length of the pipe when rapid cooling starts), and there is the possibility that rapid consumption of LN2 would deplete the reservoir, thereby lowering the surface coverage. While the local behavior during cooling is more complicated than the surface averaged behavior illustrated in Figure 3.7 and Figure 3.8, the averaged behavior provides evidence that cooling rates approaching the full-immersion rates are achievable with a higher mass flow rate. The 2-L prototype test campaign was needed to determine how closely a realistic system could match the full-immersion rates.

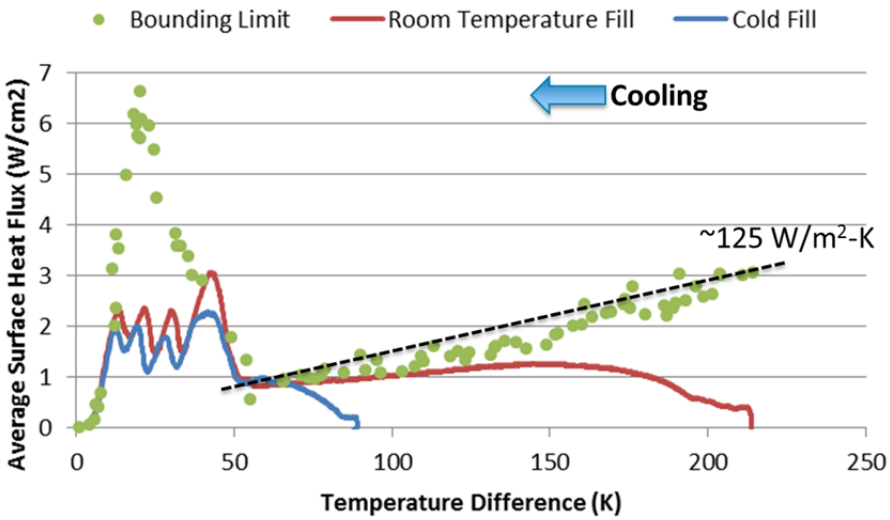

Figure 3.8. Concept of Filling the Annulus Space with LN2 to Achieve Maximum Cooling: Annulus Cases (9 mm) Compared to Full-Immersion Data (Jin et al. 2009)

3.3.1.2 2-L Type-I Prototype Tank: Prototype Design to Study Cooling Rates

The 2-L prototype system was designed to study cooling rates in a safe and configurable test environment. Figure 3.9 shows the system components. At the heart of the prototype system is a commercially available 2-L aluminum tank with a minimum wall thickness of 0.165 inches (4.2 mm). A custom dewar (i.e., vacuum jacket vessel) was fabricated to surround the aluminum tank. A baffle support was designed to position the aluminum tank within the dewar cavity. A foam plug was used to take up extra space in the dewar and provide insulation to reduce heat loss through the flat end plate.

Figure 3.9. 2-L Type-I Tank Prototype LN2 Wall Cooled System

PNNL worked with Hexagon Lincoln and Cryofab, the dewar manufacturer, to design the dewar for function, configurability, and safety. Some of the dewar design features adversely affected the insulation capability of the system, such as the extra vent port at the rear of the dewar and the flat (non-insulated) end plate, but the insulation performance of the dewar was demonstrated to be sufficient for the purposes of short-term cooling. The dewar design was not sufficient for dormancy testing, which is a much larger time scale.

The aluminum pressure vessel was cut through the middle to provide access to the inside surface to apply thermocouples. Figure 3.10 shows the general location of thermocouples. Note that space was limited in the end zones (A and E) so only two thermocouples were located there instead of three. As shown in Figure 3.11, the two extra thermocouples were applied to the outside of the test system to provide information about the thermal efficiency of the dewar. The two halves of the aluminum pressure vessel were welded back together prior to testing. For this test campaign, it was not necessary for the pressure vessel to maintain an internal pressure, so the purpose of welding was to ensure a proper conduction path between the two halves.

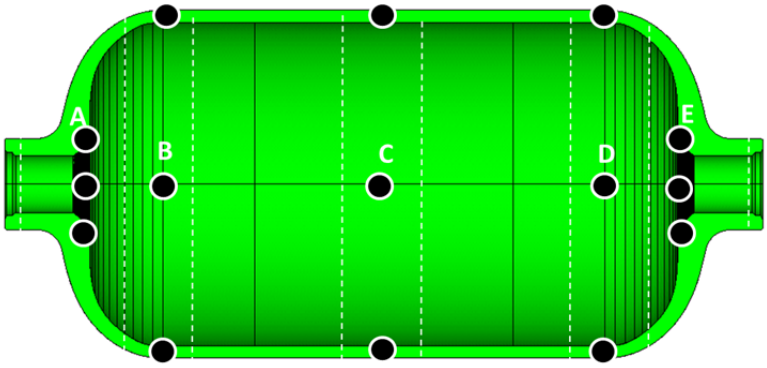

Figure 3.10. Type-I Prototype Tank LN2 Cooled Wall: Thermocouple Zones

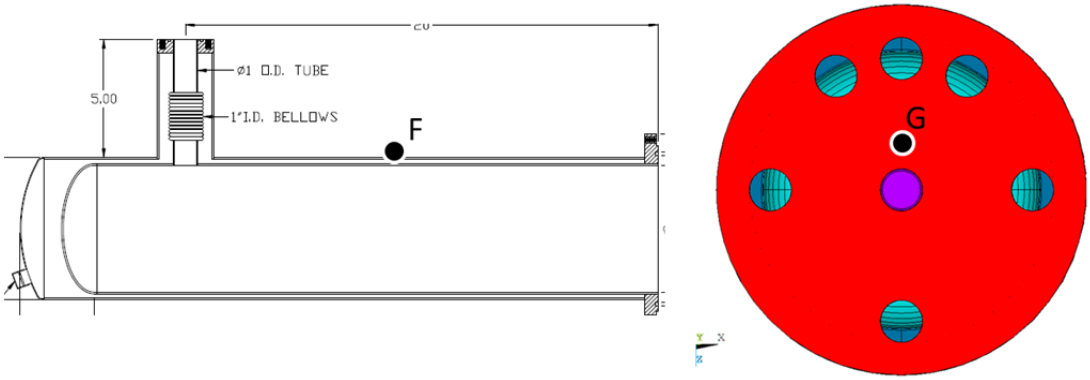

Figure 3.11. Type-I Prototype Tank: Additional Thermocouples F (left) and G (right)

Even though the dewar insulation was much less effective than a realistic system, it was so effective at maintaining cryogenic temperatures that outside assistance was necessary to speed up the warm up between test cases. Dry compressed air was used to blow air through the dewar vents to enhance natural convection. It took a few minutes of compressed air flow to raise the temperature from 90 K to 160 K, while allowing it to warm up naturally would take a few hours. A sketch of the aluminum pressure vessel with its aluminum support structure is shown in Figure 3.9. The purpose of the support structure is to position the pressure vessel within the dewar cavity and manage the gap space. In the second test series a tube system replaced the support structure. In all test cases the pressure vessel was oriented with the maximum gap at the top to ensure a clear path to the rear vent was available for the gaseous nitrogen and steam. The bottom of the aluminum pressure vessel was in contact with the dewar wall. The line of contact offered a conduction path between the aluminum vessel and the stainless steel dewar, but in the short-duration cooling scenarios of the test campaign that conduction path is not expected to affect the overall cooling efficiency in a significant manner.

3.3.1.3 Type-I Prototype Tank – First Test Series

The first test series considered two methods for introducing LN2 into the prototype system: 1) a direct line from the LN2 supply and 2) a 5-L reservoir that was fashioned from steel pipe. Figure 3.12 shows photographs of the reservoir fill system. The upper right photo shows the reservoir filling process, which was done directly form the LN2 supply or filled by pouring LN2 in from a secondary vessel. The photograph on the left shows the valve handle that is turned to empty the reservoir into the dewar. The approximately 5-L capacity of the reservoir provided an estimated 67 g/s of LN2 to the prototype in 1 to 2 minutes. The direct line from the LN2 supply provided an estimated 15 g/s of LN2 once the

delivery system cooled down to cryogenic temperatures. The cool-down period of the direct line was important to note because it caused a significant warm up of the aluminum tank until the supply line cooled down sufficiently. The supply line was insulated, as shown in the bottom right photo, but it was approximately 6 to 8 feet (183 to 244 cm) in length. Gaseous nitrogen was always the first species to flow from the supply line until it cooled enough to allow LN2 to flow. This phenomenon affected the cooling rates for all of the direct line cases.

Figure 3.12. Type-I Prototype Tank: Reservoir Fill System for First Test Series

The best cooling rate of the first series was achieved in Case 15, which was a reservoir fill case that began with an average aluminum tank temperature of 160 K. Figure 3.13 shows the thermocouple data recorded within the aluminum tank. The LN2 reservoir was empty at 63 seconds, but the temperature continued to decrease for at least another 2 minutes. It was typical for the temperature to remain at a saturation limit for many minutes before the temperature started increase. In this case, the average temperature reached a minimum of 85 K at 346 seconds.

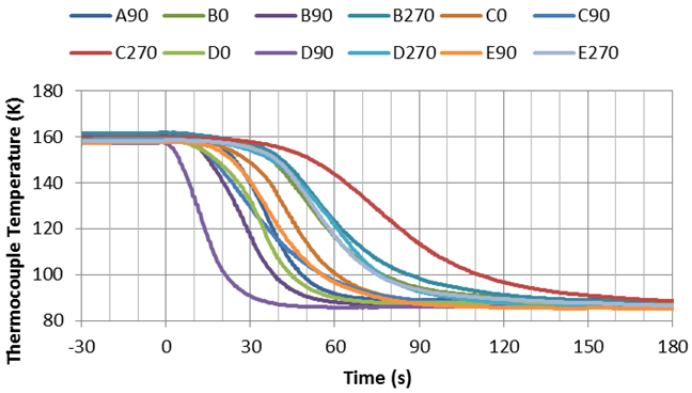

Figure 3.13. First Test Series: Case 15 Thermocouple Results Showing the Best Cooling Rate

Figure 3.14 compares the average thermocouple data to the ideal target, which is estimated from the aluminum tank surface area and the experimentally determined heat-transfer coefficients under full immersion in LN2. The ideal target is a simple estimate of the cooling rate that can be accomplished with full immersion in LN2. As will be discussed in more detail in the next section, the ideal target is not the physical limit of cooling rate because it does not consider the true three-dimensional geometry of the pressure vessel and variations in wall thickness. It serves as a useful target or benchmark of cooling rate performance. The comparison between ideal target and average thermocouple temperature data shows that the prototype cooling rate is similar to full immersion for the first 40 seconds, but the steep cooling rate expected during full immersion is missing. Considering the temperature variation at locations within the aluminum vessel that are apparent in Figure 3.13 it can be concluded that the surface area of the prototype case is not evenly covered with LN2. The ideal target curve assumes the aluminum tank is fully covered with an ample supply of LN2, the wall thickness is uniform, and heat conduction occurs instantaneous. The reality of the prototype test seems to be an uneven surface coverage of LN2 with local cold spots driving the cooling down rate, with conduction playing a critical role in transporting heat and equalizing temperature.

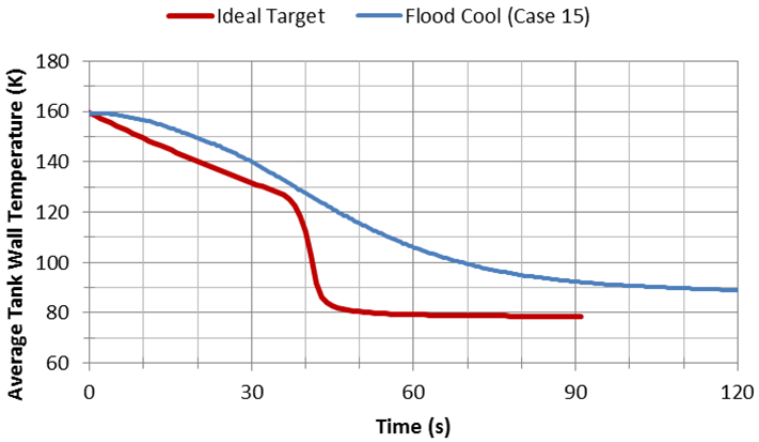

Figure 3.14. First Test Series: Case 15 Average Temperature Compared to Ideal (full immersion)

An example of a case, Case 8, with a direct line from the supply is plotted in Figure 3.15. Instead of the steel reservoir pictured in Figure 3.12, the insulated supply line also visible in Figure 3.12 was used to flow LN2 directly into the prototype for a specified amount of time. The supply valve was kept open for 183 seconds (approximately 3 minutes). This test demonstrates the unintended warm up of the aluminum vessel during the first minute. It also demonstrates the continued cooling of the tank for over 3 minutes after the supply valve was closed. The time duration of the test also shows how relatively slow the cooling rate was compared to the reservoir fill cases (e.g., Case 15). It is concluded that the direct line cases are not sufficient because of their limited LN2 mass flow rate due to the narrow diameter of the insulated supply line.

A total of 16 data sets were collected in the first test series, and they indicated a need to test at higher mass flow rates. One important observation of the first test series was the determination that the gas pressure within the dewar remained negligible with even the highest mass flow rate cases. The digital pressure transducer was well calibrated in the 5 to 50 psi (0.5 to 3.5 bar) range at room temperature, and never recorded pressure data at higher levels in the calibration range for any test. While no conclusive pressure readings were collected, the low range of the data gave confidence that increasing LN2 mass flow rate and reducing vent capacity were safe practices to pursue in the second round of testing.

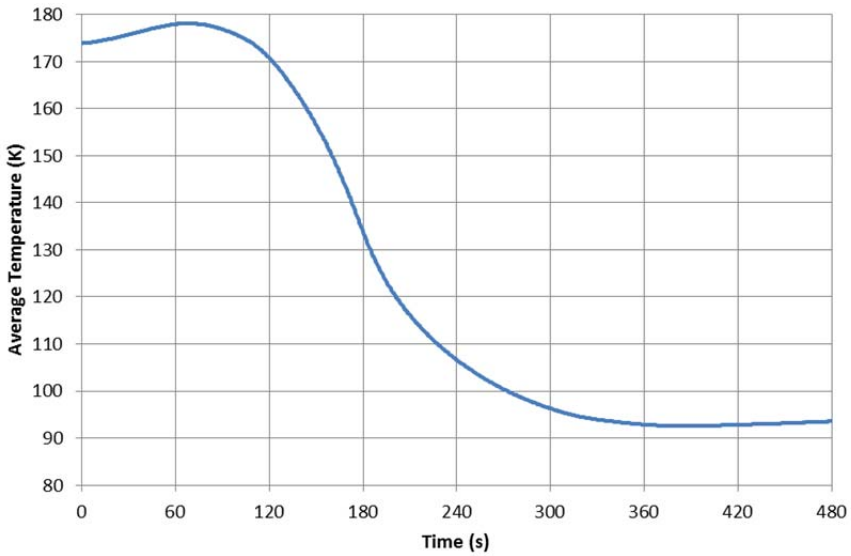

Figure 3.15. First Test Series: Case 8 – 3-Minute Timed Fill

3.3.1.4 Type-I Prototype Tank: Second Test Series

The second test series built upon the experience of the first test series and sought to increase the LN2 mass flow rates to demonstrate the highest cooling rates possible for the prototype system. A second goal was to try to enhance the cooling efficiency of the direct supply line delivery of LN2 by using tubes to direct the flow of LN2 against the sides of the aluminum pressure vessel. Figure 3.16 shows the second test series configuration. The left photograph shows a new reservoir made from a spare carbon fiber tank. The new tank has a volume capacity of about 6 L and is situated at the rear port of the dewar, providing a more direct route for the LN2 to reach the aluminum tank. The right two photos show the shower spray configuration, which divides the flow of LN2 with a T junction. Each of the lines has slits in the tubes that try to spray the sides of the aluminum tank with LN2. The tubes also act as a support structure to keep the aluminum tank from floating and cutting off the flow path to the back vent.

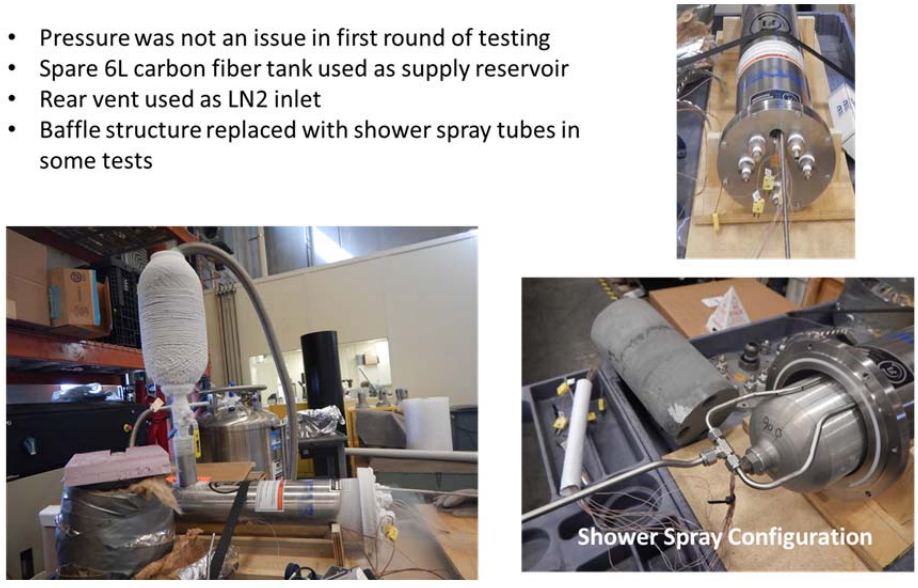

Figure 3.16. Type-I Prototype Tank: Second Series Test Configuration

The best cooling rates came from using the 6-L reservoir at the rear port. Case 19 used the shower spray tubing as a replacement for the baffle structure. Case 32 used the baffle structure, and is similar to Case 15 from the first series with a change in reservoir size and location. Figure 3.17 shows the average temperature history for both cases compared to the ideal target, which is the same target definition as in the previous section and assumes full immersion of the aluminum tank in a bath of LN2. Both of the experimental cases show a favorable comparison to the ideal target up to 40 seconds. After 40 seconds, both test cases fail to reach the 80 K floor of the target temperature. The fact that both experimental curves cross the ideal target line is not a violation of physical laws, but is an indication that the ideal target is an over-simplification of the true limit of cooling and the construction of the average temperature from limited thermocouple data also is simplified.

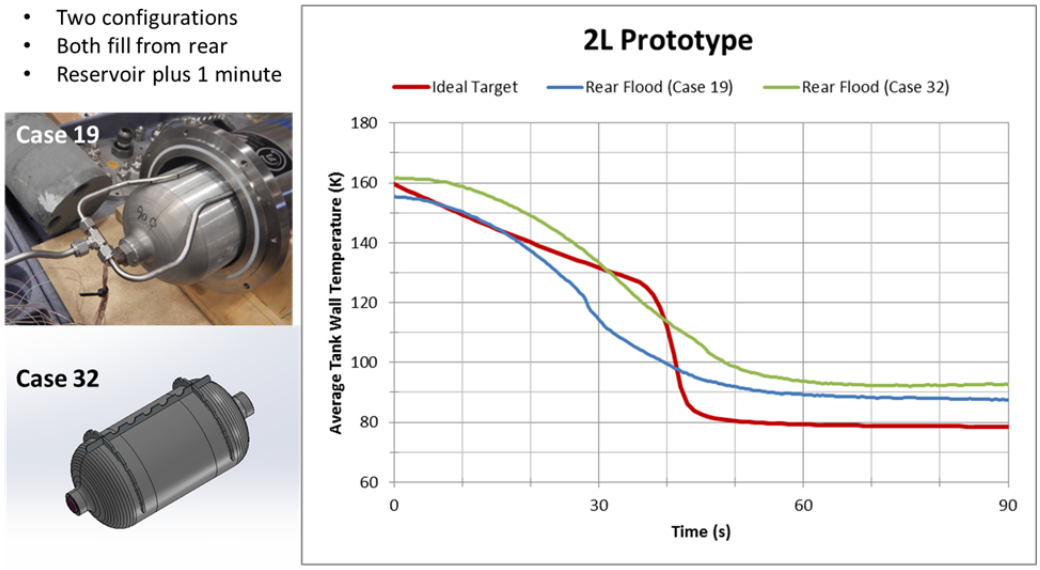

Figure 3.17. Type-I Prototype Tank: Flood Cool Cases – Average Temperature History for Both Cases (19 and 32) Compared to the Ideal Target

To further explain how the average thermocouple data can pass below the full-immersion ideal target, Figure 3.18 shows a comparison between the minimum, average, and maximum thermocouple data for Case 19 compared to the ideal target. The first thing to note is that the starting temperature for the ideal target is exactly 160 K, while the test started slightly lower at 155 K. This accounts for some of the difference, but the greatest difference in performance is indicated by the minimum thermocouple data curve. This curve represents the minimum reading across all thermocouples at each point in time. The pressure vessel drawing in Figure 3.11 shows the approximate thermocouple locations, but also notes the difference in wall thickness around the pressure vessel geometry. The coldest thermocouple reading occurs in the thin-walled section where there is much less material to cool than in the end-boss regions. Also note that both ends of the pressure vessels contain end plugs that add to the total mass of the pressure vessel. The ideal target temperature is constructed considering the outside surface area of the actual pressure vessel and the total mass while neglecting heat conduction and geometry effects.

The ideal target calculation is flawed because, locally, the thin-walled regions can cool much faster than the thicker end regions. In addition, the average temperature based on thermocouple data is flawed because nine thermocouples are on thin-walled locations while four are on thick-walled locations. A more accurate estimate of energy removal could be accomplished by weighting the thermocouple data differently; that is, by assigning more weight to data that represent the end regions and less weight to data that represent the thin cylindrical section of the tank. However, for the purposes of this study, the

estimates and averages are close enough to conclude that the rate of energy removal demonstrated in this test series is sufficient to meet the DOE target goals, with some room for improvement based on the LN2 mass flow rate.

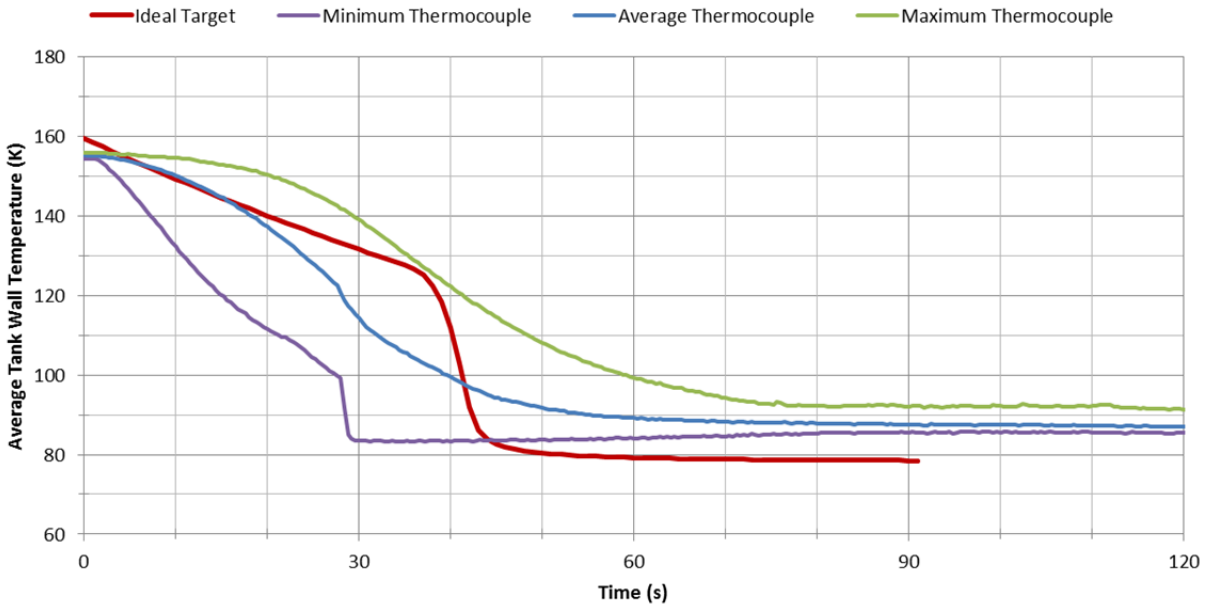

Figure 3.18. Type-I Prototype Tank: Second Test Series – Case 19 Comparison to Ideal Target

The shower spray cases did not provide a sufficient cooling rate to meet DOE target goals. Figure 3.19 shows the average thermocouple data for a case with the rear vent closed (Case 26) and open (Case 24). The tubing used to construct the shower spray configuration was standard Swagelok 0.25-inch (6.35 mm) diameter tubing. Each of the side tubes was perforated to direct LN2 against the aluminum pressure vessel. Each tube was also crimped at the ends to force the LN2 to exit the tube through the perforations. This method of delivering LN2 was not expected to match the reservoir cool cases, which delivered a much greater mass flow rate over a much shorter time period. The reservoir cooled cases could cool the aluminum tank from 160 K to 90 K in approximately 1 minute, while the shower spray cases requires 7 to 9 minutes, and spent the first 4 to 5 minutes in a net warming period for the tank. It is envisioned that a filling station would use a direct LN2 line connection to a real cryo-adsorbent tank system implementation; this test demonstrates that the LN2 line at the filling station needs to be pre-cooled to minimize unwanted thermal energy transfer to the cryo-adsorbent system.

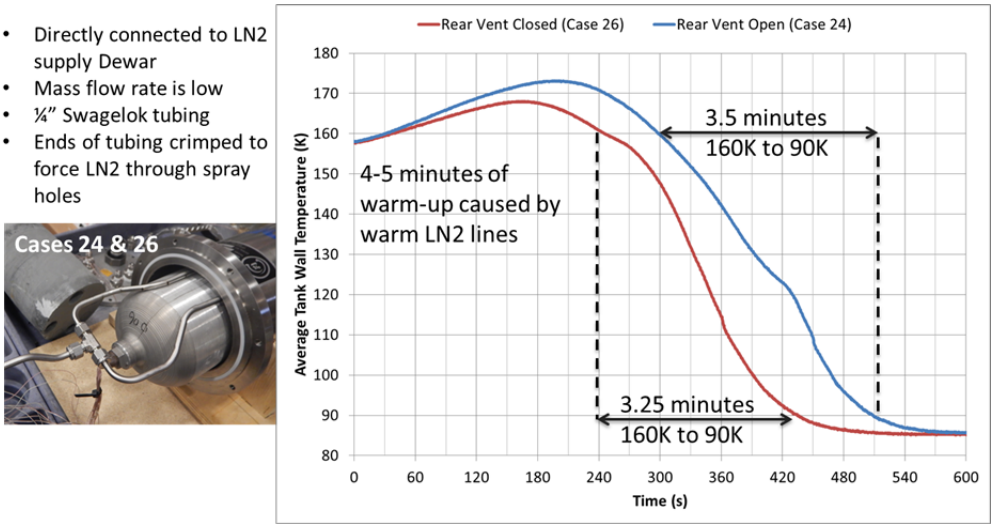

Figure 3.19. Type-I Prototype Tank: Second Test Series Shower Spray Cases (Cases 24 and 26)

3.3.1.5 Type-III Prototype Tank Test

As an extra test series, Hexagon Lincoln fabricated a Type-III tank using the Type-I aluminum tank as a liner and tested the tank cooling performance in the prototype system under reservoir fill and shower spray LN2 delivery conditions. The Type-III tank is shown in Figure 3.20. All test cases showed a distinct disadvantage compared to the Type-I tank performance. The fundamental problem is believed to be the heat conduction behavior of the carbon fiber overwrap. While aluminum is a relatively good conductor of heat, carbon fiber in resin has a thermal conductivity that is approximately 30 times lower.

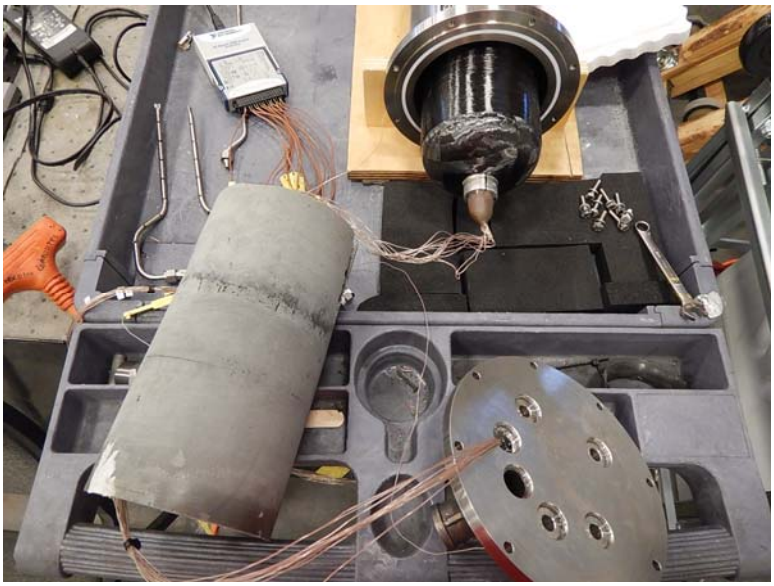

Figure 3.20. Type-III-Prototype Tank Test Configuration

Figure 3.21 presents a comparison of Type-III tank cooling performance using reservoir cooling is compared to Type-I performance. All cases used the 6-L carbon fiber composite tank as the reservoir. The data show that Type-III tanks are much slower to cool and never reach 90 K. The reservoir is expected to have emptied in the 60 to 120 second range, which was enough to cool the Type-I tank to a useful

temperature. The temperature data suggest that the 6-L reservoir did not provide enough total LN2 to cool the Type-III tank; surface coverage of LN2 must have been low after about 120 seconds. Additional reservoir capacity or higher mass flow rates could potentially help the system cool faster, but the existing data set do not demonstrate that Type-III tanks can be cooled in an acceptable amount of time using the LN2 wall-cooled concept. Additional reservoir capacity is not expected to improve cooling during the first 60 seconds by much, and cooling in approximately 60 seconds is needed to demonstrate that the scaled-up system will meet DOE target goals.

Cooling rate performance for the Type-III tank is no better in the shower spray case, but the sustained LN2 delivery succeeds in cooling the tank to 90 K. Figure 3.22 shows the cooling performance of the Type-III compared to the Type-I tank cooling in the shower spray case. Note that the unintended heat-up of the aluminum is higher and takes longer to cool down to the starting temperature in the Type-III case. With the same LN2 delivery system, the Type-III tank takes approximately two times longer to cool. This mass flow rate system was not good enough to meet the cool-down targets for the Type-I tank and is even worse for the Type-III tank.

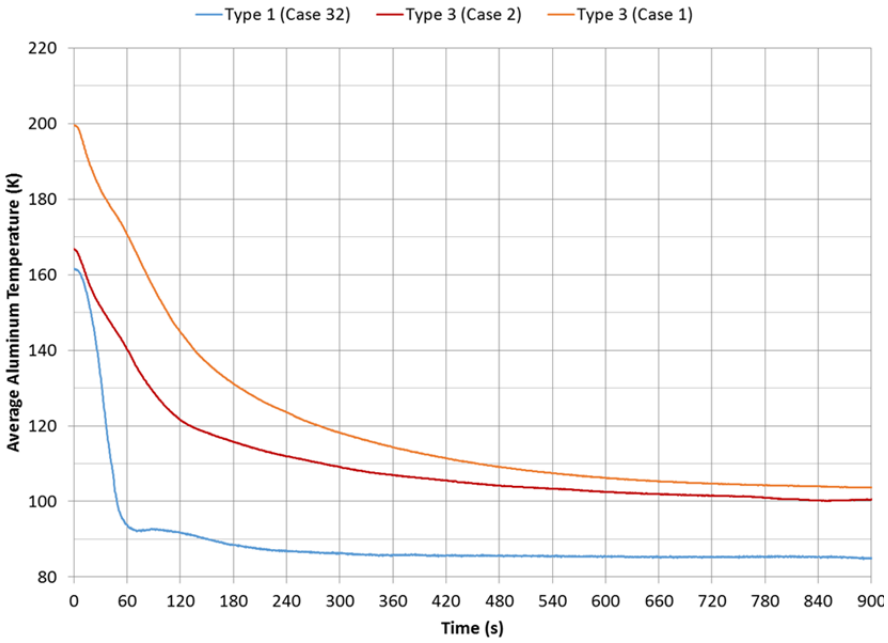

Figure 3.21. Type-III Prototype Tank Testing: Reservoir Cooling

3.3.2 Analysis and Results of Prototype Testing

The temperature data collected during testing is used to construct an average surface heat flux versus temperature relationship. It is assumed that a full-scale system that uses the same type of LN2 delivery system will have a similar average surface heat flux. Realistically, a system with a form-fitting vacuum jacket and multilayer vacuum insulation would be expected to have better cooling performance because of the superior insulation and less void space. Mass flow rates can also be increased beyond the limitations of the test system, thereby offering even more room for improvement.

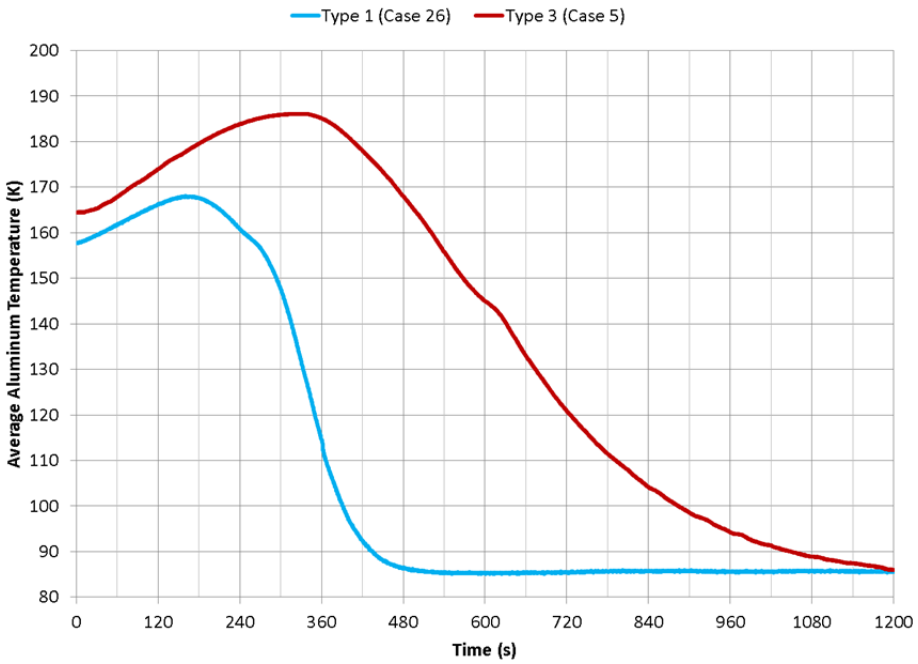

Figure 3.22. Comparison of Type-I and Type-III Prototype Tank Shower Spray Cases

3.3.2.1 Experimentally Demonstrated Cooling Heat-Flux to Scale-Up Results

To compare the different test iterations completed during the two rounds of testing, the cooling behavior in all cases is translated into an estimate of surface heat flux. This calculation assumes that the thermal energy change of the aluminum pressure vessel (based on the material heat capacity and change in average temperature) exits the pressure vessel evenly through the total surface area (1063 cm^2). The heat capacity of aluminum is temperature dependent, so the amount of energy required to lower the tank temperature by one degree Kelvin can change significantly in the temperature range of interest (80 K to 160 K). This method for characterizing the cooling behavior of each case captures the net cooling effect of a number of complex physical processes and test case variables, such as mass flow rates, total time durations, localized cooling effects, and vent capacity. The assumption is that whatever the specifics of the test cases were, if the same conditions are applied to larger or smaller tanks with properly scaled-up LN2 mass flow rates, then the same average heat fluxes can be achieved. Relatively larger LN2 mass flow rates lead to relatively higher heat fluxes. Warm-up effects caused by direct connection to the LN2 supply are indicated in the data as negative heat fluxes (negative is an intrusion of heat, positive is the desired removal of heat).

Figure 3.23 shows plots the heat flux versus temperature for cold-fill cases from both test series. The curves generally have a gentle hump or hill type shape, and most have a pronounced peak that corresponds to local rapid cooling. The conditions that cause rapid cooling are dependent on the local temperature and the locally available supply of LN2. Because of surface boiling physics, noticeably higher heat flux is expected to occur at local temperatures between 90 K and 125 K. Rapid cooling can consume all of the available LN2 and be limited by how quickly the incoming LN2 can replace the boiled-off LN2. The data in Figure 3.23 generally shows three tiers of heat flux, with the back flood cases demonstrating the highest flux, the front flood case showing a medium flux, and the spray cases associated with the lowest flux. The rank of the tiers is consistent with the estimated LN2 mass flow rates of each tier.

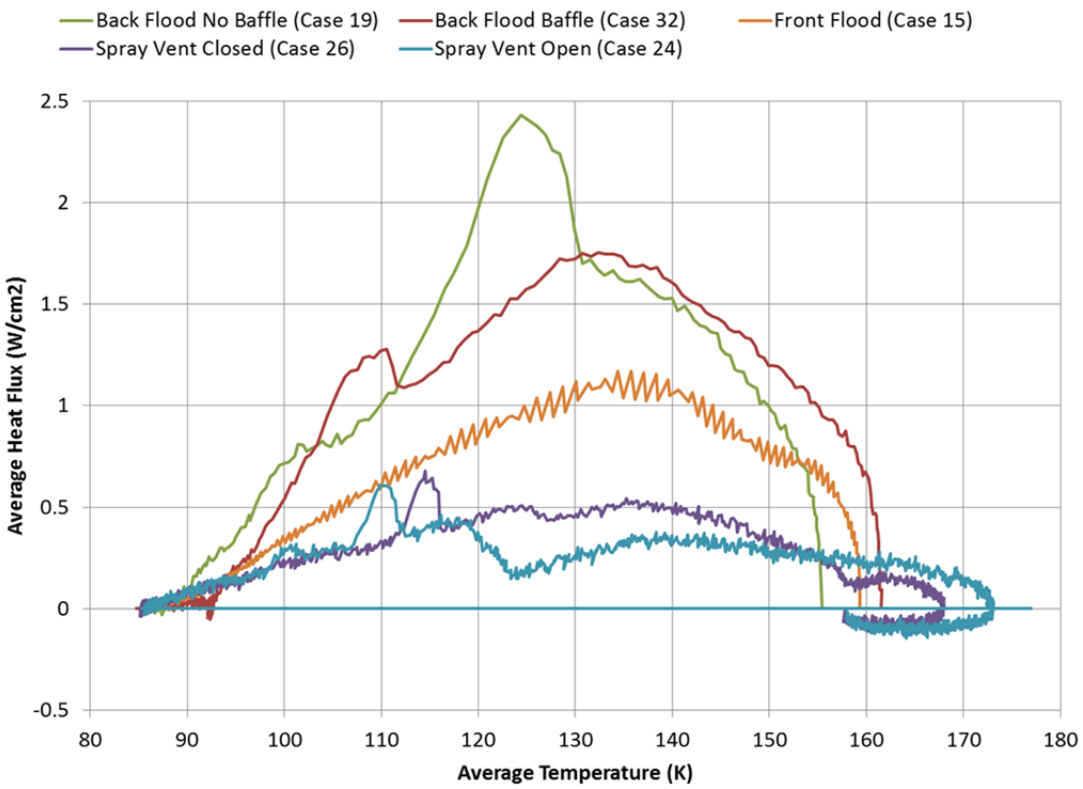

Figure 3.23. Summary of Heat Flux in Cold-Fill Cases from Two Rounds of Prototype Testing

The direct connection cases offer the lowest tier of cooling performance, but this is easily explained by the relatively low mass flow rate. In previous testing on insulated pipe walls, the flow rate of the direct LN2 delivery system was determined to be a steady 15 g/s once the supply lines cooled down. A direct measurement of LN2 mass transfer was not made in this test series because of the anticipated use of reservoirs to achieve higher mass flow rates. Figure 2.1 shows the flux behavior in the cases that were directly connected to the LN2 supply. In each case, negative flux indicates an initial warming of the aluminum pressure vessel caused by warm nitrogen gas from the supply line. Cases 7, 9, and 10 were collected during the first test series, and the supply line was connected directly to the port at the 6 o'clock of the dewar end plate. The LN2 flow path was along a horizontal hole in the foam plug. The rear vent was open in all of the first series cases because of concerns about potential pressure buildup from the boiling nitrogen. The two shower spray cases were conducted in the second test series when pressure was no longer a concern, such that in Case 24 the the rear vent remained open and in Case 26 the rear vent was closed. In both shower spray cases the LN2 was piped through the 12 o'clock port and the spray of LN2 was directed at the top and sides of the pressure vessel so the overspray would flow down the sides.

The reservoir fill cases offer superior cooling for the 2-L prototype based on temperature-history and heat-flux data. This is ascribed to a relatively larger mass flow rate compared to the direct supply line cases. In the first test series cases, the reservoir was approximately 5 L in capacity and was empty after about 1 minute of flow. The second test series used a 6-L capacity tank and tended to empty in the same time. In addition, cases were run in the second series with the LN2 flow from the supply continuing to flow into the reservoir for 1 minute after the reservoir valve was turned on or off, which provided the maximum possible mass flow rate that was achievable with the equipment available. The mass flow rates are estimated to be 67 g/s in the front flood cases, 81 g/s in the back flood cases, and 96 g/s in the back flood cases with additional flow from the supply dewar. These three LN2 supply conditions are approximately 450%, 550%, and 650% higher than in the direct-connect cases.

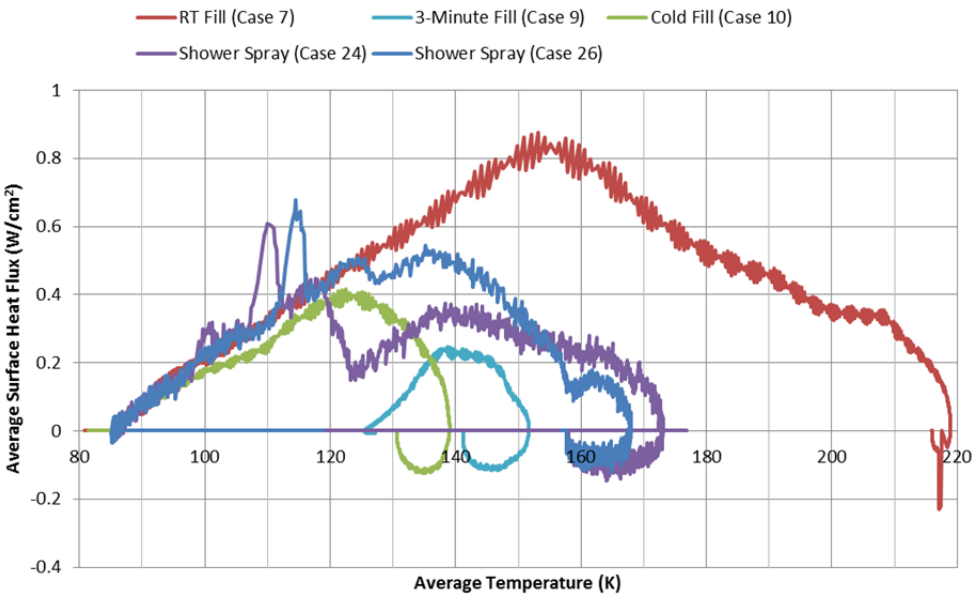

Figure 3.24. Flux Behavior of Direct Connection to LN2 Supply Cooling Cases

The strategy of flooding the dewar with as much LN2 as possible works to maximize surface area coverage with LN2, but it also raises the question of how much LN2 flow is really usable. Excess LN2 was observed leaving through the vent as liquid droplets in the nitrogen steam. In addition, excess LN2 in the dewar after the fill test was completed often kept the temperature low for many minutes before natural warming began. The reservoir fill system used in testing did not allow for easy measurement of LN2 mass flow rates, but two test cases were run to evaluate the amount of over-supply of LN2 into the 2-L prototype dewar.

Figure 3.25 shows the comparative cooling times (left) and comparative heat flux profiles (right). Case 30 begins at room temperature and Case 31 begins at 160 K (cold fill). Regardless of the starting temperature, one 6-L reservoir full of LN2 was sufficient to cool both cases to the desired temperature. This indicates that an excess amount of LN2 was used in the cold-fill case beyond the necessary minimum. Another interesting observation is that the reservoir emptied in both cases in about 1 minute, but steady cooling continued in the room-temperature case for about 4 minutes. This indicates that LN2 was held within the dewar for 6 minutes or more. The flux comparison shows a significantly higher flux in the temperature range of interest for Case 31. This can be explained by the amount of surplus LN2 held within the dewar: the more LN2 the dewar holds, the more surface area of the pressure vessel is covered, so the heat flux acts over a larger area. This comparison case demonstrates that the most rapid cooling is achieved by committing excess liquid nitrogen into the system, beyond the ideal amount. The extra amount is expected to be system dependent, and will depend on the specific cooling rates that are needed. This issue is discussed in more detail when full-scale tank performance is considered.

The importance of LN2 mass flow rate also is illustrated in Figure 3.26. The difference between the cases is that Case 32 used a full 6-L reservoir and the LN2 supply line continued to fill the reservoir for one minute after the reservoir valve was opened. Case 31 only used a full 6-Lreservoir without additional LN2 from the supply. Case 32 offers noticeably higher heat flux and cooled from 160 K to 100 K approximately 30% faster, which agrees with the heat-flux profile. Below 100 K, the two cases were approximately equal. This suggests that the extra heat flux due to the extra LN2 flow in Case 32 consumed all the extra LN2 to reach 100 K faster, and a similar amount of LN2 remained in both cases at temperatures below 100 K.

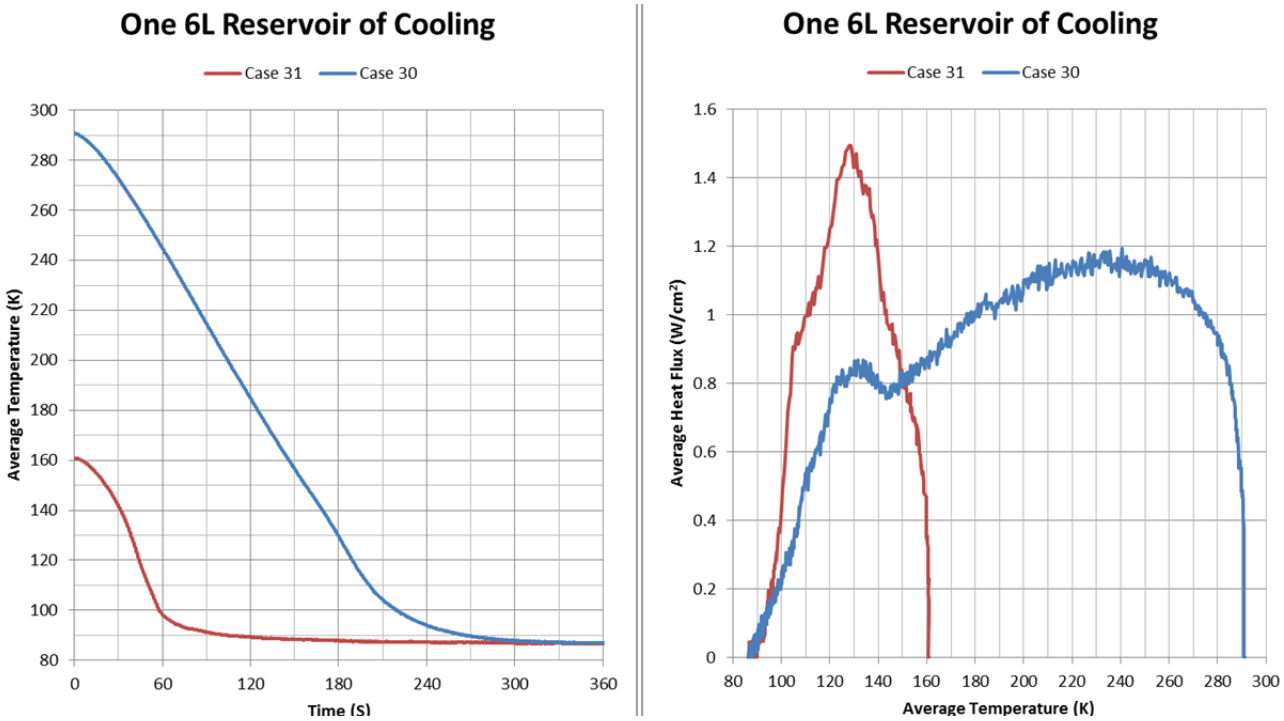

Figure 3.25. Performance of Cooling with Consistent 6-L Supply of LN2. Comparative cooling times (left) and comparative heat-flux profiles (right).

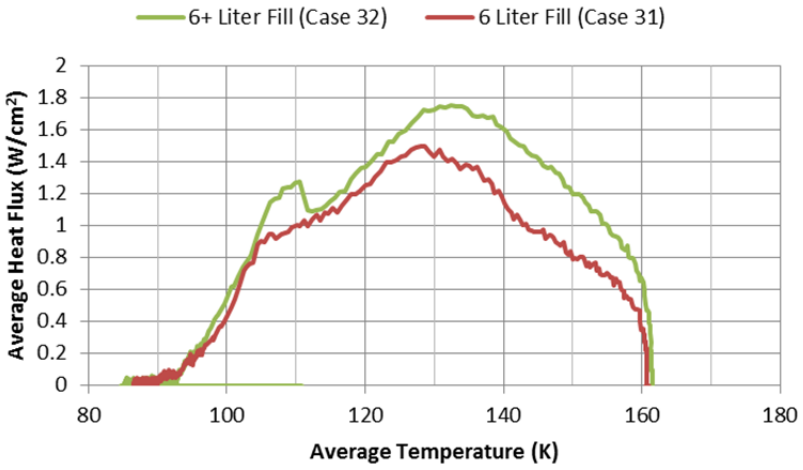

Figure 3.26. Rear Fill Reservoir Effect of Continued LN2 Flow

The best heat-flux profile witnessed during testing occurred for Case 19, which was nearly identical to Case 32. Data for Case 19, 31, and 32 are shown in Figure 3.27. The difference is that for Case 31 and Case 32, a 45°elbow was placed on the front plate exit vent in an attempt to reduce LN2 lost as spray from the front plate of the dewar. Case 19 had a slightly wider opening in the front plate where the thermocouple wires passed through. It was difficult to say whether the 45°elbow made any difference on the results. The different flux profile of Case 19 is expected because of the difference in starting temperature (i.e., 155 K for Case 19 and 160 K for the Cases 31 and 32). Case 19 shows improved performance in the 110 K to 130 K range, and was therefore used to represent the highest tier of cooling performance applied to full-scale design performance estimates.

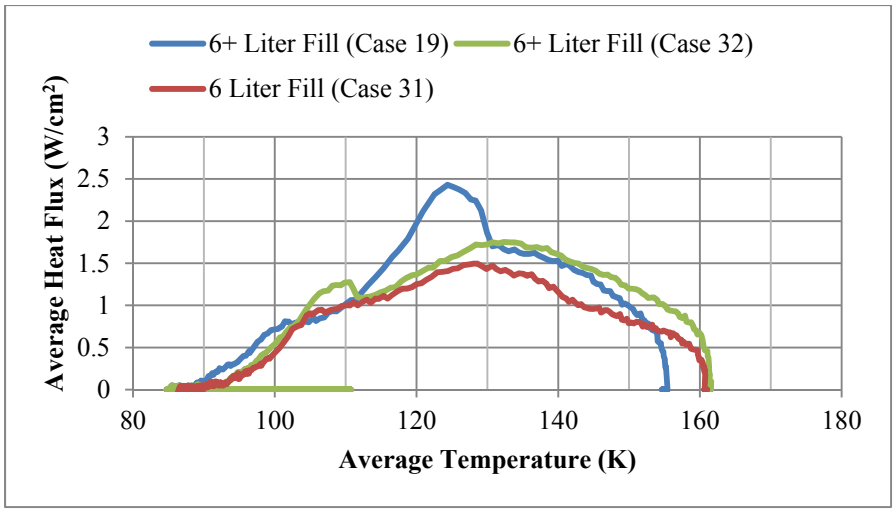

Figure 3.27. Rear Fill Reservoir Comparison of Average Heat Flux

3.3.2.2 Projected Full-Scale Cooling Performance Results

A full-scale prototype system defined by Savannah River National Laboratory using their system model is the current basis for cost estimation and comparison to target goals. The mass of the aluminum pressure vessel is 59.6 kg, and it has a surface area exposed to the LN2 cavity of 26,500 cm^2. The governing assumption is that the LN2 mass flow rate is scaled as necessary to achieve the same heat-flux profiles observed during testing. Differences in geometry, wall thickness, and aspect ratio are all ignored for this performance projection, which is plotted in Figure 3.28. The ideal curve represents an estimate of the full-immersion cooling performance for the full-scale system. The "Back Fill" curve represents cooling equivalent to the temperature-heat-flux profile from Case 19, and cools the tank from 160 K to 90 K in approximately 130 seconds, which is well within the DOE target goal of a 3.3 minute fill-up period. However, the desired fully cold temperature is 80 K, which was not demonstrated to be achievable during testing. The 10 K difference in temperature is expected to be addressed via flow-through cooling on the adsorbent material inside the pressure vessel. As another option, increases in LN2 mass flow rate beyond those tested might be able to make up that difference. However, based on the natural surface boiling behavior, a natural difficulty in lowering the temperature of the tank from 90 K down to 80 K is expected. Also note that the "Front Fill" curve (Case 15) also meets the target goal, cooling to 90 K in 190 seconds, but it represents the lowest tier of cooling rates that can meet the goal. The spray case, representative of the bottom tier of cooling performance, only reaches 110 K during the 3.3 minutes (198 seconds) allowed for fill-up. Note that the LN2 supply lines are assumed to be pre-chilled, so LN2 is delivered immediately to act on cooling the pressure vessel without causing initial warm up. If the warm-up behavior was included in this projection the cooling performance would be even worse than that shown in Figure 3.28.

Note that each of the performance estimates are tied to the LN2 mass flow rates and delivery configurations that were used in testing. A shower spray case with relatively thicker tubing or a relatively higher supply pressure could potentially achieve much better cooling rates. A back-fill case with a larger reservoir of LN2 might also demonstrate faster cooling. The mass flow rate of LN2 is expected to be the most important factor to determine the cooling performance of the system. The curves in Figure 3.28 show that both types of reservoir cooling are projected to cool a full-scale tank from 160 K to 90 K in 3.3 minutes, which would meet the DOE target goal. The projections assume the mass flow rates are appropriately scaled up to achieve the same surface flux behaviors identified in the previous section.

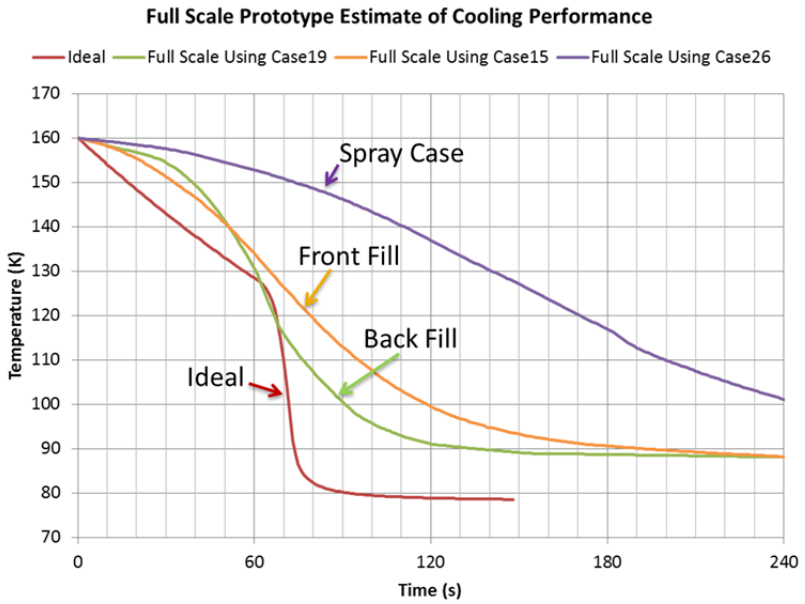

Figure 3.28. Performance Projection of Full-Scale Cooling Performance

3.3.2.3 Effects of Mass Flow Rate on Cooling Performance

Because so much of the cooling performance is related to the mass flow rate of LN2, an estimate needs to be made on how large the mass flow rate of LN2 needs to be to achieve the target cooling goals. The empty volume of the LN2 cavity can be used to calculate how much LN2 can be stored by the system, and how the fill level correlates to cool able surface area. As mentioned above, the mass of the full-scale pressure tank is 59.6 kg, it has a surface area exposed to the LN2 cavity of 26,500 cm^2, and the volume available to fill with LN2 is 12.6 L. For simplicity, it is assumed that the fraction of area exposed to LN2 is equal to the fraction of volume filled, such that 50% volume (6.3 L) of LN2 in the LN2 cavity equates to 50% effective area (13,250 cm^2). The ideal flux based on full-immersion testing is applied to the effective area to determine the energy removed in one incremental time step, using temperature-dependent heat capacity for aluminum. This calculation method estimates cooling performance based on a constant mass flow rate. More complex mass flow rate profiles can be evaluated, but constant mass rates illustrate the performance well enough for our purpose.

Figure 3.29 shows the full-scale tank cooling projections for a number of hypothetical mass flow rates between 50 g/s and 250 g/s. The 50 g/s mass flow rate is relatively low and at 198 seconds the tank is only cooled from 160 K to 133 K. In this case the constant mass flow rate is largely consumed as it enters the LN2 cavity, and by 198 seconds, the LN2 cavity has ramped up steadily to 40% full. As the volume fill percentage is also taken to be the percent of surface covered, LN2 boiling only occurs over a small fraction of the available surface area. The 75 g/s mass flow rate is the minimum needed to achieve cooling from 160 K to 90 K in 198 seconds, and reaches a maximum of 60% full before transition boiling quickly reduces the stored LN2 to 20% full. The 150 g/s case represents a potential limit on the LN2 mass flow rate because it reaches 97% of the LN2 storage capacity of the system. The higher mass flow rates all exceed the LN2 volume capacity of the system, which provides a saturated 100% coverage, but would also waste a certain amount of LN2 that would be lost through the vent in the postulated constant mass flow system. Cooling performance in the 200 g/s and 250 g/s mass flow rate ranges could alternatively be achieved with a variable-flow rate system that front-loads delivery of LN2 to maximize surface coverage over time and minimizes the loss of LN2.

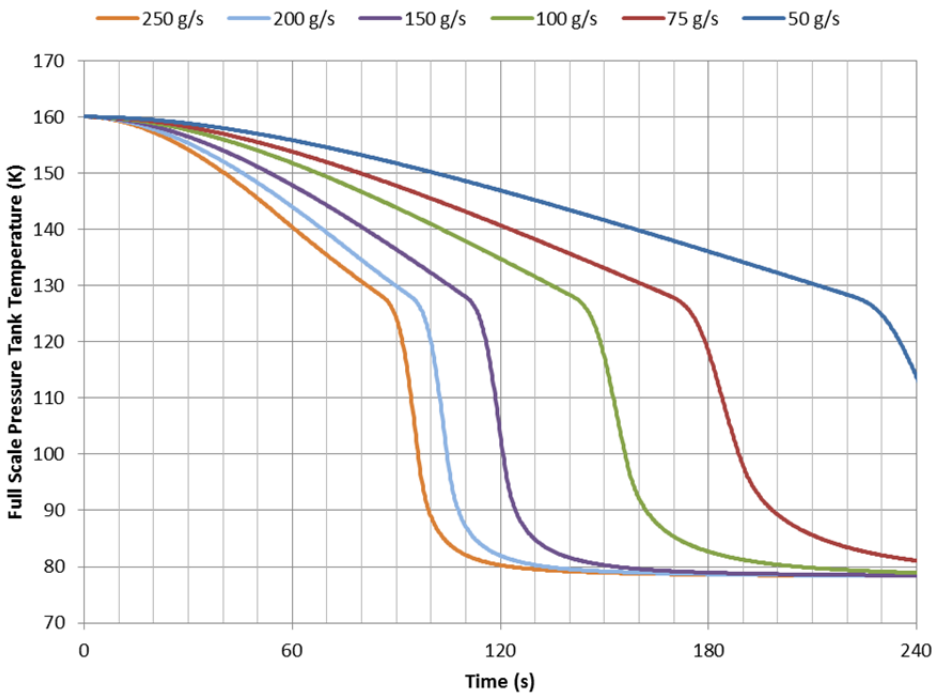

Figure 3.29. Full-Scale Tank Cooling Projections by Mass Flow Rates

In all cases, the total energy required to cool the full-scale pressure tank from 160 K to 80 K is equivalent to the energy of 14 kg of boiled LN2. Because surface coverage and holding a certain volume of LN2 is important to achieve rapid cooling rates, it may be necessary to use more than 14 kg of LN2 in the cooling process to achieve the cooling time goals. For example, the 150 g/s case ends the simulated cooling time with 60% of the LN2 reservoir filled with LN2, which is an extra 6 kg present in the system at 125 seconds. The 75 g/s case has 2 kg of spare liquid nitrogen left at 198 seconds. The LN2 loss can be minimized by managing the LN2 flow through a timed delivery or a variable-flow delivery that is tailored to provide just enough LN2 to the system.

Another factor that was not considered in these performance projections so far is the need to also cool the inside layer of the vacuum jacket, which is a 2-mm thick sheet of aluminum and represents 25% additional mass. The vacuum jacket layer is cooled in parallel to the pressure vessel liner, drawing liquid nitrogen from the shared supply, and is expected to cool much faster because of the similar surface area and substantially smaller mass. This would affect the cooling performance of the tank early in the cooling process but cease to have a significant effect once the vacuum jacket temperature reaches the 80 to 90 K range. In total, 14 kg of LN2 are needed to cool the pressure tank, and 3.5 kg of LN2 are needed to cool the vacuum jacket. The best way to overcome the extra thermal mass of the vacuum jacket is to front-load the additional 3.5 kg of LN2. If a constant LN2 flow is necessary, the cooling time projections shown in Figure 3.29 still offer a reasonable estimate if the mass flow rates are increased by 25% (e.g., the 150 g/s curve corresponds to an adjusted mass flow rate of 188 g/s). Table 3.4 provides performance projections for the full-scale system based on timed fill durations and selected fill assumptions.

3.3.3 Structural and Thermal Fatigue Analysis of LN2-Cooled Tank

We evaluated thermal-mechanical stresses in the LN2-cooled tank concept during refueling considering a fatigue life of 1500 cycles. The goal was to identify any necessary design criteria to avoid failure of the pressure vessel under combined thermal-mechanical loading.

Table 3.4. Full-Scale System Performance Projections

LN2 Mass Flow Rate (g/s)	LN2 Mass Flow Duration (s)	Total LN2 Delivered during Fill (kg)	Time to 90 K (s)	Temperature at 198 s (K)	LN2 Remaining at 198 s (kg)
188	93.0	17.5	143.8	84.3	0.52
188	102.4	19.25	131.6	81.1	1.56
188	88.0	16.5	161.2	87.6	0.19
150	116.8	17.5	157.0	84.7	0.64
125	140	17.5	171.8	85.7	0.74

As the name implies, the LN2 cooled tank concept uses LN2 cooling to enhance the thermal performance of a hydrogen storage vessel. A Type-I aluminum vessel is packaged inside a vacuum-insulated vessel. LN2 is injected into an annulus between the inner vacuum jacket and the hydrogen vessel to pre-cool the tank before filling with cryogenic hydrogen. There is concern that LN2 at 77 K will thermally shock the warmer vessel causing thermal stresses high enough to limit the fatigue life of the vessel. In the following discussions, we summarize our results on the study of physical limits of LN2 cooling, compare these limits with the measured cooling performance of bench-scale tests, and our thermal stress analysis of a full-scale 200-L tank to compare with the reported fatigue limits of the vessel material. The analysis shows that the vigorous boiling action of LN2 limits the achievable heat transfer. The heat transfer through the aluminum wall thickness is faster than the heat-transfer rate from the tank surface. This results in small thermal gradients and small thermal stresses.

3.3.3.1 The Physical Limits of Liquid Nitrogen Cooling

Jin et al (2009) determined the heat-transfer coefficient for LN2 immersion cooling at atmospheric pressure. Heated blocks were immersed in a LN2 dewar, and the recorded temperature history was used to calculate the heat-transfer coefficient. The abundant volume of LN2 in the dewar means that this is a measurement of the bounding heat-transfer rates for LN2 cooling at 1 atmosphere. Figure 3.30 shows the measured temperature history, and Figure 3.31 plots the surface heat-transfer coefficient as a function of the temperature gap (ΔT). This is the total heat-transfer rate, which includes all conduction, convection, radiation, and phase-change effects.

Figure 3.31 shows that the heat-transfer rate is constant when $\Delta T > 50$ K. The strong boiling action creates a vapor layer between the LN2 and the hotter metal that limits the heat-transfer rate to approximately 125 W/m^2K. As the ΔT decreases from 50 K to 20 K, the heat-transfer rate increases rapidly to a peak of about 3500 W/m^2K. The heat-transfer rate then decreases from the peak value as the ΔT decreases below 20 K. Figure 3.30 shows that the largest fraction of cooling time corresponds to the low cooling rate when $\Delta T > 50$ K. The temperature-dependent heat-transfer coefficient was implemented in our ANSYS thermal models (www.ansys.com) as shown in Figure 3.32.

Bench-scale LN2 cooling tests were performed by Hexagon Lincoln using the experimental setup shown in Figure 3.33 for proof-of-concept testing of the LN2 cooled tank design.

Figure 3.34 shows the temperature histories of thermocouples placed along the length and around the perimeter of the inner pipe. These temperature plots show the same cooling characteristics of the immersion tests performed by Jin et al (2009). That is, relatively constant cooling occurred initially followed by rapid cooling when the temperature difference decreased to about 30 K. The plot shows that the temperatures are colder at the bottom and side of the pipe (thermocouples 3 and 2, respectively) suggesting that the LN2 flows down over the pipe and pools at the bottom. The data also shows that there is about a 100 second lag in the temperatures from the LN2 inlet to outlet ends.

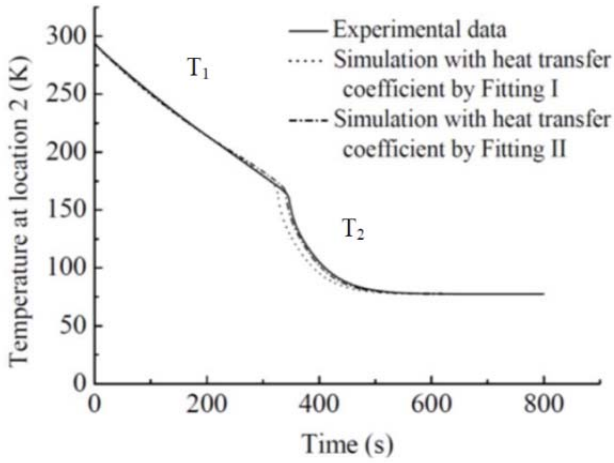

Figure 3.30. Temperature vs. Time Relationship for LN2 Immersion Tests from Jin et al (2009)

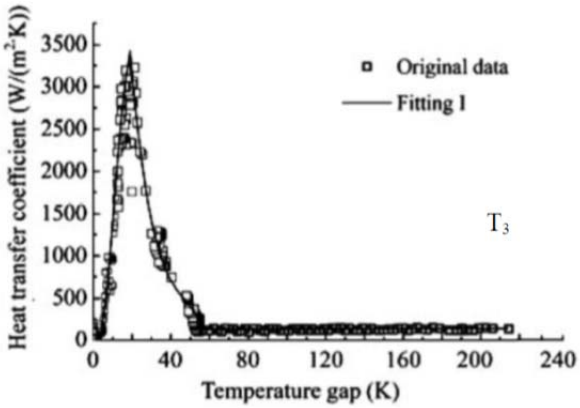

Figure 3.31. Heat-Transfer Coefficient vs. Temperature for LN2 Immersion Tests from Jin et al (2009)

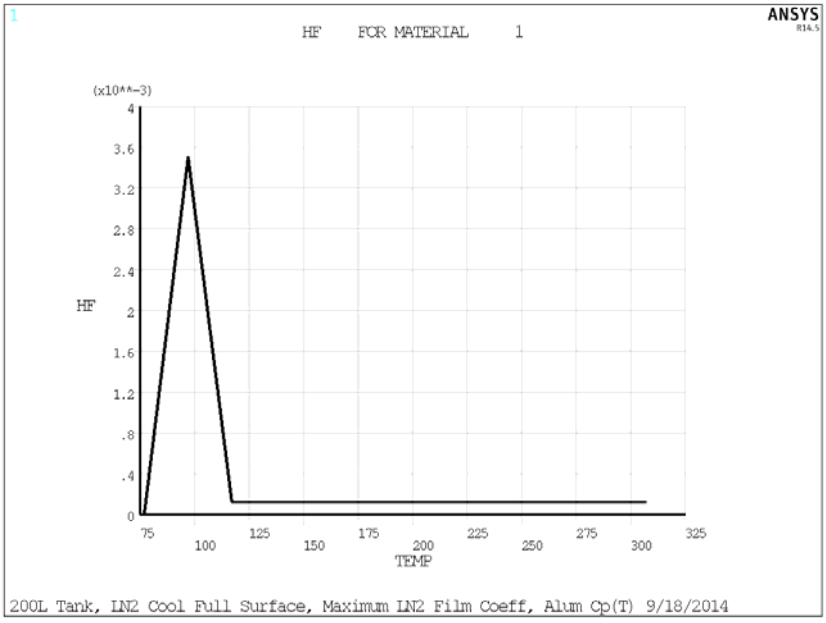

Figure 3.32. LN2 Heat-Transfer Coefficient vs. Temperature in the ANSYS Thermal Models

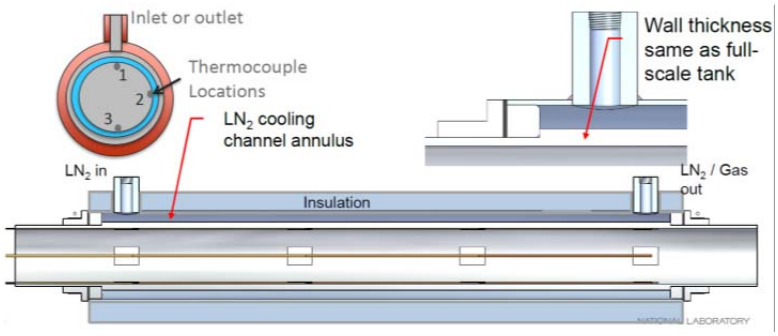

Figure 3.33. Schematic of the Bench-Scale LN2 Cooling Test Setup

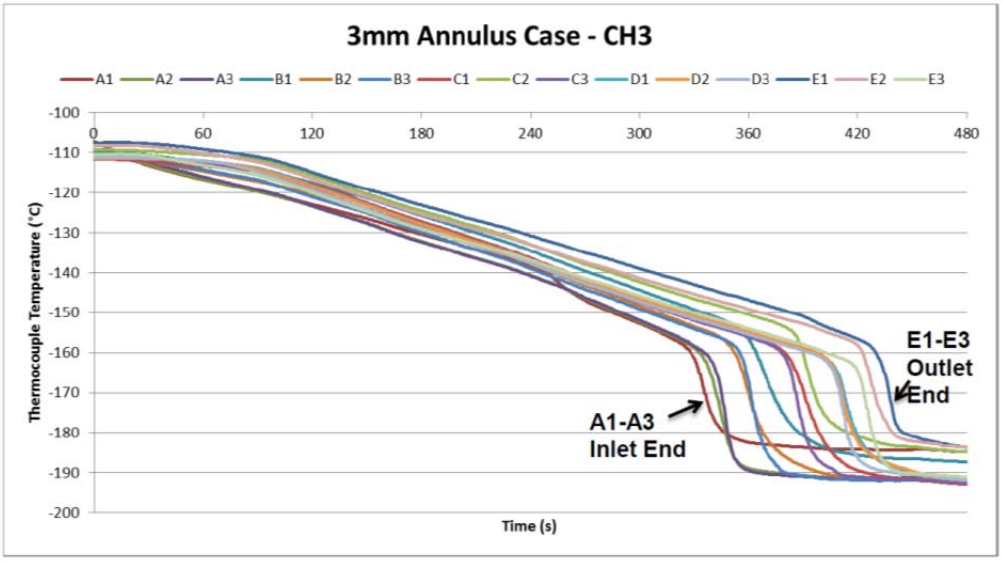

Figure 3.34. Temperature Data from the Bench-Scale LN2 Cooling Test

A two-dimensional axisymmetric finite-element model of the cooling test was constructed that includes the temperature dependency of the heat-transfer rate, shown in Figure 3.35.

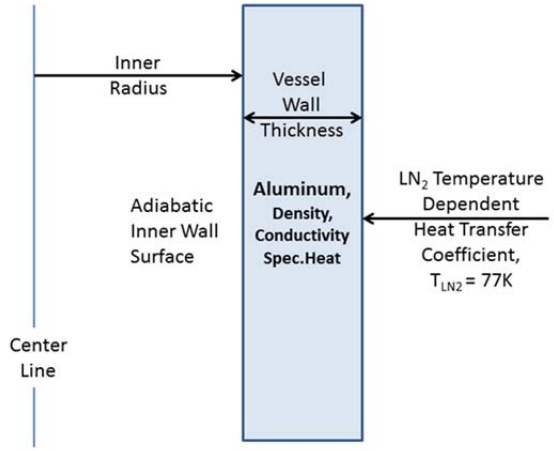

Figure 3.35. Finite-Element Model of Cooling Test; Temperature-Dependent Specific Heat of Aluminum

Input parameters for the test set up were the pipe outside radius (35 mm) and the wall thickness (17 mm). Temperature-dependent specific heat of the aluminum pipe also was modeled because it decreases rapidly in the cryogenic range as shown in Figure 3.36.

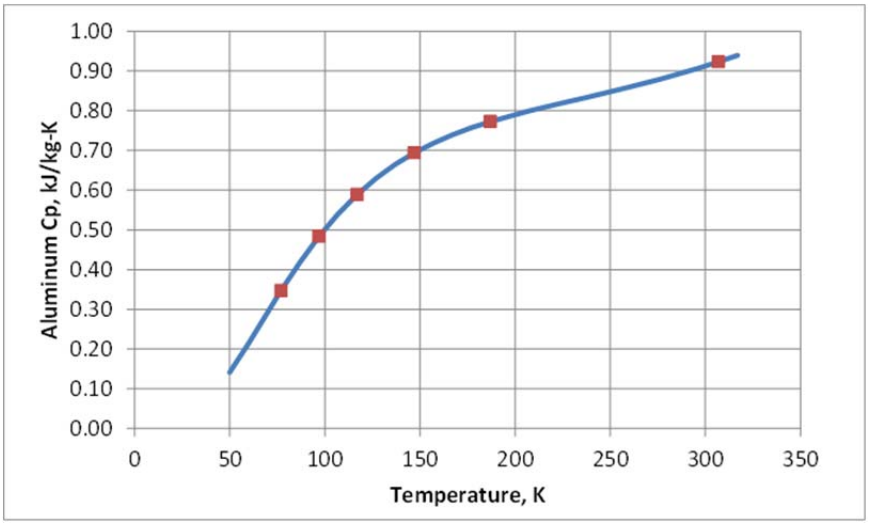

Figure 3.36. Modeled Temperature-Dependent Specific Heat of Aluminum

National Institute for Standards and Testing equations for aluminum specific heat were used.[11] The initial temperature of the pipe was 160 K and the LN2 temperature of 77 K was defined for the surface heat-transfer boundary condition. The initial model (using heat-transfer coefficients from Jin et al. 2009) showed that the tube cooled faster than the actual test as shown in Figure 3.37.

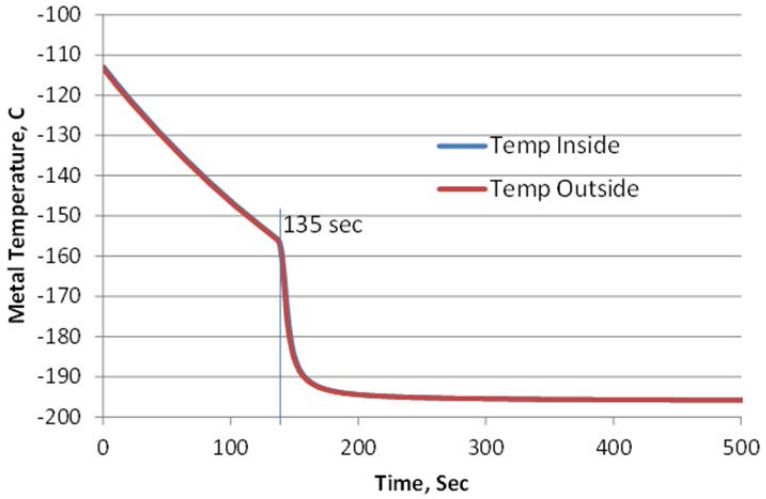

Figure 3.37. Predicted Cooling History by Jin et al. (2009) Hf = 125 W/m^{2}K at ΔT >50 K

The heat-transfer coefficient for high ΔTs (125 W/m^{2}K) was reduced to 50 W/m^{2}K where the model gave approximately the same cooling time (330 seconds) to reach the steep temperature decrease in the experimental test (Figure 3.38). This indicates that there is a significant available margin to increase the LN2 cooling efficiency toward the physical maximum.

[11] http://cryogenics.nist.gov/MPropsMAY/materialproperties.htm

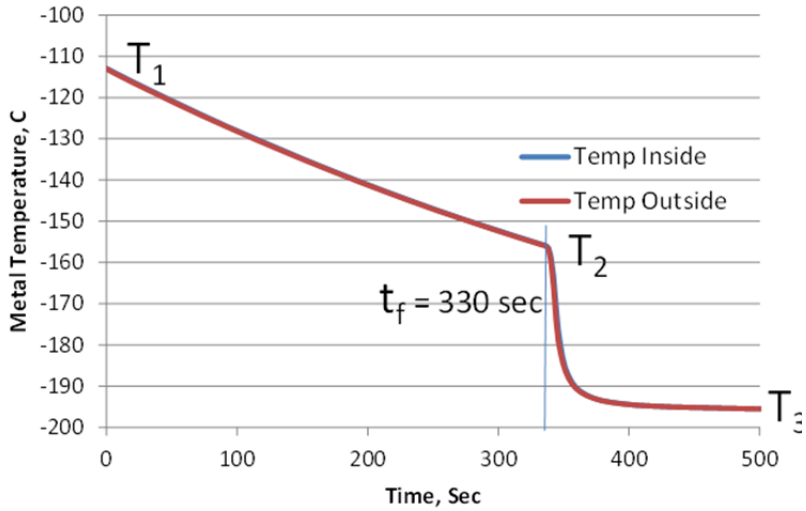

Figure 3.38. Cooling History with Reduced Hf = 50 W/m^{2}K for ΔT >50 K

The transient thermal model predicts that the outside and inside wall temperatures will be nearly the same throughout the cooling history shown in Figure 3.37 and Figure 3.38. This can be explained by comparing the thermal conductance of the aluminum pipe wall to the LN2 surface heat-transfer coefficient. The pipe wall conductance (9824 W/m^{2}K) is the conductivity (167 W/mK) divided by the wall thickness (0.017 m). Throughout most of the cooling cycle the surface heat-transfer coefficient is ~125 W/m^{2}K which is only 1% of the wall conductance. Even the peak value (3500 W/m^{2}K) is only one-third of the wall conductance. Therefore, heat transfers much faster through the aluminum wall than it transfers away though the vaporization of LN2. Thus the temperature gradient in the aluminum will be small and the associated thermal stresses also will be small.

A simple approximation is also possible for the near linear decrease in temperature seen in the experimental data and models. For the temperatures, T_1, T_2, and T_3, and the cooling time, t_f, shown in Figure 3.38, the ΔT as a function of time can be written:

$$\Delta T(t) = (T_1 - T_2)\left(1 - \frac{t}{t_f}\right) + (T_2 - T_3) \tag{3.1}$$

Equating the heat removal through time to the decrease in temperature times the specific heat for a cylinder with outer radius, R_o, and internal radius, R_i,

$$2\pi R_o H_f \int_0^{t_f} \Delta T(t)dt = \rho C_p \pi (R_o^2 - R_i^2)(T_1 - T_2) \tag{3.2}$$

where H_f is the surface heat-transfer coefficient (50 W/m^{2}K = 50E-6 W/mm^{2}K), ρ is the density (0.0027 g/mm^3), and Cp is the average specific heat of aluminum in the temperature range of interest (~0.7 J/gK). The integral of ΔT is:

$$\int_0^{t_f} \Delta T(t)dt = t_f\left(\frac{T_1 + T_2}{2} - T_3\right) \tag{3.3}$$

and the final cooling time, t_f, can be expressed as:

$$t_f = \rho C_p \frac{R_o^2 - R_i^2}{2R_o}(T_1 - T_2) \Big/ H_f \left(\frac{T_1 + T_2}{2} - T_3 \right) \tag{3.4}$$

For the bench-scale cooling test with T_1 = 160 K, T_2 = 115 K, T_3 = 77K, R_o = 35mm, R_i = 18mm, and H_f = 50E-6W/mm^{2}K,

$$t_f = (0.0027)(0.7)\left(\frac{35^2 - 18^2}{2(35)} \right)(160 - 115) \Big/ (50E-6)\left(\frac{160+115}{2} - 77 \right) = 362\,\text{sec} \tag{3.5}$$

The test setup shown in Figure 3.33 has a very small OD-to-thickness ratio (OD/t_{wall} = 70/17 = 4); therefore, it has a larger ratio of cooling area to material volume than a thin-walled pressure vessel (i.e., OD/t_{wall} >10). For thin-walled cylinders, the material volume is approximately equal to the surface area at the average radius times the thickness. Then the cooling time can be approximated as

$$t_f = \rho C_p t_{wall}(T_1 - T_2) \Big/ H_f \left(\frac{T_1 + T_2}{2} - T_3 \right) \tag{3.6}$$

The limiting thickness, t_{wall}, for a specified cooling time, t_f, can then be estimated as

$$t_{wall} = t_f H_f \left(\frac{T_1 + T_2}{2} - T_3 \right) \Big/ \rho C_p (T_1 - T_2) \tag{3.7}$$

If the cooling time were limited to 4 minutes (240 sec) with H_f= 50E-6 W/mm^{2}K, then the maximum wall thickness would be

$$t_f = 240(50E-6)\left(\frac{160+115}{2} - 77 \right) \Big/ (0.0027)(0.7)(160 - 115) = 8.5mm \tag{3.8}$$

At the physical heat-transfer limit (H_f = 125E-6W/mm^{2}K), the maximum thickness would be 21 mm. Limiting the thickness also limits the tank radius-to-thickness ratio (R/t) for a required pressure. Table 3.5 lists estimated maximum radius and required L/D ratios of a 200-L tank with a maximum operating pressure of 100 bar for Aluminum 6061-T6 (tensile strength = 52 ksi = 358 MPa) with a stress ratio of 4 on burst per NGV3/CSA (allowable stress = 90 MPa). Note that the calculated L/D ratio is unreasonably large for the heat-transfer rate measured from the bench-scale tests (H_f= 50E-6W/mm^{2}K). Even at the maximum heat-transfer rate the tank would be nearly 2 m long to achieve the 240 second cooling time.

Table 3.5. Summary of Tank Dimension of 200-L Tank for a 240 Second Cooling Time

Hf (W/mm^{2}K)	Cooling Time (s)	Maximum Thickness (mm)	Maximum Radius (mm)	Minimum Tank Length (m)	L/D Ratio
5.00E-05	240	8.5	76.5	10.90	71.3
1.25E-04	240	21.3	191.3	1.82	4.7

3.3.3.2 Thermal Stress Analysis of the Full-Scale Tank

A finite-element model was developed of the conceptual full-scale tank design to calculate the thermal-mechanical stresses during the cool-down cycle. The hydrogen pressure vessel of the full-scale tank design is assumed to have a maximum OD of 0.5 m and an internal volume of 200 L. The minimum wall thickness is 26 mm for a maximum operating pressure of 100 bar (10 MPa) and a membrane stress limit of 90 MPa. The tank length is approximately 1.3 m for the 200-L volume. Using equation (6), the estimated cooling time is about 300 seconds for the 26-mm wall thickness. The ANSYS models simulate a two-dimensional, axisymmetric section of the tank cross section. Hemispherical domes were assumed for simplicity of constructing the model. The following two cooling conditions illustrated in Figure 3.39 were considered to bound the thermal stress analysis:

1. LN2 cooling of the cylinder section only. Higher thermal stresses will occur because the end temperatures will lag behind the cylinder temperatures.
2. LN2 cooling of the full tank surface. Temperature gradients causing differential thermal contraction stresses will be very small until late in the cool-down cycle when the surface heat-transfer rate peaks.

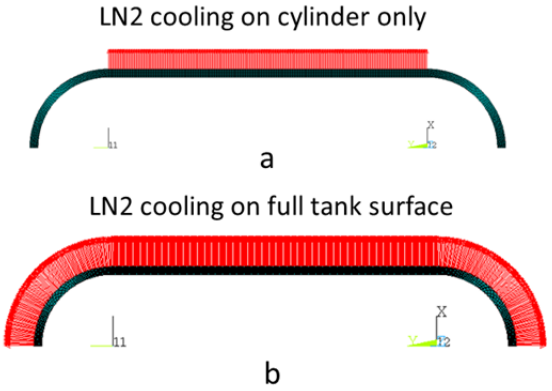

Figure 3.39. Full-Scale Tank Two-Dimensional Axisymmetric Finite-Element Models with (a) Cooling the Cylinder Section Only, and (b) Cooling the Full Tank Surface

The cooling cycle begins at a uniform tank temperature of 160 K and proceeds until the tank has cooled to near the LN2 temperature of 77 K at 1 atm. Thermal stresses were monitored throughout cool-down to determine when the maximum stress occurred. The stress intensity (the maximum difference between any two of the three principal stresses) was calculated through time for comparison with the fatigue limit of the tank alloy, Aluminum 6061-T6. Note that this is the same alloy used for the 2-L prototype hydrogen tank. Figure 3.40 shows the fatigue S-N curves[12] for Al-6061-T6 from Mil-Handbook-5J (DOD 2003). The stress intensity corresponding to the 10 MPa applied pressure was also calculated using the ANSYS model. The pressure-induced stress intensity of 102 MPa was added to the thermally induced stress intensity. For comparison, the ANSYS models also were run with the combined pressure and thermal loads. The maximum stress intensity was nearly identical to that of the pressure load alone (102 MPa). The principal stresses shifted slightly, but the maximum difference remained the same. Therefore, it is considered conservative to evaluate the pressure and thermal stress intensities separately and then adding them.

[12] Alternating stress amplitude (S a) vs. number of cycles (N f) to failure.

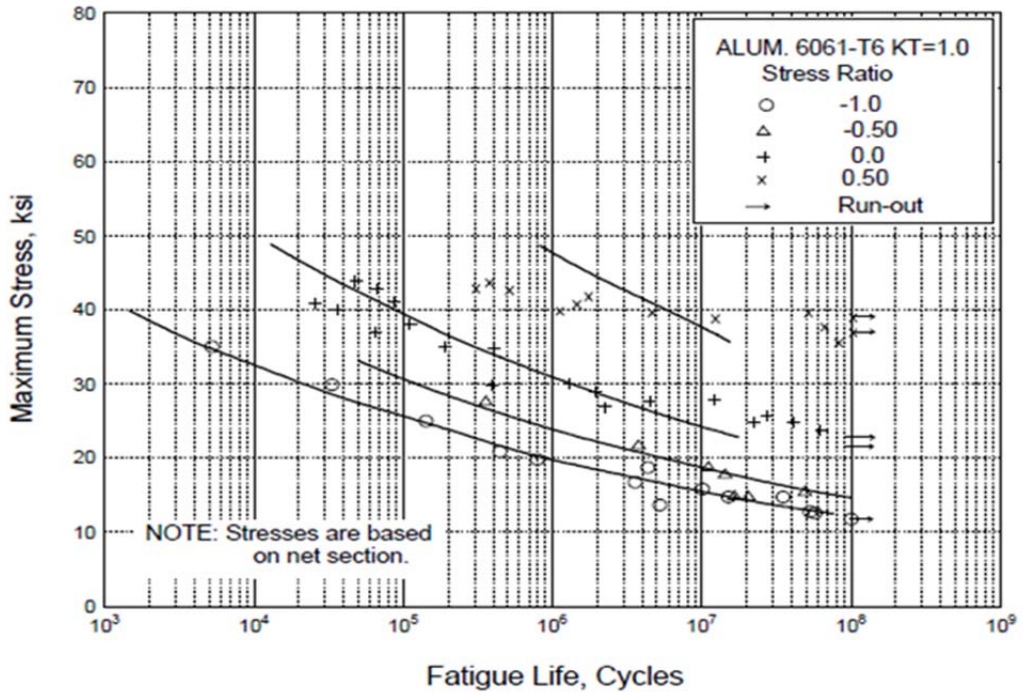

Figure 3.40. Fatigue S-N curves for Aluminum 6061-T6

Figure 3.41 summarizes the results of Case 1 where LN2 cooling was confined to only the cylinder section of the tank. The temperatures at the dome center and the mid-length of the tank are plotted through time, and the maximum stress intensity at the tank shoulder also is plotted throughout cool down. The finite-element contour plots show the temperature distribution (above) and the stress intensity distribution (below) at the location and time of the maximum stress intensity. The maximum stress intensity (16 MPa) occurs when the temperature difference is greatest between the cylinder and the ends of the tank. This is expected, and because the goal is to provide uniform cooling over the entire tank, this case is expected to provide an upper-bound estimate of the stress intensity due to uneven tank cooling. Figure 3.41 also shows that the cooling time to reach the steep temperature decrease is about 300 seconds, which is similar to the cooling time predicted using the hand calculation of Equation 3.6.

Figure 3.42 shows the temperature and maximum stress intensity histories of Case 2 with uniform cooling over the entire tank surface. For uniform cooling, the maximum stress intensity (8 MPa) is lower than in Case 1, and it occurs during the steep temperature decrease in the cooling transient. Figure 3.41 shows that this same condition appears as a sub-peak in the Case 1 results during the steep temperature decrease in the cylinder wall. Considering both cases, the maximum stress intensity caused by LN2 cooling is only 16 MPa. Adding the pressure and thermal stress intensities gives a maximum of 118 MPa (17.2 ksi)**.**

Conservatively using the R = -1 fatigue curve for fully reversing stress cycles in Figure 3.40 shows that a cyclic stress of 19 ksi corresponds to 1,000,000 cycles to fatigue crack initiation. This far exceeds the minimum 1500 cycles required by the project milestone. Therefore, the inner aluminum vessel can easily be designed to withstand 1500 pressure and LN2 cooling cycles.

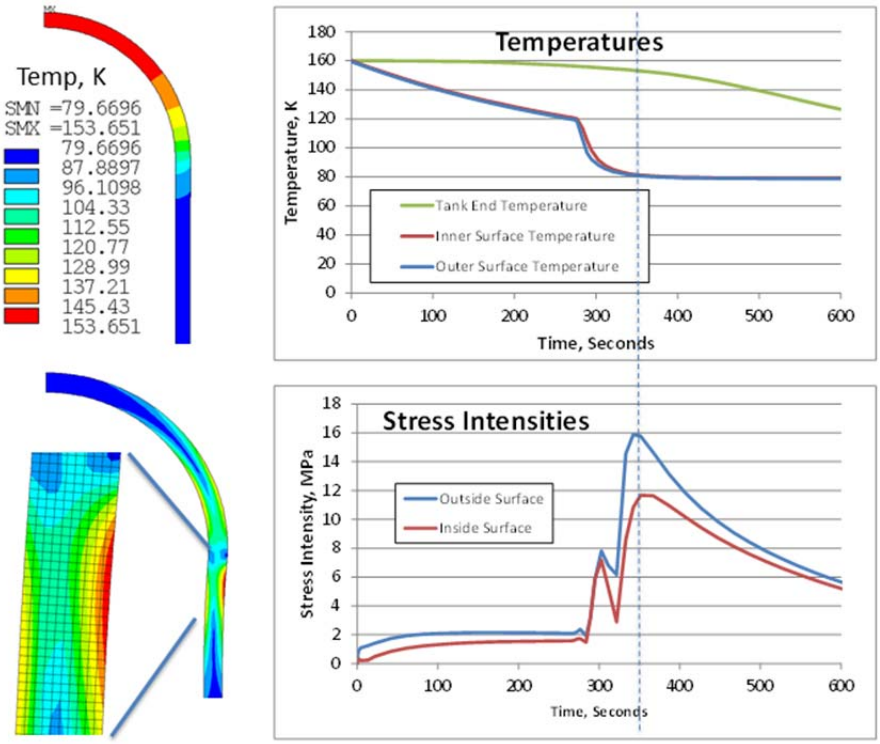

Figure 3.41. Temperature and Stress Intensity Histories when LN2 Cooling is Applied to Only the Cylinder Section of the Tank

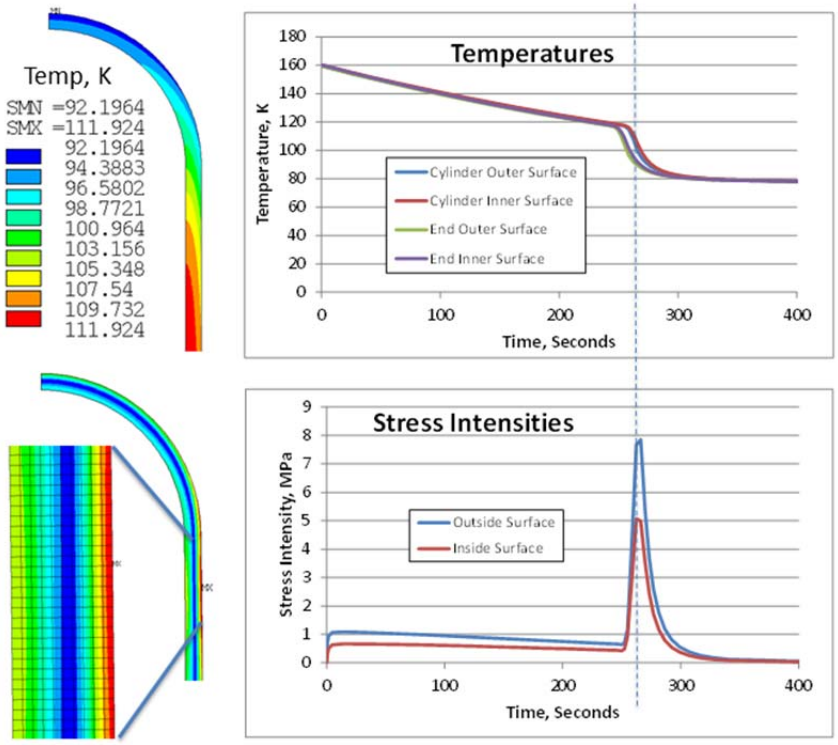

Figure 3.42. Temperature and Stress Intensity Histories when LN2 Cooling is Applied to the Full Surface of the Tank

3.3.4 Summary of LN2 Cooled-Wall Tank Development

The LN2 Cooled-Wall Tank concept uses a separate stream of LN2 to cool the pressure tank wall from 160K to 80K rather than using more expensive cold hydrogen from the refueling stream to perform this cooling. To demonstrate this concept, Proof-of-Concept tests were performed by flowing LN2 through the annulus of concentric aluminum pipes to mimic a Type-I tank. These initial tests were followed by the study of a Type-I, 2-L aluminum prototype tank inside of a dewar. These two configurations demonstrated that the tank cooling rate is initially slow and becomes more rapid as the temperature difference between the surface and the LN2 is reduced to 10-50K. High flow rates of LN2 are needed to achieve the DOE target goals and flow rate is more important to rapid cooling than an even flow distribution across the tank surface. These tests also demonstrated that pressure buildup within the LN2 cavity was negligible. A final test was run on a Type-III prototype tank, which demonstrated very low cooling rates that did not meet DOE target goals.

The results of the experimental work were used to estimate the heat flux of a full-scale system and calculate the time and mass flow of LN2 required to cool the tank from 160K to 80K. The analysis indicates that the tank can be cooled to 90K well within the DOE Target of 3.3 minutes, however to fully cool to 80K cannot be achieved within the DOE Target limit. Higher flow rates of LN2 will cool the tank more rapidly but result in loss of excess LN2. The total energy to cool the full-scale tank from 160 K to 80 K is equivalent to the energy of 14 kg of boiled LN2, however, approximately 3.5 kg additional LN2 is required to cool the outer vacuum jacket and 2.5 to 5.25 kg additional LN2 is required to cool the tank within the DOE Target of 3.3 minutes, depending upon the LN2 flow rate. To minimize the loss of excess LN2, the flowrate should be regulated during cooling and the flow stopped well before the tank reaches its final temperature.

A model of the tank cooling using the LN2 cooled-wall concept was developed in an effort to understand the thermal stresses of the full-scale tank caused by refueling events. The stress intensity was calculated and compared to the fatigue limit of the tank alloy, Aluminum 6061-T6. The results showed that the predicted cyclic stress of 19 ksi corresponds to 1,000,000 cycles to fatigue crack initiation. This far exceeds the minimum 1500 cycles required by DOE Targets.

3.4 Balance of Plant for Cryo-Adsorbent System

The BOP for the cryo-adsorbent hydrogen storage system includes all the components of the storage system with the exception of the adsorbent material itself and the storage vessel in which it is housed. Based on comments from the original equipment manufacturers (OEM) and the HSECoE tech team, the storage systems had to be designed to be stand alone; that is, they did not assume that any components from the fuel cell (i.e. radiator) or other vehicle systems could be shared. This limitation made the mass and volume projections larger than if the fuel cell, storage, or heating, ventilation, and air conditioning systems were integrated. The vehicle and fuel cell can provide power and heat as well as control, but all other needs of the storage system have to be provided independently for the rest of the vehicle. The BOP will include such components as filters, heat exchangers, pumps, piping, valves, and instrumentation.

Appropriate BOP selection and application is a critical aspect to achieving proper function, safety, and robustness when designing and engineering any system. There are a number of challenges in designing an adsorbent system, such as simultaneously maximizing volumetric and gravimetric hydrogen storage capacity while minimizing cost. In addition, the BOP and their individual component materials have to be compatible with conditions and chemicals to which they will be exposed. In the case of a cryo-adsorbent system, the materials must be compatible with cryogenic temperatures and high-pressure hydrogen.

System architects and members of the HSECoE team developed the BOP equipment list as they defined the system and produced a system piping and instrumentation diagram. The object is to reduce the number and complexity of components in the system while still meeting the system's functions and requirements. In addition to specifying the system components, estimates of the required temperatures, pressures and flow rates for each of the BOP components also are needed. With this information the BOP components can be identified and a bill of material can be generated. Each item on the bill of material is researched to identify off-the-shelf components that meet the system's requirements and conditions that the component will be exposed to. This includes ensuring compatible materials. Once the manufacturer and part number are selected, the cost, mass, and volume of each component are cataloged.

In some cases a BOP component will not be commercially available. Under those conditions, the component must be designed in sufficient detail that the materials required for its manufacture can be estimated and the steps required to fabricate it can be assumed. Preliminary steps for manufacturing the component also will ensure that it can be built with conventional fabrication techniques. Using this information, the component cost can be estimated. Additional analysis may be required to verify that the design is sound. For example, in some cases the part is analyzed for thermal and mechanical stresses.

3.4.1 Balance-of-Plant Component Library

In an effort to provide consistent set of BOP components for the various hydrogen storage systems being developed in the HSECoE, a BOP component library has been developed. This library is a Microsoft Excel spreadsheet with tabs for each of the major BOP components based on their function (Table 3.6). In each tab is a list of commercially available products to consider. Each product has the temperature and pressure regimes that are acceptable for operations. Hydrogen compatibility was considered when selecting each component before it was included. Product literature is provided for each component via a hyperlink where the components can be purchased or more information can be obtained. The choices for materials of construction (e.g., o-rings), pressure (operating pressure and burst pressure), operating temperature, size, dimensions, and medium for use also are provided. The mass and volume of each component is included to assist in estimating the overall system mass. In some cases cost is also included.

Table 3.6. Components in the BOP Component Library Relevant to Cryo-Adsorbent Systems

BOP Categories Available in the BOP Current Component Library		
Check Valves	Heat Exchangers	Tubing
Control Valves	Heat-Transfer Fluids	Tank Liner Materials
Filters	Insulation	Pressure Vessels and Containment
Flow Controllers	Pressure Sensors	Pressure Relief Devices
Fluid Pumps	Temperature Sensors	Manual Valves
Gas Pumps	Pressure Regulators	Filters
Rupture Disks	Fittings	Automatic Valves

The spreadsheet anticipates not only the BOP materials for the cryo-adsorbent storage systems, but also for the chemical hydrogen storage and metal-hydride materials. As a starting point, a representative model of some of the key BOPs has been selected for each of the storage systems on a separate spreadsheet tab. The BOP for the cryo-adsorbent system is shown in Table 3.7.

Table 3.7. Initial Component List from BOP Component Library for the Cryo-Adsorbent System

Description	Pressure psig/bar	Dimensions (cm) L x W x H or L x diameter	Weight (g)	Volume (L)	Representative Model
Check valve	6000/414	6.1 x 3.2 x 2.8	154	0.04	K220T1-3PP-1450/Circo Seal
Pressure relief device	2500/173	7.1 x 2.54	288	0.036	8100-55T1T1 /Circo Seal
Pressure relief device	1450/100	10.8 x 2.54	437	0.055	M5180T1-3MP-1450/Circo Seal
Automatic Valve 2-way	3000/205	19 x 5	1723	0.37	SV30A2NC6P04D/Circo Seal Controls
Automatic Valve 3-way	3000/205	19 x 5	1723	0.37	SV30A32P6P04D/Circo Seal Controls
Pressure regulator	5000/345	13 x 6.3	1093	0.41	20-1234-2911 /Tescom Industrial Controls
Pressure transducer	7250/500	6.9 x 2.23	215	0.027	AST2000M-00448-B1-F1-417/American Sensors Technology
Tubing	6500/450	0.95 OD x 0.16 wall	0.32 kg/m		SS-T6-S-065-6ME/ Swagelok 316 SS

The BOP component library can be made available on the HSECoE website at the conclusion of the engineering center for others to use, although it will require updates to maintain its utility for system designers.

3.4.2 Development of the Cryo-Adsorbent BOP

3.4.2.1 Phase I

Working with the other HSECoE partners in 2011, PNNL developed a baseline cryo-adsorbent system with its requisite BOP. This initial Phase I design was based on a 200 bar tank. Once the individual components were specified, the mass, volume, and cost estimates for this baseline system could be determined. The Phase-I system design is shown in Figure 3.43. For this system the total mass was calculated at 145 kg, and the total mass for the BOP components was 25.6 kg. The total system volume was 238 L and the BOP represented 19.6 L of that volume. Pie charts showing the mass and volume of distribution of key components are shown in Figure 3.44.

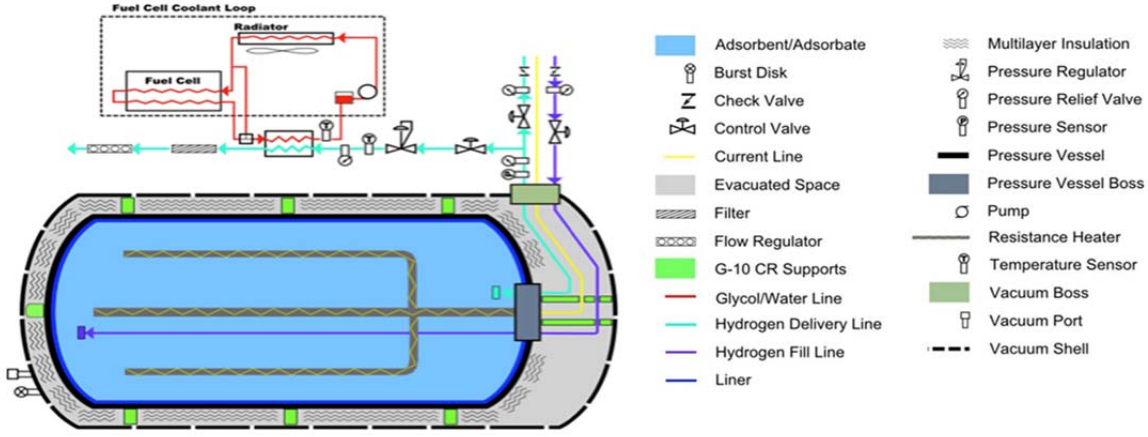

Figure 3.43. Phase I Process Flow Diagram for a Generic Cryo-Adsorbent System

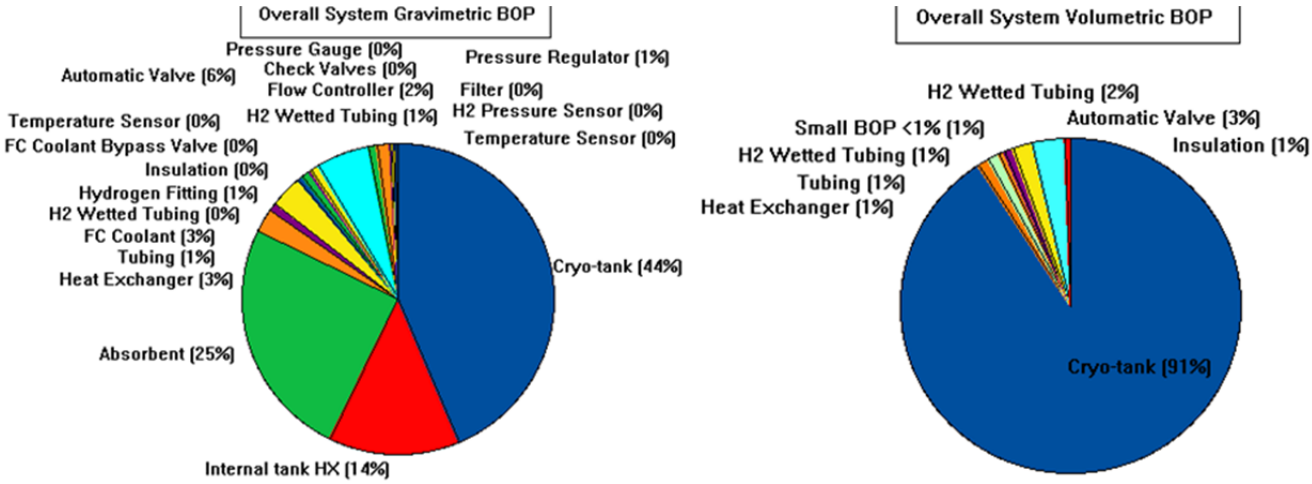

Figure 3.44. Mass (left) and Volume (right) Distributions of the System Components for Phase I

3.4.2.2 Phase-II Designs

During Phase II, two separate designs were initiated: MATI and Hexcell. Work was done to minimize the BOP components and reduce the mass volume and cost for each of these systems. The mass and volume was first reduced by reducing the system pressure, which decreased from 200 to 100 bar. This reduction in pressure reduced the mass and volume of the valves and heat exchanger. The cryo-adsorbent BOP mass and volume were reduced by 46% and 57%, respectively (Table 3.8).

Table 3.8. Improved BOP Mass/Volume at the Beginning of Phase II (May 2012)

	Phase 1 Mass (kg) (200 bar)	Phase II Mass (kg)	Phase II Goal (kg)	Phase I Volume (L)	Phase II Volume (L)	Phase II Goal (L)
Flow-Through Cooling	25.6	13.8		19.6	8.4	
MATI		9.85	17		10.45	18.5
Flow-Through Cooling Reduction		-46%			-57%	

During Phase-II, work continued to identify approaches to reduce the overall system mass and volume. Meetings were held with the HSECoE members and the OEMs to consider each component in the BOP and determine 1) if it is required for the operation, maintenance, or safety of the system, and 2) if it could be consolidated or replaced with other components. For example, the two-way valves could be replaced by three-way valves and the number of instruments can be reduced. In addition, alternative components were identified to replace those BOP components that are either large or heavy. The process flow diagrams for this first level of mass and volume reduction for both the MATI and Hexcell cooling systems are shown in Figure 3.45.

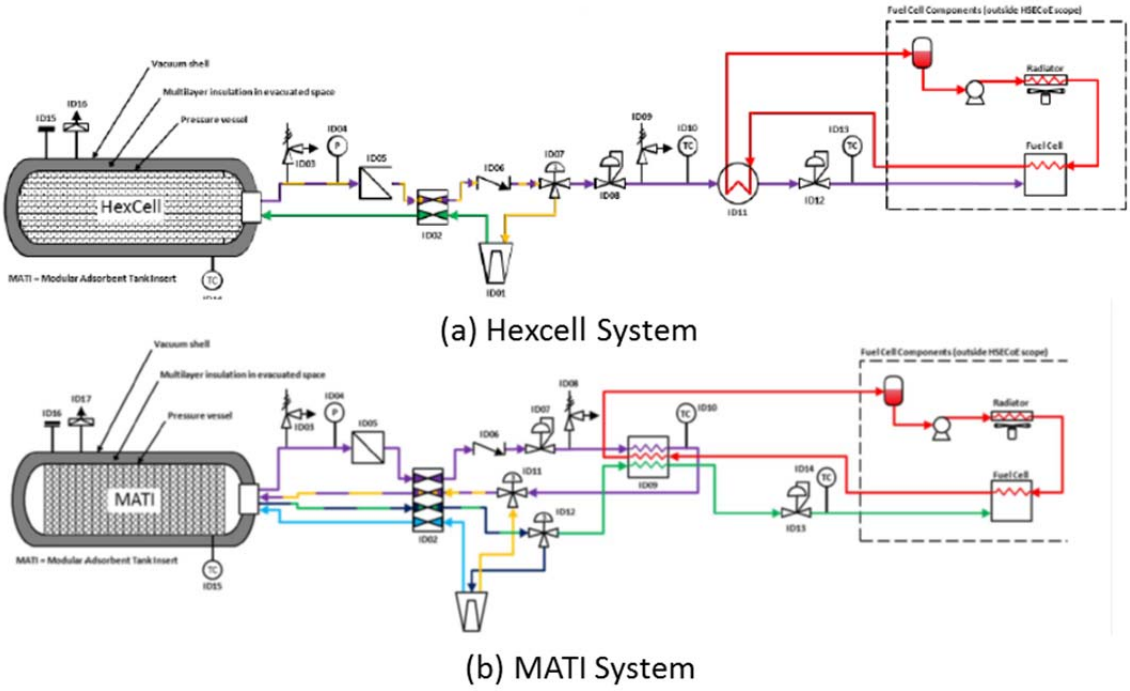

Figure 3.45. Phase-II Preliminary Designs for the (a) Hexcell System and the (b) MATI System

3.4.2.3 Consolidated Valve Block

In an effort to further minimize the BOP cost, mass, and volume for the cryo-sorbent hydrogen storage system, 11 of the valves and instrumentation interfacing with the storage tank were combined into a single housing for both the MATI and the Hexcell designs. This consolidated BOP component included ports to attach pressure relief valves, a check valve, pressure and temperature sensors, pressure regulators, and isolations valves. By combining these components, the system installation time is reduced, the number of fitting required was reduced, and the system cost is minimized. The components consolidated into a single Aluminum 6061 structure are shown within the red dashed line in Figure 3.46.

To reduce the housing mass, unnecessary material was removed from the block. The original design had a mass and volume of 5.7 kg and 4.1 L. By removing additional metal from the design, the mass and volume of the block were reduced to 3.9 kg and 0.6 L, respectively, as shown in Figure 3.47 and Table 3.9. The consolidated valve block was designed either as an independent component or to be installed directly on the top of the tank. In either case, it provides for hydrogen and LN2 flow into and out of the tank.

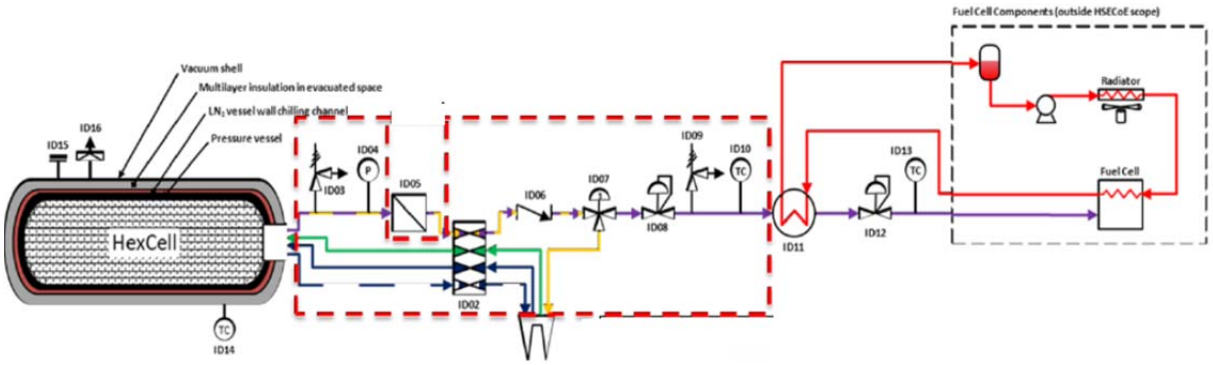

Figure 3.46. Components Combined into the Consolidated Valve Block for Both the Hexcell and MATI Systems Shown within the Red Dashed Line

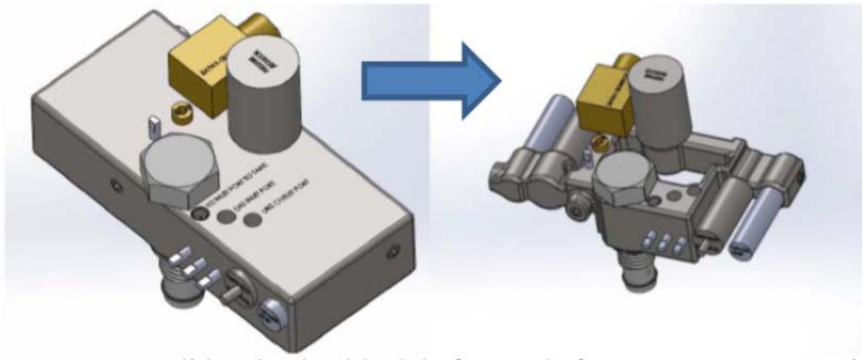

Figure 3.47. Consolidated Valve Block Before and After Removal of Unnecessary Material. This version was designed to be installed on top of the tank.

Table 3.9. BOP Bill of Materials and Masses: Original Phase II and Improved with the Consolidated Valve Block

Consolidated Block Component Only		
Original Components	Mass (kg)	Volume (L)
Separation/isolation valves	2.03	1.58
Pressure relief/gauges	0.11	0.04
Hydrogen pressure sensor	0.004	0.025
Check valves	0.13	0.48
Three-way solenoid valve	2.03	1.58
Pressure regulator	1.09	0.41
Pressure relief/gauges	0.11	0.025
Temperature sensor	0.2	0.02
Subtotal for Original Components	5.7	4.2
Improved Consolidation Version	3.9	0.6

Total BOP Mass		
Original Components	Mass (kg)	Volume (L)
Insulated tubing	0.24	1.5
Hydrogen wetted tubing	0.6	4.5
Multiport receptacle	1	1
Heat exchanger	6.7	5.2
Filter	0.2	0.001
Pressure regulator	1.009	0.41
Temperature sensors	0.4	0.04
Vacuum port	0.1	0.01
Burst disk	0.1	0.01
Consolidated Valve Block	5.7	4.2
Original Total BOP Mass	10.3	12.7
Improved Total BOP Mass	8.5	9.2

A structural analysis was performed on this component to ensure that pressure cycling and thermal stresses would not result in premature failure. This analysis was done by evaluating the smallest bridge sections between ports and assuming an operating pressure of 100 bar (Figure 3.48). For these sections, the peak equivalent stress was determined to be 5.7 ksi. Using a stress limit of 7.5 ksi from NGV3 and CSA, this results in a demand to capacity ratio of 0.77 (CSA Group 2014). At these conditions, the part has a pressure fatigue limit of more than 5 million cycles.

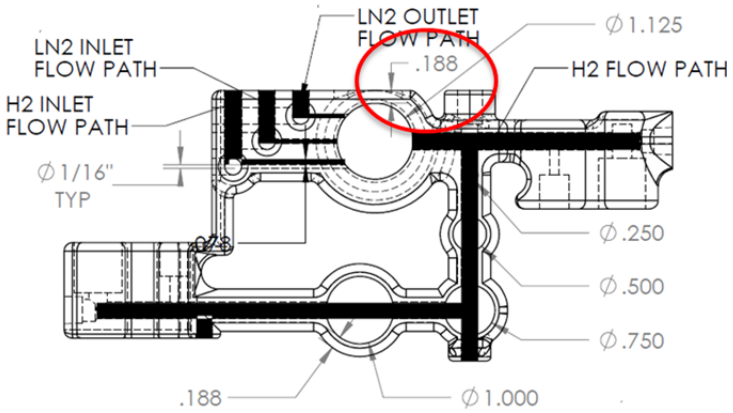

Figure 3.48. Minimum Dimensions of the Consolidated Valve Block

In addition, the thermal gradients and the resultant thermal stresses are small because the heat-transfer rates associated with boiling of the LN2 in the boundary layer are smaller than the heat transfer associated with heat movement through high thermally conductive aluminum. The measured heat-transfer coefficient of LN_2 on the surface is 0.35 W/cm^2/K for a ΔT of 20 K (Jin et al. 2009). When compared to heat flow within the part due to aluminum conduction, with part distances of approximately 1 cm, the heat-transfer within the aluminum is 1.67 W/cm^2/K. As a result, the aluminum conductivity is larger than the heat transferred from the LN_2. The thermal gradients through the aluminum will be small and the resultant thermal stresses would be small as well. Thus, this analysis indicates minimal impact of part thermal cycling. These two analyses indicate that the consolidated valve block design is structurally acceptable.

3.5 Cryo-Adsorbent System Cost

Cost estimates for two adsorbent systems, one with a honeycomb aluminum heat exchanger named Hexcell and the other with a MATI heat exchanger, were undertaken. The system costs included the media, tanks, valves, and other BOP equipment, manufacturing, and assembly costs. The system costs were developed based on system models for each type of adsorbent system and a BOP. BOP components were identified that were recognized as being compatible with hydrogen and met operational pressures and temperatures. The only component differences between the two systems were the sizes of the tanks, the heat exchangers in the pressure vessels, two additional valves in the MATI system, four additional fittings, two different heat exchangers for conditioning hydrogen entering the fuel cell, and the compressed MOF-5 pucks for the MATI system compared with the powder for the Hexcell system. The differences led to differences in the size and weights of the two systems.

3.5.1 Objectives

The cost model was used to develop an estimate of the system costs and, in turn, the $/kWh of useable hydrogen stored to determine how close the system approached the DOE developed cost target of

$10/kWh for 2020 and the ultimate target of $8/kWh (DOE and US Drive 2015). The system costs also were used in the well-to-wheels analysis to determine the life-cycle costs of the two adsorbent systems and its impact on the total fuel cost for the adsorbent systems. The cost model only develops the system's first cost starting at the car's fuel receptacle edge and ending just before the fuel cell. As such, the cost estimate does not provide a cost for adsorbent systems over their lifetimes (e.g., it does not include maintenance costs). Cost estimates were developed for annual production of 10,000, 30,000, 80,000, 130,000, and 500,000 units and maintained in constant 2007$. Progress ratios were used to adjust prices of materials and BOP items as quantities increased.

3.5.2 System Design Used for Costing

The designs for costing the Hexcell and MATI systems are shown in Figure 3.49 and Figure 3.50, respectively. The key for the types of components is shown in Figure 3.51. The dashed lines in both figures indicate components that were consolidated and known as the "elevated design." The "elevated design" decreased the number of fittings for the Hexcell system from 49 to 18 and from 49 to 23 for the MATI system. The system diagrams do not show the components that were added during the comparison of the HSECoE system costs to Strategic Analysis costs (James 2015). Strategic Analysis suggested that we add a controller, a vent relief valve, and an automatic shutoff valve. They also suggested that we add two components to defuel the system. The defueling components were not added to our system as the current system can be defueled through the fill receptacle if required.[13]

The black dashed box indicates the components of the fuel cell system that were not a part of the cost estimate because they were outside of the scope of the onboard hydrogen storage system, and they are expected to be part of the existing fuel cell vehicle. They include the pump, radiator, reservoir, fan, and fuel cell. The list of components for the Hexcell system costed can be seen in Table 3.10 and Table 3.11. The MATI bill of materials is not provided as it only differed by the MATI heat exchanger, the hydrogen conditioning heat exchanger, 1 solenoid valve, one manual valve and four fittings.

3.5.3 Methodology

The methodology for conducting the cost estimate of the adsorbent system can be divided into three parts: 1) developing a bill of materials, 2) estimating the costs (prices) of materials and BOP items, and 3) estimating the manufacturing costs for the storage tank components. The hydrogen storage tank has three basic sections: 1) pressure tank, 2) chiller wall and 3) vacuum shell. A manufacturing cost estimate was also developed for the valve block. The block reduced the number of fittings, which in turn lowered the cost of the adsorbent storage-system assembly.

[13] Strategic Analysis along with Argonne National Laboratory develops independent system designs and conducts cost estimates of onboard storage systems for the US Department of Energy.

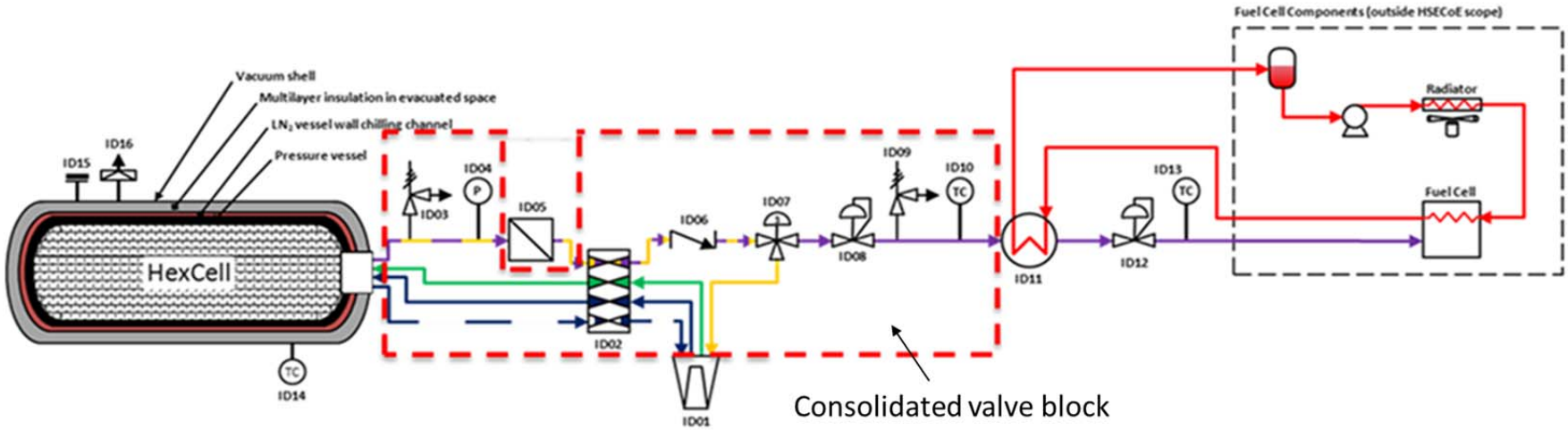

Figure 3.49. System Design for Hexcell System

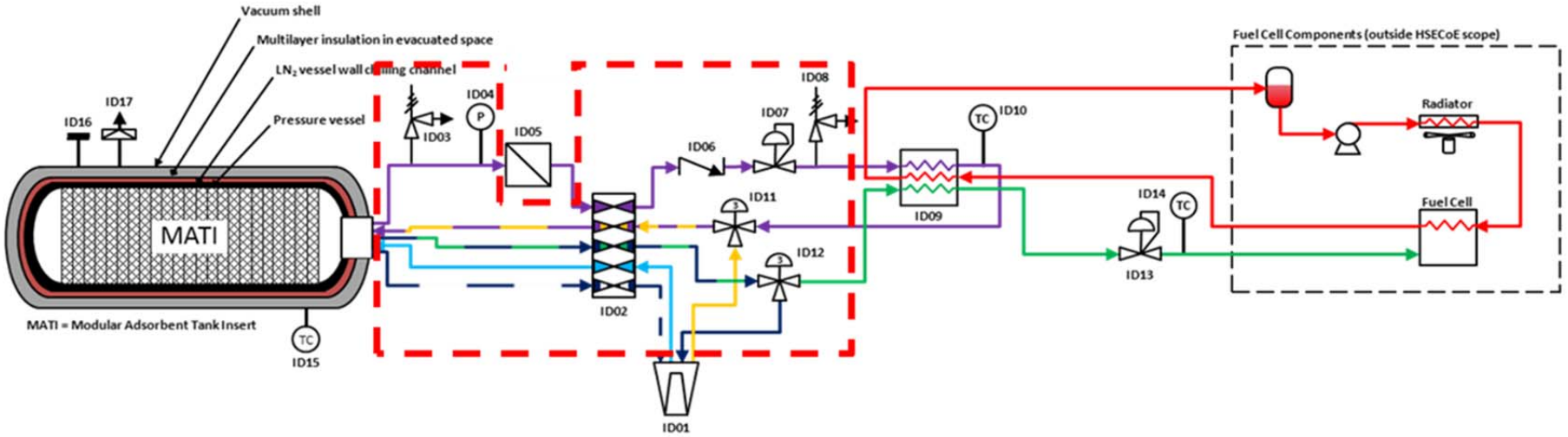

Figure 3.50. System Design for MATI System

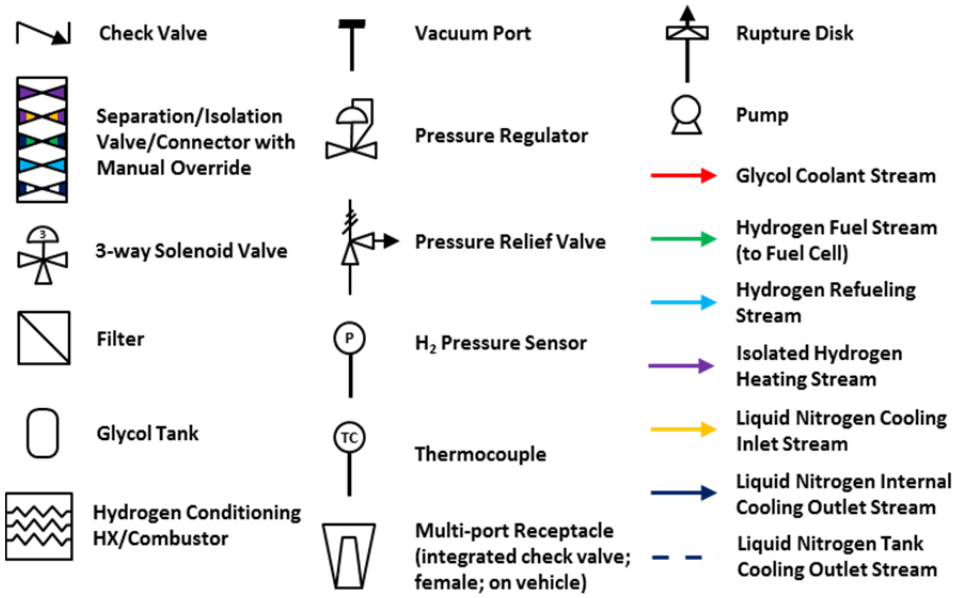

Figure 3.51. Key for System Components Shown in Figure 3.49 and Figure 3.50

3.5.3.1 Bill of Materials

Diagrams of the two adsorbent systems and their respective bills of materials were developed in conjunction with the system modeler and the manager of the BOP components. The system components for costing are described in Section 3.4.2 and shown above in Section 3.5.2. Each system was divided into the following subsystems: tanks, media, heating loop, valves, and other BOP components. The bill of materials for the Hexcell system can be found in Table 3.10 and Table 3.11. Similar components are required for the MATI system. For each adsorbent cost model, the system modeler provided the volume, capacity, and weights of the tanks that were developed to deliver a useable hydrogen capacity of 5.6 kg. The system modeler also identified the operating pressure, temperature, flow rates, and number and types of valves, solenoids, pumps, etc., that were required to operate the system. Valves and other BOP components that met the operating requirements were identified. When possible, a supplier and model number were identified and documented in the bill of material; in other cases, only a type of component was identified. The operating pressures, temperature ranges, and activity to be accomplished were useful in discussing components with manufacturers as they sometimes would suggest less expensive components that could do the same job. If manufacturers suggested alternative components, other team members reviewed the alternatives to ensure operational compatibility with temperatures, pressures, and hydrogen service that would be encountered.

The tank includes four basic components: 1) the inner pressurized tank that weighs slightly more than 58 kg, 2) the Hexcell heat exchanger that weighs slightly less than 8 kg, 3) the chiller wall that weighs approximately 28 kg, and 4) the vacuum shell that weighs slightly more than 14 kg. Several types of multilayer vacuum super insulation (MLVSI) were examined, but the Lydall CRS insulating wrap was chosen because it appeared to be the lowest cost material that met the operational requirements.

Other components needed to complete the system were added. These included the boss, getter, and spacers for separating the chiller wall from the pressure tank, and spacers to separate the layers of MLVSI. The material quantities were updated based on data from the system modeler. The medium is

composed of ~30 kilograms of MOF powder, which stores 5.6 grams of useable hydrogen. The hydrogen was costed at the DOE target of $3.00/kg.

Table 3.10. Hexcell Bill of Materials

Adsorbent System Components				
Tank	PNID	Category	Component	Part Number/Detail
ADS	ID18	Tank		
ADS	ID18-1	T	Aluminum Tank; T6061-T6	
ADS	ID18-2	T	Boss and Plug	
			LN2 Wall Chiller Channel	
ADS	Added	T	G10 Spacers for LN2 Chiller Channel	0.266-in. spacers 1 in. long from 3 × 4 × 0.375 ft; 6480 per sheet; cost of 4.6¢ each in 2015 dollars. Used Costimator to estimate.
ADS	ID18-3	T	G10 Rings for Vacuum Tank	3 ft ×4 ft × ½-in. board
ADS	ID18-4	T	Multilayer Vacuum Superinsulation Lydall	Lydall CRS insulating wrap
ADS	ID18-5	T	Vacuum Shell	
			Getter	
ADS	ID18-6	T	Honeycomb Aluminum Heat Exchanger	
ADS	ID18-7	T	Heater Elements Cable Heater	Watlow 24 V; 4.65 w/cm^2; 4.5 m long
ADS	Added	T	Brackets	18-in. diameter fuel tank brackets with straps
ADS		Media		
ADS	ID18-8	M	MOF-5	
ADS	ID19	M	Hydrogen	
ADS		Heating Loop		
ADS	ID11	HL	Heat Exchanger	GEA PHE MPNS5X12-16 (1-in. MPT)
ADS	ID11	HL	Tubing	Gates 1.0-in. inner diameter straight coolant line. Product # 41781516
ADS	ID11	HL	Distilled Water	
ADS	ID11	HL	FC Coolant	60 wt% ethylene glycol/water mixture
ADS	ID11	HL	Hose Clamp	Gates stainless-steel hose clamp. Product # 74080016
ADS	ID11	HL	FC Coolant Bypass Valve	ASCO three-way 24 V solenoid series 8320. Product # 8320G182
ADS	ID11	HL	Insulation	K-Flex Insul Sheet with pressure-sensitive adhesive
ADS	ID11	HL	Hydrogen Fitting	Swagelok ½-in. female to NPT 1-in.female. Product # SS-810-7-16
ADS	ID10	HL	Temperature Sensor	7710-20-CA

Table 3.11. Hexcell Valve and other BOP – Bill of Materials

Absorbent System Components				
Tank M	PNID	Category	Item	Part Number or Detail
ADS		Valves and Other BOP		
ADS	ID01	BOP	Multiple Port Receptacle	WEH Gas Technology
ADS	ID02	BOP	Separation Valve with Manual Override	26 Series 2-Way Ball Valve
ADS	ID17*	BOP	Insulation	For tubing
ADS	ID17*	BOP	Tubing SS 316	ss316—Swagelok SS-T4-S-035-6ME
ADS	ID17*	BOP	Hydrogen Wetted Tubing	¼-inch SS Insulated Tubing
ADS	ID17*	BOP	Hydrogen Wetted Tubing	¼-inch SS Tubing (Swagelok 6L-T4-S-049-20)
ADS	ID07	BOP	Automatic Valve	Circle Valve Technologies, Inc. Item # 8104-300PPAA5S, 8000 Series Solenoid Valves
ADS	ID06	BOP	Check Valves	K220T1-2PP-1/Circle Seal
ADS	ID08	BOP	Pressure Regulator	TESCOM 20-1263-24-01 Circle Seal
ADS	ID12	BOP	Pressure Regulator	Swagelok KPR1GRA 422A300000
		BOP	Controller	4/30/2015, AX020510 6 input, 5
ADS	ID05	BOP	Filter	Mott Corporation (need particle size details)
ADS	ID12/ID13	BOP	Temperature Sensor	GP50 Temperature Transmitter 7710-2-CA
ADS	ID16	BOP	Burst Disk	Swagelok
ADS	ID15	BOP	Vacuum Port	JNWMVCR2514
ADS	ID03	BOP	Pressure Relief Valve	M5180T1-4MP-1450/Circle Seal
ADS	ID09	BOP	Pressure Relief Valve	8100-55T1T1/Circle Seal
ADS		BOP	Elevated Design	From Elevated Design – Hexcell
ADS	Added	BOP	Vented Relief Valve	Added based on Strategic Analysis comparison
ADS	Added	BOP	Automatic Shutoff Valve	Added based on Strategic Analysis comparison
ADS	ID04	BOP	Hydrogen Pressure Sensor	Kulite Ct-190 Cryogenic Pressure Transducer or GP:50 Pressure Transducer 7720-2-RT-G-CA

The last section includes the elements used in the heating loop that were used to warm hydrogen to the temperature required to enter the fuel cell. The cooling loop is composed of a heat exchanger, tubing, clamps, coolant (a mix of ethylene glycol and water), insulation, a coolant bypass valve, and a temperature sensor. All of the hydrogen fittings were included in this section although they could have been included in the Valve and other BOP section.

The last section of the bill of materials, valves, and other BOPs is shown in Table 3.10. The valves and other BOP section contain primarily the components required to control the hydrogen intake and release to the fuel cell. Multiple receptacles to input hydrogen and nitrogen into the pressurized hydrogen tank

are the first items. The multiple receptacles were approximated using two receptacles from WEH Gas Technology, as a multiple port receptacle in one component was not found as an off-the-shelf component. The wetted tubing was estimated using a combination of insulation and tubing. To reduce the number of fittings and actions taken to assemble the complete system, a number of the components listed in the table were combined into a block of valves and sensors as the "elevated design." The fittings were a significant cost component at just over $10 per fitting, which amounted to a total cost of $195. The combined valves and sensors were added back into the costs as the "elevated design" shown in Table 3.11.

The MATI system bill of materials looks remarkably similar to the Hexcell bill of materials, except that the MATI heat exchanger replaces the Hexcell heat exchanger inside the pressure vessel. In addition, the MATI system has a different heat exchanger to condition hydrogen entering the fuel and provide additional heat to the MATI to speed hydrogen release. The MATI system also has an additional solenoid and manual valves.

3.5.3.2 Pricing of Materials and Balance of Plant Components

Once materials and BOP components were identified, manufacturers were contacted to determine pricing and costs. A list of components and small volume prices is provided in Appendix A. Manufacturers were asked to provide pricing at each level of production required, but often manufacturers/distributors would only provide pricing for a limited numbers of units. The primary reason given was that currently the company did not have capacity to manufacture that many units per year. Some of the manufacturers contacted were very small and would require a significant expansion of their facilities to reach the annual quantities required to meet each of our annual production-level cost estimates. Some manufacturers would give at least two quantities and associated prices. In addition, some manufacturers would not provide pricing as it was their policy to not supply end-users directly or they were limited by their distribution agreements. In certain cases, prices were obtained from local suppliers because the distribution warehouses would not provide pricing.

The analysis assumed that auto manufacturers would deal directly with manufacturers rather than through distributors to get the best price. The prices used in the analysis were adjusted to reflect manufacturer prices if the prices were obtained from distributors. For each level away from the manufacturer, a 30% price reduction was taken to account for the markup from the manufacturer price.[14,15]

Two of the components in the Valves and BOP section were initially priced, but based on OEM feedback were significantly reduced in cost. They were the pressure sensor and the filter. The OEM indicated the price obtainable in series production, and the price was reduced to that level using a progress ratio.

Pricing of materials and BOP components required the use of progress ratios to move from low levels of production to higher volumes. A progress ratio is based on the ability to learn as manufacturing quantities increase. The initial basis for progress ratios emanated from "labor learning" (i.e., knowledge gain through experience) and sometimes is referred to as the learning curve. The progress ratio as used in this estimating process embodies cost decreases that are obtained from technological progress, economies of scale, and learning curves. The progress ratio is often stated as a fraction (NETL 2013). Tsuchiya and Kabayashi (2004) indicate that progress ratios range from 80 to 95% for mechanical products and 70 to 85% for semiconductors and electronic devices. The implication of a progress ratio is that for every doubling of production volume, the cost of producing that volume is the progress ratio (70 to 95) percent of the previous volume. However progress ratios have a bottom limit for production costs, which is the

[14] Personal communication with Frank Hampshire, Motor and Equipment Manufacturers Association, January 26, 2011.
[15] Personal communication with Ron Rossi, Automotive Aftermarket Industry Association, January 26, 2011.

material cost for the item being produced. In other words, costs can approach the cost of materials in production, but the progress ratio cannot cause production costs to go below the cost of materials. In addition, prices at different volumes, if available, were used to develop progress ratios. In other cases, where only one price was obtained, a progress ratio was developed based on how immature the market was, how low the current production capacity was, and the type of material or product for which a high volume price was being forecast. The progress ratio is defined as

$$P = (1-2^{-b}) \tag{3.9}$$

where P is the learning rate at which costs decline for doubling of output, and 2^{-b} is the progress ratio. All costs and prices were adjusted to 2007$ for Phases II and III using the Gross Domestic Product Implicit Price deflator. Finally, the model estimates and pricing were examined by one of the OEMs to determine whether any of our prices were out of line with their expectations based on their purchase records.

3.5.3.3 Manufacturing Costs

Manufacturing costs are based on the levelized costs of capital, labor, O&M, and electricity costs. Electricity costs were broken out if the equipment consumed significant electricity. Major capital costs for each manufacturing step were estimated based on quotes from the manufacturers. The machinery costs were then scaled to meet the required levels of production. Buildings were assumed to provide a 30 year life while equipment was based on a 7 year life. The cost to install equipment was assumed to be 65% of the free-onboard price. The cost of the major equipment was multiplied by 4.55 to obtain an estimate of the total capital cost of the manufacturing facility, including the cost of the building and auxiliary equipment (Peters and Timmerhaus 1991).

Annualized capital costs were separated into building and equipment and estimated separately using a 10% after-tax rate of return. The cost recovery factors are outlined in the assumptions section. The cost factors for equipment and buildings are based on the following formulas. A cost recovery factor was developed separately for equipment and buildings. The first equation provides a factor to annualize capital to a before tax rate of return, and the second equation adds a factor to the first to account for taxes adjusted for tax depreciation to reach an after-tax rate of return.

$$CRF = (i*(1+i)^{\wedge n}/(((i*1)^{\wedge n})-1) \tag{3.10}$$

where

CRF is the capital recovery factor
i is the discount rate
n is the life of the asset.

$$FCRF=CRF*(1-t*NPV)/(1-t) \tag{3.11}$$

where

FCRF is the fixed charge recovery factor after taxes
t is the effective tax rate
NPV is the net present value of depreciation over life of the asset.

Multiplying the appropriate FCRF by the investment cost of equipment and buildings provides the annualized cost of capital per piece of equipment and buildings. Dividing the annualized costs of capital and equipment by the number of production units produced per year provides the cost per production unit.

Electricity. For equipment with significant electricity requirements, the cost of electricity was estimated separately. The electricity costs for each piece of equipment with known energy requirements was estimated using expected operating hours and the industrial rate of electricity from the Energy Information Administration ($0.0644/kWh).

O&M and Labor. O&M costs include labor costs. O&M excluding labor was assumed to be 2% of total installed capital costs. Labor was estimated based upon the number of people required to operate each piece of equipment. A burdened labor rate of approximately $50/hour was used for all process labor. A three shift basis was assumed.

In conjunction with rest of the team, approaches were developed to build the pressure vessel, insert the Hexcell heat exchanger into the pressure vessel, load the MOF-5, add the end cap with boss and plug, install the chiller wall and vacuum shell, and load the powdered MOF into the Hexcell system. Figure 3.52 provides an example of the process flow diagram for constructing the pressure vessel. Equipment was selected. Equipment manufacturers were identified, contacted and asked for quotes. In addition, to the extent that manufacturers were willing to discuss equipment requirements, the number of laborers and speed of machinery were discussed.

The cost for the “elevated design” with the consolidated components was estimated using an off-the-shelf cost estimating software called *Costimator*™. The estimate was developed based on the process shown in Figure 3.53, and on the conceptual drawing shown in Figure 3.54. In addition, a computer-aided design (CAD) provided information on the size of the block, the number and size of holes to be drilled in the consolidated component block. The CAD design was only developed for the Hexcell system. The additional parts and a 20% adder were used to estimate the cost of the “elevated design” for the MATI system. The process flow provided a guide to the steps that needed to be undertaken using *Costimator* to develop the cost estimate for the Hexcell “elevated design” block.

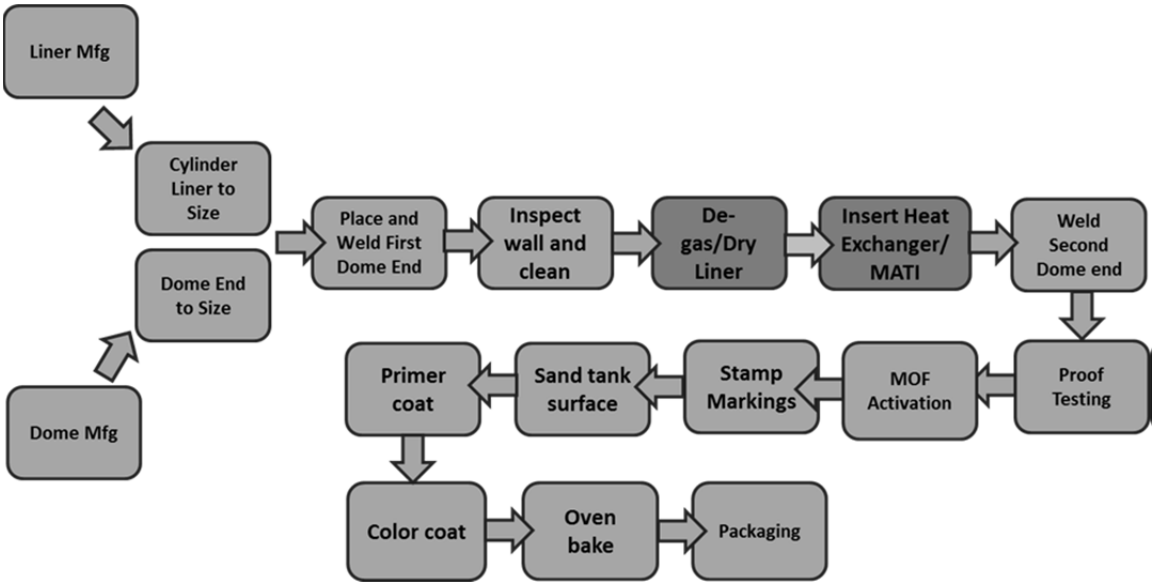

Figure 3.52. Process Flow for Constructing the Pressure Vessel

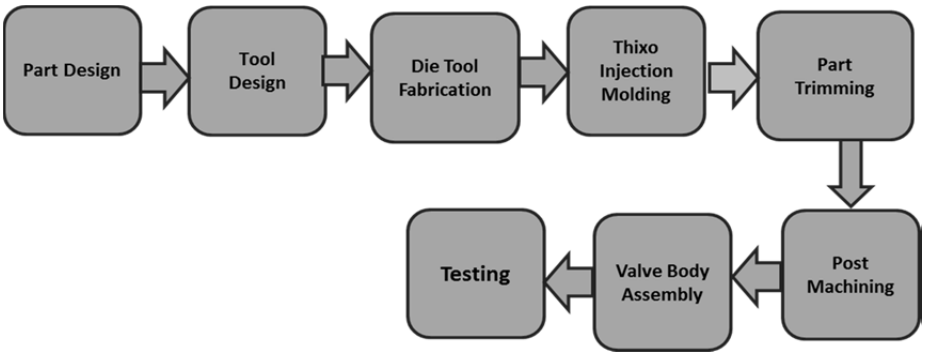

Figure 3.53. Process used to Develop Component Block

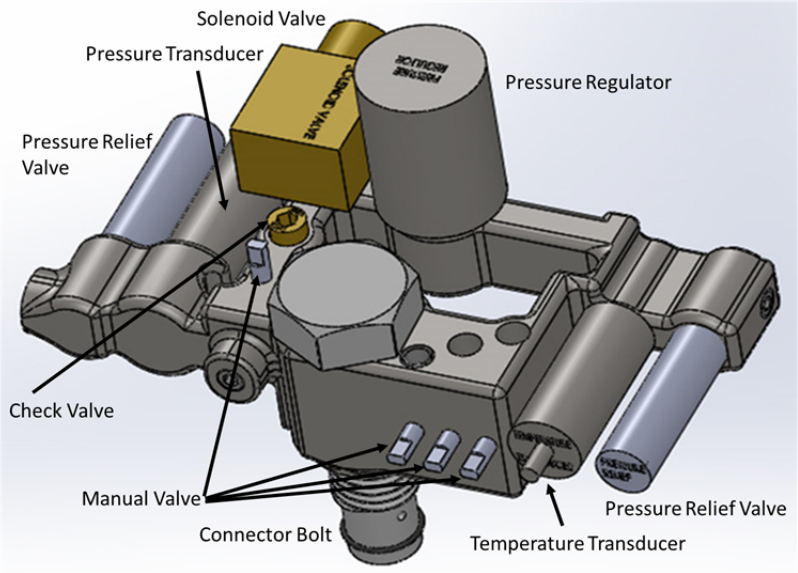

Figure 3.54. CAD Drawing of Component Block

3.5.3.4 Assumptions

During Phase II, the HSECoE worked with Strategic Analysis to determine primary material costs such as aluminum, stainless steel, and carbon fiber that would affect all analyses by both estimators. The motivation behind the materials price agreement was that differences in the system cost estimates at should be primarily due to design and material quantity differences, not differences in prices of the materials used. The primary material costs in the model, including those agreed with Strategic Analysis, are shown in Table 3.12. Some of the most significant costs drivers in the adsorbents system were the MOF-5 media plus the aluminum tank material. The original MOF media costs were obtained from Strategic Analysis who was working with BASF. The price provided was estimated at $13.53/kg for 50,000 systems with 50 kg/system.[16] The agreed upon prices (in 2007$) at 500,000 units of production were $10/kg for MOF-5, $4.45/kg for Aluminum 6061-T6, and $4.92/kg[17] for Stainless Steel 316 (MEPS 2010) at 500,000 units of production. The prices for MOF-5 were adjusted using a progress ratio of 0.85 that was derived by matching the $13.53/kg and the $10.00/kg at the two different quantities.

Table 3.12. Major Material Costs for the Adsorbent System (2007$/system)

Material/Units of Production	10,000	30,000	80,000	130,000	500,000
Aluminum Al 6061-T6 ($/kg)	7.52	6.93	6.44	6.22	4.45
Stainless Steel 316 ($/kg)	9.20	8.48	7.89	7.61	4.92
MOF-5 ($/kg)	24.33	18.95	15.17	13.58	10.00

Progress ratios for materials reflect an approach to show the quantity discounts that would be expected between low-production quantities and high-production mill or manufacturer prices. In all cases, we had large volume prices and we found that small quantities often could contain at least a 100% markup over the large volume prices. For BOP components, the vast amount of components had progress ratios in the 0.90 to 0.95 range. Progress ratios in this range remove the larger margins associated with small volumes. The progress ratios used were similar to those deduced from a fuel cell estimate by James et al. (2002). Note also that the OEMs reviewed the pricing in the model to ensure that the values were approximately correct within their databases. In certain cases, such as filters and temperature sensors, OEMs indicated better high-volume prices than the estimate obtained from the progress ratio provided. In those cases, the progress ratio was adjusted to reflect the better price given by the OEMs.

The assumptions used in estimating manufacturing and assembly costs are shown in Table 3.13. The rates are standard assumptions for building and equipment lifetime. The manufacturing cost estimates are supposed to provide for a full economic recovery of the asset in the specified lifetime. The estimation methodology provides a 10% after-tax recovery rate for capital. Building lifetime was assumed to be 30 years while equipment life was set at 7 years. The federal tax rate was assumed at 35%, while the state corporate tax rate was assumed to be 6%.

Table 3.13. Major Economic Assumptions for Estimating Manufacturing Costs

Economic Assumptions	
Building Lifetime	30 years
Equipment Lifetime	7 years
Modified Accelerated Cost Recovery	20 years
After-Tax Rate of Return	10.0%
Federal Tax Rate	35.0%

[16] Results were provided in an e-mail from Mike Veenstra, July 31, 2014.
[17] Alcoa Aluminum quote from Robert Grothe, Alcoa, June 7, 2012.

Economic Assumptions	
State Tax Rate	6.0%
Effective Tax Rate	38.9%
Property Tax Rate	0.01
Insurance Rate	0.01
O&M Rate	0.02
Weighted Labor Rate	49.69 $/hour
Cost Recovery Factors	
Building Cost Recovery Factor	10.60%
Value of Building Depreciation	44.80%
Building After-Tax Recovery Factor	14.34%
Equipment Cost Recovery Factor	20.50%
Value of Equipment Depreciation	73.00%
Equipment After-Tax Cost Recovery Factor	24.10%

3.5.4 Results and Discussion

The Hexcell system at $2,998/system or $16.08/kWh for 500,000 units of production was slightly less expensive than the MATI system at $3,275 or $17.56/kWh. Both systems exceed the 2020 target of $10/kWh and the ultimate target of $8.00/kWh. More than $1,100 in savings for the Hexcell system and more than $1,400 for the MATI system would need to be found to reach the 2020 cost target. The Hexcell system has a lower cost because of its simpler design compared to the MATI design, which includes a complex but effective heat exchanger. The MATI heat exchanger, however, is much more expensive than the Hexcell heat exchanger, but conversely, the MATI heat exchanger along with the compressed pucks reduces the size of the pressure vessel. The reduction in size, however, is not enough to overcome the added cost of the MATI heat exchanger and the addition of the two valves and the additional MOF-5 in the pucks. The heat exchanger adds $160 per system, the additional densified MOF-5 increases the cost another $193, and the valves $49 more. The hydrogen temperature conditioning heat exchanger for the MATI system is approximately the same cost as the similar component in the Hexcell system.

Hexcell System. A summary of the Hexcell system costs are shown in Table 3.14 The table shows the costs at production levels of 10,000, 30,000, 80,000, 130,000, and 500,000 units. The use of progress ratios and scaling factors for equipment are primarily responsible for the decreasing costs across the different levels of production. Our discussion focuses on the costs at 500,000 units. Valve costs are the largest component of costs at over $900. Tank components, at $685, are the second largest component. The breakdown of total costs is shown in Figure 3.55. Manufacturing costs for the tank comprise only 11% of the total system costs but represent 33.5% of total pressure vessel system costs, which is very close to the estimated costs of manufacturing tanks at 35.5% based on the total estimated cost. The material cost of the Hexcell heat exchanger is only a small portion of the tank costs at $38. The MOF-5 ($317) is approximately 11% of the total costs. Valves make up a significant amount of the cost ($919) or 31% of the costs. In addition, the costs of the fittings were a significant portion of other BOP ($196) or about 7% of total costs. The multiple port receptacles also made up a significant portion of cost ($230) or almost 8% of total costs. The costs of the controller ($106), the vent relief valve ($14), and the automatic shutoff valve ($9) added a total of $129 to the system costs based on input from Strategic Analysis on additional components required for the system. More detailed costs can be found in the Appendix A.

Table 3.14. Estimated Costs of the Hexcell System by Major Groups (2007$)

Item/Nmber of Units	10,000	30,000	80,000	130,000	500,000
Tank Components	1,151	1,035	945	905	685
Tank Manufacturing	1,795	949	620	530	343
Media	746	585	472	425	317
BOP					
Valves	1,687	1,395	1,189	1,102	919
Other BOP	1,066	857	734	686	580
Assembly	392	301	238	212	154
Total	6,838	5,122	4,197	3,859	2,998
$/kWh	36.67	27.46	22.51	20.69	16.08

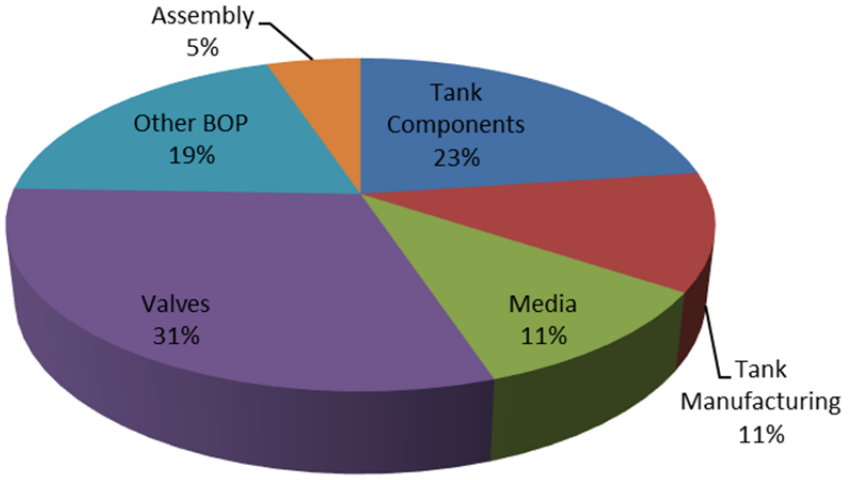

Figure 3.55. Breakdown of Major Components of Hexcell System Cost

Table 3.15 shows the breakdown of Hexcell manufacturing costs. Tank manufacturing and assembly costs total $343. BOP assembly and final inspection add another $154 for a total of $497 in manufacturing and assembly costs. Quotes for equipment included a curing oven, autoclave, friction stir welders, annealing furnaces, billet saws, hydraulic presses, cylinder extrusion presses, and vacuum pumps. Some equipment for which the team didn't have expertise such as handling MLVSI was taken from TIAX (Alhuwalia et al 2009). MLVSI wrapping on the outside of the LN2 chiller wall is the most expensive manufacturing task of the tank manufacturing costs primarily because of the number of hours estimated for the task. Equipment was only a small portion of the costs. Material loss totaling 12% was partially from the manufacturing process and partially from the bursting of tanks to assure the quality and safety of the tanks. Hexagon Lincoln provided the capital and labor requirements for the Final Inspection. Capital and labor for final inspection was taken from TIAX information previously mentioned. Where information could be gleaned from team members, manufacturing equipment costs and labor were used.

Table 3.15. Breakdown of Hexcell Manufacturing Costs (2007$)

System Component/Number of Units	10,000	30,000	80,000	130,000	500,000
Inner Tank Manufacturing Costs Excluding Chiller Wall	875	400	236	201	122
Equipment Labor and O&M Costs	741	289	141	112	58
Hexcell Insertion	10	8	6	5	4
MOF Loading	59	46	36	32	24
Burst Tank Material Losses	7	4	3	3	2
Material Lost	58	54	50	48	34
MLVSI	286	220	175	156	113
LN2 Chiller Wall	491	226	131	105	62
LN2 Chiller Wall Manufacturing	302	114	51	35	14
Material Lost	28	26	24	23	17
Assembly	160	86	56	47	31
Outer Tank Assembly	83	60	45	40	26
Material Lost	14	13	12	12	8
Vacuum Processing	48	34	26	22	15
Cryogenic Tank Inspection	13	9	7	6	5
Total BOP Assembly and Final Inspection	392	301	238	212	154

As previously discussed, the costs for manufacturing the valve block, assembly, inspection, and testing were developed using *Costimator*. The cost of the component is driven primarily by the costs of the valves which account for 82% of the costs. Assembly, inspection, and pressure testing account for 7% of the costs. The negative values associated with the valve body were an attempt to remove the costs of five valve bodies because the valves were inserted into the component without their bodies. Valves were obtained, the bodies removed, and the weight was estimated. The material costs of the valve bodies were then estimated and removed from the costs of the component.

A tornado chart representing the risks of the Hexcell system cost estimates in $/kWh are shown in Figure 3.56. The tornado analysis only looks at the risks one at a time rather than a Monte Carlo analysis, which estimates the impact of the combined risks. Note that risks are expected to be primarily to the upside. While the tornado analysis evaluates the risks in $/kWh, the following discussion will relate the risks to the impact on total system cost. The highest upside cost risk is for valves ranging in total system costs from $826 to $1,378 for total valve costs around a midpoint of $919. The upside risk occurs primarily because of the degree to which valve costs were reduced using the progress ratios. Some are as low as one-fifth their original price. Included in this group are pressure and temperature transducers whose price declined to one-fiftieth of their original price. A portion of this decline resulted from OEM input on the pressure transducer. The price of aluminum is the second highest risk but is showing more downside potential than other components.

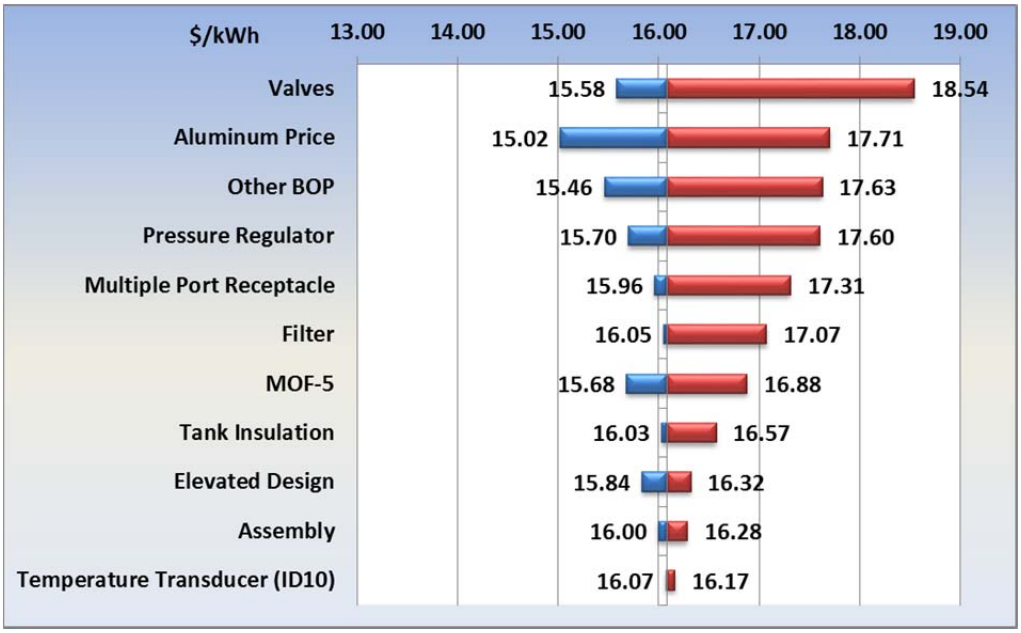

Figure 3.56. Tornado Chart of Major Component Risks for the Hexcell System ($/kWh)

The costs for the Hexcell "elevated design" with consolidated components are shown in Table 3.16.

Table 3.16. Breakdown of Hexcell System Consolidated Component Manufacturing Costs (2007$)

	Quantity	10,000	30,000	80,000	130,000	500,000
Wastage	1	0.14	0.12	0.11	0.10	0.10
Body Material	1	5.86	5.40	5.03	4.85	3.47
Diecasting	1	1.41	1.41	1.41	1.41	1.41
Body Machining	1	16.58	16.54	16.54	16.54	16.54
Inspection of Body	1	12.19	12.18	12.18	12.18	12.18
Plugs	12	1.59	1.59	1.59	1.59	1.58
Insert Plugs	12	1.26	1.18	1.14	1.13	1.13
Pressure Relief Valve (ID03 and ID09)	2	123.47	86.69	63.22	54.07	50.04
Pressure Transducer (ID04)	1	95.82	70.63	53.80	47.02	32.35
Temperature Transducer (ID10)	1	71.93	47.34	32.58	27.08	16.22
Check Valve (ID06)	1	39.58	29.74	23.04	20.31	14.31
Pressure Regulator (ID08)	1	216.78	198.18	182.94	175.83	157.53
Solenoid Valve (ID07)	1	54.71	46.29	39.88	37.04	30.19
Manual Valve (ID02)	4	187.47	144.90	115.13	102.74	74.92
Valve Body	5	(9.02)	(8.31)	(7.73)	(7.46)	(4.82)
Tank Connector	1	4.60	4.58	4.44	4.44	4.44
Teflon O-Ring	1	10.77	10.39	10.07	9.92	9.50
Assembly	1	15.35	15.34	15.34	15.34	15.34
Inspection of Assembled Parts	1	13.99	13.99	13.99	13.99	13.99
Pressure Testing	1	87.83	29.59	11.29	7.04	1.95
Total		952.31	727.80	596.00	545.17	452.34
Valves		780.73	615.47	502.86	456.64	370.71
Machine and Testing		171.57	112.33	93.14	88.53	81.62

The price for aluminum 6061-T6 ranges from $2.23/kg to $6.68/kg with a midpoint of $4.45/kg. The downside potential occurred because the price of aluminum has been in steady decline for the last 4 years providing a prospective for price decreases. At the time of our quote from Alcoa, basic aluminum prices were around $1.00/lb, and currently they are around $0.66/lb.[18] Other BOP ranges from $464 to $869, with a midpoint at $580. The components in other BOP include the controller, burst disks, and fittings, all of which declined by half. The pressure regulator declines by approximately half from the quotes to the prices at 500,000 units. The multiple port receptacles were another item that declined significantly from the original quote, approximately by one-sixth of the original price quote. There could be cost savings based on the design of an actual multiple receptacle rather than being estimated by the cost of two receptacles. MOF-5 has been produced in reasonable quantities and the manufacturer contributed to the cost estimate so the upside risk is lower. However, MOF-5 is still a significant contributor to the cost of the system. The temperature transducer was limited in its upside risk because of OEM input.

MATI System. The MATI system cost totaled $3,275 or $17.56/kWh (Table 3.17). The most significant component of the tank components cost is the $200 for the MATI heat exchanger, which is a significant cost increase over the over the cost of the Hexcell heat exchanger. To see a breakdown of the individual components in Table 3.17, refer to the MATI cost tables in Appendix A. In addition, the quantity of MOF-5 increases significantly from 30 kg in the Hexcell system to 49 kg in the MATI system, thus increasing the total MOF cost to $493 from $299. The two additional valves increase the price $49 over the Hexcell system. The MATI assembly cost is slightly more expensive than the Hexcell assembly cost because extra parts that are included in the assembly compared with the Hexcell system. Because of the increased amount of MOF-5, the valves drop from 31% of the total cost in the Hexcell system to 27% of the cost for the MATI system while media increases from 11% to 15%. Costs for the remaining components remain pretty much the same (Figure 3.57)**.**

Table 3.17. Estimated Costs of the MATI System by Major Group (2007$)

Item/Number of Units	10,000	30,000	80,000	130,000	500,000
Tank Components	1,497	1,116	977	932	742
Tank Manufacturing	1,906	964	606	511	322
Media	1,217	952	765	687	510
BOP					
Valves	1,671	1,360	1,146	1,057	873
Other BOP	1,170	952	824	774	660
Assembly	428	329	260	232	168
Total	7,889	5,672	4,579	4,192	3,275
$/kWh	42.30	30.42	24.56	22.48	17.56

[18] www.infomine.com

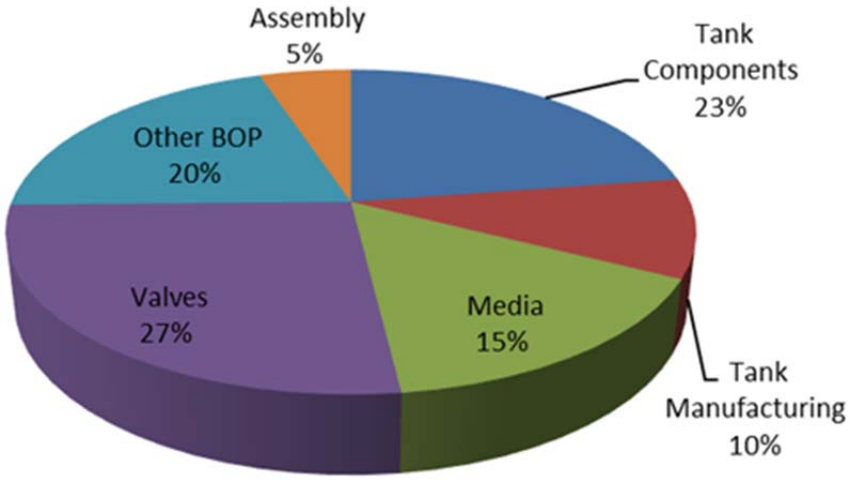

Figure 3.57. Breakdown of Major Components of MATI System Cost

The only differences in manufacturing costs are due to the MOF-5 loading cost being incorporated into the MATI cost model. OSU developed a cost model for the MATI system and had it vetted by a manufacturer. That model was used by the HSECoE to estimate the cost for the heat exchanger system. In addition, during the course of this project, OSU discovered that they could use aluminum 3003 which is about two-thirds the cost of aluminum 6061-T6. Use of the aluminum-3003 cost resulted in a significant reduction in final MATI cost to approximately $200 for the system costs. The manufacturing costs for the MATI system are provided in Table 3.18.

Table 3.18. Breakdown of MATI Manufacturing Costs (2007$)

System Component/Number of Units	10,000	30,000	80,000	130,000	500,000
Inner Tank Manufacturing Costs Excluding Chiller Wall	991	419	226	185	104
Equipment Labor and O&M Costs	835	332	164	130	67
MATI Insertion	100	39	18	13	6
MOF Loading	This is part of the MATI cost estimate				
Burst Tank Material Losses	7	4	3	2	1
Material Lost	48	44	41	40	28
MLVSI	286	220	175	156	113
LN2 Chiller Wall	488	222	128	103	60
LN2 Chiller Wall Manufacturing	302	114	51	35	14
Material Lost	25	23	21	21	15
Assembly	160	86	56	47	31
Outer Tank Assembly	81	58	44	39	26
Material Lost	13	12	11	11	8
Vacuum Processing	48	34	26	22	15
Cryogenic Tank Inspection	13	9	7	6	5
Total BOP Assembly and Final Inspection	428	329	260	232	168

One increase in manufacturing costs was associated with the formation of the MOF-5 puck that is placed inside the MATI. The original plan was to manufacture the puck by extrusion, but because the experimental results were undertaken with the enhanced puck or a puck that contained aluminum pins, extrusion was no longer a choice. The puck needed to be built with a die that could hold the aluminum pins, be inserted into another die, and pressed to form the puck. The approach taken was to estimate the cost of producing one puck including the pins and then use progress ratios to determine the cost at 500,000 units. *Costimator* was employed to estimate the costs of making the dies, and the price of a hand press was obtained. Labor to insert the pins into the die was estimated by actually inserting pins

into a die and estimating the time to press a puck. The levelized costs of the one puck was calculated and extrapolated to the number of pucks required to fill one MATI system. The cost per MATI system was then estimated using a range of progress ratios from 0.70 to 0.75 to obtain costs between $4 and $16 per system at 500,000 units. The cost without the pin-containing die was $6 per system. It seems unreasonable to more than double the cost of the puck to account for the die and mechanical equipment. Therefore, 30% was added to the system capital to account for the die and required mechanical equipment, which placed the progress ratio approximately half way between the two end points.

The complex manufacturing process indicates that an alternative approach to producing pucks with pins needs to be investigated to improve heat conductivity in the puck**.** The complex manufacturing approach does not lend itself to low-cost, high-volume production.

The MATI system "elevate design" with consolidated component cost is very similar to the Hexcell system "elevated design" cost (Table 3.19). Approximately 20% more material was used based on the designer's expert opinion because of the additional volume required for the two additional components. There is an added solenoid valve and one more manual valve. The total cost at $503.64 is approximately $50 more than the Hexcell component. The "elevated design" reduced the number of fittings from 49 to 23**.**

Table 3.19. Breakdown of MATI System "Elevated Design" Manufacturing Costs (2007$)

Item	Quantity	Units	10,000	30,000	80,000	130,000	500,000
Wastage	1	piece	0.17	0.14	0.13	0.12	0.12
Body Material	1	piece	7.17	6.61	6.15	5.93	4.25
Diecasting	1	piece	1.41	1.41	1.41	1.41	1.41
Body Machining	1	piece	16.68	16.66	16.65	16.65	16.64
Inspection of Body	1	piece	12.19	12.18	12.18	12.18	12.18
Plugs	12	pieces	1.59	1.59	1.59	1.59	1.58
Insert Plugs	12	pieces	1.404	1.308	1.272	1.26	1.26
Pressure Relief Valve (ID03 and ID09)	2	pieces	123.47	86.69	63.22	54.07	50.04
Pressure Transducer (ID04)	1	piece	95.82	70.63	53.80	47.02	32.35
Temperature Transducer (ID10)	1	piece	71.93	47.34	32.58	27.08	16.22
Check Valve (ID06)	1	piece	39.58	29.74	23.04	20.31	14.31
Pressure Regulator (ID08)	1	piece	216.78	198.18	182.94	175.83	157.53
Solenoid Valve (ID07)	1	piece	109.41	92.59	79.76	74.09	60.37
Manual Valve (ID02)	4	pieces	234.34	181.12	143.91	128.43	93.65
Valve Body Removal	5	pieces	(10.68)	(9.84)	(9.16)	(8.83)	(5.71)
Tank Connector	1	piece	4.60	4.58	4.44	4.44	4.44
Teflon O-Ring	1	piece	10.77	10.39	10.07	9.92	9.50
Assembly	1	piece	17.61	17.59	17.59	17.59	17.59
Inspection of Assembled Parts	1	piece	13.99	12.19	13.99	13.99	13.99
Pressure Testing	1	piece	87.83	29.59	11.29	7.04	1.95
Total			1,056.07	810.71	666.88	610.12	503.64
Valves			880.65	696.46	570.11	518.00	418.74
Machine and Testing			175.42	114.26	96.77	92.12	84.90

The primary difference between the MATI tornado chart shown in Figure 3.58 and the Hexcell system tornado chart is the midpoint of the columns, which is $17.56/kWh for the MATI system versus $16.10/kWh for the Hexcell system. The same risk factors were applied in both cases. The higher costs of

the MATI system cause the size of the risks to increase proportionately to the added costs for valves and the reduced cost of aluminum because of the decreased amount of aluminum in the pressure tank components.

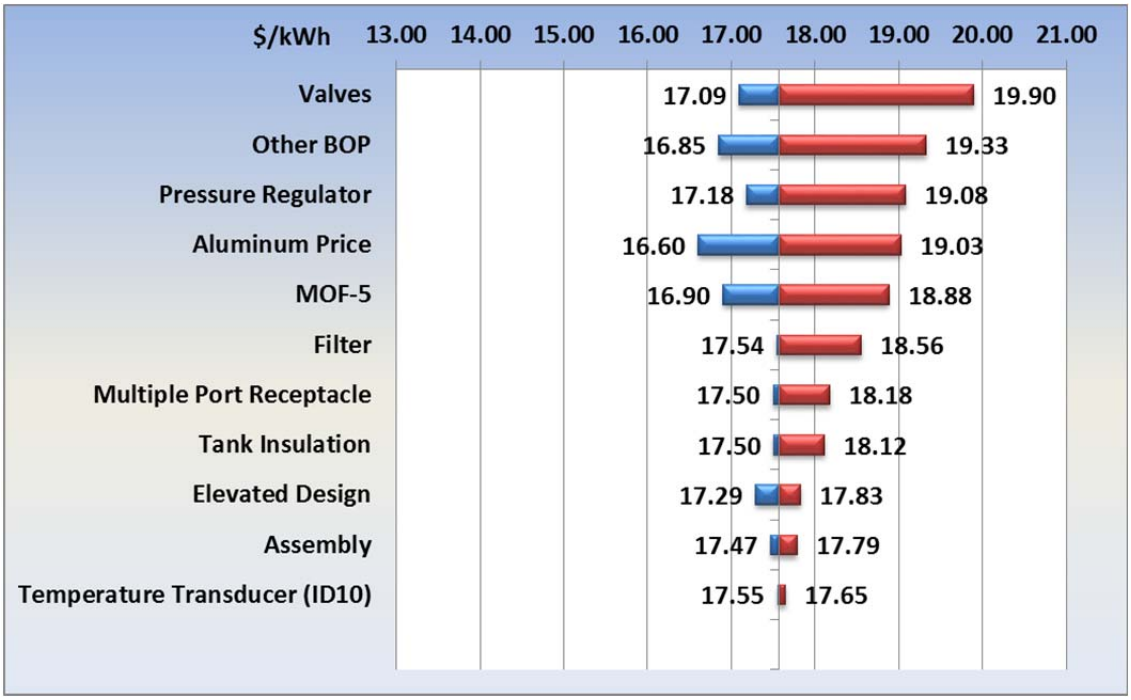

Figure 3.58. Tornado Chart of Major Component Risks for the MATI System ($/kWh)

3.6 Hydrogen Compatibility of Polymers at Cryogenic Temperatures and Under Hydrogen-Saturated Conditions

The objective of this study is to evaluate material compatibility for the cryogenic tank and consolidated BOP components for cryo-adsorbent hydrogen storage systems. For these initial tests, materials that represent different polymeric materials that could be used the BOP components were chosen and mechanically tested at ambient temperature or LN2 temperature, and with or without hydrogen saturation. Measured material property data are presented in this section.

3.6.1 Impact of Cryogenic Temperatures on Polymer Properties

In the design of a Type-IV pressure vessel, HDPE is often the most common liner material selected. This thermoplastic has acceptable hydrogen compatibility and performs well at ambient temperatures (Wong 2010, Newhouse 2010, Villalonga et al. 2011, McLaughlan et al. 2011). In Type-IV pressure vessel tanks, the inner liner provides no strength benefits to the overall system. The liner serves to minimize gas permeation into the fiber reinforced polymer subsequently reducing hydrogen embrittlement that can lead to premature failure of the fiber reinforced polymer composite shell (Wong 2010). In addition, the liner can serve as a corrosion barrier when needed. Figure 3.59 shows a schematic cross section of heating-loop patented liner technology currently used in Type-IV pressure vessel construction. When designing a Type-IV pressure vessel for cryogenic applications, further considerations of the mechanical properties of the liner are warranted. While HDPE performs well at ambient temperatures, it may have unacceptable properties at cryogenic temperatures. One major area of concern is the effect of cryogenic temperatures

on the elongation of the liner material. As polymers cool, their modulus and strength increase while the elongation at break (EAB) decreases. If this elongation is below a minimum threshold the liner can fail.

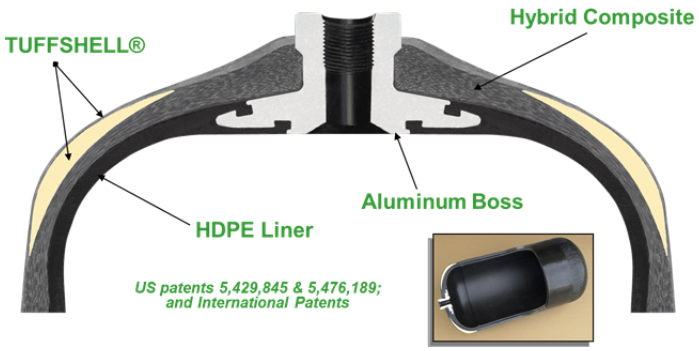

Figure 3.59. Schematic Cross Section of Heating Loop Patented Liner Technology Currently used in Type-IV Pressure Vessel Construction

Upon conducting a literature review we determined that a large knowledge gap exists in the mechanical performance of potential Type-IV pressure vessel tank liners at cryogenic temperatures (Shalaby 1981, Menczel 2008). This research aims to bridge this gap by providing fundamental research regarding the mechanical properties of nine potential thermoplastic liner materials: 1) HDPE, 2) ultra-high molecular weight polyethylene (UHMWPE), 3) ethylene tetrafluoroethylene (ETFE), 4) fluorinated ethylene propylene (FEP), 5) perfluoroalkoxy alkanes (PFA), 6) polytetrafluoroethylene (PTFE), 7) polyimide (PI), 8) polychlorotrifluoroethylene (PCTFE), and 9) polyvinylidene fluoride.

3.6.1.1 Tensile Properties of Polymers

Approach

The standard design and test protocols used for measuring the tensile properties of polymers, ASTM D638/ISO 527-1 (ASTM 2008, ISO 2012), do not provide guidance for the testing of these materials at sub-ambient temperatures. Several tests had been conducted to determine if samples could be flash frozen in LN2, removed from the liquid and tested at ambient temperatures. This method relied on fast loading and testing of each sample and was found to provide inconsistent results likely because of the rapid heat absorption of the frozen sample especially at the grip interface. In addition, samples cooled in this fashion were difficult to load in the test grips, resulting in slippage or premature failure.

Looking at other tensile standards, some guidance is provided in ASTM E1450 (ASTM 2009) for testing structural alloys in immersed liquid helium. In this method, a specially designed vacuum-insulated dewar is fitted to a universal test stand where the sample and grips are fully immersed in the cryogenic fluid. The schematic is shown in Figure 3.60.

For measuring samples at 77 K, a standard foam dewar was found to be satisfactory and provided ample insulation for short-term tensile testing. Figure 3.61 shows PNNL's cryogenic tensile testing apparatus Version I.

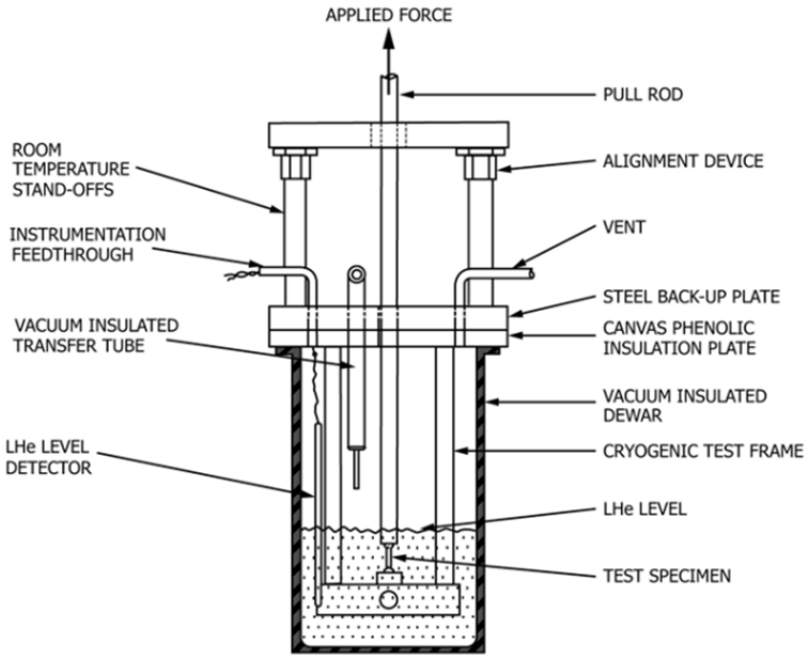

Figure 3.60. ASTM E1450 Schematic of Tensile Test Apparatus for Testing at 4 K

Figure 3.61. PNNL Cryogenic Tensile Testing Apparatus, Version I

Results and Discussion

The largest technical hurdle associated with the cryogenic tensile testing involved developing the methods to adequately grip the samples to minimize slippage. At cryogenic temperatures, polymers become increasingly brittle and their surfaces harden. This creates significant challenges for gripping the samples as the commonly accepted method of using cross-hatched grip faces and significant clamping force to bite into the tab regions commonly resulted in sample fracturing within the grips during the loading process. Typical hydraulic self-tightening clamps also proved to be inadequate as the clamping mechanism did not properly engage while submerged in liquid nitrogen. In addition, several attempts with low clamping forces using vice action grips with cross-hatched faces proved inadequate because the likelihood of

samples slipping was high. Ultimately, using an alternating diamond grit coated grip face with a sheet of G-10 fixed face and moderately high clamping forces in a vice action grip proved to be acceptable. Once this method was developed the testing was fairly straightforward.

As expected, most of the samples had a significant reduction in their EAB when tested in LN2 as can be seen in Table 3.20. Figure 3.62 shows the cryogenic ASTM tensile testing results.

While the strength of the polymer liner is relevant in Type-IV fiber reinforced pressure vessels, the composite provides the primary axial and hoop strength to the vessel whereas the liner primarily provides corrosion resistance. When considering the application of cold or cryo-compressed gas, the EAB of the liner becomes a significant driver. If under these cryogenic conditions the liner has insufficient elongation, liner expansion during pressurized filling can cause crazing or micro-cracks within the liner, leading to a premature failure. This was a motivating factor for developing an understanding of the effects of cryogenic temperatures on the EAB of the polymer liner. One example of an extreme difference between room temperature and cryogenic temperatures was seen in the ECTFE samples. These samples had a 94% reduction in EAB compared to data for room-temperature testing (10% strain at break). Coincidentally, the strength at break was nearly 355% of the room-temperature data (~21.7ksi) as shown in Figure 3.63 and Figure 3.64. When used as a tank liner in cold gas Type-IV fiber reinforced pressure vessels, EAB is the most important factor to be considered in materials selection. In Type-IV fiber reinforced pressure vessels, the axial and hoop strength comes directly from the fiber reinforced outer material with the ultimate strength and moduli significantly higher than the weaker thermoplastic liner.

Table 3.20. Ultimate Tensile Strength and EAB of Candidate Tank Line Materials Measured at 77 and 296 K, Respectively

Material	Tensile Stress at Break -190 K (Ksi)	EAB -190 K (%)	Tensile Stress at Break 25°C (Ksi)	EAB 25°C (%)
ETCFE[a]	21.65	6.68	6.09	104.65
HDPE[b]	18.58	5.80	6.17	61.09
HDPE[c]	--	--	3.38	54.42
HDPE[d]	--	--	5.88	45.52
PVDF[e]	22.06	2.23	--	--
PVDF[f]	--	--	--	--
PVDF[g]	--	--	--	--
PTFE	10.82	2.60	--	--
PCTFE	20.54	6.03	--	--
PFA	20.18	5.73	--	--
PI SP-1	13.39	3.60	--	--
ETFE	13.95	3.10	--	--
UHMWPE	23.91	5.53	--	--
Epoxy	13.29	5.65	--	--
FEP	20.30	8.10	--	--

[a] ECTFE (ethylene chlorotrifluoroethylene)
[b] HDPE: off-the-shelf stock material
[c] HDPE: extruded sheet material
[d] HDPE: injection molded material
[e] Polyvinylidene fluoride (PVDF): 6000 grade injection molded material
[f] PVDF: 9000 grade injection molded material slow shot speed
[g] PVDF: 9000 grade injection molded material fast shot speed.

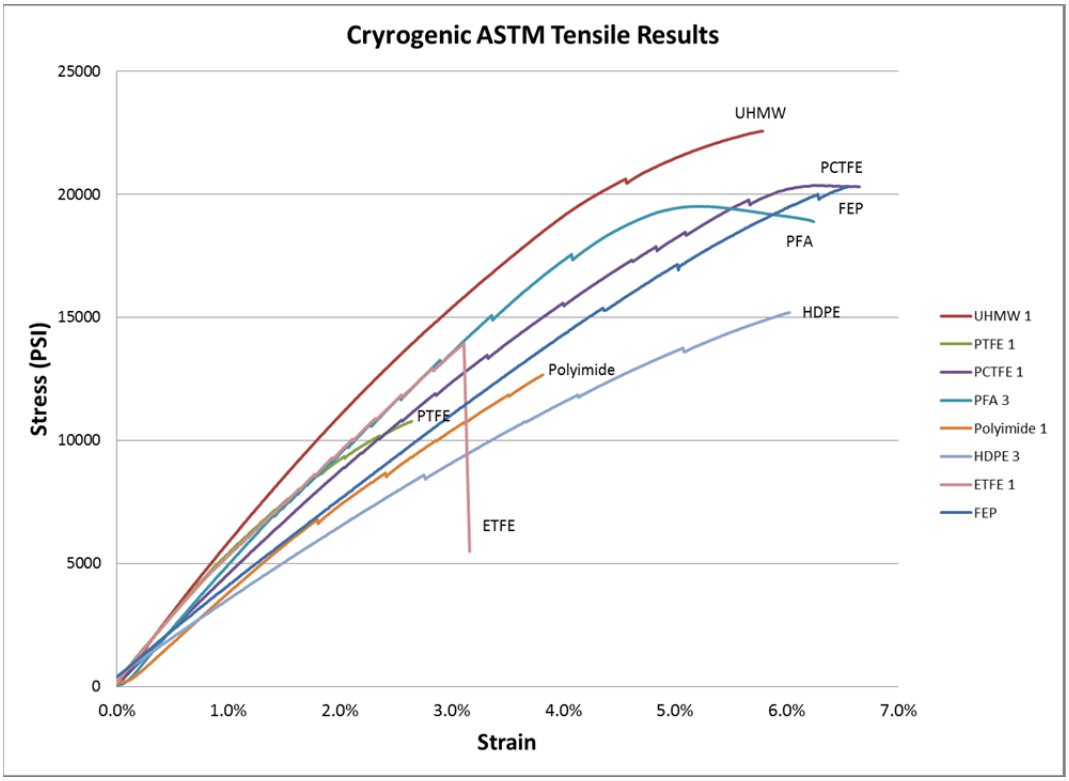

Figure 3.62. Cryogenic ASTM Tensile Testing Results

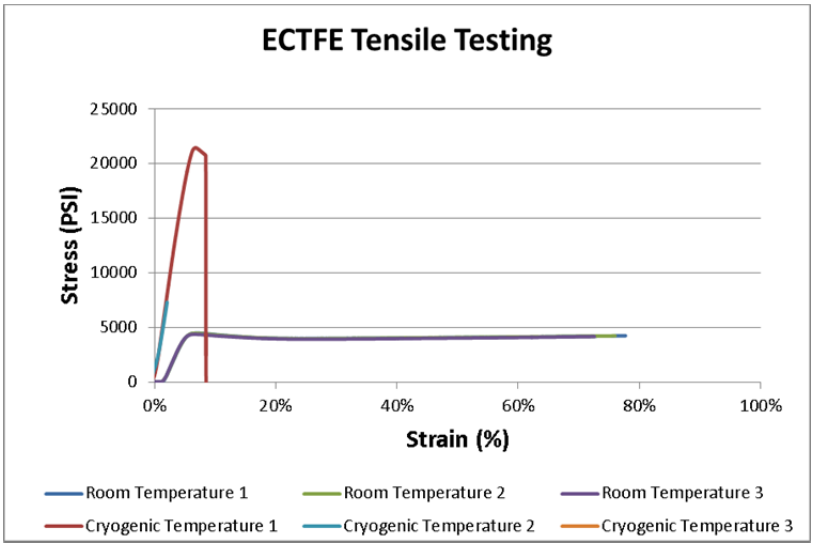

Figure 3.63. Comparison Results of ECTFE Tensile Testing at Room and Crygrogenic Temperatures

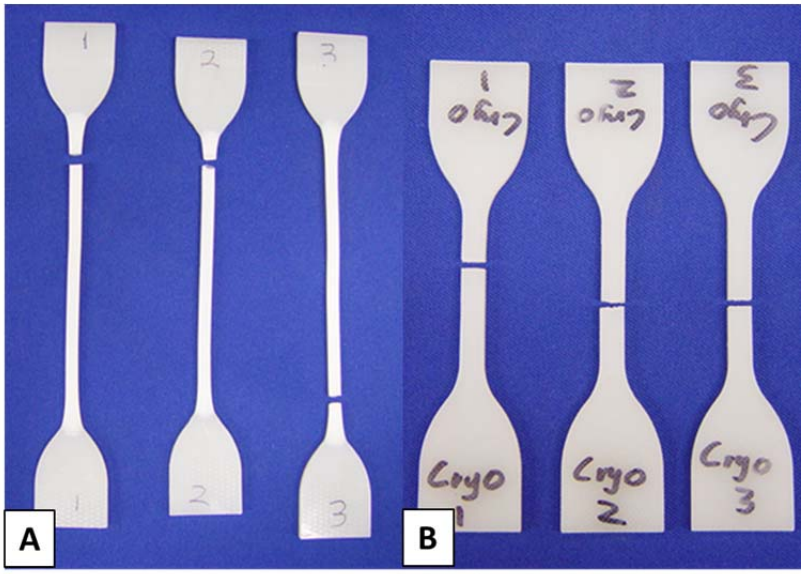

Figure 3.64. Tensile Tested ECTFE Samples: (A) Ambient Tested, and (B) Cryogenically Tested

We found that as a class, the halogenated polymers all performed well with the highest EAB and strength at break with the exception of the PTFE samples. Interestingly, the polyethylene samples had similar EAB (5.8% for HDPE and 5.53% for UHMWPE), while the strength at break was significantly different (18.6 ksi for HDPE and 23.9 ksi for UHMWPE). Another unexpected result was the extremely low EAB of the PTFE samples. These samples had an average cryogenic EAB of 2.6% while reported literature values at room temperature are approximately 330% higher. This was the largest reduction in EAB among the test specimens. Finally, the injection molded PVDF samples proved to be a greater challenge to test than any of the other candidate materials. Every tested sample broke in the grips and, in one case, in three separate locations simultaneously during the testing process as seen in Figure 3.65.

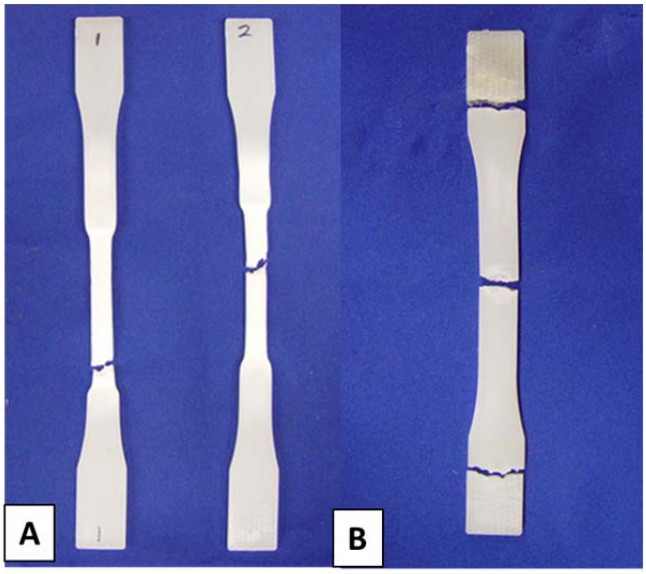

Figure 3.65. Tensile Tested PVDF Samples: (A) Ambient Tested and (B) Cryogenically Tested

3.6.1.2 Dynamic Mechanical Analysis of Polymers

Dynamic mechanical analysis is a powerful tool commonly used for thermal-mechanical evaluation of polymeric materials. Small oscillatory deformations at frequencies and amplitudes within the linear viscoelastic region can yield remarkable insight into the molecular interactions of polymer chains (Newhouse 2010). Commonly, this method is used to measure the glass transition temperature (T_g) of polymers but other properties of interest such as the storage modulus (E'), a measurement of the elastic characteristics (solid nature), can be used to provide relative comparisons of the stiffness and dampening of a polymer at multiple temperatures in a single experiment. The shape of this curve can be used to determine not only the glass transition temperature but also the onset of the glassy region indicating significant reduction or elimination of the viscoelastic properties. Figure 3.66 shows representative viscoelastic response of polymers through the glassy/rubbery regions as measured by the storage modulus curve in a DMA experiment.

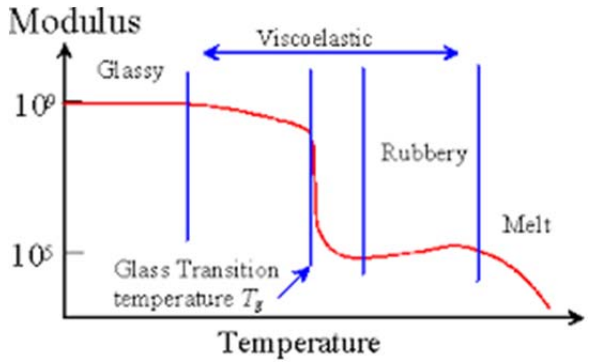

Figure 3.66. Representative Viscoelastic Response of Polymers through the Glassy/Rubbery Regions as Measured by the Storage Modulus Curve in a DMA Experiment

Approach

To complement the cryogenic tensile testing, a series of DMA experiments were performed on the candidate thermoplastic materials. Rectangular bars approximately ⅛ inch thick by ¼ inch wide by 1¼ inches long were machined from as-received sheets and finished with 600 grit polishing. Samples were tested on a TA Instruments Q800 DMA using a standard dual-cantilever clamp. A multi-strain temperature ramp from -145 to 30°C and a heating rate of 2°C/min were used to measure the storage and loss modulus, E' and E", respectively. An oscillation frequency of 1 Hz with 15 µm amplitude was used for these tests. These parameters were determined by performing ambient strain sweeps to determine the linear viscoelastic region.

Results and Discussion

The two grades evaluated were from the same product line but with different melt viscosities. A second variation of the low melt viscosity resin using two different injection shot speeds also was evaluated for differences in processing. In addition to these PVDF variations, the HDPE and ETFE materials also were evaluated. Similar to the previous tensile test, the ETFE and HDPE had similar trends in overall change of storage modulus between cryogenic and ambient temperatures, indicating the potential for significant challenges when using these materials between ambient and cryogenic conditions. Surprisingly, the three variations in the PVDF samples showed minimal differences in the storage modulus values.

This is relevant when considering the material requirements of a potential cryogenic pressure vessel liner as polymers in the glassy region become brittle and are more likely to fail from stress cracking/crazing. An ideal material would exhibit small differences between cryogenic and ambient temperatures indicating that the material does not undergo a significant stiffening of the modulus resulting in less elastic behavior at cryogenic operating temperatures. If a material has a high ΔE' this can be detrimental if the material is flash cooled from ambient to below its T_g minimizing its elongation which can cause premature failure due to stress cracking or separation from the fiber reinforced polymer wall. Another common signal used in DMA is the loss modulus (E''). This signal represents the energy dissipated as heat (viscous nature) and is historically used to determine the glass transition as indicated by a sharp peak commonly located within range of the slope transition in the storage modulus signal.

Based on the previous tensile results, temperature scans of the halogenated polymer class were giving initial priority. Many of the materials exhibited stark differences between cryogenic storage modulus values and ambient. Figure 3.67 and Table 3.21 shows the DMA dual-cantilever results of selected candidate polymers. Storage moduli are shown in solid curves, and loss moduli are shown in dashed curves.

The greatest difference was in the PTFE samples. This material had the highest cryogenic storage modulus indicating the material was extremely stiff and most likely extremely brittle. The PI material on the other hand, showed very little change in storage modulus between cryogenic and ambient. In addition, the measured glass transitions were near reported embrittlement temperatures indicating potential limitations of these materials at cryogenic temperatures. Operational temperatures below the glass transition have the potential to be problematic as the polymers become extremely glassy and more prone to potential failure caused by the rapid expansion of the pressurized gas during pressure vessel filling.

Once the prioritized samples were characterized, several variations of the injection modeled PVDF material were evaluated using DMA. Figure 3.68 and Table 3.22 show DMA dual-cantilever results of select candidate polymers.

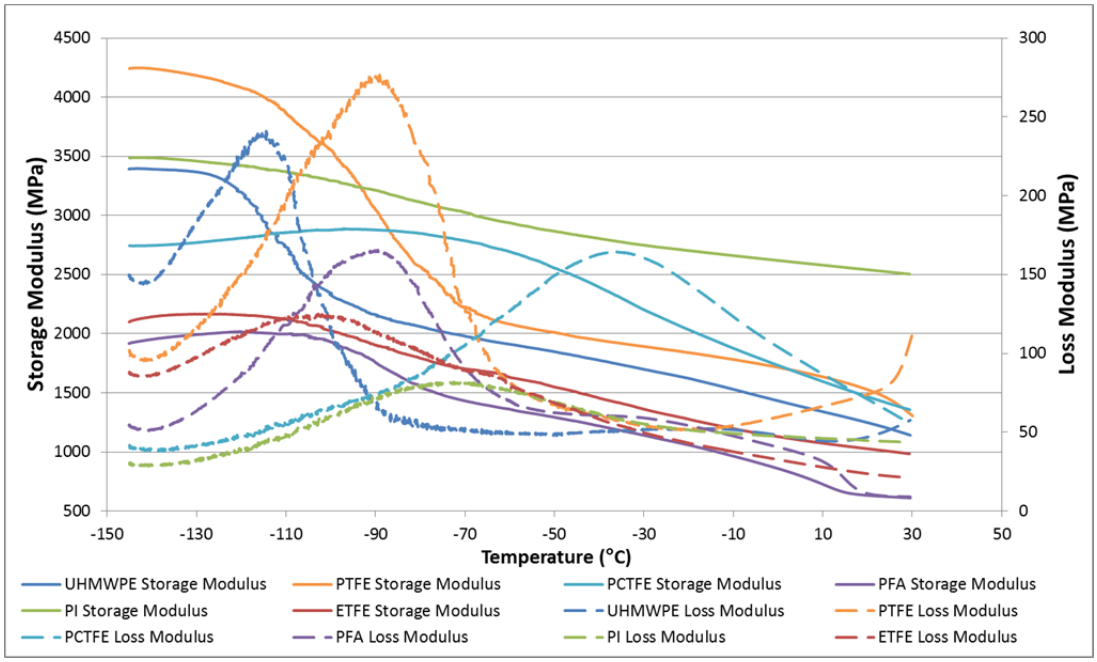

Figure 3.67. DMA Dual-Cantilever Results of Selected Candidate Polymers. Storage moduli show in solid curves and loss moduli shown in dashed curves.

Table 3.21. DMA Dual-Cantilever Results of Select Candidate Polymers. Glass transition recorded at loss modulus (E'') peak.

Sample	Storage Modulus -145°C (GPa)	Storage Modulus 25°C (GPa)	Glass Transition Tg (°C)
PTFE	4.24	1.48	-89.05
PCTFE	2.74	1.43	-36.00
PFA	1.92	0.62	-89.49
PI	3.49	2.53	-72.47
ETFE	2.10	1.01	-100.72
UHMWPE	3.39	1.22	-114.44

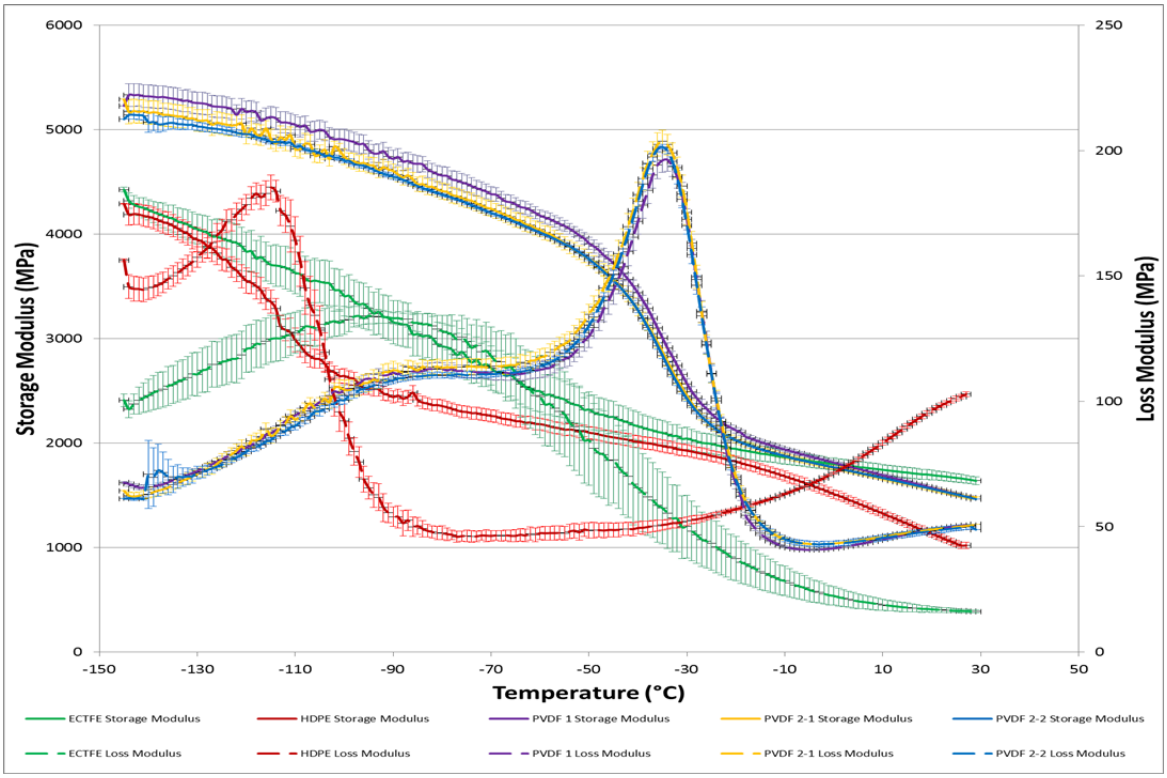

Figure 3.68. DMA Dual-Cantilever Results of Select Candidate Polymers. (Green) ECTFE sheet stock, (Red) HDPE sheet stock, (Purple) injection molded PVDF standard grade, (Yellow) injection molded PVDF low melt viscosity grade slow shot, (Blue) PVDF low melt viscosity grade fast shot.

Table 3.22. DMA Dual-Cantilever Results of Select Candidate Polymers. Glass transition recorded at loss modulus (E'') peak.

Sample	Storage Modulus - 145°C (GPa)	Standard Deviation	Storage Modulus 23°C (GPa)	Standard Deviation	Glass Transition T_g (°C)
ECTFE	4.43	0.021	1.68	0.044	-77.30
HDPE	4.29	0.001	1.07	0.029	-112.50
PVDF 1	5.23	0.000	1.54	0.015	-33.63
PVDF 2-1	5.29	0.000	1.53	0.016	-35.28
PVDF 2-2	5.10	0.000	1.53	1.010	-34.93

3.6.2 Impact of Hydrogen and Cryogenic Temperatures on Polymer Properties

Hydrogen-induced materials property degradation is of serious concern for hydrogen storage and delivery environments, especially for components exposed for long periods to high-pressure or cyclic hydrogen pressure loadings. In fact, it is well known that many metals exposed to hydrogen degrade by forming hydrides, surface blistering, or strength embrittlement (Fukai 2005, Jones and Thomas 2008, Lu and Kaxiras 2005, Lee 1976, Zhao and Carpenter 2005). Some ceramic materials also undergo degradation. For example, PZT, used in high-pressure hydrogen actuators undergoes degradation under high-pressure hydrogen in the form of blistering and lead migration (Alvine et al. 2010, 2012; Aggarwal et al. 1998; Ikarashi 1998). Polymeric components are of concern also. Materials that could degrade in the presence of hydrogen include structural polymers, such as HDPE, and elastomers, such as polyisoprene, for uses in

hydrogen storage and delivery, where pressures can reach between 35 and 70 MPa (5000 and 10,000 psi) (Mori and Hirose 2009, Ahluwalia et al. 2012, Zheng et al. 2012). Polymers are used extensively in hydrogen applications. For example, structural polymers such as HDPE are used as liners in high-pressure

Type-IV hydrogen tanks (Mori and Hirose 2009, Ahluwalia et al. 2012, Zheng et al. 2012) and in pipelines (Kane 2008), while elastomers are used in valves, sliding seals and other components for high-pressure hydrogen (Yamabe et al. 2011, Yamabe and Nishimura 2009).

While there is an abundance of information on the hydrogen degradation mechanisms in metals and some ceramics, there is still little information in the literature about the detrimental effects of hydrogen on polymers (Castagnet et al. 2010, Jaravel et al. 2011, Boyer et al. 2014, Alvine et al. 2014). Absorption in polymers differs from that of absorption in metals (Fukai 2005) in that disassociation of the hydrogen is not expected to occur within the material. This means that the primary damage mechanisms in polymers are expected to be mechanical in origin rather than chemical (Kane 2008). Our previous observations and those of other groups indicate that damage effects can include bubble or void formation, surface blistering, dilation, and changes in modulus and strength (Alvine et al. 2014). The saturated concentration in the polymer is proportional to the exterior applied pressure (Yamabe and Nishimura 2009), and it is thus expected that any detrimental effects are more serious at higher pressures.

3.6.2.1 Approach

To evaluate the effects of high-pressure hydrogen saturation on the polymeric materials at cryogenic temperatures, an identical set of polymeric samples (five samples each plus five backups) were exposed to hydrogen pressurized to 5000 psi for a period of approximately 60 hours at room temperature. The samples were loaded into a high-pressure hydrogen autoclave and flushed five times with ambient-pressure argon to remove residual oxygen. The autoclave was then flushed with low-pressure 99% hydrogen gas to remove the argon and pressurized to 5000 psi at 99.99% hydrogen at room temperature. During the course of the soak, the pressure dropped slightly to 4700 psi at approximately 40 hours and was re-pressurized to 5000 psi for the remainder of the test.

After soaking, the hydrogen pressure was vented quasi-rapidly for approximately 1 minute to ambient pressures. The autoclave was opened over the course of 5 minutes, and the samples were immediately placed in LN2 to cool. It is expected that the bulk of the cooling to LN2 temperatures took 10 minutes based on a visual inspection of the boil-off rate. After the samples had reached LN2 temperatures and immediately prior to testing, the length and diameter were measured and input into the Bluehill data collection system for running the compression tests. Prior to each test, the load was balanced and the sample brought into contact with the top platen to start the test**.** Samples were run according to ASTM D695 for rigid plastics as shown in Figure 3.69**.** To ensure that time dependent effects were measured, the order of the samples was cycled systematically**.** However, no significant time dependent effects were

observed in this series of tests**.** Additional tests were performed that will be referred to as "cryo-only." These tests were not exposed to hydrogen but were exposed to the liquid nitrogen bath and served as a baseline set of tests to evaluate the effect of high-pressure hydrogen saturation.

We chose an initial set of five polymers—HDPE, PTFE, PCTFE, ECTFE, and polyaryletheretherketone (PEEK)—that are under consideration for use in cryo-adsorbent hydrogen systems in a range of applications as shown in Table 3.23. These materials are all known to be serviceable at cryogenic temperatures and were expected to perform reasonably well at LN2 temperatures for seals, seats, pistons, and containment. Because the applications in question primarily involve using the material in compression geometries (e.g., seals), a compression style test of the mechanical properties was carried out for each material.

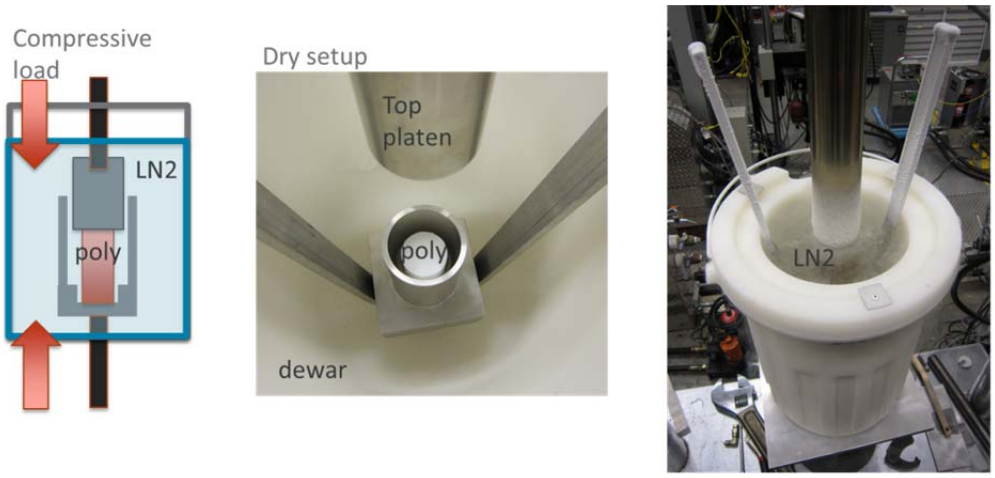

Figure 3.69. Cryo-Compression Test Fixture. (Left) Schematic of the test fixture. (Middle) Photograph of the lower platen in the dewar with a loaded polymer sample. (Right) Photograph of testing under LN2.

Table 3.23. Polymer Selection and Cryo-Adsorbent Application

Use	Material	Check valves	Control valves	Tanks and Pipes
Seals	PTFE	x	x	
	PEEK	x		
Pistons	PEEK	x	x	
Seats	PCTFE		x	
	ECTFE		x	
Containment/pipes	HDPE			x

Samples were cut from extruded rod stock to 2 inches in length by 1 inch in diameter. With the exception of the ECTFE, the rod stock was purchased with a 1-inch diameter. The ECTFE was received at 1.3 inch diameter and had to be turned down on a lathe. Ends were carefully cut at 90° angles and given a rough polish with 400 grit sandpaper to ensure uniform loading. A specially designed set of platens were machined for this purpose to ensure rapid self-centering of the samples within the plates and included a protective shield. The shield prevented shards from the failed samples from falling into the liquid nitrogen bath to a high degree. In addition, the shield was designed to protect the HDPE thermos that contained the

LN2 bath around the sample. For each test, the dewar bath was topped off to ensure the steel fixtures reached LN2 temperatures. During all tests, proper personnel protective equipment, including face shields and cryogenic gloves, were used to ensure safe handling of the LN2. Airflow had been previously measured to ensure adequate ventilation during testing.

3.6.2.2 Results and Discussion

Stress-strain curves of the different plastics under compression are shown in Figure 3.70. Both the hydrogen-saturated and baseline tests showed the same qualitative behavior in the stress-strain curves and the failure mechanisms. The HDPE and PTFE failed by barreling and shear mechanisms. The ECTFE showed barreling and some cohesive delamination upon failure. The PEEK and PCTFE had brittle fracture failure modes. Interestingly, the PCTFE only exhibited elastic failure prior to rupture. The PTFE showed significant compression and did not strictly follow the rigid plastic behavior. This is not completely unexpected for a cryogenic seal material however. Three material properties were extracted from the stress-strain curves for analysis and comparison between hydrogen-saturated and baseline: modulus, yield stress (or peak stress for PCTFE), and total elastic strain. Yield stress was calculated at a 0.5% offset from the elastic region, and the total elastic strain was calculated from the modulus and yield stress. Because PCTFE only behaved elastically, peak stress at failure was used instead of yield stress. The results are shown in Table 3.24 for both sets of samples.

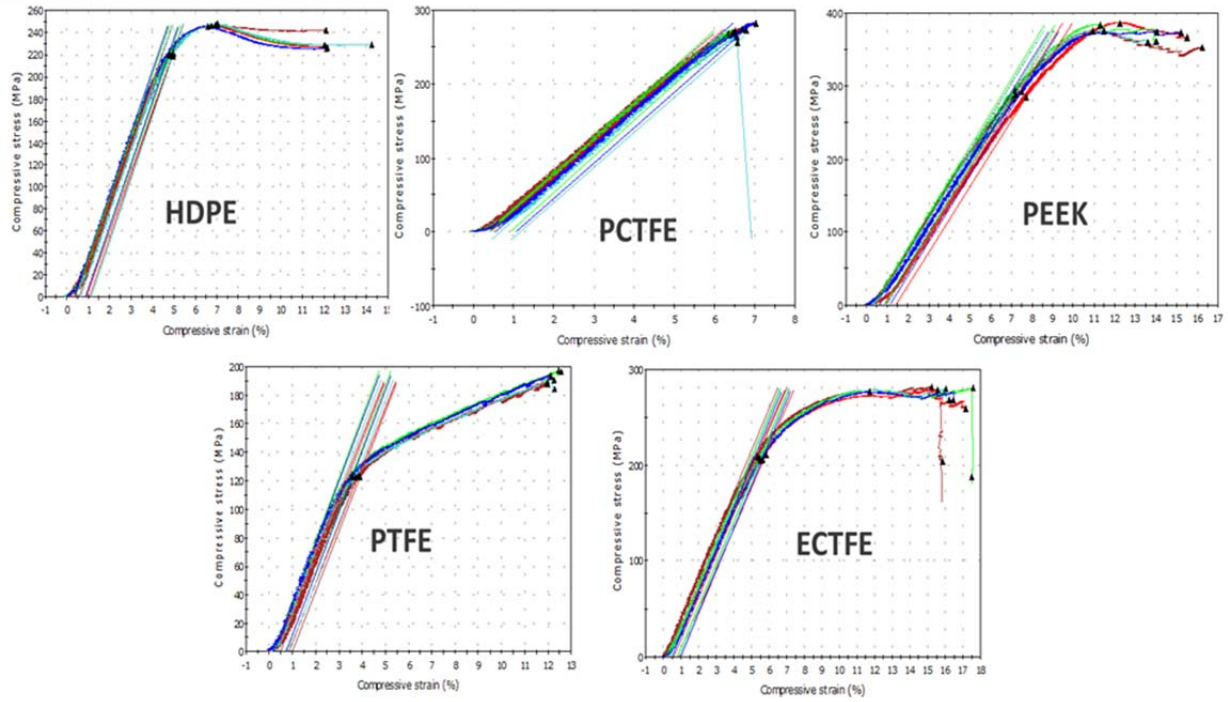

Figure 3.70. Stress-Strain Curves for the Different Plastics under Cryogenic Compression Testing. These data are for the hydrogen-saturated tests, but are qualitatively identical for the baseline cryogenic tests. The lines are linear fits to the elastic regions of the data.

From the data, it can be seen that the statistical sampling is quite good, with the possible exception of the PCTFE peak stress (likely due to the elastic failure mode). In addition, an increase in the elastic modulus is observed for the hydrogen-loaded samples for all materials by a statistically meaningful amount. Conversely, three of the materials—HDPE, PTFE, and ECTFE—show a decrease in the yield stress with

hydrogen loading compared to the baseline. Interestingly, there is no statistically significant change for PCTFE or PEEK.

To more easily compare the hydrogen data to the baseline, we plotted the yield stress and modulus for the various materials (Figure 3.71).

Table 3.24. Materials Property Comparison

Material	Hydrogen Soak	Modulus (MPa)	Standard Deviation (MPa)	Yield Stress (MPa)	Standard Deviation (MPa)	Peak Stress (MPa)	Standard Deviation (MPa)	Total Elastic Strain	Standard Deviation
HDPE	None	5069.9	198.4	224.8	1.5			0.044	0.002
	60 hours,	5615.9	110.2	220.9	1.2				
	5000 psi							0.039	0.001
PTFE	None	4131.6	83.8	134.5	0.1			0.033	0.001
	60 hours,	4247.6	93.6	123.4	0.9				
	5000 psi							0.029	0.001
ECTFE	None	4179.4	120.1	218.7	8.2			0.052	0.002
	60 hours,	4396.7	69.7	207.9	2.5				
	5000 psi							0.047	0.001
PCTFE	No	4541.7	49.1			259.1	14.9	0.057	0.003
	60 hours,	4756.9	69.5			271.9	6.6		
	5000 psi							0.057	0.002
PEEK	None	4474.1	73.3	287.6	9.2			0.064	0.002
	60 hours,	4589.9	39.1	288.3	4.5				
	5000 psi							0.063	0.001

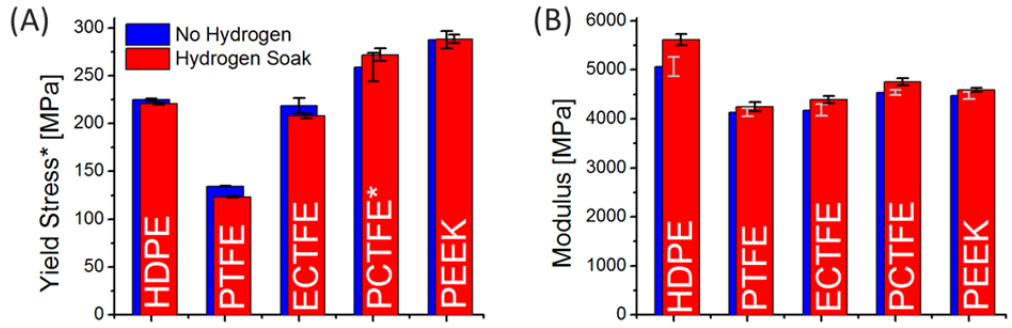

Figure 3.71. (A) Yield Stress (or peak stress for PCTFE) and (B) Modulus Data are Shown for the Five Sets of Materials as a Comparison between Hydrogen-Loaded and Baseline Cryogenic Testing

To explain the increase in compression modulus for the hydrogen-loaded polymers, we suggest the following possible explanation shown schematically in Figure 3.72. Upon saturation of the polymer with pressurized hydrogen, any voids in the polymer will fill with high-pressure hydrogen. While this hydrogen will begin to diffuse from the sample upon depressurization, it takes at least 1 hour for samples of this size to make an appreciable difference. In addition, the drop in temperature due to the LN2 will drop the modulus significantly. Pressurization of the voids in the material will add an additional spring constant and increase the modulus of the material in compression.

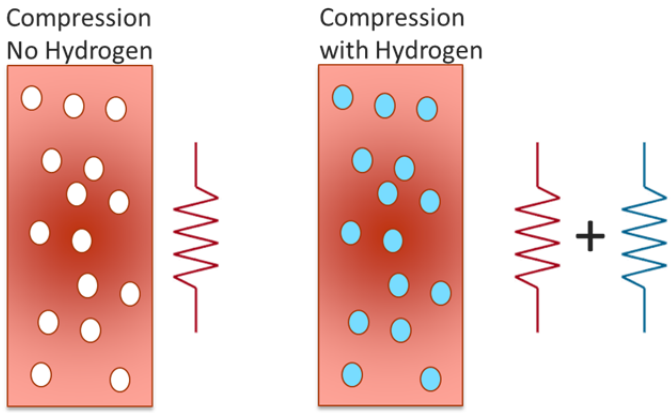

Figure 3.72. Schematic of Possible Explanation for an Increase in Compressive Modulus in Hydrogen-Saturated Polymer Samples. Upon saturation, pressurized hydrogen will fill all voids in the polymer. This will add an increased spring modulus to the system in compression.

In addition, the local pressurization of the polymer by the hydrogen adds local loading to the polymer and causes premature yield of the material. Given the ideal gas law, 5000 psi hydrogen at room temperature equates to approximately 10 MPa at LN2 temperature. Thus, we should expect the yield stress to drop by this level. Indeed, the drop for HDPE, PTFE, and ECTFE is between 4 and 11 MPa as expected from this argument.

Interestingly, the PCTFE and PEEK materials, which undergo brittle failure, do not show a decrease in yield strength, while they do still show the increase in modulus. It is possible that, given the failure mechanism, these materials form a crack network during compression that leads to the rapid degassing of the hydrogen. Such a crack network may explain why a similar decrease in yield strength is not observed. Further study is warranted to understand this better.

3.7 Conclusions and Recommendations for Cryo-Adsorbents

3.7.1 Pressure Vessel Development

The *Tankinator* code was developed to provide quick estimates of tank characteristics, specifically pressure tank mass, material cost, and basic dimensions for Type-I, Type- III, and Type-IV tanks. The examples provided here show a prediction accuracy of approximately ±10% against commercially available tanks for all types. This level of accuracy is sufficient for conceptual design evaluation, but physical prototype design is a step beyond the intended capabilities of the *Tankinator* code.

Type-I pressure vessels are the only practical tanks that can meet the needs of the cryo-adsorption system. Type-III tanks were considered, but the specific thermal and mechanical loading cycle makes it impossible to share the load between the liner and the carbon fiber shell effectively. Type-IV tanks were considered, but the separation of the liner at cryogenic temperatures in the absence of 35 bar pressure is not acceptable. This leaves the Type-I pressure vessel as the only practical tank solution. The *Tankinator* code has been made available to the public.

Two modifications to the code are recommended: 1) modifying the treatment of translation efficiency and 2) adding a netting analysis worksheet for Type-IV tanks. Justification for these two modifications follows.

The treatment of translation efficiency is not precisely explained in the current version of *Tankinator* (Rev 3). The fact that the design strength has a 90% translation efficiency already built into the composite material strength is not stated. Enough information is provided that a user can back out the composite strength and compare it to unidirectional lamina strength data, but this would not be clear to a casual user.

A netting analysis spreadsheet tool has already been developed by staff at PNNL. It would be straightforward to include the tool in the *Tankinator* code as another estimate of Type-IV tank mass. This is a valuable tool that would increase the utility *Tankinator* code and may provide predictions closer to realistic tank characteristics.

3.7.2 LN2 Cooled-Wall Tank Concept

The LN2 cooled-wall concept was designed to address a technical problem associated with the cryo-adsorbent tank syste—cooling the large thermal mass of a pressure vessel wall.

Prototype testing has demonstrated that the concept will meet the DOE refueling target goals by scaling up the average surface heat flux determined through testing. Beyond the projection of scale model results to full scale, the cooling performance also was considered from an LN2 mass flow rate perspective. The mass flow rate is critical to system function, as system performance is dependent on the energy of boiling that is available as well as the surface coverage. For maximized cooling rates, excess LN2 is needed beyond the amount predicted by a strict energy balance to ensure sufficient surface coverage. The delivery of LN2 to meet DOE target goals while minimizing LN2 consumption is its own design problem.

The LN2 temperature-dependent heat-transfer rates implemented in the thermal study were then applied to a model of the 200-L full-scale hydrogen pressure vessel. Two bounding thermal cases where evaluated that gave a maximum cyclic stress intensity of only 16 MPa compared to the 102 MPa stress intensity corresponding to the 10 MPa operating pressure. For the assumed Al-6061-T6 tank material, the total stress intensity of 118 MPa (17.2 ksi) corresponds to over 1,000,000 fully reversing stress cycles to initiate a fatigue crack. Therefore, a full-scale aluminum pressure vessel can be designed to easily withstand the 1500 cooling and pressure cycles required by the project milestone.

Test data demonstrate that the LN2 wall-cooled tank concept can feasibly cool the tank wall from 160 K (or higher) down to 90 K rapidly enough to meet DOE target goals, but cooling to temperatures below 90 K is physically challenging because of the surface heat-transfer physics. Cryo-adsorbent systems should be designed with this physical limitation in mind. Flow-through cooling has to account for cooling in the 90 K to 80 K range.

LN2 delivery lines at the filling station need to be pre-cooled. The prototype testing used insulated LN2 lines, but the energy losses associated with those lines was significant over the time period of interest and led to unacceptable cooling times. Delivering LN2 efficiently remains a technical challenge of this design concept.

At this intermediate stage of system development, the current analysis has not evaluated the foreseeable list of the balance of tank components that may also be subjected to thermal cycling. Therefore, throughout the design and development phase, it will be important to consider the effects of differential thermal contraction of different materials in contact. It is recommended that materials with similar coefficients of thermal expansion be used when possible to minimize differential thermal effects.

3.7.3 Balance of Plant

The BOP for the cryo-adsorbent hydrogen storage system includes all the components of the storage system with the exception of the adsorbent material itself and the storage vessel in which it is housed. A BOP component library was developed, and during Phase II, two separate designs were initiated—MATI and Hexcell. Work was done to minimize the BOP components and reduce the mass volume and cost for each of these systems. The mass and volume was first reduced by decreasing the system operating pressure from 200 to 100 bar. This reduction in in operating pressure resulted in reduced mass and volume of the valves and heat exchanger. The cryo-adsorbent BOP mass and volume were reduced by 46% and 57%, respectively

Maintenance may be a concern for the consolidated BOP component. It has the advantage of being a single device, but a failure of any one component in the block may require replacement of the entire block. OEMs will have to determine tradeoffs relative to this concern.

Thermal mismatch evaluation of dissimilar materials continues to be a concern for the design that connects the consolidated valve block directly to the tank. For an aluminum valve body connecting to the aluminum tank boss with a stainless-steel bolt, for example, cooling the assembly from room temperature to 80 K will cause differential contraction between the aluminum and the stainless-steel. Initial pre-stress would have to be at least 14,500 psi to just account for differential strain of the bolt compared to the valve body. As a result, similar metals may be required between these three components.

3.7.4 System Cost Modeling

Estimated costs for the two adsorbent systems are provided in Table 3.25. The Hexcell system, a system with a honeycomb aluminum heat exchanger inside the pressure vessel, costs $2,998/system ($16.08/kWh). With only a few differences, the MATI system weighed less but cost more than the Hexcell system at $3,275/system ($17.56/kWh). The MATI heat exchanger allowed for more MOF-5 to be inserted into the pressure vessel while reducing its overall mass size by 19 kg. However, the added cost of MATI and the costs of the additional valves and fittings required to complete the system offset the reduced size.

Table 3.25. Summary of Adsorbent System Costs

	Hexcell	MATI	MATI – Hexcell	2020 Target	Ultimate Target
Total System Costs (2007$)	2,998	3,275	276	1,865	1,492
Costs per KWh ($/KWh)	16.08	17.56	1.48	10.00	8.00

Neither system achieved the 2020 cost target of $10/kWh although further comparisons could be conducted with a compressed hydrogen system. These adsorbent systems at only 100 bar have the potential to be competitive with compressed hydrogen systems at 700 bar in cost and performance while also facilitating lower infrastructure costs with the lower operating pressures**.**

Assembly costs are the least well known within the cost estimate. More effort could be placed on understanding the processes associated with assembly. No complete assembly of either system was attempted. Experiments only studied portions of the assembly, and a full-scale prototype was not built. Without development of the representative prototype, a full understanding of the manufacturing and assembly requirements for the onboard storage system is incomplete.

The cryogenic valves at 31% of costs could be studied in depth to reduce the system costs However, when we were undertaking the costing of the "elevated design," we started to estimate the costs of the valves in the block and were quickly deterred by an individual in the industry who believed that there is considerably more involved in the construction of the valve than would be shown in our cost model.

Prices of some of the valves, for which we obtained quotes, were substantially higher than the values estimated at 500,000 units. Thus, even though valves account for a significant portion of the system cost, the risk is high that the valves could be more expensive than estimated.

An additional recommendation would be to pursue a new adsorbent medium, one with a higher adsorbent capacity and a lower cost per kilogram. Currently the MOF-5 media comprises 11% to 15% of the cost of the two systems. Thus, there is considerable room for savings with more research.

3.7.5 Materials Compatibility

Expanding the knowledge of the performance of polymers under cryogenic and pressurized hydrogen conditions is an essential step in developing next-generation high capacity hydrogen storage systems. While many challenges still exist in developing acceptable and reliable test methods, this work has begun to develop the initial building blocks that will be needed in future work. It is hard to draw finite conclusions about the performance of these materials at this time, but it is clear that current knowledge available is poor and substantial testing will be required to bring this concept to the forefront of hydrogen storage technology.

One objective of this task was to begin to develop an understanding of the thermal-mechanical properties of potential pressure vessel liner materials. Additional research into the effects of cyclic fatigue, creep, and stress relaxation are essential. It is also of interest to measure the cryogenic to ambient coefficient of thermal expansion measurements as those values are rarely reported in the literature and could pose significant issues if the liner shrinks at a rapid rate creating significant separation between itself and the fiber reinforced polymer.

A second objective of this task was to begin to understand the impact of high-pressure hydrogen on polymer mechanical properties at cryogenic temperatures. Additional testing is required with hydrogen-saturated samples at ambient temperature to separate the impact of cryogenic temperatures and the hydrogen-saturation effect. While compressive testing provides an understanding of one mechanical property, further testing is required to analyze such things as tensile strength and tribological effects under similar conditions.

4.0 Metal Hydride Balance of Plant and Cost Estimate

Metal hydride storage materials undergo chemical reaction during the charging and discharging process similar to chemical hydrogen storage materials, however, the reactions are reversible and they can be refueled onboard the vehicle with the only the addition of high pressure hydrogen. Metal hydrides that have been evaluated for hydrogen storage include elemental metallic hydrides (e.g. palladium and titanium hydrides), intermetallic hydrides (e.g. mixtures of Ti, Cr, Fe, etc.), and ionic hydrides (e.g. Ca, Na) (Hirscher 2010). One class of ionic hydrides, the "complex hydrides" were selected for as the basis for study in the HSECoE. For these materials, hydrogen is covalently bonded to another element form a "complex" anion (e.g. $LiAlH_4$, $NaBH_4$). $NaAlH_4$ (sodium alanate) was selected as the surrogate material for future studies and material comparisons for the HSECoE because 4 wt% capacity and it hydrogenation and rehydrogenation at moderate conditions and rates (Bogdanovic et. al. 1997).

During Phase I, PNNL led the BOP and Cost Estimation tasks for the sodium alanate onboard hydrogen storage system. The tasks provided the system components and BOP that were used to estimate system costs. No work was performed on metal hydride materials during Phase II and III. A DOE decision was made at the end of Phase I that metal hydrides could not meet the DOE performance targets and work in that area was recommended not to continue.

4.1 Balance of Plant, Tanks, and Components

PNNL, working with other HSECoE partners, developed a baseline mass, volume, and system cost based on a metal hydride system with requirements to store 5.6 kg of usable hydrogen using sodium alanate. The system architect and other team members provided information on predicted pressures, temperatures, and flow rates. Using that information PNNL selected components that met those requirements and sized them appropriately. The system for which costs were estimated is shown in Figure 4.1. The primary components of the system included two tanks filled with sodium alanate, titanium(III) chloride and enhanced natural graphite (ENG). Sodium alanate was the medium used to provide hydrogen, and ENG and titanium(III) chloride were added to provide better thermal conductivity for rapid release and capture of the hydrogen.

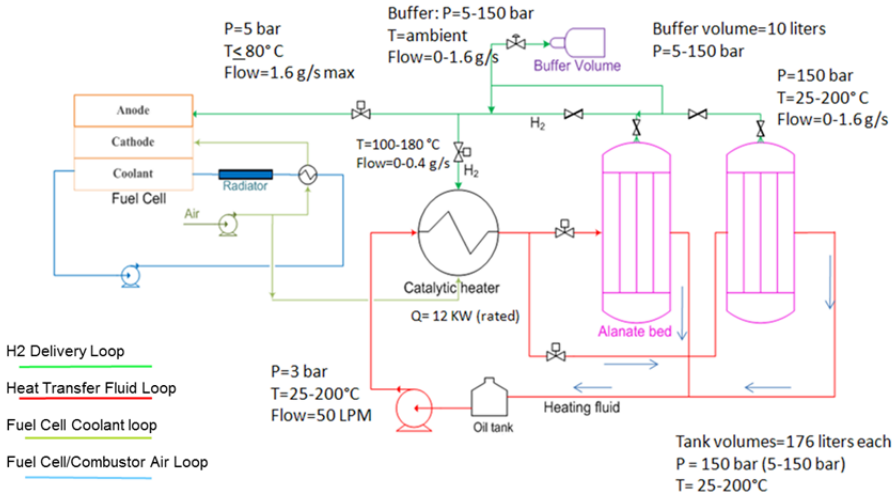

Figure 4.1. Schematic of Sodium Alanate Onboard Storage System

Table 4.1. Bill of Materials for Two-Tank Sodium Alanate System

Item	Description	Number	Mass (kg)	Proposed Item
System Components				
Storage Vessel 1	One of two metal-hydride storage vessels	1	61.00	Dynatek V174
Storage Vessel 1	One of two metal-hydride storage vessels	1	61.00	Dynatek V174
H_2 Valve 1	Pressure regulator	2	1.09	20=1234-2911/Tescon Industrial Controls
H_2 Valve 2	Check valve	2	0.15	K220T1-3PP-1450/Circor Seal
H_2 Valve 3	Pressure relief valve	3	0.29	8100-55T1T1/Circor Seal
H_2 Valve 4	Manual valve	4	0.60	MV-60-T1-04/ Circor Seal
Coolant Valve 1	Isolation valve for oil circulation	2	3.50	Assured Automation C26N 1, Actuator EV1S1V1RXV4
Coolant Fluid	Coolant system fluid volume	14 L	11.23	Paratherm MR
Coolant Pump	Oil recirculating pump	1	26.30	Dankoff Solar Suncentric Model 7443, 48 V
Coolant Lines	All coolant wetted lines	5 m	6.00	Swagelok SS-T16-S-083-6ME
Pressure Gauge	Pressure gauge for fuel cell inlet	1		Tescom Pressure Gauge 62837-10000N25
Flow Controller 2	Control valve for catalytic converter	1		South Bend Controls PSV 400 Series, Part No. 400112400
Radiator HX 1	Heat or cool fuel cell	1		
H_2 Lines	All H_2 wetted lines	12 m	1.44	Swagelok SS-T4-S-035-6ME
System Insulation	Insulation for all system lines			
Pressure Relief Valve	Pressure relief for metal-hydride tanks	2		Circor Seal Model 8100-55T1T1
Pressure Transducer	Measures pressure	1		AST2000M-00448-B1-F1-417 American Sensors Technology
Catalytic Heater		1	0.95	OSU design and cost
Buffer Tank	Provides H_2 for startup and transient operations	1		
Oil Tank	Vented, non-vented expansion requirements	1		
Storage Vessel				
Sodium Alanate	With x mole% titanium(III) chloride dopant and 5 to 10% wt% ENG to enhance thermal conductivity	94.0 kg/tank		
Titanium Chloride	Titanium(III) chloride	10.1 kg/tank		
ENG		11.5 kg/tank		
Internal Heat Exchanger 1		1	12.00	Tube and fin
Internal Heat Exchanger 2		1	12.00	Tube and fin

The onboard storage system was designed no to use any fuel cell components based on guidance from the U.S. DRIVE Hydrogen Storage Tech Team. For example, the heat exchanger used to warm the heating fluid used only waste heat from the fuel cell but did not use the fuel cell radiator. This limitation made the mass and volume projections larger than if the fuel cell, storage systems, HVAC, etc., were integrated.

Table 4.1 provides the bill of materials for the sodium alanate onboard hydrogen storage system. The bill of materials is divided into two sections: the system components and the storage vessel components. The onboard storage system required two storage vessels instead of one to contain all of the sodium alanate required to provide 5.6 kg of usable hydrogen. The two tanks were required because of size limitations for

the individual tank (based on OEM feedback). The vessel components section indicates that 94 kg of sodium alanate was required per tank. In addition, 10.1 kg of titanium(III) chloride dopant and 11.5 kg of ENG were required per tank for enhanced thermal conductivity. In addition, each tank contained an internal fin and tube heat exchanger to further enhance thermal conductivity.

The bill of materials also indicates some of the masses associated with each of the components. For those components for which masses were not calculated, estimates were later derived to calculate system masses and volumes. Figure 4.2 shows the mass and volume projections based on the bottoms-up approach along with the 2010 and 2015 targets for comparison. The mass of the system is dominated by the weight of the storage material, but the storage vessel containers, at 61 kg each, and internal heat exchangers, at 12 kg each, comprise 36% of the total. The oil pump and loop also represents 8% of the total system mass. For the volume projection, most of the volume (86%) is taken up by the storage vessels but other significant contributors include the oil pump/loop (5%) and the hydrogen buffer tank (3%).

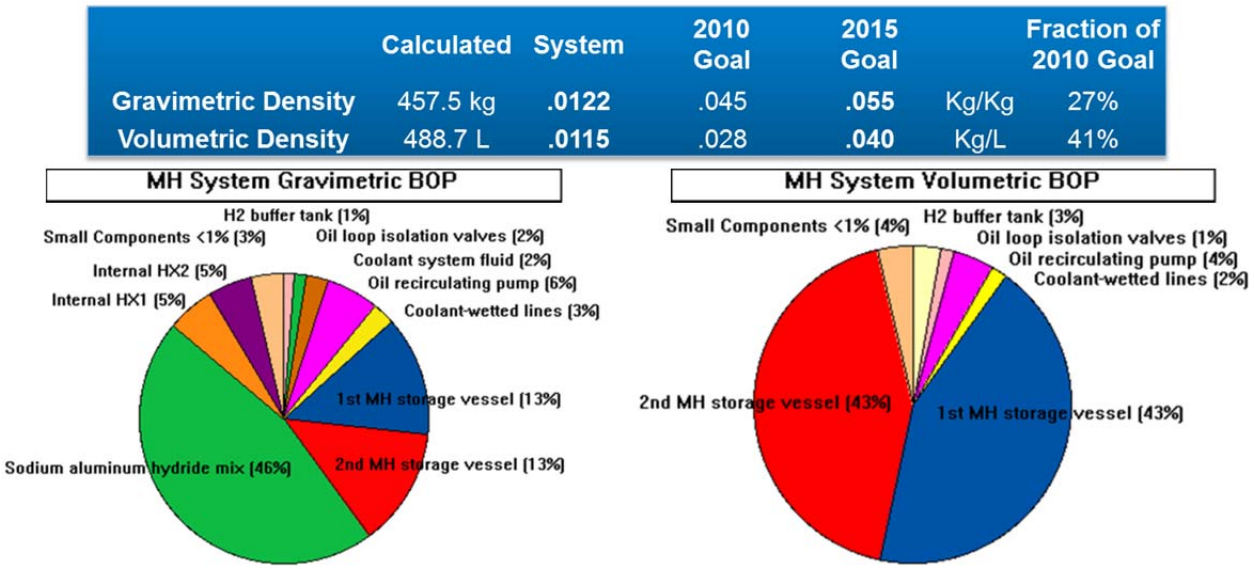

Figure 4.2. Baseline Metal-Hydride System and BOP Mass and Volume Projections

Some of the plans for Phase 2 were to improve on the mass and volume projections for future metal-hydride systems. For the system mass a combination of improved tanks, BOP, and heat exchanger designs were recommended. The baseline metal-hydride system employed two Type-III tanks, which included metallic liners. A combination of compacting the material to use a single tank, switching to a lighter weight, polymer lined, Type-IV tank and reducing major BOP components like the weight of the oil pump and internal heat exchanger was expected to lead to a 50% reduction in the tank and BOP weight. These changes would result in a 25% overall system gravimetric improvement and a 25% volumetric system improvement. Further system mass and volume improvement can be realized by using higher capacity hydrogen storage materials with lower heats of reactions. Figure 4.3 shows the results of a system scenario analysis, which doubled the materials gravimetric capacity, halved the material enthalpy, and reduced the system to a single lighter weight tank. The scenario resulted in a metal hydride with a 54% and 50% reduction in gravimetric and volumetric density, respectively.

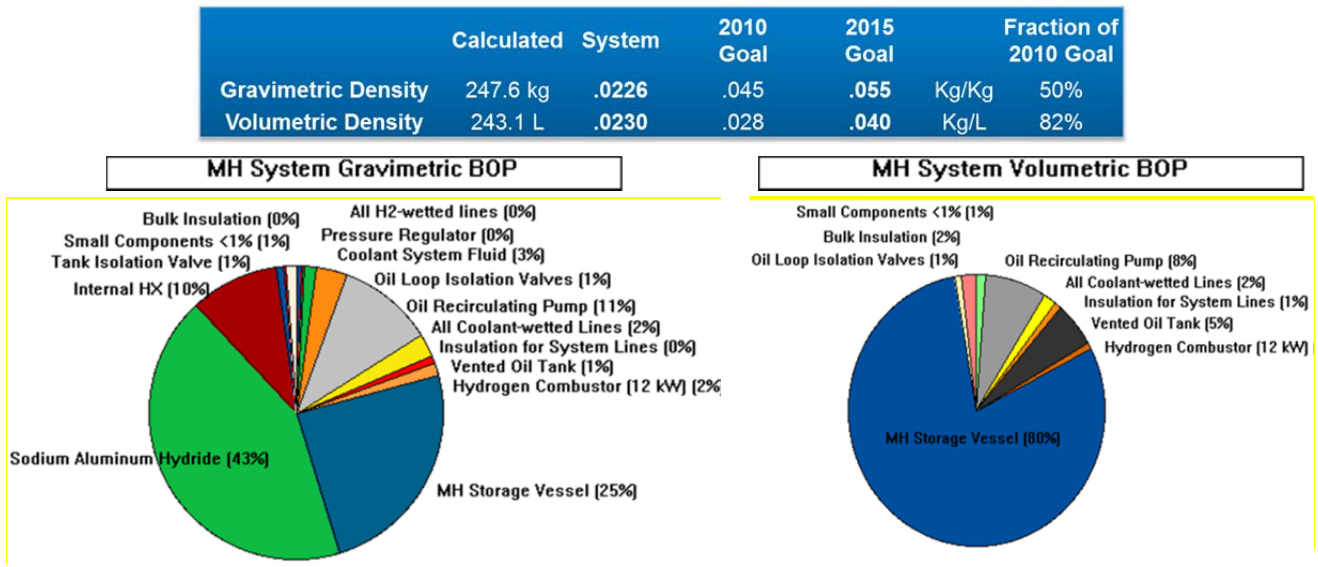

Figure 4.3. Reduced Mass and Volume Scenario Analysis for a Metal-Hydride System

The design of suitable and reliable lightweight containers for future hydrogen storage systems was identified as a key objective of the HSECoE. To support this activity, a series of carbon fiber and metal and polymer lined tank designs were analyzed using an ANSYS finite-element model. The HSECoE needed to determine a realistic range of weights and volumes for the tanks. The initial model was developed using tables comparing different liner materials and pressure combinations that would give the system architects an initial estimate of tank weight and volume. The model was later refined by working with HSECoE partner, Lincoln Composites (currently Hexagon Lincoln) to provide a more detailed analysis to minimize the tank weight and volume. A simple computational tool, *Tankinator* (developed by PNNL), for estimating the mass and material composition of cylindrical Type-I, Type-II, Type-III, and Type IV vehicular hydrogen storage tanks was developed and is available to the public on the HSECoE website (http://hsecoe.org/models.php). The tool is useful for cross-comparison of various pressure vessel types, to estimate gravimetric, volumetric, and cost performance of hypothetical tanks in the conceptual phases of design. The "Tankinator" tool provides an estimate of basic tank geometry and composition from a limited number of geometric and temperature inputs. This estimate covers the tank shell material only; all other component masses needed to be added to determine full system mass. The model uses finite element analysis to confirm that the wall thicknesses predicted by the estimation tool result in an acceptable stress state. More information on the "Tankinator" tool can be found in Section 3.2.

One of the BOP components evaluated during the Phase 1 activities for the HSECoE was the hydrogen combustor. An earlier study by TIAX (DOE 2013) on a sodium alanate system design estimated the hydrogen combustor at 9.3 L and 22.3 kg. Oregon State University, one of the HSECoE partners, was asked to determine if an alternative could be developed. Hydrogen storage involves coupled heat and mass-transfer processes that are significantly impacted by the size, weight, cost, and performance of system components. Micro-technology devices that contain channels of 10 to 500 microns in characteristic length offer substantial heat and mass-transfer enhancements by greatly increasing the surface-to-volume ratio and by reducing the distance that heat or molecules must traverse. These enhancements often result in a reduction in the size of energy and chemical systems by factors ranging from 5 to 10 over conventional designs, while attaining substantially higher heat and mass-transfer efficiencies (DOE 2011).

Combining the combustion and heat exchanger systems and the use of microchannels for enhanced heat and mass transfer was found to drastically reduce the size and weight required for this function, while simultaneously increasing efficiency. The OSU led team, using microchannel architecture, developed a test-cell microchannel combustor that had a projected system design of only 1 L and 3.8 kg for the 12 kW baseline metal-hydride storage system. This is a ninefold and sixfold improvements in volume and weight, respectively, over a conventional design (DOE 2013). A substantial reduction in the combustor cost is also expected. A substantial safety benefit of a microscale combustor is that flames cannot be sustained in the sub-millimeter microchannels. Figure 4.4a is a sketch of the integrated microchannel combustor/heat exchanger that would be used to safely and efficiently produce heated oil, which is used to discharge hydrogen from the storage bed. Figure 4.4b is a photograph of a unit cell used to experimentally validate the performance and size estimates of the integrated microchannel combustor. Testing of the single unit cell resulted in a measured efficiency of 92% (thermal energy transferred to the oil/chemical energy in the feed stream).

4.2 Material and System Cost Estimation

4.2.1 Introduction

Cost estimates for the sodium alanate system included estimating the costs of the media, tanks, valves, and other BOP equipment. The manufacturing and assembly costs were estimated using an analogy approach as the actual steps associated with manufacturing and assembling the tank and components were not understood at the end of Phase I. The analogies were based on Quantum's tank estimate (Leavitt and Johnson 2010) and Directed Technologies, Inc.'s fuel cell estimation process (James et al 2002). The system costs were developed based on schematics shown in Figure 4.1, and the BOP components shown in Table 4.1. The BOP task provided proposed component model numbers, and manufacturers were contacted for pricing information.

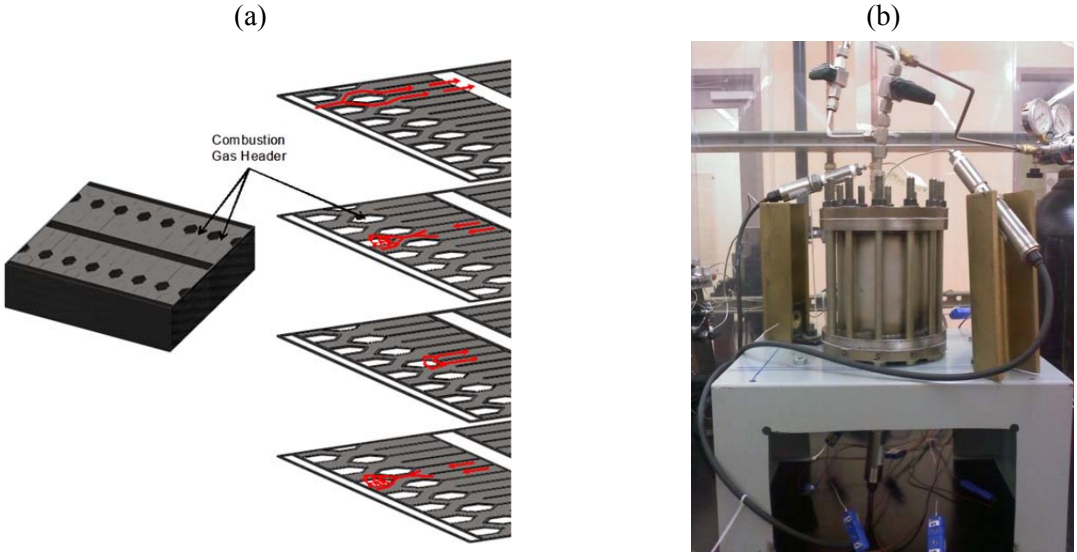

Figure 4.4. a) Integrated Microchannel Combustor Sketch and b) Unit Test Cell

4.2.2 Objectives

A cost model was developed to estimate of the system costs and the cost per kilowatt hour of usable hydrogen stored to determine how close the system approached the DOE developed cost targets. During Phase I, the cost targets were removed for revision. At the time, cost targets had been at $4 and $2 per kWh for 2010 and 2015, respectively. DOE recently revised the cost targets to $10/kWh for 2020 and the ultimate target of $8/kWh (DOE and USDrive 2015). The values for the system were used in the well-to-wheels analysis to determine the life-cycle costs of the sodium alanate system and its impact on the total fuel cost for the sodium alanate systems. The cost model only develops the system's first cost starting at the edge of the car and ending just before the fuel cell. As such, the cost estimate does not provide an average cost for the adsorbent systems over their lifetime. Cost estimates, based on DOE requirements, were developed for 10,000, 30,000, 80,000, 130,000, and 500,000 units of annual production and maintained in 2005$ constant dollars. Progress ratios were used to adjust prices of materials and BOP items as quantities increased.

4.2.3 Approach

A mix of approaches was used to estimate the sodium alanate system costs. A bottom-up approach was used for obtaining the initial costs of all system components including the tanks. For example, at the end of Phase I, elements of the tank geometry such as wall thickness requirements for the tank were not known. Comparison of carbon fiber and metal thicknesses using netting requirements provided tank weights less than those associated with similar tanks from commercial tank manufacturers. Lincoln Composites (now Hexagon Lincoln) and another manufacturer indicated that U.S. Department of Transportation requirements impact the weight. Another company indicated that, because of the Department of Transportation certification requirement, lots above 10,000 do not afford much in the way of scales of economy. Thus, commercially available Type-III tanks that met the pressure, temperature, and size requirements and were already in production were identified. The manufacturer was contacted, and prices for tanks at low and high volumes were obtained.

The costs for different materials were obtained from the manufacturer. For sodium alanate, prices were obtained for varying quantities and ranged from $150 to $450/kg. The price provided for 500,000 units was $9/kg after adjustment to 2005$. The media cost varied considerably on the source of titanium dopant used. Price quotes for titanium(III) chloride ranged from $11,000 to $15,000/kg. ENG prices also were obtained from manufacturers, with the price ranging from $25 to $132/kg for small quantities and $10 to $25 for large quantities. OSU provided the cost of the combustor using their microchannel cost model. A heat exchanger model developed by OSU also was used to parametrically estimate the costs of the in-tank heat exchangers.

Most BOP component manufacturers, especially valve manufacturers, could not provide large quantity estimates because they did not have the annual production capacity. Estimates that were provided became the basis for discounts and progress ratios to determine costs at the differing levels of production. Discounts were applied to the vendor estimates if the cost estimate was from a distributor or retailer and not the manufacturer. Communications with automobile parts manufacturers and after-market parts industry indicated that a 30% markup was added for each level that a part went through. Thus, for each level away from the manufacturer that a price quote was received, a 30% price reduction was taken.[19,20]

[19] Personal communication with Frank Hampshire, Motor and Equipment Manufacturers Association, January 26, 2011

[20] Personal communication with Ron Rossi, Automotive Aftermarket Industry Association, January 26, 2011.

Progress ratios were used to evaluate prices for components and materials at different levels of consumption. Progress ratios and their meaning are described in Section 3.5.3.2.

4.2.4 Results

The cost of the two-tank sodium alanate system was about $8,000/system or $42.9/kWh. The cost was driven primarily by the requirement for two tanks at $3,756. The two tanks were required because more than 200 kg of media were required to release the 5.6 kg of usable hydrogen. Media totaled about $2,100 for the system. The BOP accounts for most of the remaining cost at approximately $1,800/system. A summary of the estimated system costs for the baseline, sodium alanate system is shown in Table 4.2.

Table 4.2. System Cost for Sodium Alanate (2005$)

	Production Amount				
	10,000	30,000	80,000	130,000	500,000
Total Costs	20,201	18,267	16,679	14,804	8,008
$/kWh					42.90

Item	10,000	30,000	80,000	130,000	500,000
Tanks ($/system)	5,187	4,652	4,250	4,073	3,756
Media ($/system)	9,016	8,843	8,588	7,373	2,105
Media Cost ($/kg)	39	38	37	32	9
BOP ($/system)	4,347	3,307	2,570	2,290	1,817
Assembly ($/system)	1,652	1,465	1,271	1,068	329

An analysis was undertaken to determine the impacts of a one tank system assuming that a material with two times the hydrogen carrying capacity was found. The analysis resulted in an improvement to $26.8/kWh for high volume production of 500,000 units per year. This is still significantly above the DOE 2020 and Ultimate hydrogen storage system cost targets of $10/kWh and $8/kWh, respectively.

Costs for BOP components are provided in Table 4.3. The BOP cost per system produced ranged from about $4,350 at 10,000 units to $1,800 units at 500,000 units. The decrease in costs was primarily due to the effect of progress ratios. The remaining discussion of BOP costs will focus on the costs at 500,000 units. The most expensive items in the list are the microchannel combustors as estimated by OSU at $188/unit for 500,000 units. Another relatively large cost was the isolation valves at $135 apiece. Prices for this valve were received from the manufacturer at 10,000 and 500,000 units. The progress ratio for the isolation valves progress ratio was 0.90, not a significantly large progress ratio. Based on a review of the literature on auto manufacturing practices, we assumed that auto manufacturers would force further reductions in costs (Planning Perspectives, Inc. 2009, Keller 2005). The pumps were a different issue where there progress ratio was significant at 0.70, driving the price down from $800 at 10,000 units to $108 for 500,000 units. The primary driver of costs often was just the sheer number of items required. For example, there were two check valves, two coolant valves, two flow controllers, and five pressure relief valves. Potential cost savings could be introduced by designing a system that reduced the number of valves required.

Figure 4.5 provides a breakdown by major system components. The media and the tanks comprise approximately 73% of total system costs. Valves add another 12%, while other BOP components provide 10% and assembly another 4%.

A comparative analysis of the HSECoE estimate and a previous TIAX estimate (DOE 2013) was undertaken to understand the differences in the two estimates. The TIAX estimate ranged from $11 to $14/kWh as compared with the HSECoE estimate of $42.9/kWh. The main differences in assumptions between the HSECoE and TIAX are identified in Table 4.4.

Comparing the HSECoE results to the TIAX results revealed that media costs were higher but on the same order as the previous studies. TIAX estimated sodium alanate costs at approximately $5/kg, although they stated that manufacturers indicated the cost of the processed mixture would be in the $10/kg region. The HSECoE estimated the costs at $9/kg at 500,000 units based on manufacturer quotes. The HSECoE media weighed 231 kg compared with 172 kg for the TIAX estimate, a difference of approximately 40%. Another significant difference between the TIAX estimate and the HSECoE estimate was the requirement for two tanks instead of just one. In addition, HSECoE obtained a price estimate for the Type-III tank from tank manufacturers while TIAX provided a cost estimate for the Type-III tank based on modeling of material plus processing costs. As previously noted at the time of the estimate, models were indicating lower thicknesses than were found in manufactured models in the marketplace. The HSECoE price for one tank was estimated to be approximately $1,500, whereas TIAX estimated the tank at $580.

Table 4.3. BOP Cost Estimates for Sodium Alanate System by Component

Item	Number/Volume/Length	10,000	30,000	80,000	130,000	500,000	Each
Internal to Tank Heating Fluid							
Oil tank	1	94	78	66	61	49	49
Oil pump	1	808	459	277	216	108	108
Coolant valve	2	157	133	114	106	86	43
Oil (Paratherm MR)	14 L	63	58	54	52	47	3
Tubes	5 m	91	88	86	85	83	17
Isolation valves	2	489	414	357	331	270	135
Hydrogen							
Blower for combustor	1	293	224	177	157	113	113
Catalytic heater (12 kW)	1	740	504	358	302	188	188
Flow controller	2	291	291	291	255	255	127
H_2 lines	12 m	37	37	36	36	35	3
Pressure transducer	1	50	43	37	34	28	28
Pressure regulator	1	125	120	114	112	106	106
Valves							
Check valves	2	138	104	80	71	50	25
Pressure relief valves	5	388	263	186	157	97	19
Manual valves	4	80	80	80	80	80	20
Pressure gauge	1	21	20	20	19	19	19
Cooling Hydrogen to Ambient Temperature							
Heat exchanger	1	437	352	200	180	171	171
Buffer tank	1	44	41	38	36	33	33
Total BOP		4,347	3,307	2,570	2,290	1,817	

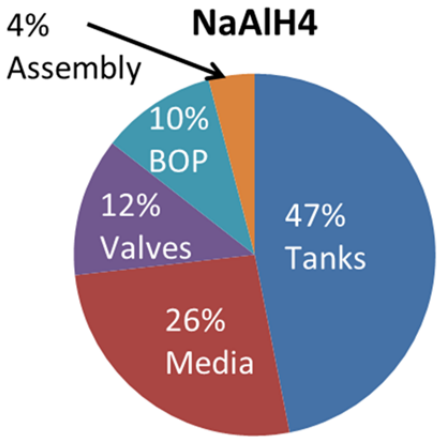

Figure 4.5. Cost Breakdown for Major System Components

Table 4.4. Comparison of HSECoE and TIAX Assumptions for Sodium Alanate

HSECoE Estimate	TIAX Estimate
• No highly aggressive progress ratios –Not enough design to be aggressive –Still nearly halves the cost of most parts –Consistent with economic theory on monopoly pricing vs. competitive pricing. • Weight = 457 kg • Cost/kg = $20 • Two tanks – Estimates obtained from Dynatek – Extra associated BOPs • Dehydriding System –~$1,000 for one system –Valves and pumps –These components need more attention. • Media needed = 231 kg –$9.00/kg – Obtained quotes, reduced with progress ratios to quantity – Titanium(III) chloride is pyrophoric material • 489 L	• Needs to be updated –$40 regulator is now $160 in most reports – Most BOPs listed at $40 each • Weight = 327 kg • Cost/kg = $6to $8 • One tank – Estimate made from component prices plus processing costs • Dehydriding System –$471 for one system – Cost breakdown is not provided. • Media needed = 172 kg –$4.85/kg –Estimated using basic plant costs –Based on information provided; a first-look type of estimate • 293 L

BOP costs in the HSECoE estimate were on the order of three to five times higher than in the TIAX estimate. The catalytic combustor as estimated by OSU at $188 was approximately six times more expensive than the TIAX combustor at $33. The blower cost at $113 and flow controller cost at $127 were significantly higher than TIAX's costs of $50 and $40, respectively. The blower estimate came directly from the manufacturer. The BOP associated with the heat exchangers in the two tanks also added significant cost at nearly $650 as compared with $78 in TIAX estimate. The oil pumps were similarly priced with HSECoE at $107 and TIAX at $90. The HSECoE estimate included two isolation valves at $135 each while there did not appear to be a similar item in the TIAX BOP. Another large difference was the sheer number of BOP components required by the HSECoE system as compared with the TIAX system. The HSECoE system required 31 components while the TIAX estimate had only 13 components, four of which were not in the HSECoE estimate. They were the hydrogen fill port, two coolant fill ports, and a fitting. The TIAX items would be required so their costs would need to be added to the HSECoE

system. In addition, later estimates by the HSECoE indicated that more than one fitting would be required to connect all the components. Based on the schematic in Figure 4.1, approximately 40 fittings would be required. In Phase I, the HSECoE assumed that all the joints would be welded, an assumption that later was found to be unjustified.

4.2.5 Comparison to Other Phase I Cost Estimates

Figure 4.6 compares the metal-hydride system to other HSECoE Phase I system cost estimates. The metal-hydride system costs ($42.9/kWh) primarily because of large amount of media needed to deliver 5.6 kg of usable hydrogen and its two tanks were almost two times more expensive than the solid AB system (~$24/kWh) and almost three times more expensive than the higher pressure (200 bar) MOF-5 system ($15/kWh). Valve costs were similar to the MOF-5 system.

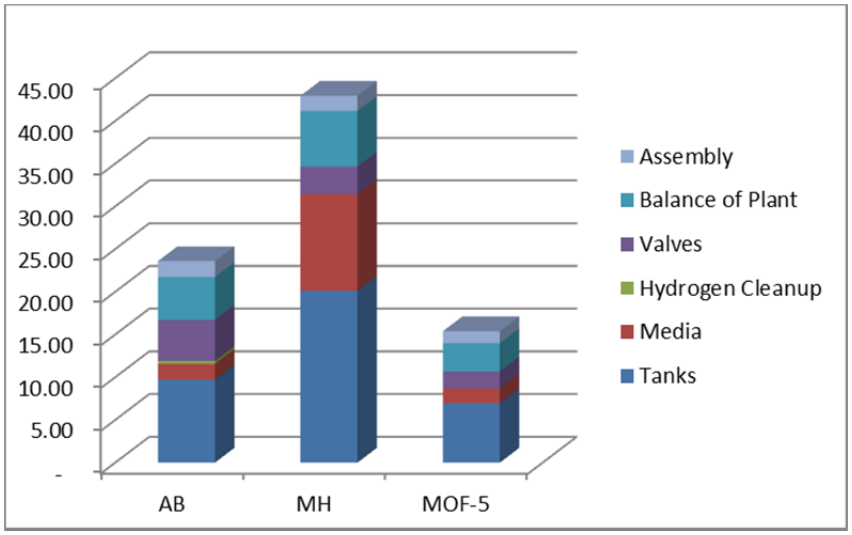

Figure 4.6. Comparison of Phase I System Cost Estimate

4.2.6 Conclusions for Metal Hydrides

The cost estimate for the sodium alanate onboard hydrogen storage system at $42.9/kWh was considerably higher than the initial DOE targets for 2010 and 2015 of $2/kWh and $4/kWh, respectively. Even the recently revised targets for 2015 of $10/kWh and $8/kWh for the ultimate target are significantly below the estimated $42.9/kWh. The volume of the sodium alanate needed to deliver 5.6 kg of usable hydrogen was the reason for the high cost of the system. This, in turn, required two tanks rather than one to meet OEM criteria for tank size limits. The tanks accounted for 43% of the system costs. Sodium alanate was called “novel” by one of the manufacturers, indicating that it is not a chemical in high demand which could have driven their estimated costs for the material. In addition, there was wide variation in prices for the titanium(III) chloride dopant. The media added another 32% to the cost of the system. Thus, the tanks including media account for more than 75% of the cost of the system. Methods to substantially lower the system cost for future metal-hydride systems involve reducing the system to a single-vessel design through a combination of compaction and/or finding a higher yielding metal hydride, and reducing the size and the costs of the oil circulating pump and hydrogen combustor. Adoption of these methods is expected to reduce the overall system cost for sodium alanate system by more than 25%.

5.0 References

Aggarwal S, SR Perusse, CW Tipton, R Ramesh, HD Drew, T Venkatesan, DB Romero, VB Podobedov, and A Weber. 1998. "Effect of Hydrogen on Pb(Zr,Ti)O_3-Based Ferroelectric Capacitors." *Applied Physics Letters* 73(1973-1975). doi:http://dx.doi.org/10.1063/1.122339.

Ahluwalia R, Q Hua, J-K Peng, S Lasher, K McKenney, and J Sinha. 2009. *Technical Assessment of Cryo-Compressed Hydrogen Storage Tank Systems for Automotive Applications*. ANL/09-33, Argonne National Laboratory, Argonne, Illinois. Available at http://energy.gov/sites/prod/files/2014/03/f9/cyro_compressed_auto.pdf.

Ahluwalia RK, TQ Hua, and JK Peng. 2012. "On-Board and Off-Board Performance of Hydrogen Storage Options for Light-Duty Vehicles." *International Journal of Hydrogen Energy* 37:2891. doi:10.1016/j.ijhydene.2011.05.040.

Alvine KJ, V Shutthanandan, WD Bennett, CC Bonham, D Skorski, SG Pitman, ME Dahl, and CH Henager, Jr. 2010. *Applied Physics Letters* **97**, 221911. doi:10.1063/1.3517445.

Alvine KJ, M Tyagi, CM Brown, TJ Udovic, T Jenkins, and SG Pitman. 2012. "Hydrogen Species Motion in Piezoelectrics: A Quasi-Elastic Neutron Scattering Study." *Journal of Applied Physics* 111:053505. doi:http://dx.doi.org/10.1063/1.3691114.

Alvine KJ, TA Kafentzis, SG Pitman, KI Johnson, DC Skorski, JC Tucker, TJ Roosendaal, and ME Dahl. 2014. "An In-Situ Tensile Test Apparatus for Polymers in High Pressure Hydrogen." *Review of Scientific Instruments* 85(10): 105110. doi:10.1063/1.4899315.

ASTM D638-08. 2008. "Standard Test Method for Tensile Properties of Plastics" ASTM International, West Conshohocken, Pennsylvania.

ASTM E1450-09. 2009. "Standard Test Method for Tension Testing of Structural Alloys in Liquid Helium.: ASTM International, West Conshohocken, Pennsylvania.

Avrami M. 1939. "Kinetics of Phase Change. I: General Theory." *Journal of Chemical Physics* 7:1103-1112.

Bogdanovic, B.; Schwickardi, M. Ti-doped alkali metal aluminum hydrides as potential novel reversible hydrogen storage materials. 1997. *J. Alloys Compd.,* 253–254, 1–9.

Brooks, Kriston P., Troy A. Semelsberger, Kevin L. Simmons, Bart Van Hassel, 2014a, "Slurry-based chemical hydrogen storage systems for automotive fuel cell applications," *Journal of Power Sources*, Vol. 268, pp. 950-959.

Brooks, Kriston P., Richard P. Pires, Kevin L. Simmons, 2014b, "Development and validation of a slurry model for chemical hydrogen storage in fuel cell vehicle applications," *Journal of Power Sources*, Vol. 271, pp. 504-515.

Castagnet S, J-C Grandidier, M Comyn, and G Benoît. 2010. "Hydrogen Influence on the Tensile Properties of Mono and Multi-Layer Polymers for Gas Distribution." International Journal of Hydrogen Energy 35:7633-7640. doi:10.1016/j.ijhydene.2010.04.155.

Chen, Feng, Kevin Simmons, Scot Rassat , Ewa C.E. Rönnebro, Young Joon Choi, Matthew Westman,"Dynamic Mechanical Properties of Ammonia-Borane and Related Compounds for Chemical Hydrogen Storage," to be submitted to *J. Phys. Chem. B*, 2016.

Choi, Y.U., E. Rönnebro, S. Rassat, A. Karkamkar, G. Maupin, J. Holladay, K. Simmons, K. Brooks, "Kinetics study of solid ammonia borane hydrogen release – modeling and experimental validation for chemical hydrogen storage," *Phys. Chem. Chem. Phys.,* 16 (17) (2014) 7959-7968.

Choi, J.Y, M. Westman, A. Karkamkar, J. Chun, E. Ronnebro, "Synthesis and Engineering Properties of Fluid Phase Chemical Hydrogen Storage for Automotive Applications," *Energy&Fuels*, 29(10), (2015), 6695–6703.

Chambon F and HH Winter. 1985. "Stopping of Crosslinking Reaction in a PDMS Polymer at the Gel Point." *Polymer Bulletin* 13(6):499-503. Accessed May 4, 2011, at http://www.springerlink.com/content/tw64364j37686022/.

CSA Group. 2014. "Fuel System Components for Natural Gas Powered Vehicles." CSA ANSI NGV 3.1-2014/CGA 12.3-2014, Canadian Standards Association. Information available at http://shop.csa.ca/en/canada/natural-gas-and-propane-vehicle-fuel-systems-and-industrial-engines/ansi-ngv-31-2014csa-123-2014/invt/27011092014.

Devarakonda MN, KP Brooks, E Ronnebro, and SD Rassat. 2012. "Systems Modeling, Simulation and Material Operating Requirements for Chemical Hydride Based Hydrogen Storage." *International Journal of Hydrogen Energy* 37(3):2779-2793.

Eisenberg A and J-S Kim. 1998. *Introduction to Ionomers*. Wiley Interscience, New York.

Freeman W.J. 1990. Polymers: Polymer Characterization and Analysis. John Wiley, New York.

Fukai Y. 2005. *Metal-Hydrogen System Basic Bulk Properties*. Second edition, ISBN-13 978-3-540-00494-3n Springer Berlin Heidelberg New York.

Graetz J and JJ Reilly. 2005. "Decomposition Kinetics of the AlH_3 Polymorphs." *Journal of Physical Chemistry B* 109(47):22181-22185.

Hatakeyama T and FX Quinn. 1999. *Thermal Analysis, Fundamentals and Applications to Polymer Science*. Second Edition., John Wiley, New York.

Hirscher, M. (Editor), *Handbook of Hydrogen Storage, New Materials for Future Energy Storage.* Wiley-VCH Verlag GmbH & Co., KGaA, Weinheim, Germany, 2010, ISBN: 978-3-527-32273-2.

Incropera F and D DeWitt. 1985. *Fundamentals of Heat and Mass Transfer*. Second Edition, John Wiley & Sons, New York.

James B, G Ariff, and R Kuhn. June 2002. "DFMA Cost Estimates of Fuel-Cell/Reformer Systems at Low/Medium/High Production Rates." Presented at Future Car Congress 2002, Directed Technologies, Inc. Arlington, VAMEPS. 2012. "North American Stainless Steel Prices." Accessed May 8, 2012, at http://www.meps.co.uk/Stainless%20Price-N.Amer.htm.

James BD, JM Moton, and WG Colella. 2013. "Hydrogen Storage Cost Analysis." *Proceedings of the 2013 US DOE Hydrogen and Fuel Cells Program Annual Merit Review*, May 14, 2013, Crystal City, Virginia. Available at http://www.hydrogen.energy.gov/pdfs/review13/st100_james_2013_o.pdf.

James BD. 2015. "2015 DOE Hydrogen and Fuel Cells Program Review: Hydrogen Storage Cost Analysis." Strategic Analysis. Available at http://www.hydrogen.energy.gov/pdfs/review15/st100_james_2015_o.pdf.

Jin T, JP Hong, H Zheng, K, Tank ZH Gan. 2009. "Measurement of Boiling Heat Transfer Coefficient in Liquid Nitrogen Bath by Inverse Heat Conduction Method. *Journal of Zhejiang University Science*, 10(5):691-696.

Ikarashi N. 1998. "Analytical Transmission Electron Microscopy Of Hydrogen-Induced Degradation in Ferroelectric Pb(Zr,Ti)O_3 on a Pt Electrode." Applied Physics Letters 73:1955 (Oct, 1998). http://dx.doi.org/10.1063/1.122333

International Standards Organization (ISO). 2012. "Plastics – Determination of Tensile Properties, Part 1: General Principles." ISO 527-1. ISO International, Geneva, Switzerland.

Jaravel J, S Castagnet, J-C Grandidier, and G Benoît. 2011. "On Key Parameters Influencing Cavitation Damage upon Fast Decompression in a Hydrogen Saturated Elastomer." *Polymer Testing* 30(2011):811-818 doi:10.1016/j.polymertesting.2011.08.003.

Jones RH and GJ Thomas (editors). 2008. *Materials for the Hydrogen Economy*. CRC Press, Boca Raton, Florida.

Kane MC. 2008. *Permeability, Solubility, and Interaction of Hydrogen in Polymers – An Assessment of Materials for Hydrogen Transport*. WSRC-STI-2008-00009, Rev. 0, Savannah River National Laboratory, Aiken, South Carolina. Available at http://sti.srs.gov/fulltext/WSRC-STI-2008-00009.pdf.

Keller M. 2005. "Crisis in the Automotive Parts Industry." *Automotive Industries*. Versailles, Kentucky. Available at http://www.ai-online.com/Adv/Previous/show_issue.php?id=704#sthash.5WMqSilk.dpbs.

Kollár LP and GS Springer. 2003. *Mechanics of Composite Structures*. Cambridge University Press, Cambridge, England.

Leavitt M and B Johnson. 2010. "Development of Advanced Manufacturing Technologies for Low Cost Hydrogen Storage Vessels." *DOE Hydrogen Program 2009 Annual Summary*, DOE/GO-102009-2950, Washington, D.C**.** http://www.hydrogen.energy.gov/annual_progress09.html.

Lee HM. 1976. "The Solubility of Transition Metals in Hydrogen." *Metallurgical and Materials Transactions A* 7:431.

Linehan S, N Allen, B Butterick, A Chic, N Kendall, L Klawiter, S Mancroni, D Millar, D Molzahn, and S November. 2010. *Low-Cost Precursors to Novel Hydrogen Storage Materials*. Project ID #ST042, Dow Chemical Company, Midland, Michigan.

Lu G and E Kaxiras. 2005. "Hydrogen Embrittlement of Aluminum: The Crucial Role of Vacancies." *Physical Review Letters* 94, 155501. http://dx.doi.org/10.1103/PhysRevLett.94.155501.

McLaughlan PB, SC Forth, and L Grimes-Ledesma. 2011. *Composite Overwrapped Pressure Vessels: A Primer*. NASA/SP–2011–573, National Aeronautics and Space Administration, Johnson Space Center, Houston, Texas. Available at http://ston.jsc.nasa.gov/collections/TRS/_techrep/SP-2011-573.pdf.

Menczel JD, RB Prime, and PK Gallagher (editors). 2008. *Thermal Analysis of Polymers*. John Wiley & Sons, Inc.

Menard KP. 1999. *Dynamic Mechanical Analysis a Practical Introduction*. CRC Press, Boca Raton, Florida.

MEPS North American Steel (MEPS). 2010. "North American Stainless Steel Prices." Accessed on November 9, 2010, at http://www.meps.co.uk/Stainless%20Price-N.Amer.htm. This website is updated monthly.

Mori D, and K Hirose. 2009. "Recent Challenges of Hydrogen Storage Technologies for Fuel Cell Vehicles." *International Journal of Hydrogen Energy* 34(10):4569-4574. doi:10.1016/j.ijhydene.2008.07.115.

Motyka T. 2014. *Hydrogen Storage Engineering Center Of Excellence Metal Hydride Final Report*. SRNL-STI-2014-00226, Savannah River National Laboratory, Aiken, South Carolina.

National Engineering Technology Laboratory (NETL). August 2013. Quality Guidelines for Energy Sytem Studies: Techology Learning Curve (FOAK to NOAK). Accessed April 10, 2014, at http://www.netl.doe.gov/File%20Library/research/energy%20analysis/publications/QGESS_FOAKtoNOAK_Final.pdf

Newhouse N. 2010. "Tank Manufacturing, Testing, Deployment, and Field Performance." Presented at the International Forum on Pressure Vessels for Hydrogen and Natural Gas Vehicles, September 27-28, Beijing, China. Available at http://energy.gov/sites/prod/files/2014/03/f10/ihfpv_newhouse.pdf.

Ott KC. 2010. *Final Report for the DOE Chemical Hydrogen Storage Center of Excellence*. LA-UR-20074, Los Alamos National Laboratory, Los Alamos, New Mexico. Available at http://www1.eere.energy.gov/hydrogenandfuelcells/pdfs/chemical_hydrogen_storage_coe_final_report.pdf

Peters MS and KD Timmerhaus. 1991. Plant Design and Economics for Chemical Engineers. Fourth Edition, McGraw-Hill Chemical Engineering Series, Republic of Singapore.

Planning Perspectives, Inc. 2009. "Annual Automotive Supplier Survey." Birmingham, Alabama.

Rassat SD, CL Aardahl, T Autrey, and RS Smith. 2010. "Thermal Stability of Ammonia Borane: A Case Study for Exothermic Hydrogen Storage." *Energy & Fuels* 24(4):2596-2606.

Rohsenow WM, JP Hartnett, and YI Cho. 1998. *Handbook of Heat Transfer*. Third Edition, McGraw Hill, Boston, Massachusetts.

Shalaby SW. 1981. "Thermoplastic Polymers." In *Thermal Characterization of Polymeric Materials*, (E Turi, editor), pp 235-364, Academic Press.

Tsuchiya H and O Kabayashi. 2004. "Mass Production Cost of PEM fuel Cell by Learning Curve." *International Journal of Hydrogen Energy* 29(10):985-990. doi:10.1016/j.ijhydene.2003.10.011.

U.S. Department of Defense (DOD). 2003. *Department of Defense Handbook: Metallic Materials and Elements for Aerospace Vehicle Structures*. MIL-HDBK-5J. U.S. Department of Defense. Wright-Patterson Air Force Base, Ohio.

U.S. Department of Energy (DOE). June 2013. "Onboard Type IV Compressed Hydrogen Storage Systems – Current Performance and Cost." June 11, 2013. Available at http://hydrogen.energy.gov/pdfs/13010_onboard_storage_performance_cost.pdf.

U.S. Department of Energy (DOE). 2014a. DOE Fuel Cell Technologies Office, Comparison of Fuel Cell Technologies. http://energy.gov/eere/fuelcells/downloads/comparison-fuel-cell-technologies.

U.S. Department of Energy (DOE). 2014b. DOE Fuel Cell Technologies Office, Hydrogen Storage Website. http://www.eere.energy.gov/hydrogenandfuelcells/storage/hydrogen_storage_testing.html.

U.S. Department of Energy (DOE). 2014c. Hydrogen Storage Engineering Center of Excellence Web Site. Available at http://hsecoe.org/.

U.S. Department of Energy and U.S. Drive Partnership (DOE and US Drive). 2015. "Target Explanation Document: Onboard Hydrogen Storage for Light Duty Fuel Cell Vehicles." Available at http://energy.gov/sites/prod/files/2015/05/f22/fcto_targets_onboard_hydro_storage_explanation.pdf.

van Sark W. 2008. "Introducing Errors in Progress Ratios Determined From Experience Curves." *Technological and Forecasting & Social Change* 75(2008):405-415.

Villalonga S, C Thomas, F Nony, F Thiebaud, M Geli, A Lucas, K Kremer-Knobloch, C Maugy. 2011. "Application of Full Thermoplastic Composite for Type IV 70 MPa High Pressure Vessels." Presented at the 18th International Conference on Composite Materials, August 2011, Jeju, South Korea.

Westman, M., J. Chun, YJ Choi, E. Rönnebro, "Materials Engineering and Scale Up of Fluid Phase Chemical Hydrogen Storage for Automotive Applications," *Energy&Fuels,* 30 (1), (2016), 560-569.

Wong J. 2010. "Composite Tank Testing, Certification, and Field Performance." Presented at the International Forum on Pressure Vessels for Hydrogen and Natural Gas Vehicles, September 27-29, Beijing, China. http://energy.gov/sites/prod/files/2014/03/f11/ihfpv_wong.pdf

Yamabe J and S Nishimura. 2009. "Influence of Fillers on Hydrogen Penetration Properties and Blister Fracture of Rubber Composites for O-ring Exposed to High-Pressure Hydrogen Gas." *International Journal of Hydrogen Energy* 34:1977-1989. doi:10.1016/j.ijhydene.2008.11.105.

Yamabe J, T Matsumoto, and S Nishimura. 2011. "Application of Acoustic Emission Method to Detection of Internal Fracture of Sealing Rubber Material by High-Pressure Hydrogen Decompression Polymer Testing." 30:76-85. Available at doi:10.1016/j.polymertesting.2010.11.002.

Zhao Z and M Carpenter. 2005. "Annealing Enhanced Hydrogen Absorption in Nanocrystalline Pd/Au Sensing Films." Journal of Applied Physics 97, 12430. doi: 10.1063/1.1927690.

Zheng J, X Liu, P Xu, P Liu, Y Zhao, and J Yang. 2012. "Development of High Pressure Gaseous Hydrogen Storage Technologies." International Journal of Hydrogen Energy 37:1048-1057. doi:10.1016/j.ijhydene.2011.02.125

Zidan R, B Garcia-Diaz, C Fewox, A Harter, A Stowe, and J Gray. 2009. “Aluminum Hydride: A Reversible Material for Hydrogen Storage.” Accessed April 24, 2014 at http://sti.srs.gov/fulltext/SRNL-STI-2009-00015.pdf.

Appendix A

Details for Hexcell and MATI System Cost Estimates

Appendix A

Details for Hexcell and MATI System Cost Estimates

This appendix provides more detail on the Hexcell and MATI cost estimates, including prices and systems at a more detailed level than found in the main body of the report. Table A.1 includes the prices or costs used for small-volume quantities obtained through quotes from manufacturers, distributors, retailers, or websites. The information provides the basis for the estimates at higher production volumes. Table A.1 also includes the estimate of the progress ratio used to estimate the costs for higher production volumes for each item. Tables A.2 and A.3 provide greater detail on the rolled up costs found in Tables 2.10 and 2.11 for the Hexcell system and MATI systems, respectively.

Table A.1. Small Volume Prices used to Estimate System Costs

Item	Part number or detail	Comments	Small Quantity	Progress Ratio
Boss and Plug	Based on TIAX value @ 500,000 units	each	$ 15.00	0.94
G10 spacers for LN2 Chiller Channel	0.266" spacers 1" long from 3'X4' x 0.375'; 6480 per sheet cost of 4.6 cents each 2015$ Used Costimator to estimate	each	$ 2.95	1.00
G-10 Rings for Vacuum Tank	3'x4'x1/2" Board	each	$ 40.30	0.90
MLVSI	Lydall CRS Wrap	per sheet	$ 2.67	0.95
Heater Elements cable heater	Watlow 24 volt; 4.65 w/cm^2; 4.5 m length; standard leads Watlow24 v	each	$ 156.55	0.90
Brackets	18" diameter fuel tank brackets with	each	$ 204.00	0.85
Heat Exchanger	GEA PHE MPN5X12-16 (1" MPT)	each	$1,424.00	0.90
Tubing	Gates 1.0" I.D. straight coolant line. Product number 41781516	$/foot	$ 4.81	0.95
Ethylene Glycol		$/liter	$ 1.23	1.00
Distilled water		$/liter	$ 0.00	-
Hose Clamp	Gates stainless steel hose	each	$ 2.50	0.95
FC Coolant Bypass Valve	ASCO 3-Way 24V Solenoid Series	each	$ 123.33	0.95
Insulation	K-Flex Insul Sheet with PSA	$/kg	$ 5.72	0.95
Hydrogen Fitting	Swagelok 1/2" female to NPT 1" female. Product number SS-810-7-16	each	$ 35.00	0.95
Temperature Sensor	GP50 Temperature Transmitter 7710-2-CA	each	$1,350.00	0.77
Multiple Port Receptacle	WEH Gas Technology	each	$ 652.00	0.90
Separation Valve with Manual	26 Series 2-way Ball Valve	each	$ 90.00	0.95
Insulation	For Tubing	$/foot	$ 1.78	
Tubing SS 316	SS316-Swagelok SS-T4-S-035-6ME	$/foot	$ 2.46	0.99
Automatic Valve	Circle Valve Technologies, Inc. Item	each	$ 710.26	0.78
Check Valves	K220T1-2PP-1/Circle Seal	each	$ 249.00	0.84
Pressure Regulator	TESCOM 20-1263-24-01 Circle Seal	each	$ 360.00	0.95
Pressure Regulator	Swagelok KPR1GRA 422A300000	each	$ 246.00	0.95
Controller	Email from Grevill Hampson, 4/30/2015, AX020510 6 input, 5	each	$ 225.00	0.96
Filter	Mott Corporation (need particle size details)	each	$1,848.00	0.75
Temperature Sensor	GP50 Temperature Transmitter 7710-2-CA	each	$1,350.00	0.78
Burst Disk	Swagelok	each	$ 40.00	0.90
Vacuum Port	JNWMVCR2514	each	$ 43.29	0.95
Pressure Relief Valve	M5180T1-4MP-1450 /Circor Seal	each	$ 349.49	0.89
Pressure Relief Valve	8100-55T1T1 /Circor Seal	each	$ 291.00	0.78
Vent Relief Valve	Added based on SA comparison	each	$ 19.00	0.99
Automatic Shutoff Valve	Added based on SA comparison	each	$ 64.50	0.90
H_2 Pressure Sensor	Kulite CT-190 Cryogenic Pressure Transducer GP:50 Pressure Transducer 7720-2-RT-G-CA	each	$ 881.00	0.83

Table A.2. Details of the Hexcell system costs (2007$)

Hexcell System	Quantity	Units of Production (2007$) 10,000	30,000	80,000	130,000	500,000
Tank						
Aluminum Tank	58.17	437	403	375	362	259
Boss and Plug	1.00	20	19	17	16	16
LN2 Chiller Wall	28.42	214	197	183	177	126
G10 spacers	8.00	16	14	14	14	14
G-10 Rings	4.00	42	35	30	28	23
MLVSI	90.00	138	128	119	115	104
Vacuum Shell	14.28	107	99	92	89	64
Getter	1.00	18	17	16	15	14
Heat Exchanger	1.50	99	75	59	52	38
Heater Elements	1.00	31	26	23	21	17
Brackets	1.00	28	22	17	15	11
Sub-total		1,151	1,035	945	905	685
Media						
MOF-5	29.94	728	567	454	407	299
Hydrogen	5.96	18	18	18	18	18
Sub-total		746	585	472	425	317
Manufacturing Costs		1,795	949	620	530	343
Heating Loop						
Heat Exchanger	1.00	369	312	269	250	203
Tubing	2.00	3	3	3	3	2
FC Coolant	4.50	3	3	3	3	3
Hose Clamp	6.00	9	8	7	7	6
Coolant Bypass Valve	1.00	55	50	47	45	41
Insulation	1.36	3	3	3	3	2
Hydrogen Fitting	18.00	261	241	224	216	196
Temperature Sensor	1.00	94	62	42	35	21
Sub-total		796	682	598	562	475
Valves and other BOP						
Multiple Port Receptacle	2.00	419	354	305	283	230
H2 Wetted Tubing	7.00	13	12	12	12	11
H2 Wetted Tubing	16.00	17	16	16	16	16
Elevated Design	1.00	952	728	596	545	452
Pressure Regulator	1.00	174	159	147	141	126
Controller	1.00	134	126	119	115	106
Filter	1.00	185	117	78	64	36
Burst Disk	1.00	13	11	10	9	7
Vacuum Port	1.00	19	18	16	16	14
Vent Relief Valve	1.00	15	15	15	15	14
Automatic Shutoff Valve	1.00	16	13	11	11	9
Sub-total		1,957	1,570	1,325	1,226	1,023
Total All BOP		2,753	2,251	1,922	1,788	1,499
Assembly and Markup		392	301	238	212	154
Grand Total		6,838	5,122	4,197	3,859	2,998

Table A.3 Details for MATI system cost (2007$)

		Units of Production (2007$)				
	Quantity	10,000	30,000	80,000	130,000	500,000
Tank						
Aluminum Tank -- T6061-T6	48.12	362	333	310	299	214
Boss and Plug	1.00	20	19	17	16	16
LN2 Wall Chiller Channel	25.10	189	174	162	156	112
G10 spacers for LN2 Chiller Channel	8.00	16	14	14	14	14
G-10 Rings for Vacuum Tank	4.00	42	35	30	28	23
MLVSI	80.00	123	113	106	102	92
Vacuum Shell	12.75	96	88	82	79	57
Getter	1.00	18	17	16	15	14
MATI	1.00	631	322	240	222	200
Sub-total		**1,497**	**1,116**	**977**	**932**	**742**
Media						
MOF-5	49.33	1,200	935	748	670	493
Hydrogen	5.62	17	17	17	17	17
Sub-total		**1,217**	**952**	**765**	**687**	**510**
Manufacturing Costs (tank including media)		**1,906**	**964**	**606**	**511**	**322**
Heating Loop						
Heat Exchanger	1.00	369	312	269	250	203
Tubing	3.00	8	7	7	7	6
FC Coolant	4.50	3	3	3	3	3
Hose Clamp	12.00	17	16	15	14	13
FC Coolant Bypass Valve	1.00	55	50	47	45	41
Insulation	2.00	5	4	4	4	4
Hydrogen Fitting	23.00	334	308	286	276	250
Temperature Sensor	2.00	187	123	85	70	42
Sub-total		**977**	**824**	**715**	**669**	**562**
Valves and other BOP						
Multiple Port Receptacle	1.00	210	177	152	141	115
H2 Wetted Tubing	14.00	26	24	24	23	22
H2 Wetted Tubing	16.00	17	16	16	16	16
Elevated Design	1.00	1,056	811	667	610	504
Pressure Regulator	1.00	174	159	147	141	126
Controller	1.00	134	126	119	115	106
Filter	1.00	185	117	78	64	36
Burst Disk	1.00	13	11	10	9	7
Vacuum Port	1.00	19	18	16	16	14
Vent Relief Valve	1.00	15	15	15	15	14
Automatic Shutoff Valve	1.00	16	13	11	11	9
Sub-total		**1,864**	**1,488**	**1,255**	**1,161**	**971**
Total All BOP		**2,841**	**2,312**	**1,970**	**1,831**	**1,533**
Assembly and Markup		**428**	**329**	**260**	**232**	**168**
Grand Total		**7,889**	**5,672**	**4,579**	**4,192**	**3,275**

Distribution

No. of Copies

OFFSITE

1 Ned Stetson, Fuel Cell Technologies Office
1 Jesse Adams, Fuel Cell Technologies Office

No. of Copies

ONSITE

1 **Pacific Northwest National Laboratory**
1 Kriston Brooks, K6-28

Pacific Northwest
NATIONAL LABORATORY

Proudly Operated by Battelle *Since 1965*

U.S. DEPARTMENT OF
ENERGY

902 Battelle Boulevard
P.O. Box 999
Richland, WA 99352
1-888-375-PNNL (7665)
www.pnnl.gov